UNIVERSITAT POLITÈCNICA DE CATALUNYA BARCELONATECH

Numerical modeling of cracking along non-preestablished paths

by

Laura Crusat Codina

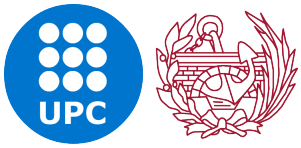

School of Civil Engineering of Barcelona
UPC BARCELONATECH

Numerical modeling of cracking along non-preestablished paths

Doctoral Thesis submitted by:
Laura Crusat Codina

Supervised by:
Ignacio Carol

Doctoral Program in Geotechnical Engineering and Geo-Sciences
Division of Geotechnical Engineering and Geo-Sciences
School of Civil Engineering (ETSECCPB)

Barcelona, September 2018

Agraïments

Després d'haver dedicat els darrers cinc anys al desenvolupament d'aquesta tesis doctoral volia remarcar que no es solament fruit d'un esforç individual sinó que s'ha realitzat amb l'ajuda de moltes parts i que ha estat un gran privilegi formar part del grup de recerca MECMAT de la secció (antic departament) d'Enginyeria del Terreny de l'Escola de Camins (UPC).

En primer lloc, estic especialment agraïda al meu director de tesi, el professor Ignasi Carol pel temps que m'ha dedicat, per la seva paciència, consells, ganes de compartir coneixement i per les seves oportunes idees en moments en que semblava difícil avançar. Sense ell aquesta tesis no hagués estat possible. També, al Dr. Daniel Garolera, amb qui he treballat conjuntament en el desenvolupament teòric i pràctic d'XFEM, a més a més, sempre s'ha mostrat molt proper a l'hora de donar un cop de mà als altres i al qual li agraeixo la seva ajuda i els bons consells que m'ha donat.

Durant aquest període també he conegut companys del departament amb qui he compartit tant dubtes sobre la part més teòrica de les nostres tesis com converses quotidianes; Ariadna, Irene, Carles, Daniel, Adrià, Lluís, Josbel i a tota la resta, gràcies per haver compatit coneixement i bons moments plegats. I parlant d'amistat, no pot faltar el meu agraïment als amics de Vilanova i de Cubelles, que m'han ajudat, animat i distret en els moments que ho he necessitat.

Com no podia ser menys, agraeixo a tota la meva família, especialment als meus pares i al meu germà per haver-me fet costat no només aquests darrers anys sinó sempre. Per haver confiat plenament en les meves decisions, per haver-me donant ànims i ajudat en tot el que ha estat possible.

Per acabar, també mencionar l'aportació econòmica en forma de beca rebuda durant gran part del meu doctorat a càrrec del Ministeri d'Economia, Indústria i Competitivitat.

Abstract

The general objective of this thesis is the numerical description of discrete cracks and their propagation using concepts of Configurational Mechanics, in such a way that their trajectory really corresponds to an energy minimum and is not predetermined by the initial mesh lines. As the first step, two existing formulations for discrete cracks and discontinuities of pre-determined orientation are revisited: the traditional zero-thickness interface elements (FEM+z), and the more recently developed eXtended Finite Element Method (XFEM). The latter method allows us to represent discontinuities running skew to the mesh lines by adding additional degrees of freedom to the nodes of the elements crossed by the discontinuity. Since the FEM+z approach has been extensively studied in the group and is fully implemented and tested, the effort in this first part of the thesis is directed to XFEM.

The XFEM is studied in detail, a formulation is developed and implemented in a Matlab code, and some examples of validation are also run. Some theoretical aspects are investigated such as the equivalence with the traditional interface elements, which is proven to hold under certain conditions, or the reason for pathological jumps observed in traditional implementations of the method using "natural interpolation", which may be attributed to lack of conformity of interpolation functions between the two sides of the original element, along the intersection with the discontinuity line. Compared to existing literature, the formulation developed and implemented exhibits two non-standard aspects: a) the re-interpolation (or "two-step" interpolation) of the variables from the nodes to the discontinuity intersection points first, and from there to the interior points of the subdomains (instead of the traditional direct interpolation by means of the original interpolation functions of the element), and b) the use of additional degrees of freedom of the "overhang" or "cantilever" type (value that the nodal displacements would have on the other side of the discontinuity in the absence of jump) instead of the traditional values of the displacement "jumps" themselves. Additional new developments relate to practical aspects of implementation such as treatment of nodes lying too close to the discontinuity, which are moved onto the discontinuity itself in order to eliminate numerical problems.

The second part of the thesis focuses on the use of the concepts and principles of Configurational Mechanics theory to modify the orientation of the cracks, in order to ensure that he trajectory obtained corresponds to an energy minimum and minimize its dependency on the original mesh layout. The long-term objective of the research undertaken is to apply these concepts to both FEM+z and XFEM. However, due to time constraints, the present thesis focuses on reviewing and discussing the theoretical concepts of Configurational Mechanics, clarifying how to use them

for crack reorientation in the context of non-linear FEM formulations, and implementing a crack reorientation scheme in combination with the traditional FEM+z formulation, while the application of the same concepts to XFEM, although conceptually similar, has been left for future development.

Configurational forces are defined as the energy gradients relative to the nodal position of the mesh nodes. Therefore, reorienting the fractures in the direction indicated by these forces should minimize the elastic global energy and fracture trajectories should be reproduced more realistically. Based on this idea, an additional "configurational" loop is added to the standard scheme of incremental-iterative process for "deformational" non-linear structural analysis. For each iteration of the new configurational loop, configurational forces are evaluated and the coordinates of some nodes are modified according to the direction indicated by those forces. The underlying FEM+z non-linear model incorporates the non-linear constitutive law for discrete cracks and discontinuities based on fracture concepts proposed by (Carol et al., 1997). A new iterative strategy of the indirect displacement control (IDC) type, which is based on fracture dissipation, has been developed. As in other IDC methods, the external load (or prescribed displacement) factor is not pre-established and is updated at each iteration in order to satisfy the indirect constraint, in this case the increment of dissipated fracture energy, which is adjusted so that fractures open only by one element length at each load increment. The change of nodal coordinates at each configurational iteration is applied selectively; only fracture tip nodes of the interface elements that begin to open (change of elastic to elasto-plastic state) are allowed to change their configurational position, while all other nodes are considered configurationally "prescribed".

Implementation in Matlab code and application of the proposed crack realignment procedure in application examples, have shown a number of practical problems to solve. One of most important is the discretization error intrinsic to the FEM, which is also reflected in the elastic energy evaluated for any given mesh. If significant, this energy "background noise" may generate spurious gradients that may interfere with the "physical" configurational energy gradients (e.g. energy gradients due to change of physical orientation of a crack). Solutions implemented to reduce this problem include: a) local grid refinement (LGR) procedures with deformational as well as configurational parametrization, and b) the use of quadratic elements. A second problem also observed as the process advances and the nodes change position, is mesh distortion and element entanglement. This has required the implementation of a "mesh relaxation" algorithm which, after each configurational iteration, is applied to the elements around the nodes which have just been moved. Finally, for all the nodes changing position for any reason, a procedure has been implemented to guarantee proper transport of the displacement values at the new nodal locations.

The examples of application mostly consist of simple crack propagation problems for which the fracture path is known a priori, either for physical reasons (e.g. symmetry) or by experimental results. The initial mesh layout is chosen such that mesh lines do not coincide with (and in fact zig-zag significantly with respect to) the known crack path. This includes, three-point beam bending with a centered load, beam bending with eccentric load, L-shaped panels and a two-notched structure in which the two cracks evolve simultaneously. In all the examples presented, the procedure implemented works successfully, that is, mesh lines do succeed in reorienting themselves during configurational iterations, so that the developing crack progressively matches the known physical trajectory.

Resum

L'objectiu general d'aquesta tesi és la descripció numèrica de fractures discretes i la seva propagació utilitzant conceptes de la Mecànica Configuracional, de tal manera que la seva trajectòria realment correspongui amb un mínim d'energia i no estigui predeterminada per les línies de la malla inicials. Com a primer pas, es revisen dues formulacions existents per a fractures discontínues i discontinuïtats d'orientació predeterminada: els elements tradicionals de gruix zero (FEM+z) i el mètode eXtended Finite Element Method (XFEM) desenvolupat recentment. Aquest últim mètode ens permet representar discontinuïtats que es troben a les línies de malla afegint graus de llibertat addicionals als nodes dels elements travessats per la discontinuïtat. Atès que l'enfocament de la formulació FEM+z ha estat àmpliament estudiada en el grup i està totalment implementada i provada, l'esforç en aquesta primera part de la tesi es dirigeix a XFEM.

El mètode d'XFEM s'ha estudiat detalladament, desenvolupat i implementat una formulació en un codi MATLAB, i s'han realitzat alguns exemples de validació. S'investiguen alguns aspectes teòrics, com l'equivalència amb els elements junta tradicionals, corroborat sota certes condicions, o la raó dels salts patològics observats en les implementacions tradicionals del mètode. Aquestes es deuen a la utilització de la "interpolació natural" i es pot atribuir a la manca de conformitat de les funcions d'interpolació entre ambdós costats de l'element original, al llarg de la intersecció amb la línia de discontinuïtat. En comparació amb la literatura existent, la formulació desenvolupada i implementada en aquesta tesi presenta dos aspectes no estàndards: a) la re-interpolació (o "interpolació en dos passos") de les variables dels nodes als punts d'intersecció de la discontinuïtat en primer lloc, i d'aquí als punts interiors dels subdominis (en comptes de la interpolació directa tradicional mitjançant les funcions d'interpolació originals de l'element), i b) l'ús de graus addicionals de llibertat del tipus "voladís" o "*cantilever*" (valor que els desplaçaments nodals tindrien a l'altre costat de la discontinuïtat en absència de salt) en comptes dels valors tradicionals del desplaçament de "salt". A més a més, es presenten altres aspectes pràctics innovadors sobre la implementació, com el tractament de nodes que es troben molt propers a la discontinuïtat, aquests es traslladen a la mateixa discontinuïtat per tal d'eliminar problemes numèrics.

La segona part de la tesi es centra en l'ús dels conceptes i principis de la teoria de la Mecànica Configuracional per a modificar l'orientació de les fractures, per tal de garantir que la trajectòria obtinguda correspongui a un mínim energètic i minimitzi la seva dependència respecte la malla original. L'objectiu a llarg termini de la investigació realitzada és aplicar aquests conceptes tant a FEM+z com a XFEM. Tanmateix, a causa de les limitacions de temps, la present tesi es centra en la revisió i discussió dels conceptes teòrics de la Mecànica Configuracional, aclarint com utilitzar-los

per a la reorientació de fractures en el context de formulacions no lineals de FEM i implementant un esquema de reorientació de fractures en combinació amb la formulació tradicional de FEM+z, mentre que l'aplicació dels mateixos conceptes a XFEM, encara que conceptualment són similars, s'ha deixat per a desenvolupaments futurs.

Les forces configuracionals es defineixen com a gradient d'energia en relació amb la posició nodal dels nodes de malla. Per tant, reorientar les fractures en la direcció indicada per a aquestes forces ha de minimitzar l'energia global elàstica i les trajectòries de fractura s'han de reproduir de forma més realista. Basat en aquesta idea, s'afegeix un llaç "configuracional" addicional a l'esquema estàndard del procés iteratiu incremental per a l'anàlisi estructural no lineal "deformacional". Per a cada iteració del nou llaç configuracional, s'avaluen les forces configuracionals i les coordenades d'alguns nodes es modifiquen segons la direcció indicada per aquestes forces. El model no lineal de FEM+z incorpora la llei constitutiva no lineal per a fractures discontínues i discontinuïtats basades en els conceptes de fractura proposats per Carol et al. (1997). S'ha desenvolupat una nova estratègia iterativa del tipus control de desplaçament indirecte (IDC), que es basa en la dissipació de la fractura. Com en altres mètodes IDC, el factor de càrrega externa (o desplaçament prescrit) no està preestablert i s'actualitza a cada iteració per satisfer la restricció indirecta, en aquest cas l'increment de l'energia de fractura dissipada, que s'ajusta de manera que les fractures obrin només la longitud d'un element en cada increment de càrrega. El canvi de coordenades nodals en cada iteració configuracional s'aplica selectivament; únicament els nodes de la fractura que es troben formant la punta dels elements junta que comencen a obrir (canvi d'estat elàstic a elasto-plàstic) poden canviar la seva posició configuracional, mentre que tots els altres nodes es consideren configuracionalment "prescrits".

La implementació en el codi Matlab i resolució d'exemples d'aplicació mitjançant el procediment de realineació de fractures proposat, han mostrat una sèrie de problemes pràctics per resoldre. Un dels més importants és l'error de discretització intrínsec al FEM, que també es reflecteix en l'energia elàstica avaluada per a qualsevol malla donada. Si és significatiu, aquesta energia "soroll de fons" pot generar gradients falsos que puguin interferir amb els gradients d'energia configuracionals "físics" (per exemple, gradients d'energia a causa del canvi d'orientació física d'una esquerda). Les solucions implementades per reduir aquest problema inclouen: a) els procediments locals de refinament de la malla o *Local Grid Refinement* (LGR) amb parametrització deformacional i configuracional, i b) l'ús d'elements quadràtics. Un segon problema també s'observa a mesura que avança el procés i els nodes canvien de posició, és la distorsió de malles i possible solapament entre elements. Això requereix la implementació d'un algoritme de "relaxació de malla" que, després de

cada iteració configuracional, s'aplica als elements del voltant dels nodes que s'acaben de moure. Finalment, per a tots els nodes que canvien la posició per qualsevol dels motius esmentats anteriorment, s'ha implementat un procediment per a garantir el correcte transport dels valors de desplaçament a les noves ubicacions nodals.

Els exemples d'aplicació consisteixen principalment en problemes de propagació de fractures simples per als quals es coneix a priori la ruta de la fractura, ja sigui per raons físiques (per exemple, simetria) o per resultats experimentals. El disseny de la malla inicial es tria de manera que les línies de malla no coincideixin amb (i de fet, zig-zag significativament pel que fa a) la coneguda trajectòria de fissura. En els exemples s'inclou, la flexió de tres punts d'una biga amb una càrrega centrada, la flexió de la biga amb càrrega excèntrica, panells en forma de L i una estructura de dues entalles en què les dues esquerdes evolucionen simultàniament. En tots els exemples presentats, el procediment implementat funciona correctament, és a dir, les línies de malla aconsegueixen reorientar-se durant les iteracions configuracionals, de manera que el desenvolupament progressiu de la fractura coincideix amb la trajectòria física coneguda.

Contents

Chapter 1

Introduction

1.1 Background and Motivation

Discontinuities such as cracks or fractures play a fundamental role in the description of mechanical processes in solids, in many engineering fields. In general, a discontinuity represents a plane of weakness that may modify substantially the state of stress and deformation of the surrounding continuum material, and therefore needs to be analyzed in detail and taken into account in any analysis. The study of cracking and fractures in solid structures or domains and the subsequent effects in their overall mechanical response, has been for decades one of the most active topics in solid mechanics in general, and in particular in Structural and Geotechnical Engineering, and lately also in Petroleum Engineering. The studies developed cover a large variety of aspects of the discontinuities in solids, among which two may be especially emphasized. First, from the theoretical viewpoint the theory of Fracture Mechanics and in particular the energetic propagation criteria based on energy release rates and fracture energy parameters, and even more precisely the non-linear fracture models such as cohesive crack (Dugdale, 1960) or the Fictitious Crack Model (FCM) (Hillerborg et al., 1976), may be considered fundamental bases for any study of the formation and propagation of cracks and fractures. Second, from the computational viewpoint the different numerical methods proposed in recent years for formation, evolution and residual effects on the mechanical behavior of structures or geological, are also an essential ingredient to reach accurate results and reliable predictions.

Focusing on numerical models for cracks or discontinuities, traditional classifications of the methods distinguish first between smeared and discrete approaches. Smeared approaches (Rashid, 1968) rely on the classical continuum elements with nodal displacements, including any open-

ing/sliding of the discontinuities in an "averaged" manner within the continuum deformations. Similarly, the laws governing the formation/evolution of the discontinuities have to be embedded into the continuum constitutive laws which inevitably exhibit softening; "fixed crack" and "rotating crack" models are early examples of that representation (Rots, 1988). This approach has the advantage of geometric simplicity, since in principle it should require a standard continuum FE mesh. However, already in the 80s a number of mathematical problems were identified, such as a pathological mesh dependency and lack of uniqueness of the solution, or difficulties of the standard continuum finite elements to represent general deformation states including opening/sliding of discontinuities. As a remedy, regularization techniques were proposed, such as the crack-band model, non-local continuum, Cosserat continuum, gradient plasticity, or gradient damage (Bažant and Oh, 1983; Pijaudier-Cabot and Bažant, 1987; Lasry and Belytschko, 1988; de Borst et al., 1995; Peerlings, 1999; de Borst, 2002; de Borst et al., 2004). However, neither of these methods provides a universal solution, and in general they require dense meshes in the zones subject to damage and fracture, the location of which in a general context is not known a priori. Recently, the new "phase-field" approach has emerged as an alternative. In these models, a new field variable similar to a damage parameter is added, with an additional diffusion-type equation which is coupled to the traditional mechanical equations. The overall system leads to the regularized solution of the mechanical localization problem (Miehe et al., 2010; Wu and de Lorenzis, 2016; Wu et al., 2017). Phase-field modeling is able to simulate complex fracture processes in a unified framework, including crack initiation, propagation, or merging and branching, without the need for external ad-hoc criteria. However, this technique also seems to require very dense meshes in the fracture zones, the location of which are not known a priori of the analysis in a general loading context.

The second big family of methods for crack representation belong to the discrete crack approach. This approach, often attributed to Ngo and Scordelis (1967), tries to represent the cracks/discontinuities explicitly by duplicating nodes and leaving the crack faces as free boundaries or (more conveniently in case of crack closure or friction/sliding) inserting zero-thickness interface elements (Rots, 1988). The crack opening criterion can be described via LEFM theory (e.g. Ingraffea et al., 1987), or more generally using Non-linear Fracture Mechanics (NLFM) concepts on the basis of the normal stress tractions along the Fracture Process zone (FPZ) line or plane, e.g. via Fictitious Crack Model (FCM) (Hillerborg et al., 1976), or generalizations using also normal and shear stress tractions in the FPZ generally in the form of a constitutive law for the cohesive interface elements (i.e. Stankowski et al., 1993; Carol et al., 1997; Caballero et al., 2008a; Wu and Wriggers, 2015). Meshwise, original discrete approaches were linked to LEFM and

implied continuous remeshing in order to be able to represent, at least approximately, the singular stress state at the crack tip (Ingraffea et al., 1987, FRANC code). Later, however, with the use of zero-thickness interface elements, the option was developed of pre-inserting interface elements along the expected crack path if that is known *a priori* (e.g. Rots, 1988), or otherwise pre-inserting interface elements along all potential crack trajectories (Stankowski, 1990; Vonk, 1992; Carol and López, 1998; López, 1999). This in general provides enough freedom for the crack to propagate, but has two disadvantages: (1) the increase in the number of nodes, and (2) cracks have to follow the mesh lines. The first problem is addressed by some authors by resolving first the stress tractions transmitted across neighbor elements and inserting the interfaces only when those stress tractions exceed the strength (Camacho and Ortiz, 1996). However, this requires quadratic elements and implies topological changes during the analysis. The second problem can be reduced by using a good strategy for FE meshing that includes in the lines the main potential crack paths, something easier in the case of microstructure (since there are known weakness planes/lines), but not so easy in the general case, and one of the motivations of the methods proposed in the present thesis.

In recent years, other methods not so clearly included in the smeared or discrete crack approaches have been proposed, such as meshless methods, EFEM, XFEM, etc. (Dvorkin et al., 1990; Belytschko et al., 1996; Belytschko and Black, 1999; Wells and Sluys, 2001; Zi and Belytschko, 2003; Borja, 2008; Nguyen et al., 2008; Belytschko et al., 2009; Das et al., 2015b). Among them the eXtended Finite Element Method (XFEM) deserves special attention. It basically consists of enriching the deformation degrees of freedom of the continuum finite element mesh by adding extra degrees of freedom to the nodes of the elements crossed by the discontinuity. The additional variables normally have the meaning of discontinuity displacement jumps, which are then interpolated over the affected elements in a way that ensures the continuity of the jump across neighbor elements. This in general avoids the need for additional non-mechanical artifacts (such as "tracking algorithms") required by other methods. The method, originally proposed by Moës et al. (1999) has the advantage of representing fractures without the need of modifying the underlying mesh topology. In addition, several authors Jirásek and Belytschko (2002); Zi and Belytschko (2003); Unger et al. (2007); Meschke and Dumstorff (2007) had presented interesting results of XFEM simulating crack propagation. In some of those papers, the crack is free to propagate through the mesh. However, the criteria for crack propagation and especially for crack propagation direction is not always based on consistent energetic considerations, and the crack tip representation adds considerable complexity in terms of the enrichment functions, etc. In the case of multiple discontinuities each one of them requires one set of enrichment variables for the elements crossed, plus

interaction variables in the elements crossed by more than one intersecting discontinuity (one set of element nodal variables for each pair of intersecting discontinuities, additional to the variables normally required for each of them). All that requires considerable bookkeeping and makes difficult to implement XFEM for the general case with multiple cracks, especially when those cracks propagate, which in general would imply continuous changes in number of nodal variables and information to store/update. A restricted version of XFEM for geomechanical applications has been proposed with multiple interacting but a priori fixed discontinuities, as it would correspond to the most relevant fractures found in a geological domain (Das et al., 2015a, 2016a,b). This version is the one considered in this thesis as another potential basis for more general crack propagation strategies.

With the general objective of developing a crack propagation approach with no pre-established trajectories, another essential ingredient is the criterion for crack propagation and, especially, for crack propagation direction. As already mentioned, most of the existing procedures rely on local criteria at the cracking point, such as direction of maximum tensile stress (Erdogan and Sih, 1963; Nuismer, 1975; Belytschko and Black, 1999; Dumstorff and Meschke, 2007). However, Fracture Mechanics (FM) principles imply that the energy dissipated at crack sites comes mainly from elastic energy released by stress unloading in the surrounding areas. One powerful way to introduce those concepts in standard FE analysis may be achieved by means of Configurational Mechanics (CM), which is concerned with the overall elastic energy changes due to changes in the material configuration (i.e. the original geometry of the structure/domain). Applied in the FEM context, configurational forces may be interpreted as vectors indicating the direction in which the coordinates of each node should be moved, in order to maximize or minimize the change of the overall elastic energy of the structure. These forces are obtained by the derivative of the energy with respect to the initial position of the node ("configuration"), and involve the so called Eshelby (pseudo-stress) tensor. The concept has obvious application for fracture propagation, since configurational forces at the crack tip will indicate the direction opposite to which that point should be moved (i.e. in which the crack should propagate) to maximize the overall elastic energy release. This idea, which has already been proposed and, to some extent also developed, in the literature (Denzer et al., 2003; Nguyen et al., 2005; Steinmann and Maugin, 2005; Miehe et al., 2007; Steinmann et al., 2009; Miehe et al., 2010; Kaczmarczyk et al., 2014), seems the ideal way to provide the necessary (but often missing) energetically consistent criterion for crack propagation direction.

In the context described, the main motivation of this thesis is to achieve the development of a model, that one the one side provides the possibility for the cracks to develop freely throughout

the mesh (and not constrained to the initial or background mesh), but at the same time does not represent an excessive or unmanageable burden on the calculations. At the same time, a second motivation is to incorporate in this model the necessary concepts and tools of Configurational Mechanics, so that the developing cracks take the orientations that are optimal from the global energetic viewpoint of the structure/domain. Two of the methods described above, namely the FEM+z and XFEM, seem capable of describing the behavior of solids with existing discrete discontinuities of known pre-determined location. They both seem possible good departure points to develop a strategy for general cracking. In this context, the thesis objectives, methodology and the document organization are described in the following.

1.2 Thesis objectives

As already mentioned, the final objective of the thesis is to describe and model the behavior of structures/domains undergoing discrete cracking along non-preestablished paths. In this thesis, this final objective is approached in two steps: (1) reviewing first the existing methods for discrete fractures with path fixed *a priori*, and (2) adding an iterative scheme based on Configurational Mechanics concepts, in which, by simply moving nodes, the crack geometry and orientation would be changed to provide a more realistic and physical crack path minimizing the overall elastic energy.

In the first review step (1), two methods have been selected that seem suitable to be modified according to step (2): the traditional Finite Element Method with zero-thickness interface elements (FEM+z), and the eXtended Finite Element Method (XFEM).

While FEM+z is an approach which was proposed in the early 70s (Goodman et al., 1968), has been developed and tested extensively, can be considered well established, and is already implemented in a number of FE codes including some commercial (e.g. ABAQUS), and also in the research group's code DRAC (López, 1999; Segura and Carol, 2004; Caballero, 2005; Segura, 2007; Idiart, 2009; Idiart et al., 2011; Garolera, 2017), XFEM can be considered a relatively novel technique only present in a limited number of research codes and some aspects of this method are still subject of research papers and to debate. In particular, several authors report spurious oscillations in the results, especially when the discontinuity lies near regular nodes, but also to a lesser extent in normal situations when this is not the case (e.g. Menouillard and Belytschko (2010); Sanders et al. (2009)). Also, by considering the type and number of additional variables introduced in XFEM, and the nature of the interpolation used to describe the jump fields, inevitable questions arise about the equivalence between this technique and the traditional FEM+z approach.

On the other hand, when it comes to step (2), i.e. incorporating the possibility of moving

nodes to accommodate the fracture trajectory to provide energy minima by using concepts such as Configurational Forces, the final objective is indeed to apply these methods to both FEM+z and to XFEM. However, as it has turned out, Configurational Mechanics is originally based on the general framework of Finite Deformation, which has required to first develop and implement a basic MATLAB code in this context. Then theoretical aspects such as for instance developing new small strain expressions for the configurational forces, reconciling them with their large strain counterparts, and derivations of such expressions at the FE level, have required considerable effort. Finally, implementation in MATLAB code of the new iterative scheme, with many associated algorithms (such as dissipation-based IDC, mesh relaxation, transport of variables, etc.), and have turned out time-consuming, and for this reason the new mesh realignment scheme has been developed only for FEM+z method, while extension to XFEM has been finally left out of the scope of this thesis for further future work.

In this context, the specific objectives that have been set for the present thesis are the following:

1. To develop, implement in MATLAB code and test an XFEM formulation for the treatment of pre-fixed discontinuities which overcomes reported problems such as spurious oscillations (in general, and more pronounced when the discontinuity crosses mesh lines too close to a node).

2. To investigate the theoretical comparison potential equivalence between the Finite Element Method with zero-thickness interface elements (FEM+z) and XFEM.

3. To implement in Matlab code the FEM+z formulation, including large deformations with the constitutive hyper-elastic laws for the continuum.

4. To formulate the problem of cracking along non-preestablished crack trajectories in FEM+z, as a problem of minimization of energy dissipation in large strain theory (Configurational Mechanics), and following the same principles of the formulation in small strain theory context.

5. To implement an iterative scheme to solve the problem of node relocation for energy minimization, and develop all the numerical techniques necessary for that purpose (including the appropriate iterative techniques, mesh disentanglement/relaxation if necessary, variable transport, etc.).

6. To verify the scheme developed with examples in which, by departing from an initial mesh

layout not well aligned with known crack trajectories, the mesh gets realigned properly during the process.

1.3 Methodology

The work contained in this thesis is related mainly to the areas of mechanical behavior of discontinuities, using concepts of Fracture Mechanics, Configurational Mechanics and numerical methods such as the Finite Element Method, zero-thickness interface elements, or XFEM. The methods developed may be used in the context of Solid Mechanics, Structural Mechanics, and Geomechanics, with potential applications in Civil, Geotecnical or Petroleum Engineering.

The development of the doctoral thesis takes place within the MECMAT research group (Mechanics and Nanotechnology of Engineering Materials) of the Universitat Politècnica de Catalunya (UPC). One of the research lines of this group is fracture modelling in the field of rock and concrete mechanics and most models and formulations developed in the group have been implemented in the group's general purpose FE code DRAC (Prat et al., 1993), which is in constant development by the members of the group (López, 1999; Caballero, 2005; Segura, 2007; Idiart, 2009; Garolera, 2017). In this thesis, however, and as explained below, the models developed have been implemented preliminarily in a separate MATLAB code for verification and testing. The present thesis has been partially supported within the framework of the project funded by MEC-Madrid entitled BIA2012-36898 *Mechanics of expansive processes in cement and concrete at micrometric scale, and applications*.

The literature review has been mainly focused on two aspects of the thesis: (1) discrete crack methods and in particular the eXtended Finite Element Method (XFEM) and (2) theory of Configurational Mechanics and application to crack propagation analysis. Additionally, more specific literature reviews has been carried out for specific aspects of the research such as energy-based IDC iterative methods, mesh relaxation methods, and other specific topics.

In the development of the thesis, the main efforts have been devoted to three aspects of the research:

1. Theoretical aspects of the formulations and methods such as XFEM, equivalence to FEM+z approach, explanation for spurious oscillations, Configurational Mechanics concepts, formulation of configurational forces for the finite element at and large and small strain , etc.

2. Numerical implementation and MATLAB code development: the strategy followed in the MECMAT group is that new theories and methods be developed first in separate simpler codes

and only after implemented/tested successfully be incorporated to the main code DRAC. In this spirit, two codes have been developed, one for the description of pre-fixed joints using a new XFEM formulation proposed, and the other for FEM+z including also the algorithm for moving the nodes for proper crack realignment, which incorporates an extra loop using configurational forces.

3. Application of the codes to solve simple verification examples. In the case of the XFEM code, the examples are chosen to be able to verify that the new XFEM formulation proposed and implemented can reproduce correctly the results known from theoretical solutions, and can also solve the problems identified in existing formulations such as spurious oscillations of various kinds. In the case of the FEM+z with crack realignment strategy, the examples have been aimed at verifying that the resulting model can successfully replicate the correct crack path, via proper realignment of the interface elements originally introduced in the mesh with orientations zigzagging the correct path, or also clouding the area where the crack must develop.

1.4 Thesis organization

The thesis document is organized in four chapters: the introduction, one chapter devoted to discrete cracking along pre-established path using XFEM, another devoted to crack realignment formulation based on FEM+z, and a final one with conclusions and future work.

The present Introduction starts with the background and motivation of the research done, explains the objectives established and the methodology followed in the thesis development, and ends with a brief description of the contents of each chapter.

The second chapter contains a brief introduction of Fracture Mechanics and interface elements and its main focus is on a particular version of the eXtended Finite Element Method (XFEM) with sub-interpolation to represent discrete fractures of known path. From a theoretical viewpoint, the equivalence of this new XFEM formulation to the traditional FEM+z approach is demonstrated for some specific cases, an explanation is found for oscillations reported in common XFEM formulations based on natural interpolation. Implementation aspects are described and finally, examples simulations to test the implementation of XFEM's code are also presented. The content of this chapter corresponds to a paper submitted and recently accepted in final form in a JCR journal (Crusat et al., 2018).

The third chapter focuses on crack propagation along non-preestablished paths using concepts

of Configurational Mechanics. It contains the detailed formulation of the configurational forces for finite elements at both large and small strain, and the selective change of nodal location. Auxiliary techniques, such as a new indirect displacement control iterative strategy based on fracture dissipation, or node relaxation strategies, are also detailed in this chapter. Apart from the theoretical development, examples of verification are presented in which the propagation path is approximately known.

Finally, last chapter summarizes the conclusions of the work presented in previous chapters, together with some ideas for future research. In addition, to facilitate the understanding of the numerical development of the XFEM formulation (Chapter 2), the interpolation matrix form for different configurations are developed in fully detail in Appendices A, B, C. Moreover, it is proven that XFEM can present spurious oscillations due to the use of a formulation based on natural shape functions; this formulation and its interpretation are found in Appendix D. Otherwise, Appendices E and F contain the derivative with respect to nodal coordinates of the shape function Cartesian derivatives used in FEM discretization of configurational forces, and the Jacobian derivative with respect to nodal coordinates.

Chapter 2

Representation of discrete fractures of known path

2.1 Introduction

The discontinuous displacement field associated to the presence of discontinuities has been incorporated in the FE analysis using different techniques such as standard continuum elements with appropriate softening laws (traditional "smeared approach", Mosler and Meschke, 2004; Oliver, 1989; Weihe et al., 1998), interface elements ("discrete approach", Gens et al., 1989; Carol et al., 1997; Kaliakin and Li, 1995), elements with embedded discontinuities Manzoli and Shing (2005); Linder and Armero (2007); Alfaiate et al. (2003); Jirásek (2000), or the extended finite element method (XFEM, Belytschko et al., 2003; Belytschko and Gracie, 2007; Fries and Belytschko, 2006, 2010; Sukumar et al., 2001; Mohammadi, 2008).

In the context of the present thesis, the interest is focused on approaches that represent fracture in a discrete manner, and which may be considered as suitable candidates for introducing crack realignment algorithms based on Configurational Mechanics concepts. After careful consideration, two formulations have been selected for this purpose: the traditional Finite element method with zero-thickness interface elements (FEM+z) and the more innovative method XFEM.

The content of the chapter is organized as follows: After this Introduction (Sec. 22.1), Section 2.2 discusses general aspects of fractures and Fracture Mechanics, and numerical methods to represent discontinuities. Section 2.3 is devoted to zero-thickness interface elements, including a summary of the formulation, the normal/shear cracking constitutive model and some aspects of interest for the numerical implementation. Section 2.4 deals with XFEM. General XFEM concepts

and the detailed XFEM formulation proposed, including the derivation of the stiffness matrices and force vectors based on the Principle of Virtual Work are included in Section 2.4.1. Section 2.4.2, discusses moving nodes which lie too close to the discontinuity, onto the discontinuity itself, and the resulting special configurations. In Section 2.4.3, the equivalence between the XFEM and zero-thickness interface elements is demonstrated for the "2-2" quadrangular configuration, and other configurations are discussed. Section 2.4.4 reports the numerical results obtained with the proposed formulation for three examples of application. These results are compared to either closed-form solution or to other numerical results from the literature. Finally, Section 2.4.5 summarizes the main achievements of the chapter and gives some concluding remarks. Appendices A to C at the end of the thesis, include specific expressions of the formulation matrices for quadrangular and triangular elements, and Appendix D includes a review of the standard natural interpolation scheme, with the possible explanation for the oscillations observed in the case of a skew discontinuity. An example of application showing comparison with new sub-interpolation scheme is also provided.

2.2 Preliminaries and general considerations

2.2.1 Fracture Mechanics theory

Fracture Mechanics is a scientific field of mechanics focused on defects and the study of propagation on stressed bodies under different conditions.

Cracks and their propagation play an essential role in most Engineering fields; in Structural Engineering (Fig. 2.1a) they may cause failure, but also excessive deformability, loss of water or gas tightness, or other serviceability problems. Fractures and faults in geological structures may be source of deformability and failure in Geotechnical Engineering (Fig. 2.1b), or induced seismicity in Petroleum Engineering of gas storage facilities.

Although the evaluation of the risk of fracture nowadays relies very much on numerical methods, those are developed on the basis of Fracture Mechanics theories. Fracture Mechanics theories try to establish the conditions under which cracks may propagate. They are based on concepts borrowed from continuum mechanics (such as stresses or energy), but in order to predict failure they introduce new paradigms, either if they are based on the intensity of the stress field near the crack tip (local stress intensity factor approach) or on a structural energy balance (global fracture energy approach).

Historically and also conceptually, two approaches to the formulation of Fracture Mechanics principles can be identified: Linear elastic Fracture Mechanics (LEFM) and Non-linear Fracture Mechanics (NLFM).

(*a*) (*b*)

Figure 2.1: The presence of mechanical discontinuities in concrete structures and in a geological environment. (a) Beam bending test (image from web: engineering.purdue.edu, Purdue University) (b) Geological discontinuity in a rock mass (left abutment of Canelles Dam in the Pyrenees mountains).

LFEM

Linear elastic Fracture Mechanics (LEFM) approaches the study of crack propagation assuming that, (1) the crack tip has zero dimension, (2) at the crack tip stresses become singular and non-linear phenomena take place with energy dissipation, and (3) the deformation in the remaining volume of the body remains linear elastic according to the generalized Hooke's law.

The most relevant contributions to this theory are usually attributed to Inglis (1913), Griffith (1921) and Irwin (1958).

Inglis (1913) was the first to describe the dependency of stress concentration factor k, a the tip of an elliptical hole in a stressed plate, on its radius of curvature $\rho = b^2/a$ (Fig.2.2a), as:

$$k = \frac{\sigma_A}{\sigma} = 1 + \frac{2a}{b} = 1 + 2\sqrt{\frac{a}{\rho}} \tag{2.1}$$

When the hole is circular, $a = b$, $\rho = a$ so stress concentration factor $k = 3$ (Fig.2.2b), but if the ellipse becomes very elongated tending to a crack, $a >> b$ so $k \to \infty$. However, Inglis's stress concentration factor only depends on geometric shape (no size), while the opposite can be observed in experiments, i.e. larger cracks propagate more easily than shorter ones.

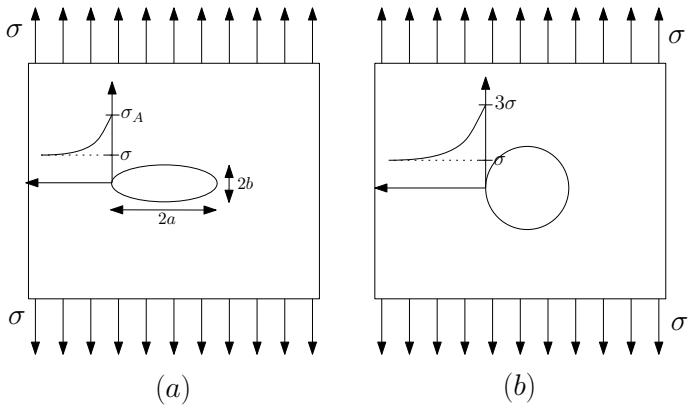

Figure 2.2: Stress concentration around a hole in a stressed plate. (a) General elliptical hole (b) particular case, circular hole ($a = b$).

Griffith (1921) noticed this fact, and analyzed other factors, concluding that the elastic potential energy could be a better indicator of fracture formation. Griffith proposed that the strain energy has to be equal or greater than energy released to create a new faces of fracture. This can be translated into two conditions:

1. Stresses at the crack tip exhibit a stress concentration and are characterized by a stress concentration factor, which depends on radius of curvature and on the crack length.

2. For crack propagation, strain energy released should be equal or larger than fracture energy (G_f) which is the energy necessary to create a unit of new crack area surface, and it is an intrinsic property of the material.

In the second World War, the U.S. Naval Research Laboratory in Washington was interested in the fracture of steel armor plating during penetration by ammunition and Irwin (1958)proposed a criterion of crack propagation based on the stress level, measured by the *stress intensity factor*. The precise definition of this factor depends on the fracture mechanism taking place; Figure 2.3 depicts the 3 basic modes of fracture, leading to the definition of respective intensity factors: K_I, K_{II}, K_{III}.

As seen in the Figure 2.3, the three modes of fracture correspond to:

- Opening mode (Mode I): the crack opens perpendicular to the crack plane.

- Sliding mode (Mode II): the crack shears normal to the crack front and crack faces are displaced transversal to their plane.

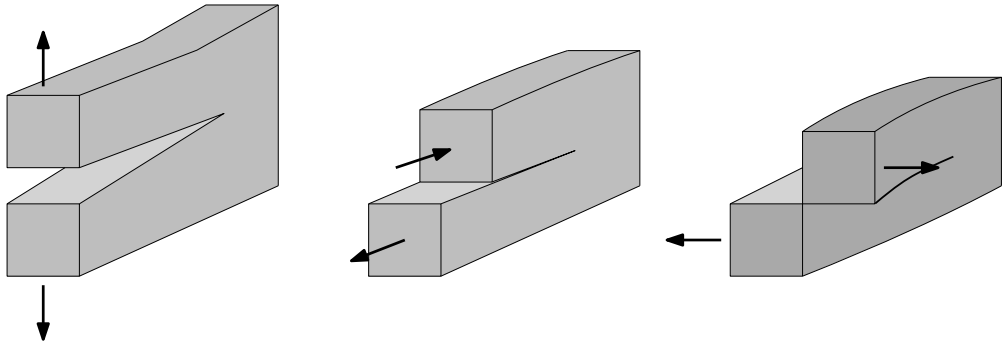

Mode I: Opening Mode II: Sliding Mode III: Tearing

Figure 2.3: Three basic kinematic crack opening modes.

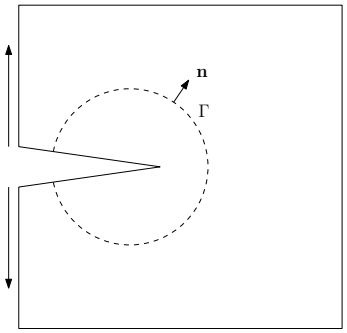

Figure 2.4: Notch in a two-dimensional deformation field, around it, the J-integral line (Γ).

- Tearing mode (Mode III): the crack shears parallel to the crack front and crack faces are displaced longitudinal to their plane.

Any crack deformation can be expressed as a superposition of these three basic kinematic crack opening modes.

The use of LEFM theory leads to correct predictions in materials where the continuum is governed by an elastic regime with a sufficiently small fracture and without affecting nearby fissures. However, this is something that, in general, rocks, concrete and quasi-brittle materials do not satisfy.

Aside from the fracture energy and the stress intensity factor approaches, another relevant approach in LEFM is the J-integral. In this approach, proposed by Rice (1968) and independently Cherepanov (1979), a moving control volume is established around the crack tip, and travels with it during crack propagation (Fig. 2.4). The energy that "flows" into the volume is evaluated as an integral over the boundary of this control volume (hence the name of J-integral), and then compared to the energy required for crack propagation.

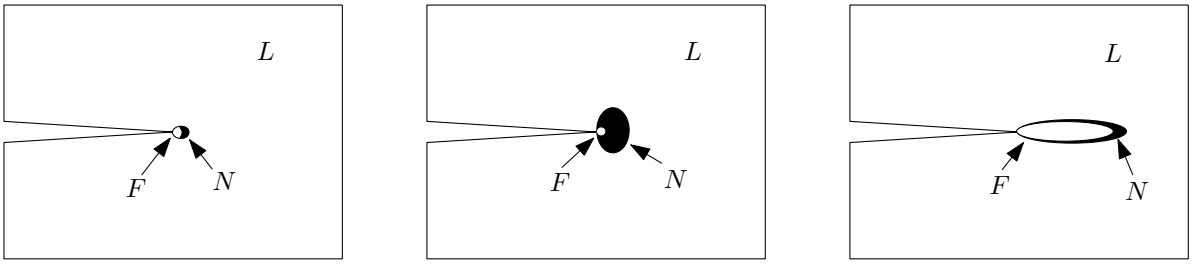

(a) (b) (c)

Figure 2.5: Fracture Process Zone (FPZ) relative domain in (a) Linear fracture (b) Metals (c) Quasi-brittle materials (concrete and rocks).

Non-linear fracture

In spite of the theoretical relevance of LEFM and the good predictions it provides in many engineering applications, it is clear that the stress fields implied by LEFM, with stresses becoming very high near the crack tip, are only an idealization. In real materials, the zone supposedly subject to very high stresses near the crack tip, either enters plastic regime, or undergoes micro-cracking. This zone is called the Fracture Process Zone (FPZ). If the FPZ is very small compared to the size of the structural member or domain, LEFM is still applicable and predictions are acceptable. In many cases, however, the FPZ is too large compared to the structural/domain size and its existence cannot be neglected. This motivates non-linear fracture theories. Metals in some cases, and also concrete and other quasi-brittle materials with large heterogeneities (aggregates in the case of concrete), usually exhibit larger FPZs in comparison with the structural member size, and require the use of non-linear fracture models (Fig. 2.5).

The first way to approximately approach non-linear fracture was based on using LEFM with equivalent parameters which should evolve as the crack propagates (e.g. the "R-curve" method, see Bažant et al., 1991).

However, the most successful non-linear fracture model is probably the cohesive crack model. In a cohesive crack, the propagation is governed by a traction–displacement relation across the crack faces near the tip. Dugdale (1960) and Barenblatt (1962) introduced this model in the early sixties for metals, while the extension to quasi-brittle materials undergoing micro-cracking is attributed to Hillerborg et al. (1976).

Fictitious Crack Model

Hillerborg's model (Hillerborg et al., 1976), usually known as the Fictitious Crack Model (FCM), introduced Fracture Mechanics into finite element analysis by considering stress traction-separation

laws acting across a line representing the potential crack extension, which is located along the FPZ ahead of the crack tip. In this way, along this line the closing stresses increase from zero at the tip of the actual pre-existing crack to the value corresponding to the uniaxial tensile strength of the material at the fictitious crack point, so that the faces of the crack are gradually closed towards the tip (Fig.2.6a).

The crack is assumed to propagate when the stress at the crack tip reaches the tensile strength (χ). When the crack opens the stress is not assumed to fall to zero immediately, but to decrease with increasing crack width r_N according to the said decay law. When the crack opening reaches the value $\bar{r}_N$ the stress has fallen to zero (Fig. 2.6c). For that part of the crack where $r_N < \bar{r}_N$, the "crack" in reality corresponds to a micro cracked zone with some remaining ligaments for stress transfer. As there is a stress to be overcome in opening the crack, energy is absorbed. The amount of energy absorbed per unit crack area in widening the crack from zero to or beyond $\bar{r}_N$ (geometrically equal to the area below the traction-separation decay curve in Fig.2.6c) must be equal to the fracture energy G_f, i.e.

$$G_f = \int_0^{\bar{r}_N} \sigma\left(r_N\right) \mathrm{d}r_N \tag{2.2}$$

The Fictitious Crack Model (FCM) reproduces the crack propagation of discrete fissures. On the other hand, the evolution of smeared cracks or crack bands can be characterized by the Crack Band Model.

2.2.2 Numerical methods for the analysis of cracks and discontinuities

Modeling the behavior of materials in the presence of discontinuities has always been a challenge in the field of computational mechanics, and the implementation of either LEFM or non-linear fracture model into modern numerical tools and in particular in Finite Element Method (FEM) has led to a number of approaches and models. In the Introduction (Sec.1.1) a first (and most traditional) classification of these methods into "discrete crack" approach and "smeared crack" was introduced. In the present Section, we will focus on those formulations proposed in which the kinematics (opening/sliding) of the crack or discontinuity, is added in some form, to the basic kinematics of the background or initial FE mesh. Initially, this corresponded clearly with the "discrete" methods, but later a number of approaches designed to overcome the problems of the "smeared approach" also added extra kinematics and, therefore, they will also be considered here.

The first type of models to be mentioned were developed in the context of LEFM, in conjunction with continuous remeshing in order to capture the new geometry of cracks and singularity at the

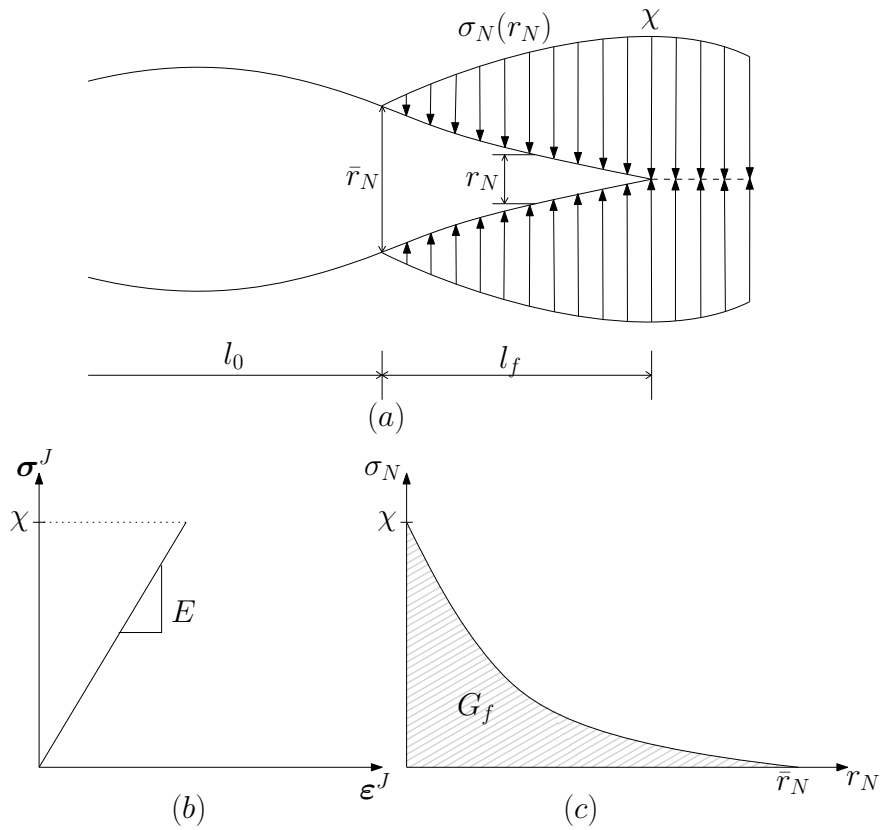

Figure 2.6: (a) Stress distribution over the fictitious crack (b) Elastic relation of the material between stress and strain until reaching the uniaxial tensile strength (c) normal stress traction-opening curve, where fracture energy is the area under the curve.

crack tip (Ingraffea et al., 1987). Later, some authors (Bouchard et al., 2000) combined this technique with nodal relaxation to release nodes, one by one, in order to enable the crack tip to propagate through the mesh. Others (Wacher and Givoli, 2006) have combined it with the moving finite element method working on improvements of this technique and formulated the String Gradient Weighted Moving Finite Element (SGWMFE). SGWMFE method is extended to include remeshing and refining as an alternative of Gradient Weighted Moving Finite Element (GWMFE) method developed by Carlson and Miller (1998). The moving finite element method was introduced in Gelinas et al. (1981), for general systems of transient partial differential equations (PDEs) in 1-D and the 2-D extension is briefly discussed. For detailed information about Moving Finite Element see Baines book (Baines, 1994), which describes work done since 90's.

On the other hand, to improve the description of the discontinuity behavior, Needleman (1987) proposed to insert potential cohesive segments at the interface between two finite elements, it

supposes an addition of extra nodes that will increase the number of components to solve the finite element equation. In the literature two proposals of inter-element crack method implementation can be distinguished (1) Needleman and Xu formulation (Xu and Needleman, 1994), where elements are initially separated and (2) Ortiz et al. (1987) where elements are split only when tensional criterion is reached or edges are contiguous to a crack tip.

Inter-element crack method is quite efficient, and cohesive crack models represent the zone with a non-linear response Dugdale (1960). Application to concrete-like materials was proposed by Hillerborg's Fictitious Crack Model (Hillerborg et al., 1976). As it is commonly known, in these models fracture energy is a parameter of the model and corresponds to the area under traction-separation curve. Generalization of the cohesive concept implies decohesion laws that involve normal as well as shear stress tractions in the FPZ, generally in the form of a constitutive law for the cohesive interface elements that are inserted along the crack path (i.e. Stankowski et al., 1993; Carol et al., 1997; Caballero et al., 2008a; Wu and Wriggers, 2015).

In recent years the progress has been made in the development of methods to describe discontinuities from the enrichment of the elements that form the finite element mesh, for example, embedded finite element method (EFEM/EED), Generalized Finite Element Method (GFEM), Partion of unity finite element method (PUFEM) and extended finite element method (XFEM).

Ortiz et al. (1987) developed approximation techniques by embedded finite element method (EFEM/EED), able to solve localized problems of discontinuity across the finite element mesh. The method exploits the fact that considerable information concerning the process of localization can be readily obtained at the element level. A simple analysis suffices to detect the onset of localization in an element and to determine the geometry of the localized deformation modes. This information is utilized to set up additional shape functions which closely reproduce the localized deformation patterns. The additional degrees of freedom are then eliminated at the element level by static condensation. Although the resulting element is non-conforming the patch test is satisfied and the convergence properties of the underlying conforming element are not altered.

Contrary to EFEM and other methods that enrich the elements with bubble functions and then perform a tracking algorithm to guarantee compliance between elements, XFEM, GFEM and PUFEM follow a nodal enrichment scheme. It consists in adding additional variables for the description of the fractures directly on the nodes, which have information from the elements that contain it. Partition of unity method was originated in the works of Duarte and Oden (1996); Melenk and Babuška (1996); Babuška and Melenk (1997). A partition of unity is defined as a set of global functions $N_i(x)$ whose value sums up to unity at each point x in the solution domain Ω,

in general in a Lagrangian FEM global basis. Within this approach, the standard approximation basis is enriched locally with special functions with extra degrees of freedom for the nodes in the domain subjected to the enrichment and without modification of the mesh topology.

Based on the same concept of partition of unity different authors developed generalized finite element method (GFEM) (Melenk, 1995; Duarte et al., 2000; Strouboulis et al., 2000) special finite element methods (Babuška et al., 1994) partition of unity finite element method (Melenk and Babuška, 1996; Babuška and Melenk, 1997) and hp clouds (Duarte and Oden, 1996; Oden et al., 1998). Several of the so-called meshless methods proposed in recent years are special cases of the Partition of unity method for example, XFEM. A feature that distinguishes the extended finite element method (XFEM) from GFEM is that the domain is locally enriched (only some nodes are enriched).

One of the greatest advances of XFEM is the description of problems of crack growth, as described its predecessors (Belytschko and Black, 1999; Moës et al., 1999; Areias and Belytschko, 2005), called initially as a minimal remeshing finite element method for crack growth. XFEM allows the crack to be arbitrarily aligned within the mesh due to the independence between the finite element mesh and the discontinuity location Fries and Belytschko (2010); Belytschko et al. (2009).

Among the numerical methods described in the paragraphs above, the FEM with zero-thickness interface elements (FEM+z) and eXtended Finite Element Method (XFEM) have been chosen for describing discrete fractures of known path (Chapter 2) and as suitable candidates for the new scheme of cracking along non-pre-established paths (Chapter 3); FEM+z because of its traditional effectiveness, and XFEM because of the advantage represented by the independent treatment of the discontinuities with respect to the continuum mesh. These methods are described in some detail in the following sections.

2.3 FEM with zero-thickness interface elements

The formulation of zero thickness interface elements is first proposed at the end of the 60s, motivated by the modeling of rock fractures in the FEM context. Initially proposed by Goodman et al. (1968) and lately improved by some authors e.g. Zienkiewicz et al. (1970); Ghaboussi et al. (1973); Desai et al. (1984); Gens et al. (1989, 1995) the formulation of interface elements has been widely implemented in FEM codes and applied to many practical rock engineering problems. The assumption of zero thickness is justified by the fact that the thickness of discontinuities in the rock mass is usually very small in comparison with the problem dimensions.

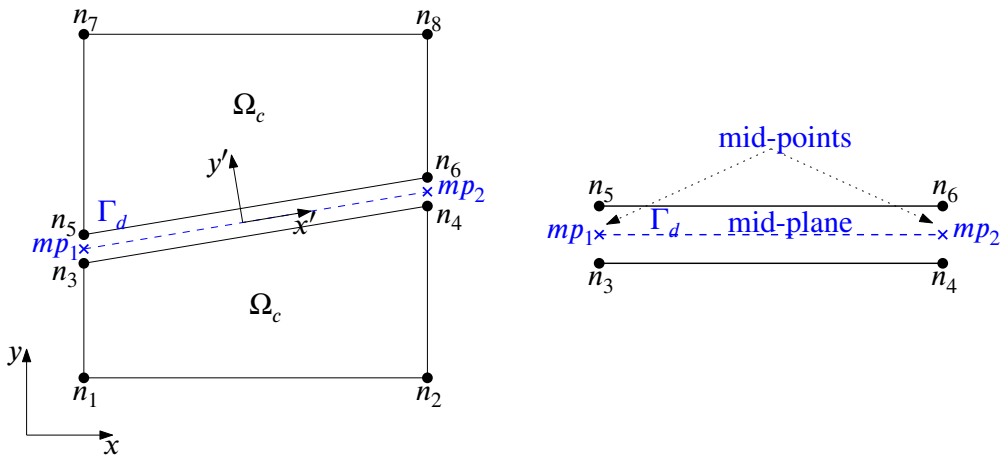

Figure 2.7: Zero-thickness interface element embedded between two quadrangular continuum finite elements, where n_i are the element nodes and mp_i are the element mid-points.

In this case, the formulation used is similar to Gens et al. (1995), and is described in Sec. 2.3.1. In the present context, interface elements will be used in conjunction to a fracture mechanics-based constitutive law with elasto-plastic structure which was first proposed by Carol et al. (1997), then modified by Caballero et al. (2008a); this constitutive law is also briefly summarized in Section 2.3.2. Finally, some practical aspects of numerical implementation are discussed in Section 2.3.3.

2.3.1 Basic formulation

Zero-thickness interface elements may be regarded as classical continuum elements in which one of the dimensions has been collapsed to become "surface elements" (in 3D) or "line elements" (in 2D), but even after collapse they preserve the two (upper and lower) faces, each with its own nodes; therefore, in contrast to surfaces or line elements the interface element exhibits double nodes (reason for which sometimes also called "double-node interface element"). Zero-thickness interface elements are usually inserted in between standard continuum elements in order to represent the possibility of variable jumps (such as opening or sliding), as it is shown in Figure 2.7. In the figure, the interface "mid plane" and the local axes (x', y') are also represented. In the case of solid mechanics, the constitutive variables defined along the element mid-plane are the normal and tangential relative displacements $\boldsymbol{\varepsilon}^J = (r_N, r_T)$, and their conjugate normal and tangential stresses $\boldsymbol{\sigma}^J = (\sigma_N, \sigma_T)$.

As Figure 2.7 depicts, the mid-plane connects the midpoints (mp_i), which are at mid-distance between each pair of adjacent nodes. The relative displacement in global axis (x, y) at the midpoints

is calculated as the difference between the nodal displacement of the adjacent element nodes. If ${\mathbf{u}_e}^J$ is the complete element nodal displacement vector of the interface element (containing the displacement components of all nodes of the interface element), this difference may be expressed using constant matrix $\mathbf{T}$ as:

$$\boldsymbol{\varepsilon}^J_{(xy)} = \mathbf{T}\mathbf{u}^J_e \tag{2.3}$$

Isoparametric interpolation of geometry and relative displacements along the interface is based on standard shape functions N_i where i varies from 1 to number of mid-points, and ξ is the local coordinate varying along the interface, with values -1 (left end) to 0 (center) and to +1 (right end). In 2D and linear elements, shape functions take the usual form:

$$N_1(\xi) = \frac{1-\xi}{2}, \;\; N_2(\xi) = \frac{1+\xi}{2} \tag{2.4}$$

The relative displacement at a point of the midplane may be expressed in the local axes (x', y'), as

$$\boldsymbol{\varepsilon}^J = \mathbf{RNT}\mathbf{u}^J_e = \mathbf{B}^J\mathbf{u}^J_e \tag{2.5}$$

where $\mathbf{N}$ is the interpolation matrix collecting all individual interpolation functions in appropriate arrangement, $\mathbf{R}$ is the rotation matrix from global x, y to local x', y' axes, and $\mathbf{B}^J$ is equal to product of the tree precedent matrices.

As said, in this type of elements relative displacement play a role equivalent to strains in the conventional continuum elements. The simplest constitutive relation between relative displacements and their conjugate stresses is a general linear expression of the type:

$$\boldsymbol{\sigma}^J = \mathbf{D}^J\boldsymbol{\varepsilon}^J + \boldsymbol{\sigma}^J_0 \tag{2.6}$$

where $\mathbf{D}^J$ is the stiffness matrix and $\boldsymbol{\sigma}^J_0$ represents an initial stress at the discontinuity which can be also expressed as $\boldsymbol{\sigma}^J_0 = -\mathbf{D}^J\boldsymbol{\varepsilon}^J_0$,and be used to describe stress-free interface deformation states $\boldsymbol{\varepsilon}^J_0$ such as thermal or chemical processes, or to account for residual (unbalanced) stresses in the context of an iterative non-linear analysis.

The Principle of Virtual Work (PVW) is applied to derive the weak equilibrium equation of the element. By this principle, the work done by external forces and internal forces should be the same, under any virtual deformation field which satisfies kinematic compatibility:

$$W_{int} = W_{ext} \tag{2.7}$$

External work is simply the product of virtual displacements and forces

$$W_{ext} = \left(\mathbf{u}_e^{vir}\right)^T \mathbf{f}_e \tag{2.8}$$

Internal work is calculated as the integral over discontinuity area of virtual strains multiplied by their conjugate stresses,

$$W_{int} = \int_\Gamma \left(\boldsymbol{\varepsilon}^{J\,vir}\right)^T \boldsymbol{\sigma}^J \mathrm{dL} \tag{2.9}$$

Replacing equations (2.8) and (2.9) into (2.7) and making pertinent operations, the weak equilibrium equation for the element takes the usual form:

$$\mathbf{f}_e = \int_\Gamma \left(\mathbf{B}^J\right)^T \boldsymbol{\sigma}^J \mathrm{dL} \tag{2.10}$$

In addition, stress tensor on the discontinuity can be replaced by constitutive equation (Eq. 2.6) and expression of relative displacement (Eq. 2.5) to relate external forces with nodal displacements.

$$\mathbf{f}_e = \left[\int_\Gamma \left(\mathbf{B}^J\right)^T \mathbf{D}^J \mathbf{B}^J \mathrm{dL}\right] \mathbf{u}_e^J + \int_\Gamma \left(\mathbf{B}^J\right)^T \boldsymbol{\sigma}_0^J \mathrm{dL} \tag{2.11}$$

from where the interface element stiffness matrix and initial force vector can be immediately identified

$$\mathbf{f}_e = \mathbf{K}_e^J \mathbf{u}_e^J + \mathbf{f}_{e\,0} \tag{2.12}$$

2.3.2 Fracture-based interface constitutive law with elasto-plastic structure

The fracture-based constitutive law for zero-thickness interface elements was originally proposed in Carol et al. (1997) and lately modified by López (1999); Caballero et al. (2008b).

The constitutive variables, defined on the interface mid-plane, are stress tractions $\boldsymbol{\sigma}^J = (\sigma_N, \sigma_T)$ and relative displacements $\boldsymbol{\varepsilon}^J = (r_N, r_T)$. A crack is assumed to start when stresses reach a hyperbolic cracking surface $F(\sigma_N, \sigma_T) = 0$ with the following expression:

$$F\left(\sigma_N, \sigma_T\right) = -\left(c - \sigma_N \tan\phi\right) + \sqrt{\left((\sigma_T)^2 + \left(c - \chi \tan\phi\right)^2\right)} \tag{2.13}$$

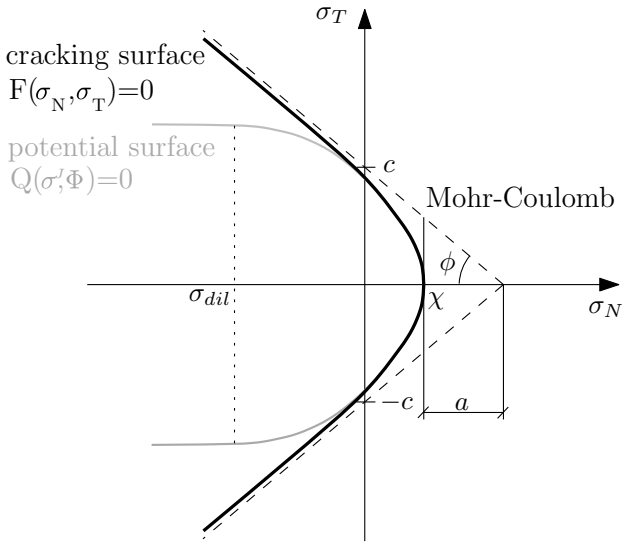

Figure 2.8: Hyperbolic cracking surface F and plastic potential Q.

The main surface parameters are: apparent or asymptotic cohesion (c), tensile strength (χ) and asymptotic friction angle ($\tan\phi$). As in any elasto-plastic model, crack relative displacements are assumed to be decomposed into elastic and plastic (here called cracking) parts: $\boldsymbol{\varepsilon}^J = (\boldsymbol{\varepsilon}^J)^{el} + (\boldsymbol{\varepsilon}^J)^{cr}$. While the elastic part is related to stress tractions using elastic stiffness, the plastic part is assumed governed by the flow rule defined in terms of a plastic potential Q:

$$\delta r_N^{cr} = \delta\lambda \frac{\partial Q}{\partial \sigma_N},\ \delta r_T^{cr} = \delta\lambda \frac{\partial Q}{\partial \sigma_T} \tag{2.14}$$

where the derivatives of Q are assumed equal to those of F in tension (associated behavior), but in compression the normal component is decreased for increasing normal stresses, vanishing totally for $\sigma_N = \sigma_{dil}$ (σ_{dil} is another parameter of the model).

During the fracture (crack opening/sliding) process, the plastic surface parameters c, χ and $\tan\phi$ change change their values. The evolution of these parameters is controlled by an internal history variable, the work spent during the fracture process per unit area of fracture (w^{cr}), which is defined as:

$$\mathrm{d}w^{cr} = \begin{cases} \sigma_N^T \mathrm{d}r_N^{cr} + \sigma_T^T \mathrm{d}r_T^{cr} & \sigma_N \geq 0 \,(\text{tension}) \\ \sigma_T^T \mathrm{d}r_T^{cr} \left(1 - \left|\frac{\sigma_N \tan\phi}{\sigma_T}\right|\right) & \sigma_N < 0 \,(\text{compression}) \end{cases} \tag{2.15}$$

where dr_N^{cr} and dr_T^{cr} represent the increment of normal and shear relative displacements of the crack

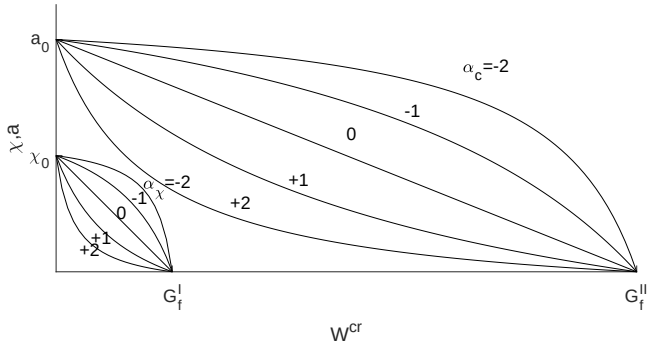

Figure 2.9: Softening laws for tensile strength (χ) and function a.

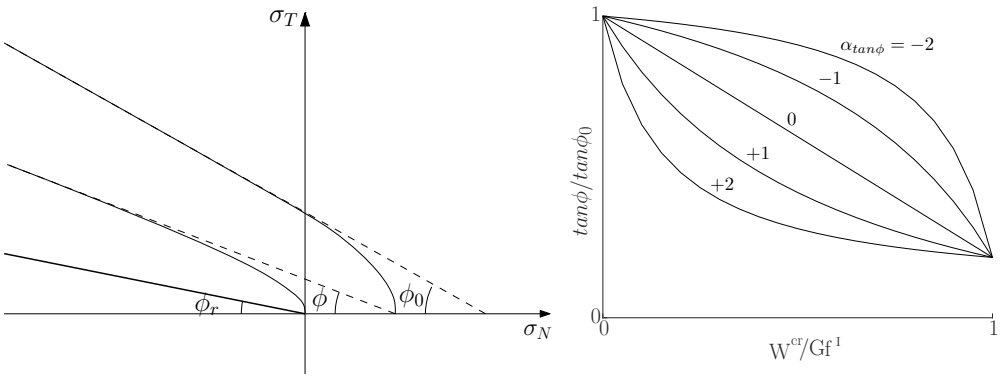

Figure 2.10: (a) Evolution of angle of internal friction. (b) Softening laws for $\tan\phi$.

(i.e. normal opening and tangential sliding).

Tensile strength (χ), asymptotic friction angle ($\tan\phi$) and parameter a (distance between hyperbola vertex and Mohr-Coulomb tip, see Fig. 2.8) are assumed to decrease linearly in terms of the intermediate scaling function $\mathcal{Y}$, defined as:

$$\mathcal{Y}(\zeta_i) = \frac{e^{-\alpha}\zeta_i}{1 + (e^{-\alpha} - 1)\,\zeta_i} \tag{2.16}$$

where $\zeta_i = w^{cr}/G_f^I$ and $\alpha = \alpha_\chi$ or $\alpha = \alpha_{\tan\phi}$. These functions are depicted in Figure 2.9 and Figure 2.10b. On the other hand, apparent or asymptotic cohesion c is obtained from values of χ, $\tan\phi$ and a with the simple relation:

$$c = (a + \chi)\tan\phi \tag{2.17}$$

Parameters G_f^I and G_f^{II} in Figures 2.9 and 2.10b correspond to the fracture energies in mode

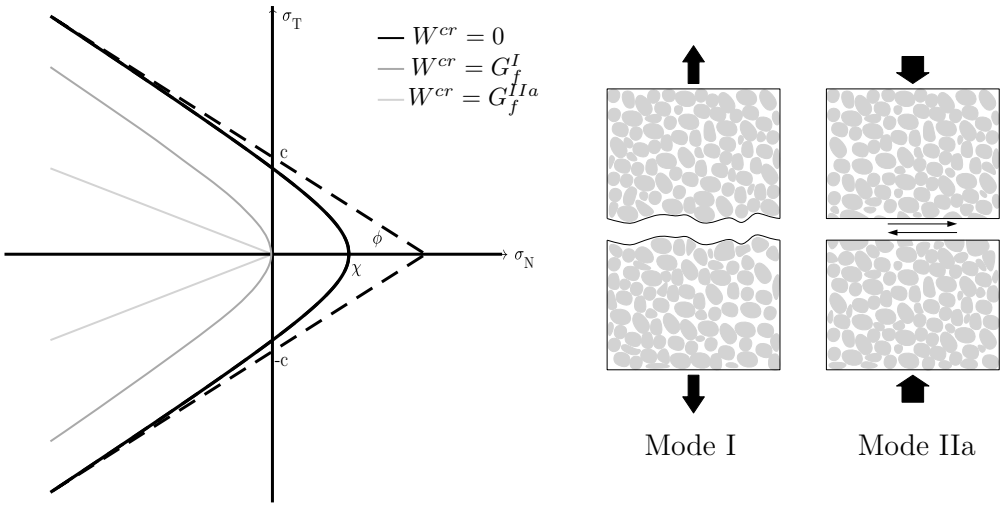

Figure 2.11: Cracking surface evolution in Mode I and Mode IIa.

I and mode IIb, which correspond to cracks developing, respectively, in pure tension, or in shear with high compression and dilatancy not allowed. With parameters evolving as in Figure 2.9 and .2.10b, a typical evolution of the initial hyperbolic fracture surface is shown in Figure 2.11; first the hyperbola moves to the left exhausting totally the tensile capacity for $w^{cr} = G_f^I$, and later degenerates into a pair of straight lines representing residual friction when w^{cr} approaches G_f^{IIa}.

2.3.3 Practical aspects of numerical implementation

The use of traditional finite element method with zero-thickness interface elements (FEM+z) can be very advantageous in mechanical problems with presence of discontinuities. Nevertheless, some disadvantages are also commented in this section.

The introduction of interface elements is useful to obtain by direct form the stress value onto the discontinuity without the need of calculating it from the elements of the continuum. The procedure based on zero-thickness interfaces has led to very realistic representation (Caballero et al., 2006; Garolera et al., 2005). However, with the systematic introduction of interface elements many nodes are duplicated (or multiplied depending on interface elements intersections) and the total number of nodes can grow considerably, and therefore the computational cost of the analysis. Additionally, the FEM system can suffer from numerical ill-conditioning if interfaces are assigned a high elastic stiffness (which is the case if interfaces do not correspond physically to deformable layers or planes, and stiffness is interpreted as the penalty coefficient necessary to evaluate stress tractions transmitted across their surface, which in general should be set to a value as high as

possible).

For those reasons, some authors have proposed approaches to simulate discrete fracture without the need of deformable double-node interface elements inserted systematically from the beginning of the analysis, although that requires first to evaluate the stress tractions transmitted between neighbor continuum finite elements, something only trivial at mid-nodes of quadratic meshes (Camacho and Ortiz, 1996; Ortiz and Pandolfi, 1999; Pandolfi et al., 1999). To remedy that, one alternative method to evaluate inter-element stresses at corner points of a FE mesh has also been proposed (Ciancio et al., 2006, 2013). This method is based on the double minimization of an objective function, representing the error between the inter-element stress tractions and the projection of the best-fit stress tensor along the planes of the interfaces converging at an element corner node. However, progressive insertion of interface elements as critical stress tractions are exceed means continuous topology changes in the mesh, which is numerically inconvenient and a serious drawback for possible later parallelization of the code.

Another drawback of fracture analysis with interface elements, is that fractures can only propagate along the mesh lines, and therefore the quality of the results depends very much on how well those lines had been laid out (that is, whether they include all relevant potential crack paths). Otherwise, the crack may develop following lines which zigzag around the correct physical path, which normally results in higher cracking and peak loads, or in the absence of peak at all (if the mesh line directions deviate too much from the expected crack trajectory. The use of refined meshes may reduce this effect, but it implies a high computational cost. This is one of the main motivations for the method developed in the following chapter of the thesis (Chapter 3), a method that allows the modification of interface elements position so that interface elements get realigned with the physical direction of cracking according to an energetic criterion provided by Configurational Mechanics.

Finally, it has to be mentioned that the results of the analysis using zero-thickness interface elements may be also influenced by the numerical integration rule (quadrature) used for the interface element. The use of integration schemes such as that of Newton-Cotes, which result in the uncoupling of the degrees of freedom of the element, has been shown to be more advantageous to avoid potential spurious oscillations (Gens et al., 1989).

2.4 Extended Finite Element Method (XFEM)

The Extended Finite Element Method (XFEM) is a relatively recent method used to model discontinuities which has evolved as a particular case of the Partition of Unity Method (PUM, Babuška and Melenk, 1997) or the Partition of Unity Finite Element Method (PUFEM, Melenk and Babuška,

1996). The main idea of this method is to enrich the standard basis that describe the continuum field of displacements, with some additional modes of deformation that describe the discontinuities in the field. The main difference with other options such as embedded discontinuities (Ortiz et al., 1987), is that the additional XFEM variables are nodal variables shared by adjacent elements, which means that the jump values at the discontinuity will be continuous across elements, therefore guaranteeing a conformity in the solution similar for instance to that obtained with zero-thickness interface elements (but not for instance with most formulations of the "embedded discontinuity" type, in which the jump variables are internal to each element, without any continuity enforced).

Most existing XFEM formulations for solid mechanics (e.g. Shibanuma and Utsunomiya, 2011; Pathak et al., 2013; Chen et al., 2012; Shedbale et al., 2013; Kumar et al., 2013) use the relative ("jump") displacements as additional variables at the nodes of the elements crossed by the discontinuity. In this case, however, the fictitious "overhang" displacements across the discontinuity, as described in Jirásek and Belytschko (2002), have been preferred over the jumps themselves, because of a clearer physical meaning, which makes more intuitive to establish the formulation, and especially to impose the necessary boundary conditions.

Another common feature of most existing XFEM formulation is the use of natural interpolation functions (the functions of the original continuum element) to interpolate the displacement within the element subdomains. In this chapter the new approach of sub-interpolation is proposed, by which the original element functions are used exclusively to interpolate the displacement values from the original element nodes to the points of intersection of the discontinuity with the element edges, while new sub-interpolation functions are used within each element sub-domain.

A reported issue of existing XFEM formulations is the oscillation observed in the results when discontinuity runs skew to the mesh Moës et al. (2006); Sanders et al. (2009), which is linked to the use of the natural interpolation scheme. According to this interpretation, the new scheme with sub-interpolation should help avoiding this problem. This improvement seems confirmed by a basic example of application provided.

A theoretical aspect of the XFEM that seems not dealt with in the existing literature is the relation and possible equivalence to the traditional approach of standard FEM with zero-thickness interface elements along the same discontinuity location Gens et al. (1989), since both approaches seem similar conceptually in that both describe the jump by using new field variables that are shared by adjacent elements. Also, in both approaches the constitutive behavior of the discontinuity may be described in terms of the same variables, namely relative (normal and shear) displacements, and stress tractions (also normal and shear), and therefore the same constitutive equations may be used.

In this chapter, this equivalence is explored successfully for the XFEM formulation proposed and a "2-2" quadrangular element configuration (the discontinuity line divides the element leaving two nodes on each side). The expression of the XFEM stiffness matrix is derived, and the equivalence is shown to the assembly of the stiffness matrices of the continuum and zero-thickness interface elements for the same configuration.

Another aspect of concern for the numerical application of XFEM formulations, is the spurious oscillations reported on the values of normal and shear stress on the discontinuity itself (e.g. Sanders et al. (2009); Laborde et al. (2005); Moës et al. (2006)), when the discontinuity line runs too close to a mesh node. These oscillations may be critical to then check shear sliding conditions, and therefore evaluate failure loads and safety factors. This problem is also examined in the chapter, by first identifying the appearance of such oscillations at locations where nodes are too close to the discontinuity location and the intersection with surrounding finite elements leads to very small or badly shaped element subdivisions. A common remedy for this problem is to move the nodes away from the discontinuity so that element sizes and aspect ratios improve Choi et al. (2012). However, the way to do this is not unique, and improvements are not drastic, which motivates to propose a new strategy consisting of the opposite: bringing the nodes onto the discontinuity itself. Although it requires identifying some additional element configurations, this strategy is developed in the thesis and shown to be very efficient, eliminating oscillations without producing other distorted elements in the vicinity. The improvement obtained with this strategy is also justified on the basis of the count of independent kinematic variables of the element.

2.4.1 XFEM formulation

General concepts and additional variables

The essential idea of the Extended Finite Element Method (XFEM) consists of enriching the standard finite element with extra degrees of freedom at the nodes, in order to represent a discontinuous field within the element. Considering $\mathbf{x}$ as any point within the element, and assuming the existence of a field discontinuity within the element domain, the displacement vector $\mathbf{u}$ at any point within the element may be expressed as the sum of two contributions from the standard continuum field, $\mathbf{u}^{FE}$ and from the enrichment functions, $\mathbf{u}^{enr}$, according to the expression:

$$\mathbf{u}\left(\mathbf{x}\right) = \mathbf{u}^{FE} + \mathbf{u}^{enr} = \sum_{k=1}^{n} N_{(k)}(\mathbf{x})\mathbf{u}^{*}_{(k)} + \sum_{i=1}^{m} N_{(i)}\left(\mathbf{x}\right)\phi(\mathbf{x})\mathbf{a}_{(i)} \tag{2.18}$$

in which $N_{(k)}$ are the shape functions for the regular (continuum) part of the displacements represented by regular degrees of freedom at the nodes, $\mathbf{u}^*_{(k)}$ ($k = 1, 2 \ldots n$, number of nodes), while $\mathbf{a}_{(i)}$ are the additional nodal variables, and function $\phi(\mathbf{x})$ is the global enrichment function defining the shape of the additional field to be superimposed to the regular displacement field, usually taken as the Heaviside function.

$$\phi(\mathbf{x}) = H(\mathbf{x}) = \begin{cases} 0 & \mathbf{x} \in \Omega^- \\ 1 & \mathbf{x} \in \Omega^+ \end{cases} \tag{2.19}$$

In the case that $\mathbf{a}_{(i)} = \mathbf{0}$, (i.e. all enrichment nodal values equal to zero), the second term disappears and the regular FE interpolation is recovered. Note that in this approach, the physical meaning of the nodal variables $\mathbf{u}^*_{(i)}$ would only correspond to the actual physical displacement on the negative part of the domain, while on the positive part physical displacements would be given by $\mathbf{u}^*_{(i)} + \mathbf{a}_{(i)}$, that is, the physical meaning of $\mathbf{u}^*_{(i)}$ would correspond to the physical displacement minus the jump. To correct this inconvenient feature, a change of nodal variables is introduced from $\mathbf{u}^*_{(i)}$ to $\mathbf{u}_{(i)}$ corresponding to the actual physical displacement on both sides of the discontinuity. In this way, on the negative side $\mathbf{u}_{(i)} = \mathbf{u}^*_{(i)}$ but on the positive side $\mathbf{u}_{(i)} = \mathbf{u}^*_{(i)} + \mathbf{a}_{(i)}$, and therefore $\mathbf{u}^*_{(i)} = \mathbf{u}_{(i)} - \mathbf{a}_{(i)}$. A favorable way to express equation 2.18 in terms of the new variables $\mathbf{u}_{(i)}$ is the following:

$$\mathbf{u}(\mathbf{x}) = \mathbf{u}^{FE} + \mathbf{u}^{enr} = \sum_{k=1}^{n} N_{(k)}(\mathbf{x})\boldsymbol{u}_{(k)} + \sum_{i=1}^{m} N_{(i)}(\mathbf{x})\,\psi_{(i)}(\mathbf{x})\mathbf{a}_{(i)} \tag{2.20}$$

where $\psi_{(i)}$ ($i = 1, 2 \ldots m$, number of nodes contributing to the enrichment) represent the corresponding enrichment functions, which in this case are different for each node and can take the simple form of "shifted Heaviside functions" (Zi and Belytschko, 2003):

$$\psi_{(i)}(\mathbf{x}) = H(\mathbf{x}) - H(\mathbf{x}_{(i)}) \tag{2.21}$$

where $\mathbf{x}_{(i)}$ indicates the coordinates of node i. Particularizing the enrichment function (2.21) for nodes belonging to each sub-domain, the resulting values of $\psi_{(i)}(\mathbf{x})$ are obtained (shown in Table 2.1), and represented in Fig. 2.13b. Combining the above function $\psi_{(i)}(\mathbf{x})$ with the standard linear shape functions, leads in the case of 1-D elements to the overall interpolation functions for the additional degrees of freedom $\mathbf{a}_{(i)}$ that are depicted in Fig. 2.13c, in which, in order to simplify notation, the following variables are used within each subdomain:

$$\mathbf{x}^- \overset{def}{=} \mathbf{x} \in \Omega^-, \quad \mathbf{x}^+ \overset{def}{=} \mathbf{x} \in \Omega^+, \quad \mathbf{x}^J \overset{def}{=} \mathbf{x} \in \Omega^J \tag{2.22}$$

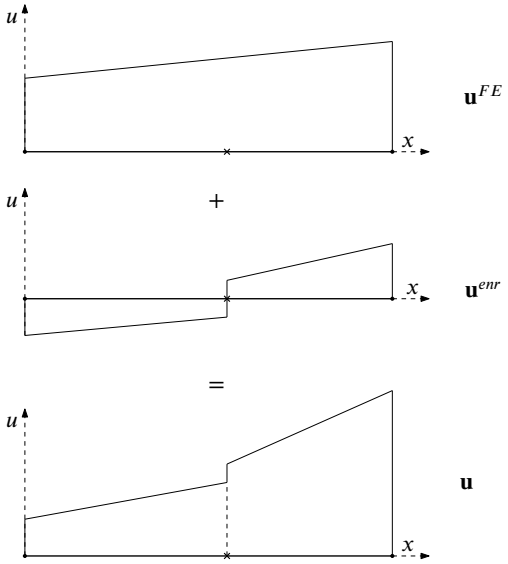

Figure 2.12: Graphical representation of the general equation of XFEM (2.20)

Table 2.1: Enrichment function, $\psi_{(i)}(\mathbf{x})$.

Point ($\mathbf{x}$)	Domain for node i	$H(\mathbf{x})$	-	$H(\mathbf{x}_{(i)})$	=	$\psi_{(i)}(\mathbf{x})$
$\mathbf{x} \in \Omega^-$	Ω^-	0	-	0	=	0
	Ω^+	0	-	1	=	-1
$\mathbf{x} \in \Omega^+$	Ω^-	1	-	0	=	1
	Ω^+	1	-	1	=	0

Choice of fictitious "overhang" displacements as additional nodal variables

The interpolation in terms of the displacement jump $\mathbf{a}$ is the most common in XFEM literature. However, due to some advantages in the definition of the boundary conditions, in the present implementation it was decided to operate with some alternative nodal variables to describe the discontinuity values: the fictitious displacements $\boldsymbol{\delta}$ of the "overhang" nodes across the discontinuity. This choice was proposed in Jirásek and Belytschko (2002), and is represented in Fig. 2.14, together with regular nodal displacements $\mathbf{u}$ and the nodal jumps $\mathbf{a}$.

As shown in Figures 2.14a and 2.14b, the relation between $\boldsymbol{\delta}_{(i)}$, $\mathbf{u}_{(i)}$ and $\mathbf{a}_{(i)}$ is slightly different for the nodes on one side or the other of the discontinuity, as given by expressions:

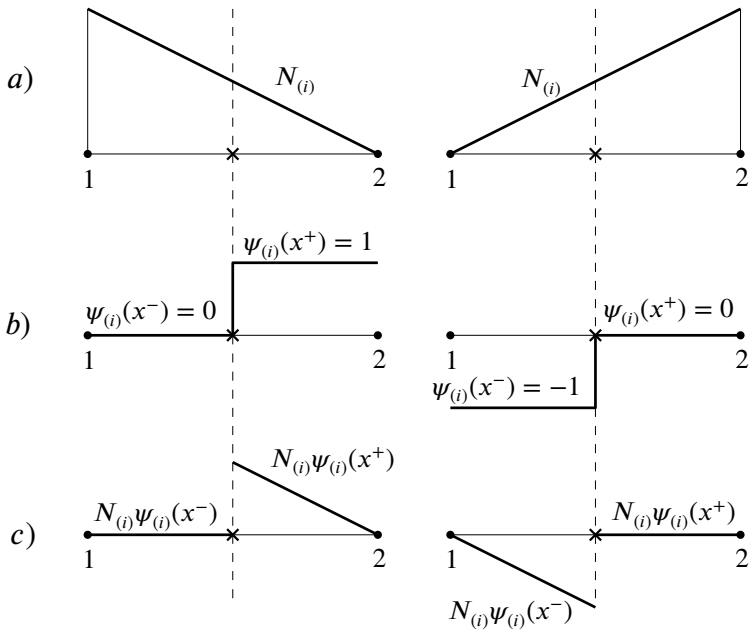

Figure 2.13: Graphical representation of (a) shape functions $\left(N_{(i)}\right)$ (b) enrichment function $(\psi_{(i)})$ and (c) product of them.

$$\begin{cases} \boldsymbol{\delta}_{(i)} = \mathbf{u}_{(i)} + \mathbf{a}_{(i)} & in \quad \Omega^- \\ \boldsymbol{\delta}_{(i)} = \mathbf{u}_{(i)} - \mathbf{a}_{(i)} & in \quad \Omega^+ \end{cases} \tag{2.23}$$

From these equations one can isolate $\mathbf{a}_{(i)}$ and replace into Eq.(2.20), which leads to the expressions for the interpolation of displacements $\mathbf{u}(\mathbf{x})$ in terms of the regular nodal displacements $\mathbf{u}_{(i)}$ and the alternative XFEM nodal variables $\boldsymbol{\delta}_{(i)}$:

$$\mathbf{u}\left(\mathbf{x}^-\right) = \sum_{i\in\Omega^-} N_{(i)}\mathbf{u}_{(i)} + \sum_{i\in\Omega^+} N_{(i)}\boldsymbol{\delta}_{(i)} \tag{2.24}$$

$$\mathbf{u}\left(\mathbf{x}^+\right) = \sum_{i\in\Omega^-} N_{(i)}\boldsymbol{\delta}_{(i)} + \sum_{i\in\Omega^+} N_{(i)}\mathbf{u}_{(i)} \tag{2.25}$$

That is, the interpolation in terms of $\boldsymbol{\delta}_{(i)}$ is always based on the regular standard shape functions, although it involves selectively the regular displacements $\mathbf{u}_{(i)}$ for those nodes on the same side of the discontinuity as the point at which the function is being evaluated, and the fictitious "overhang" displacements $\boldsymbol{\delta}_{(i)}$ for the rest of the nodes on the opposite side. Graphical interpretation is intuitive from Fig. 2.14, and the jump itself may be also expressed in a relatively simple way as:

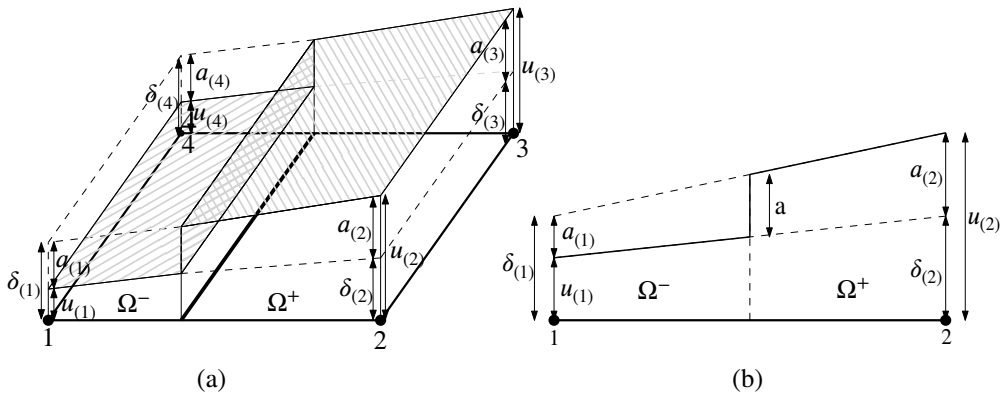

Figure 2.14: (a) Displacement field representation of a quadrangular element. Filled surfaces represent the real displacements and dashed lines the fictitious displacement. Also, subtracting real and fictitious displacements the jump is obtained. (b) One-dimensional representation of real displacement (u), fictitious displacement (δ) and jump (a).

$$\mathbf{a}\left(\mathbf{x}^J\right) = \mathbf{u}\left(\mathbf{x}^+\right) - \mathbf{u}\left(\mathbf{x}^-\right) \tag{2.26}$$

$$\mathbf{a}\left(\mathbf{x}^J\right) = \sum_{i\in\Omega^-} N_{(i)}\left(\boldsymbol{\delta}_{(i)} - \mathbf{u}_{(i)}\right) + \sum_{i\in\Omega^+} N_{(i)}\left(\mathbf{u}_{(i)} - \boldsymbol{\delta}_{(i)}\right) \tag{2.27}$$

Natural Interpolation vs double interpolation ("sub-interpolation") functions

In XFEM literature, interpolation over the element subdomains is usually made using the standard shape functions of the original element (Fig. 2.15a). However, as discussed in Appendix D which includes an example of application, this interpolation leads to a reasonable representation only if the discontinuity is parallel to faces of the element. Overcoming these difficulties for the general case of discontinuities running skew to the mesh, is the motivations of the "double interpolation" (or sub-interpolation) scheme described in the following.

Consider the four-node linear rectangular element shown in Fig. 2.15a, crossed by a discontinuity in configuration "2-2" as shown in Fig.2.16. The double interpolation scheme considered in this study, involves two steps:

1. The regular interpolation functions $N_{(i)}$ of the original element are used to interpolate the regular and additional displacement values from the original nodes to the points of intersection of the elements edges with the discontinuity line (equations (2.24)-(2.25) and Fig. 2.15b). This

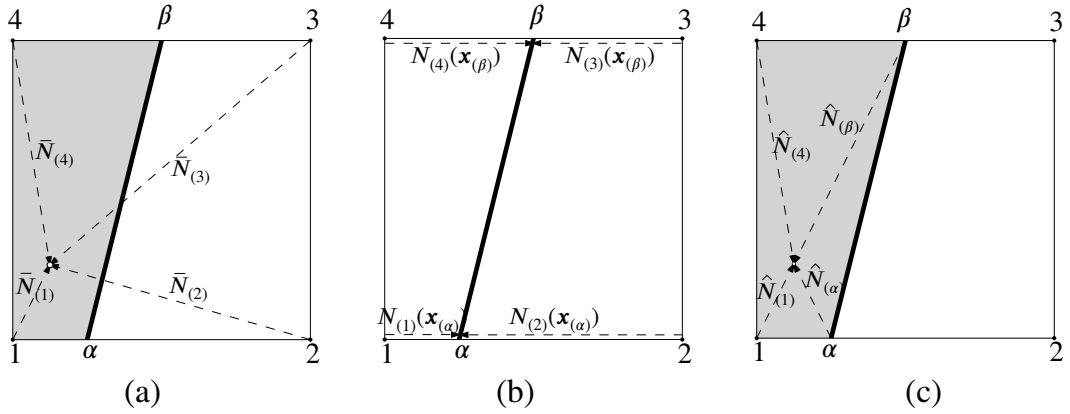

Figure 2.15: Double interpolation: (a) Resulting shape functions ($\bar{\mathbf{N}}_{(i)}$). (b) Using shape functions of the original element ($\mathbf{N}_{(i)}$) displacements in the intersection points (α , β) are obtained and then (c) From those, displacement at any point of the subdomains are interpolated using shape functions of the sub-domain ($\hat{\mathbf{N}}_{(i)}$).

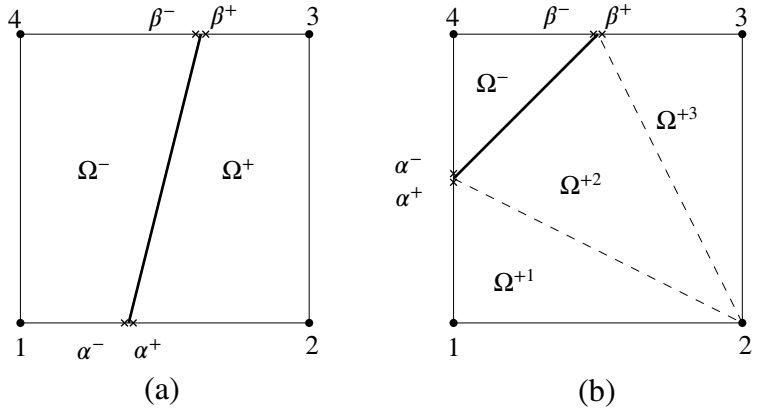

Figure 2.16: (a) "2-2" configuration. (b) "1-3" configuration.

leads to different values of $\mathbf{u}$ at points α^- and α^+ (on the left and right of the discontinuity at point α), and β^-, β^+:

$$\boldsymbol{u}^{-}_{(\alpha)} = \sum_{i\in\Omega^{-}} N_{(i)}\left(\boldsymbol{x}_{(\alpha)}\right)\mathbf{u}_{(i)} + \sum_{i\in\Omega^{+}} N_{(i)}\left(\boldsymbol{x}_{(\alpha)}\right)\boldsymbol{\delta}_{(i)} \tag{2.28}$$

$$\boldsymbol{u}^{+}_{(\alpha)} = \sum_{i\in\Omega^{-}} N_{(i)}\left(\boldsymbol{x}_{(\alpha)}\right)\boldsymbol{\delta}_{(i)} + \sum_{i\in\Omega^{+}} N_{(i)}\left(\boldsymbol{x}_{(\alpha)}\right)\mathbf{u}_{(i)} \tag{2.29}$$

$$\boldsymbol{u}^{-}_{(\beta)} = \sum_{i\in\Omega^{-}} N_{(i)}\left(\boldsymbol{x}_{(\beta)}\right)\mathbf{u}_{(i)} + \sum_{i\in\Omega^{+}} N_{(i)}\left(\left(\boldsymbol{x}_{(\beta)}\right)\boldsymbol{\delta}_{(i)}\right. \tag{2.30}$$

$$\boldsymbol{u}^{+}_{(\beta)} = \sum_{i\in\Omega^{-}} N_{(i)}\left(\left(\boldsymbol{x}_{(\beta)}\right)\boldsymbol{\delta}_{(i)} + \sum_{i\in\Omega^{+}} N_{(i)}\left(\left(\boldsymbol{x}_{(\beta)}\right)\mathbf{u}_{(i)}\right.\right. \tag{2.31}$$

2. The values of the function at those points are interpolated again ("sub-interpolated") to the interior of the sub-elements using additional regular linear interpolation functions $\hat{N}_{(i)}$ defined over the continuum sub-elements on the minus $(-)$ and on the plus $(+)$ sides of the original element in terms of local coordinates for each of those subdomains, $\mathbf{x}^{-}$ and $\mathbf{x}^{+}$ (Fig. 2.15c):

$$\mathbf{u}\left(\mathbf{x}^{-}\right) = \sum_{i\in\Omega^{-}} \hat{N}_{(i)}\left(\mathbf{x}^{-}\right)\mathbf{u}_{(i)} + \sum_{\lambda\in\alpha,\beta} \hat{N}_{(\lambda)}\left(\mathbf{x}^{-}\right)\boldsymbol{u}^{-}_{(\lambda)} \tag{2.32}$$

$$\mathbf{u}\left(\mathbf{x}^{+}\right) = \sum_{\lambda\in\alpha,\beta} \hat{N}_{(\lambda)}\left(\mathbf{x}^{+}\right)\boldsymbol{u}^{+}_{(\lambda)} + \sum_{i\in\Omega^{+}} \hat{N}_{(i)}\left(\mathbf{x}^{+}\right)\mathbf{u}_{(i)} \tag{2.33}$$

For the purpose of the Finite Element formulation in the following sections, it is convenient to express the above relations in matrix form. The displacement field at any point in the interior of the negative part of the element may be expressed as:

$$\mathbf{u}\left(\mathbf{x}^{-}\right) = \hat{\mathbf{N}}^{-}\,\mathbf{u}_{e}{}^{-} \tag{2.34}$$

where $\hat{\mathbf{N}}^{-}$ is the matrix of shape functions for the interpolation within the negative part of the element, and $\mathbf{u}_{e}{}^{-}$ is the vector of values of displacement at the corners of the negative part of the element. Those corners include the nodes of the negative part of the element and also the intersection points α, β, which may be in turn expressed in terms of the original nodal values. Therefore, $\mathbf{u}_{e}{}^{-}$ may be in turn expressed as:

$$\mathbf{u}_{e}{}^{-} = \mathbf{T}^{-}\,\bar{\mathbf{u}}_{e} \tag{2.35}$$

where $\mathbf{T}^{-}$ is a matrix containing the original shape functions of the overall element, and $\bar{\mathbf{u}}_e$ includes all displacement variables of the original element, that is, the regular $\mathbf{u}_{(i)}$ as well as the additional $\boldsymbol{\delta}_{(i)}$ nodal displacements, $\bar{\mathbf{u}}_e = \begin{pmatrix} \mathbf{u}_e & \boldsymbol{\delta}_e \end{pmatrix}^T$. Replacing this equation in the previous one,

$$\mathbf{u}\left(\mathbf{x}^{-}\right) = \hat{\mathbf{N}}^{-}\mathbf{T}^{-}\bar{\mathbf{u}}_e = \bar{\mathbf{N}}^{-}\bar{\mathbf{u}}_e \tag{2.36}$$

where $\bar{\mathbf{N}}^{(-)}$ is the final interpolation matrix for the negative side of the element (Fig. 2.15a):

$$\bar{\mathbf{N}}^{-} = \hat{\mathbf{N}}^{-}\mathbf{T}^{-} \tag{2.37}$$

In the same way, similar equations may be obtained for the positive part:

$$\mathbf{u}\left(\mathbf{x}^{+}\right) = \hat{\mathbf{N}}^{+}\mathbf{T}^{+}\bar{\mathbf{u}}_e = \bar{\mathbf{N}}^{+}\bar{\mathbf{u}}_e \tag{2.38}$$

with

$$\bar{\mathbf{N}}^{+} = \hat{\mathbf{N}}^{+}\mathbf{T}^{+} \tag{2.39}$$

The specific format and content of the interpolation matrices will depend on the type of element (e.g. quadrangular, triangular) and the type of intersection scheme with the discontinuity (e.g. "2-2", "1-3", etc). For linear quadrangular elements these matrices are specified in Appendix A. Note that since $\bar{\mathbf{u}}_e$ is composed of the two parts $\mathbf{u}_e$ and $\boldsymbol{\delta}_e$, matrices $\bar{\mathbf{N}}^{-}$, $\bar{\mathbf{N}}^{+}$ can be also decomposed into two parts, $\bar{\mathbf{N}}^{-} = [\bar{\mathbf{N}}^{-}_u \,|\, \bar{\mathbf{N}}^{-}_\delta]$ and $\bar{\mathbf{N}}^{+} = [\bar{\mathbf{N}}^{+}_u \,|\, \bar{\mathbf{N}}^{+}_\delta]$.

Matrices B and stiffness matrix K

Knowing the displacement field via equations (2.36-2.39), the strain field in the continuum part of the element can be calculated as the derivative of displacements

$$\boldsymbol{\varepsilon} = \mathbf{L}\mathbf{u}\left(\mathbf{x}\right), \quad \boldsymbol{\varepsilon} = \begin{pmatrix} \varepsilon_x & \varepsilon_y & \varepsilon_{xy} \end{pmatrix}^T, \quad \text{and} \quad \mathbf{L} = \begin{bmatrix} \partial/\partial x & 0 \\ 0 & \partial/\partial y \\ \partial/\partial y & \partial/\partial x \end{bmatrix} \tag{2.40}$$

Specifying the displacement field for the positive and negative parts of the element, one obtains matrices $\bar{\mathbf{B}}^{-}$ and $\bar{\mathbf{B}}^{+}$:

$$\boldsymbol{\varepsilon}\left(\mathbf{x}^{-}\right) = \mathbf{L}\cdot\bar{\mathbf{N}}^{-}\bar{\mathbf{u}}_e = \bar{\mathbf{B}}^{-}\bar{\mathbf{u}}_e \tag{2.41}$$

$$\boldsymbol{\varepsilon}\left(\mathbf{x}^{+}\right) = \mathbf{L}\cdot\bar{\mathbf{N}}^{+}\bar{\mathbf{u}}_e = \bar{\mathbf{B}}^{+}\bar{\mathbf{u}}_e \tag{2.42}$$

where matrices $\bar{\mathbf{B}}$, same as $\bar{\mathbf{N}}$, can be decomposed in "u" and "δ" parts:

$$\bar{\mathbf{B}}^{-} = \left[\begin{array}{c|c} \bar{\mathbf{B}}_u^{-} & \bar{\mathbf{B}}_\delta^{-} \end{array}\right], \quad \bar{\mathbf{B}}_u^{-} = \mathbf{L}\cdot\bar{\mathbf{N}}_u^{-}, \quad \bar{\mathbf{B}}_\delta^{-} = \mathbf{L}\cdot\bar{\mathbf{N}}_\delta^{-} \tag{2.43}$$

$$\bar{\mathbf{B}}^{+} = \left[\begin{array}{c|c} \bar{\mathbf{B}}_u^{+} & \bar{\mathbf{B}}_\delta^{+} \end{array}\right], \quad \bar{\mathbf{B}}_u^{+} = \mathbf{L}\cdot\bar{\mathbf{N}}_u^{+}, \quad \bar{\mathbf{B}}_\delta^{+} = \mathbf{L}\cdot\bar{\mathbf{N}}_\delta^{+} \tag{2.44}$$

Note that, same as for the corresponding matrices $\mathbf{N}$ matrices, the specific components of $\bar{\mathbf{B}}_u^{-}$, $\bar{\mathbf{B}}_\delta^{-}$, $\bar{\mathbf{B}}_u^{+}$ and $\bar{\mathbf{B}}_\delta^{+}$ will vary depending on the type of element and intersection considered.

Onto the discontinuity itself, the role of strain in the constitutive laws is played by the normal and tangential relative displacements, grouped here in vector $\boldsymbol{\varepsilon}^{J} = (u_n, u_t)^T$. These relative displacements may by obtained by simple matrix arrangement and rotation of the x, y relative displacements $\mathbf{a}$ obtained previously in Eq. (2.27):

$$\boldsymbol{\varepsilon}^{J} = \mathbf{R}\mathbf{a} = \mathbf{R}\cdot\bar{\mathbf{N}}^{J}\bar{\mathbf{u}}_e = \bar{\mathbf{B}}^{J}\bar{\mathbf{u}}_e \quad , \quad \bar{\mathbf{B}}^{J} = \mathbf{R}\cdot\bar{\mathbf{N}}^{J} \tag{2.45}$$

Continuum stresses σ are related to strains by the constitutive law, which for the purpose of deriving the stiffness matrix and initial force vectors of the finite element, are assumed to have a general linear format:

$$\boldsymbol{\sigma} = \mathbf{D}\boldsymbol{\varepsilon} + \boldsymbol{\sigma}_0 \tag{2.46}$$

where the initial stress term may account for stress-free deformations such as thermal, chemical or other swelling effects ($\sigma_0 = -D_0\varepsilon_0$). Also, in the more general context of the iterative solution of non-linear material behavior, σ and ε may be interpreted as the increment of stress and strain in the current iteration, D as the current tangential or algorithmic constitutive stiffness, and σ_0 may be interpreted as a residual (unbalanced) stress (i.e. as the difference between the previously obtained linear solution stress, and the "true" stress that, according to the non-linear constitutive equation, corresponds to the strain also obtained, see Sec.2.4.1).

Similarly, for the discontinuity, the stress traction vector $\boldsymbol{\sigma}^{J} = [\sigma, \tau]^T$ is assumed to be related

to relative displacements $\boldsymbol{\varepsilon}^{J}$ via general linear relation.

$$\boldsymbol{\sigma}^{J} = \mathbf{D}^{J}\boldsymbol{\varepsilon}^{J} + \boldsymbol{\sigma}_0^{J} \tag{2.47}$$

From here, the derivation of stiffness matrix and initial force vector follows standard FE procedures. The Principle of Virtual Work (PVW) is applied between a virtual system of nodal displacements $\triangle\bar{\mathbf{u}}_e^{vir}$ and the associated strains $\triangle\boldsymbol{\varepsilon}^{vir\,-}$, $\triangle\boldsymbol{\varepsilon}^{vir\,+}$ and $\triangle\boldsymbol{\varepsilon}^{vir\,J}$, and the corresponding conjugate forces and stress variables $\bar{\mathbf{f}}_e$, $\boldsymbol{\sigma}^{-}$, $\boldsymbol{\sigma}^{+}$ and $\boldsymbol{\sigma}^{J}$.

For XFEM, virtual displacement vector $\left(\bar{\mathbf{u}}_e^{vir\,T}\right)$ and force vector $\left(\bar{\mathbf{f}}_e^{T}\right)$ are composed of the two parts that correspond to real and fictitious degrees of freedom:

$$\bar{\mathbf{u}}_e^{vir} = \left[\begin{array}{c|c} \mathbf{u}_e^{vir\,T} & \boldsymbol{\delta}_e^{vir\,T} \end{array}\right]^T, \quad \bar{\mathbf{f}}_e = \left[\begin{array}{c|c} \mathbf{f}_u^{T} & \mathbf{f}_\delta^{T} \end{array}\right]^T \tag{2.48}$$

The virtual work done by external forces is calculated multiplying nodal virtual displacements by nodal forces.

$$W_{ext} = \left(\mathbf{u_e}^{vir}\right)^T \mathbf{f}_u + \left(\boldsymbol{\delta}_e^{vir}\right)^T \mathbf{f}_\delta = \left(\bar{\mathbf{u}}_e^{vir}\right)^T \bar{\mathbf{f}}_e \tag{2.49}$$

The virtual work of internal forces is given by the integral of the corresponding strains multiplied by their conjugate stress.

$$W_{int} = \left(\bar{\mathbf{u}}_e^{vir}\right)^T \cdot \left[\int_{\Omega^-} \left(\bar{\mathbf{B}}^{-}\right)^T \boldsymbol{\sigma}\,\mathrm{dV} + \int_{\Omega^+} \left(\bar{\mathbf{B}}^{+}\right)^T \boldsymbol{\sigma}\,\mathrm{dV} + \int_{L} \left(\bar{\mathbf{B}}^{J}\right)^T \boldsymbol{\sigma}^{J}\,\mathrm{dL}\right] \tag{2.50}$$

Imposing that the work of internal and external forces are equivalent , $W_{ext} = W_{int}$, one obtains the weak matrix form of equilibrium for the overall element including the XFEM discontinuity:

$$\bar{\mathbf{f}}_e = \int_{\Omega^-} \left(\bar{\mathbf{B}}^{-}\right)^T \sigma\,\mathrm{dV} + \int_{\Omega^+} \left(\bar{\mathbf{B}}^{+}\right)^T \sigma\,\mathrm{dV} + \int_{L} \left(\bar{\mathbf{B}}^{J}\right)^T \boldsymbol{\sigma}^{J}\,\mathrm{dL} \tag{2.51}$$

Note that this format is similar to the traditional FEM expressions, except that it includes the contribution from the negative, positive and discontinuity parts of the element.

Replacing in this equation the stresses with the constitutive laws (Eq.2.46 and 2.47), and then strains with their expressions in terms of $\mathbf{B}$ matrices and nodal displacements (Eqs. 2.41, 2.42 and 2.45), the typical finite element expression is obtained:

$$\bar{\mathbf{f}}_e = \bar{\mathbf{K}}_e \cdot \bar{\mathbf{u}}_e + \bar{\mathbf{f}}_{e\,0} \tag{2.52}$$

where

$$\bar{\mathbf{K}}_e = \int_{\Omega^-} \left(\bar{\mathbf{B}}^-\right)^T \mathbf{D}\bar{\mathbf{B}}^- \mathrm{dV} + \int_{\Omega^+} \left(\bar{\mathbf{B}}^+\right)^T \mathbf{D}\bar{\mathbf{B}}^+ \mathrm{dV} + \\ + \int_L \left(\bar{\mathbf{B}}^J\right)^T \mathbf{D}^J \bar{\mathbf{B}}^J \mathrm{dL} \tag{2.53}$$

$$\bar{\mathbf{f}}_{e\,0} = \int_{\Omega^-} \left(\bar{\mathbf{B}}^-\right)^T \boldsymbol{\sigma}_0 \mathrm{dV} + \int_{\Omega^+} \left(\bar{\mathbf{B}}^+\right)^T \boldsymbol{\sigma}_0 \mathrm{dV} + \int_L \left(\bar{\mathbf{B}}^J\right)^T \boldsymbol{\sigma}_0^J \mathrm{dL} \tag{2.54}$$

Replacing now XFEM vectors and matrices by their "u" and "δ" parts one can obtain more detailed expressions:

$$\bar{\mathbf{K}}_e = \begin{bmatrix} \bar{\mathbf{K}}_{uu} & \bar{\mathbf{K}}_{u\delta} \\ \bar{\mathbf{K}}_{\delta u} & \bar{\mathbf{K}}_{\delta\delta} \end{bmatrix} \tag{2.55}$$

where

$$\begin{aligned}
\bar{\mathbf{K}}_{uu} &= \int_{\Omega^-} \left(\bar{\mathbf{B}}_u^-\right)^T \cdot \mathbf{D} \cdot \bar{\mathbf{B}}_u^- \mathrm{dV} + \int_{\Omega^+} \left(\bar{\mathbf{B}}_u^+\right)^T \cdot \mathbf{D} \cdot \bar{\mathbf{B}}_u^+ \mathrm{dV} + \int_L \left(\bar{\mathbf{B}}_u^J\right)^T \cdot \mathbf{D}^J \cdot \bar{\mathbf{B}}_u^J \mathrm{dL} \\
\bar{\mathbf{K}}_{u\delta} &= \int_{\Omega^-} \left(\bar{\mathbf{B}}_u^-\right)^T \cdot \mathbf{D} \cdot \bar{\mathbf{B}}_\delta^- \mathrm{dV} + \int_{\Omega^+} \left(\bar{\mathbf{B}}_u^+\right)^T \cdot \mathbf{D} \cdot \bar{\mathbf{B}}_\delta^+ \mathrm{dV} - \int_L \left(\bar{\mathbf{B}}_u^J\right)^T \cdot \mathbf{D}^J \cdot \bar{\mathbf{B}}_\delta^J \mathrm{dL} \\
\bar{\mathbf{K}}_{\delta u} &= \int_{\Omega^-} \left(\bar{\mathbf{B}}_\delta^-\right)^T \cdot \mathbf{D} \cdot \bar{\mathbf{B}}_u^- \mathrm{dV} + \int_{\Omega^+} \left(\bar{\mathbf{B}}_\delta^+\right)^T \cdot \mathbf{D} \cdot \bar{\mathbf{B}}_u^+ \mathrm{dV} - \int_L \left(\bar{\mathbf{B}}_\delta^J\right)^T \cdot \mathbf{D}^J \cdot \bar{\mathbf{B}}_u^J \mathrm{dL} \\
\bar{\mathbf{K}}_{\delta\delta} &= \int_{\Omega^-} \left(\bar{\mathbf{B}}_\delta^-\right)^T \cdot \mathbf{D} \cdot \bar{\mathbf{B}}_\delta^- \mathrm{dV} + \int_{\Omega^+} \left(\bar{\mathbf{B}}_\delta^+\right)^T \cdot \mathbf{D} \cdot \bar{\mathbf{B}}_\delta^+ \mathrm{dV} + \int_L \left(\bar{\mathbf{B}}_\delta^J\right)^T \cdot \mathbf{D}^J \cdot \bar{\mathbf{B}}_\delta^J \mathrm{dL}
\end{aligned} \tag{2.56}$$

and

$$\bar{\mathbf{f}}_{e\,0} = \begin{bmatrix} \mathbf{f}_{u\,0} \\ \mathbf{f}_{\delta\,0} \end{bmatrix} \tag{2.57}$$

$$\mathbf{f}_{u\,0} = \int_{\Omega^-} \left(\bar{\mathbf{B}}_u^-\right)^T \cdot \boldsymbol{\sigma}_0 \mathrm{dV} + \int_{\Omega^+} \left(\bar{\mathbf{B}}_u^+\right)^T \cdot \boldsymbol{\sigma}_0 \mathrm{dV} + \int_L \left(\bar{\mathbf{B}}_u^J\right)^T \cdot \boldsymbol{\sigma}_0^J \mathrm{dL} \tag{2.58}$$

$$\mathbf{f}_{\delta\,0} = \int_{\Omega^-} \left(\bar{\mathbf{B}}_\delta^-\right)^T \cdot \boldsymbol{\sigma}_0 \mathrm{dV} + \int_{\Omega^+} \left(\bar{\mathbf{B}}_\delta^+\right)^T \cdot \boldsymbol{\sigma}_0 \mathrm{dV} - \int_L \left(\bar{\mathbf{B}}_\delta^J\right)^T \cdot \boldsymbol{\sigma}_0^J \mathrm{dL} \tag{2.59}$$

Note once more, that specific components of these element matrices and vectors will be different for each type of element and intersection, as the consequence of the specific expressions of matrices $\mathbf{N}$ and $\mathbf{B}$.

All previous developments in this section and in Appendix A have been formulated for quadrangular elements, for which double interpolation leads to a formulation which is different from the more common one obtained with natural interpolation. In the case of linear triangles, both formulations turn out equivalent since interpolating linearly along edges to intersection points, and then again linearly into the subdomain, leads to the same result as direct linear interpolation from vertices. Nevertheless, the same type of formulation as just presented for quadrangles is also developed for triangles in Appendix C. This is done for completeness, and also because with this format of equations it is possible to relate the XFEM formulation to the classical FEM with zero-thickness interface elements, as discussed in Section 2.4.3.

Extension to non-linear constitutive behavior of the discontinuity

The formulation described for linear constitutive behavior of the discontinuity may be easily extended to cover non-linear constitutive behavior using standard iterative FE procedures (e.g. Zienkiewicz and Taylor, 2005). In that context, and for each iteration, the element stiffness matrix and initial force vector in (2.52) take the meaning of tangential or algorithmic element stiffness matrix, and residual (or internal) element force vector, which may be evaluated from constitutive stiffness and residual (or internal) constitutive stresses of the discontinuity, by same expressions (2.53)-(2.59).

2.4.2 Moving nodes to the discontinuity and special configuration cases

As already explained in the Introduction, one of the problems with XFEM (that will be illustrated with an example in Sec. 2.4.4) is caused by nodes lying too close to the discontinuity line. In that case, the numerical results tend to produce oscillations. One possible solution to this problem consists of moving the corresponding nodes away from the discontinuity itself (e.g. Choi et al., 2012). However, this may be done in various directions and also requires deciding the magnitude of such displacement. In this thesis, the opposite strategy is adopted: to move the affected nodes onto the discontinuity itself. This can be done more easily in a unique way using the perpendicular direction to the discontinuity line (shortest distance). As the consequence, new element-discontinuity configurations are generated in which the discontinuity coincides in one or more nodes of the element. These cases deserve separate treatment and are considered in this section and in Appendices B and C.

For quadrangular elements, it is only necessary to define four types of special cases (Fig. 2.17) and the rest can be deduced by symmetry or rotation. These configurations are not particular

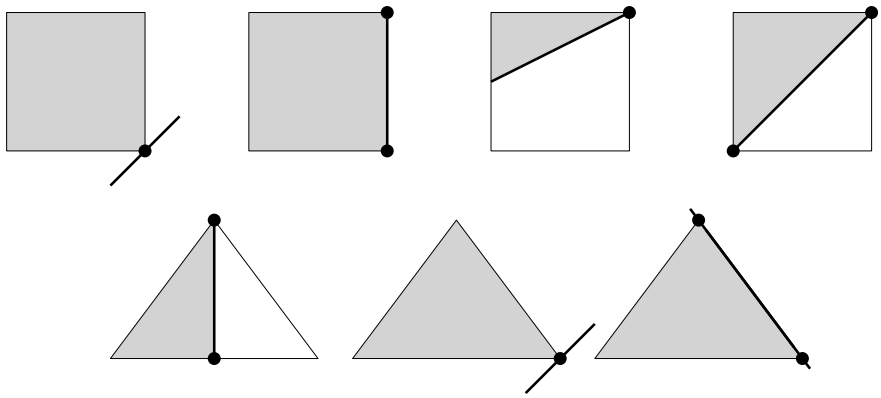

Figure 2.17: Special cases on quadrangular and triangular elements where the discontinuity coincides with nodes or edges.

cases of the "2-2" or "1-3 " configurations, because different subdomains are created, in some cases a complete subdomain disappears or changes shape and therefore its interpolation and **T** matrices also change. Particularized formulation for these four cases are developed in Appendix B. Similarly, special cases for triangles are shown in Fig. 2.17 bottom, also formulated in Appendix C.

2.4.3 Equivalence between XFEM and zero-thickness interface elements

As already suggested in previous sections, thanks to the assumption of the sub-interpolation, it is possible to establish the equivalence between the proposed formulation of XFEM, and a standard FEM formulation with zero-thickness interface elements (FEM+z) in which one standard continuum element is used for each XFEM integration sub-domain, and one zero-thickness interface is used for the discontinuity segment contained in the original element. The equivalence is first demonstrated for the case of the "2-2" discontinuity configuration on the quadrangular element, which is shown in Fig. 2.18a assuming a FEM+z formulation, and in Fig. 2.16a assuming the proposed XFEM formulation. The case of the "1-3" configuration of the same element is also shown on Fig. 2.18b, and is discussed later.

"2-2 " configuration

As seen in Fig.2.18a, for the traditional FEM+z formulation, the nodal variables would be the displacements of nodes 1 to 8, including the corner nodes 1-4 (same as in the XFEM approach) plus the four nodes 5-8 located on the right and left of each discontinuity at its intersection with the upper and lower domain limits. Comparing to the XFEM formulation, nodes 5, 6, 7 and 8

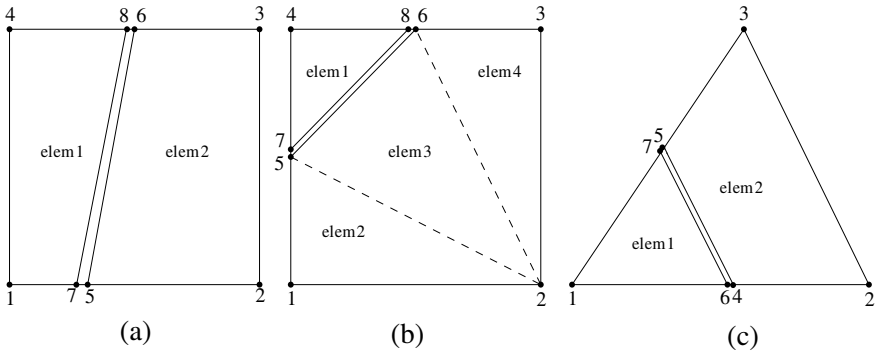

Figure 2.18: (a) Element with"2-2 " discontinuity configuration in the context of FEM+z formulation. (b) Same with "1-3 " discontinuity configuration. (c) Same with triangular element configuration.

would correspond to XFEM points α^+, β^+, α^-, β^- respectively (Fig 2.16a-2.18a). The domain would include two standard quadrangular elements, one with nodes 1, 7, 8 and 4 (corresponding to XFEM subdomain Ω^- with corner points 1, α^-, β^- and 4) and the second with nodes 5, 2, 3 and 6 (corresponding to subdomain Ω^+ with corner points α^+, 2 and β^+). The interface element would connect nodes 5, 6, 7 and 8, that is XFEM points α^+, β^+, α^- and β^-. The stiffness matrices of those elements would have expressions:

$$\hat{\mathbf{K}}^{e1}=\int_{e1}\left(\hat{\mathbf{B}}^{e1}\right)^T\mathbf{D}\hat{\mathbf{B}}^{e1}\mathrm{dV},\quad \hat{\mathbf{K}}^{e2}=\int_{e2}\left(\hat{\mathbf{B}}^{e2}\right)^T\mathbf{D}\hat{\mathbf{B}}^{e2}\mathrm{dV},\quad \hat{\mathbf{K}}^{eJ}=\int_{eJ}\left(\hat{\mathbf{B}}^{eJ}\right)^T\mathbf{D}\hat{\mathbf{B}}^{eJ}\mathrm{dL} \tag{2.60}$$

where $\hat{\mathbf{B}}^{e1}$, $\hat{\mathbf{B}}^{e2}$ are the standard FEM matrices obtained as $\hat{\mathbf{B}}^{e1}=\mathbf{L}\hat{\mathbf{N}}^{e1}$ and $\hat{\mathbf{B}}^{e2}=\mathbf{L}\hat{\mathbf{N}}^{e2}$, being $\hat{\mathbf{N}}^{e1}$ and $\hat{\mathbf{N}}^{e2}$ the same local interpolation matrices defined as $\hat{\mathbf{N}}^-$ and $\hat{\mathbf{N}}^+$ in (A.3) and (A.9). Matrix $\hat{\mathbf{B}}^J$ is the standard interface element matrix obtained as $\hat{\mathbf{B}}^{eJ}=\mathbf{R}\hat{\mathbf{N}}^{eJ}$, being $\hat{\mathbf{N}}^{eJ}$ the same matrix defined in (2.41).

Going back now to the expression of the overall element XFEM stiffness matrix (2.53), by replacing continuum $\mathbf{B}$ matrices as the product of $\mathbf{L}$ and $\bar{\mathbf{N}}$, equations (2.41-2.42), replacing interface $\mathbf{B}$ matrix as the product $\mathbf{R}\bar{\mathbf{N}}$, equation (2.45), and finally all $\bar{\mathbf{N}}$ matrices as the products of the respective $\hat{\mathbf{N}}$ and $\mathbf{T}$ matrices, equations (2.37), (2.39) and (A.17), that expression may be rewritten as:

$$\bar{\mathbf{K}}_e=\bar{\mathbf{K}}^-+\bar{\mathbf{K}}^+\bar{\mathbf{K}}^J \tag{2.61}$$

where

$$\bar{\mathbf{K}}^{-} = \int_{\Omega^{-}} \left(\bar{\mathbf{B}}^{-}\right)^{T} \mathbf{D}\bar{\mathbf{B}}^{-} \mathrm{d}\Omega = \left(\mathbf{T}^{-}\right)^{T} \left(\int_{\Omega^{-}} \left(\hat{\mathbf{B}}^{-}\right)^{T} \mathbf{D}\hat{\mathbf{B}}^{-} \mathrm{d}\Omega\right) \mathbf{T}^{-} \tag{2.62}$$

$$\bar{\mathbf{K}}^{+} = \int_{\Omega^{+}} \left(\bar{\mathbf{B}}^{+}\right)^{T} \mathbf{D}\bar{\mathbf{B}}^{+} \mathrm{d}\Omega = \left(\mathbf{T}^{+}\right)^{T} \left(\int_{\Omega^{+}} \left(\hat{\mathbf{B}}^{+}\right)^{T} \mathbf{D}\hat{\mathbf{B}}^{+} \mathrm{d}\Omega\right) \mathbf{T}^{+} \tag{2.63}$$

$$\bar{\mathbf{K}}^{J} = \int_{L} \left(\bar{\mathbf{B}}^{J}\right)^{T} \mathbf{D}^{J} \bar{\mathbf{B}}^{J} \mathrm{dL} = \left(\mathbf{T}^{J}\right)^{T} \left(\int_{L} \left(\hat{\mathbf{B}}^{J}\right)^{T} \mathbf{D}^{J} \hat{\mathbf{B}}^{J} \mathrm{dL}\right) \mathbf{T}^{J} \tag{2.64}$$

and

$$\hat{\mathbf{B}}^{-} = \mathbf{L}\hat{\mathbf{N}}^{-}, \quad \hat{\mathbf{B}}^{+} = \mathbf{L}\hat{\mathbf{N}}^{+}, \quad \hat{\mathbf{B}}^{J} = \mathbf{R}\hat{\mathbf{N}}^{J}, \tag{2.65}$$

which finally leads to:

$$\bar{\mathbf{K}}_{e} = \left(\mathbf{T}^{-}\right)^{T} \hat{\mathbf{K}}_{e}^{-} \mathbf{T}^{-} + \left(\mathbf{T}^{+}\right)^{T} \hat{\mathbf{K}}_{e}^{+} \mathbf{T}^{+} + \left(\mathbf{T}^{J}\right)^{T} \hat{\mathbf{K}}_{e}^{J} \mathbf{T}^{J} \tag{2.66}$$

Since matrices $\hat{\mathbf{N}}$ and $\hat{\mathbf{B}}$ for the $^{-}$, $^{+}$ and ^{J} contributions to the XFEM stiffness, as well as the respective domains of integration, are the same as those for elements 1, 2 and J of the standard FEM formulation, respectively, the resulting local stiffness matrices $\hat{\mathbf{K}}$ will also be identical, that is:

$$\hat{\mathbf{K}}^{e1} = \hat{\mathbf{K}}^{-}, \quad \hat{\mathbf{K}}^{e2} = \hat{\mathbf{K}}^{+}, \quad \hat{\mathbf{K}}^{eJ} = \hat{\mathbf{K}}^{J} \tag{2.67}$$

The remaining aspect would refer to the product with $\mathbf{T}$ matrices in (2.66). However, this aspect may be trivial since the $\mathbf{T}$ matrices may be interpreted as the transport assembly matrices to relocate the contributions of each local stiffness matrix in the overall stiffness matrix. In this way, each $\mathbf{T}^{T}\hat{\mathbf{K}}\mathbf{T}$ product turns out to be a global stiffness matrix with the only non-zero terms corresponding to the $\hat{\mathbf{K}}$ matrix considered, and summation of the three of them leads to the overall stiffness matrix for the XFEM element including discontinuity.

A similar expression to (2.67) could be written for the FEM+z formulation using the corresponding T matrices, which would be different from the ones above, since the overall displacement vector does not contain the same variables ($\mathbf{u}_{(1)}...\mathbf{u}_{(4)}$, $\mathbf{u}_{(5)}...\mathbf{u}_{(8)}$ for FEM+z, instead of $\mathbf{u}_{(1)}...\mathbf{u}_{(4)}$, $\boldsymbol{\delta}_{(1)}...\boldsymbol{\delta}_{(4)}$ for XFEM). However, one could consider the FEM+z formulation with a change of variables such that variables $\mathbf{u}_{(5)}...\mathbf{u}_{(8)}$ would be exchanged by $\boldsymbol{\delta}_{(1)}...\boldsymbol{\delta}_{(4)}$. That can be done easily using linear functions between node 1 and 2 for instance, and $\boldsymbol{\delta}_{(2)}$ would be the result of linear extrapolation of the straight function defined by $\boldsymbol{u}_{(1)}$ and $\mathbf{u}_{(7)}$ along the bottom side, or conversely,

$\mathbf{u}_{(7)}$ would be the linear interpolation between values $\mathbf{u}_{(1)}$ and $\boldsymbol{\delta}_{(2)}$. And this is exactly the content of the $\mathbf{T}^{-}$, $\mathbf{T}^{+}$ and $\mathbf{T}^{J}$. Therefore, Eq. (2.66) can be reinterpreted as the assembly of the FEM+z element matrices in the system of variables used in the XFEM formulation, which proves the full equivalence of XFEM formulation with double interpolation, with the traditional FEM+z formulation in the case of quadrangular elements with "2-2"discontinuity configuration.

"1-3" configuration

Fig. 2.18b shows the FEM+z mesh for the XFEM quadrangular element with "1-3" configuration of discontinuity intersection, Fig. 2.16b. The FEM+z mesh contains four triangles $e1$, $e2$, $e3$ and $e4$, that correspond to the four integration subdomains Ω^{-}, Ω^{+1}, Ω^{+2}, and Ω^{+3}, and one interface element eJ that corresponds to the discontinuity contribution ^{J}.

By similar reasoning as before, one can easily conclude that the five local stiffness matrices $\hat{\mathbf{K}}$ will be the same for both, FEM+z and XFEM. However, the assembly here turns out a little trickier. In the previous "2-2" configuration the exchange of variables was one-to-one, and was invertible, that is, the four "$\mathbf{u}$" displacements ($\mathbf{u}_{(5)}$...$\mathbf{u}_{(8)}$) of the interface nodes where exchanged by the four "$\boldsymbol{\delta}$" nodal overhang displacements of the XFEM formulation. Therefore the final system had the same number of independent variables.

However, in the present configuration, the number of variables decreases because the original four nodal displacements $\mathbf{u}_{(5)}$...$\mathbf{u}_{(8)}$ (that in the FEM+z formulation do not change from previous configuration), in the case of XFEM are reduced to only three, specifically to $\boldsymbol{\delta}_{(1)}$, $\boldsymbol{\delta}_{(3)}$ and $\boldsymbol{\delta}_{(4)}$ (while $\boldsymbol{\delta}_{(2)}$, although formally present, does not participate in the system).

This may be intuitively explained because the $\mathbf{u}$ and $\boldsymbol{\delta}$ values of corner nodes 1 and 4 participate in the linear interpolation of the displacements of interface nodes 5 and 7, and those of nodes 3 and 4 participate for nodes 6 and 8, but node 2 does not participate in either of them. This is reflected by empty columns corresponding to $\boldsymbol{\delta}_{(2)}$ in all the corresponding $\mathbf{T}$ matrices given in equations (A.22), (A.28), (A.34), (A.40) of Appendix A. Which means that no stiffness term will be assembled to the corresponding global row/column in this configuration.

Aside from practical computational problems that can be circumvented (e.g. after assembly those "inactive" $\boldsymbol{\delta}$ variables have to be identified and their values prescribed to avoid zero pivot in the solution), the mechanical effect is that the XFEM formulation has fewer independent degrees of freedom, that is, it is kinematically restricted with respect to the same mesh solved using the traditional FEM+z formulation. This means that one can expect the solution of the same physical problem using XFEM to exhibit lower accuracy (and perhaps oscillations) as compared to the one

obtained using the FEM+z approach.

Triangular elements and special configurations

In the case of triangular elements (formulation developed in Appendix C) similar reasoning leads to the conclusion that in the general case (Fig.C.1a) the XFEM formulation is always equivalent to a kinematically restricted version of the FEM+z formulation applied to the same mesh. This is easily verified by a simple variable count, since FEM+z would lead to seven nodes while XFEM leads to the number of variables equivalent to six nodes.

However, a remarkable observation is that the above conclusions (for both quadrangles and triangles) are only valid for the general intersection case in which the discontinuity does not coincide with nodes or edges. Indeed, in the special cases that intersection does coincide with nodes or edges (Fig.B.1 a to e in Appendix B), it can be easily verified that the count changes and equivalence exists again between XFEM and FEM+z formulations (e.g. in cases of Fig. B.1a, B.1c, B.1d and B.1e, the number of nodes in FEM+z would be seven, six, five and six, respectively, and the number of independent variables equivalent in XFEM too). Similarly for triangles, the number of nodes in FEM+z for especial configurations in Fig. C.1b, C.1c, and C.1d in Appendix C would be six, four and five, and also the total number of variables equivalent in XFEM.

For this reason, it should not be surprising that the proposed strategy of moving close nodes onto the discontinuity itself is not only numerically convenient because it eliminates small subdomains, but also because it leads to configurations that maximize the number of independent degrees of freedom. This beneficial effect will be shown in some of the Examples (Sec.2.4.4).

2.4.4 Example simulations

This section includes three numerical examples, including a beam bending problem and the stress distribution around a tunnel, both with linear-elastic behavior of the discontinuity, as well as uniaxial compression specimen with an inclined discontinuity sliding under shear-compression.

Elastic beam bending

The first example consists of a cantilever beam subject to a vertical load at its end, as represented in Fig. 2.19. The material is linear elastic, isotropic and homogeneous, and plane stress behavior is assumed. The elastic solution is given by beam theory, with linear distribution of normal stress and parabolic distribution of shear stress on vertical cross-sections perpendicular to the beam axis. This example was also used in previous XFEM papers such as Sanders et al. (2009), and therefore

it can be compared to both analytical solution and to numerical results. The beam dimensions are 16m of length and 4m width ($L = 16$m, $c = 2$m) and material properties for the continuum elements are Young modulus $E = 1000$MPa and Poisson's ratio $\nu = 0.3$.

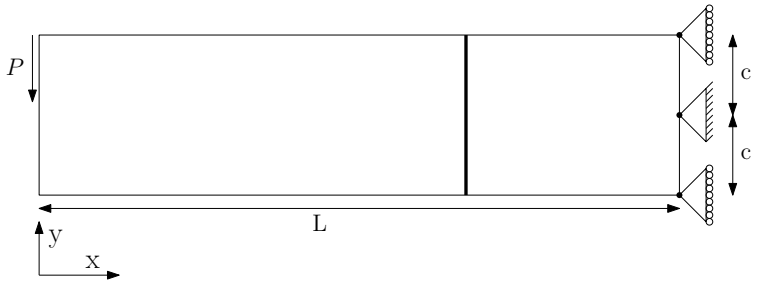

Figure 2.19: Geometry for beam bending test problem.

The stress boundary conditions are imposed on the right and left ends of the beam. The vertical load on the left end is $P = -1$MN, and is distributed on the nodes of that cross-section according to a parabolic distribution as given by beam theory. On the right-hand side, the same parabolic distribution is applied but with the opposite sign. Right top and bottom nodes are constrained in x-direction and the central node is constrained (Fig. 2.19). The distributed forces applied on both (left and right) vertical cross-sections are given by the following expressions:

$$\begin{cases} f_x(0,y) & = 0 \\ f_y(0,y) & = \frac{P}{2I}\left(c^2 - y^2\right) \\ f_x(L,y) & = \frac{PLy}{I} \\ f_y(L,y) & = -\frac{P}{2I}\left(c^2 - y^2\right) \end{cases} \tag{2.68}$$

where I is the inertia moment: $I = (2c)^3/12$.

Additionally, a vertical discontinuity is assumed located at the cross-section at $x = 11$m. Its behavior is assumed linear elastic with high stiffness values, so that it does not add any deformability, and therefore the beam behavior should be equivalent to the behavior given by beam theory (that is, without discontinuity), Eq.(2.69),

$$\begin{cases} \sigma_{xx} & = -\frac{Pxy}{I} \\ \sigma_{xy} & = \frac{P}{2I}\left(c^2 - y^2\right) \end{cases} \tag{2.69}$$

For the analysis, the beam has been discretized with various meshes, as shown in Fig. 2.20. The calculations have been run with two values of discontinuity stiffness, $K_N = K_T = 9000$MPa/m

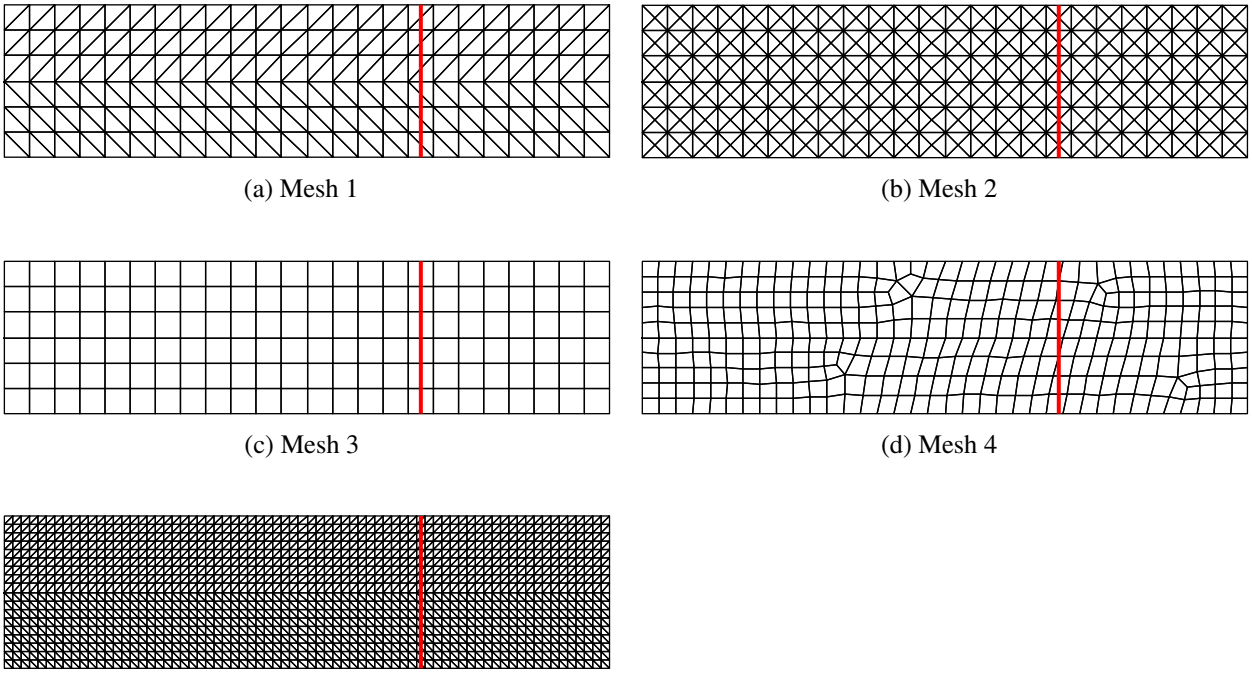

(a) Mesh 1

(b) Mesh 2

(c) Mesh 3

(d) Mesh 4

(e) Mesh 5

Figure 2.20: Meshes used to discretize the Cantilever beam of example two: (a) Biased structured triangular mesh with 12 elements across the beam depth. (b) Unbiased structured triangular mesh with 12 elements across the beam depth. (c) Structured quadrangular mesh with 6 elements across the beam depth (d) Unstructured quadrangular mesh with 10 elements across the beam depth, some of them really close to the discontinuity line (e) Structured triangular mesh with 36 elements across the beam depth (it is a refinement 1/3 of Mesh 1).

(same as in Sanders et al., 2009) and a much higher value $K_N = K_T = 10^7$MPa/m (K_N, K_T are the main diagonal components of the interface elastic stiffness $\mathbf{D}^J$ in Eq.2.47, which has been assumed with a diagonal format).

The first results presented are the comparison with the results from Sanders et al. (2009), specifically with the penalty formulation in that paper, using similar mesh and parameter values, that is, with the dense triangular Mesh 5 (Fig. 2.20e) and discontinuity stiffness $K_N = K_T = 9000$MPa/m. The results obtained are shown in Fig. 2.21 in terms of normal and shear stresses on the discontinuity cross-section, together with the predictions by beam formulas and the corresponding results from Sanders et al. (2009). As seen, there is very good match with Sander's results, something that could be expected given the equivalence of the formulations used (as explained in Sec. 2.4.1 in the case of triangles the proposed formulation coincides with the usual XFEM formulation based on natural interpolation, and also the linear elastic assumption for the discontinuity should be

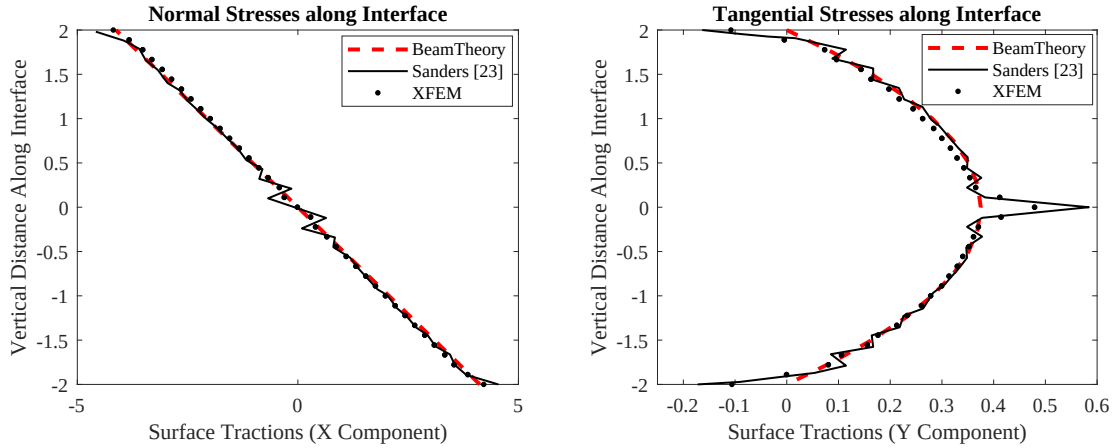

Figure 2.21: Interface tractions for XFEM discontinuity, together with analytical solution by beam theory, and results from Sanders et al. (2009).

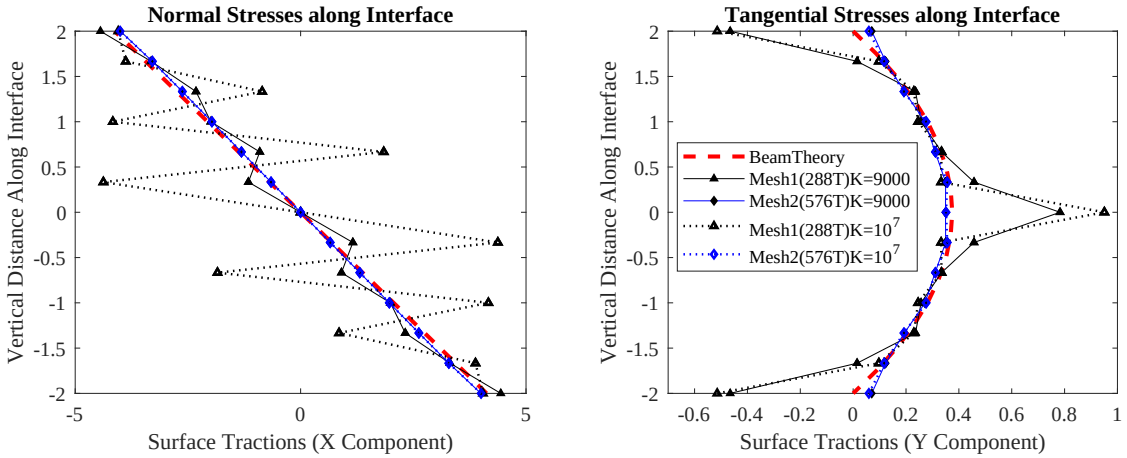

Figure 2.22: Normal and tangential stress distribution along the discontinuity using triangular elements.

equivalent to the penalty formulation in Sanders et al., 2009).

The results obtained with meshes 1 to 4, and with $K_N = K_T = 9000\text{MPa/m}$ and $K_N = K_T = 10^7\text{MPa/m}$, are shown in Figures 2.22 to and 2.24.

Fig. 2.22 shows the results obtained with triangular meshes 1 and 2 (Fig. 2.20a and 2.20b), and Fig. 2.23 and 2.24 show the results obtained with quadrangular elements, meshes 3 and 4 (Fig. 2.20c and 2.20d).

As seen in Fig. 2.22, XFEM calculations using linear triangles with "biased" orientation seem very sensitive to the discontinuity stiffness (penalty) values of K_N, K_T; the results obtained with

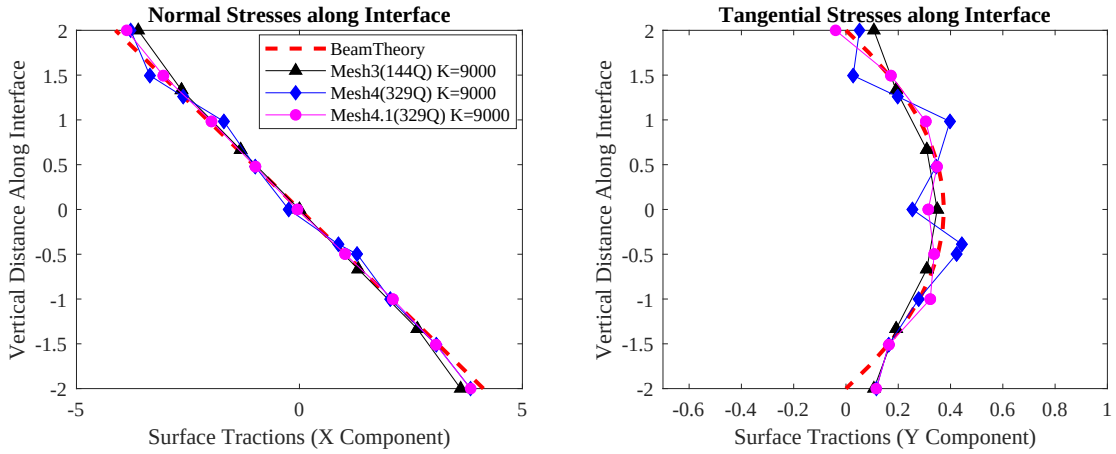

Figure 2.23: Normal and tangential stress distribution along the discontinuity using quadrangular elements and $K_N = K_T = 9000\text{MPa/m}$.

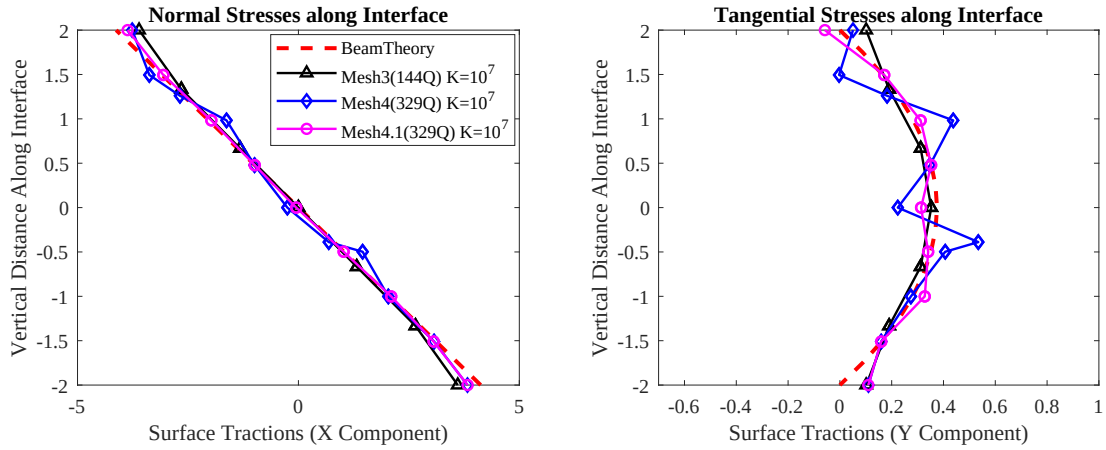

Figure 2.24: Normal and tangential stress distribution along the discontinuity using quadrangular elements and $K_N = K_T = 10^7\text{MPa/m}$.

the low density mesh 1 with the value $K_N = K_T = 9000\text{MPa/m}$ (same as used in Sanders et al., 2009) already show some oscillations, but if that value is increased in three orders of magnitude to $K_N = K_T = 10^7\text{MPa}$, oscillations become much larger, clearly excessive. On the other hand, mesh 2 is also made of linear triangles with similar density, but using an unbiased more symmetric arrangement, and the discontinuity is made to coincide with a line of "central" nodes to each mesh cell. In that case, the solution is much smoother and becomes insensitive to higher stiffness values.

In Fig. 2.23, the results for quadrangular meshes 3 and 4 using $K_N = K_T = 9000$ MPa/m are depicted, and Figure 2.24 shows the results for the same meshes using $K_N = K_T = 10^7$ MPa/m.

Mesh 3 is a regular mesh with discontinuity intersecting elements in a very favorable way, which shows very accurate smooth results. Mesh 4 is a random mesh of similar density, in which some nodes happen to fall very close to the discontinuity line. This is reflected in some oscillations observed in the results for that mesh. Mesh 4.1, also listed in captions of Figures 2.23 and 2.24, is very similar to Mesh 4 with the only difference that the nodes closest to the discontinuity have been moved onto the discontinuity itself (strategy proposed in this section to remedy this situation). As seen in the results, this strategy really succeeds in eliminating the oscillations. Also to be mentioned, all results for quadrangular elements seem much less sensitive (or not sensitive at all) to the increase of stiffness coefficient in three orders of magnitude from 9000 to 10^7MPa/m, and similar accuracies are obtained with much lower density of elements as compared to linear triangles, provided the strategy of moving close nodes the discontinuity itself is applied.

Tunnel cross-section

The second example consists of a tunnel of 6m radius in the center of a square 120 × 120m domain with a distributed load of 8MPa on the top, 4MPa on the right side and prescribed normal displacements on bottom and left boundaries (Fig. 2.25). A XFEM radial discontinuity with high elastic stiffness is also considered, which will allow us to evaluate normal and shear stresses along this line and compare them to the theoretical values given by the Kirsch solution (Kirsch, 1898).

Elastic parameters for the continuum are $E = 5000$MPa and $\nu = 0.25$. Normal and shear elastic stiffness values for the discontinuity are $K_N = 10^8$MPa/m and $K_T = 10^8$MPa/m. This case has been solved with a random quadrangular mesh as discussed in the following paragraphs.

The mesh considered is shown in Fig. 2.26a, consisting of 920 quadrangular elements, 25 of which are crossed by the XFEM discontinuity.

Fig. 2.27 shows the normal and shear stress distribution along the discontinuity line (dots) together with the closed-form solution (continuous line). It can be seen that the XFEM results are in general very close to the analytical solution except near the section around $x \simeq 18$m where some oscillating values are observed. Analyzing it in detail, the highest oscillation corresponds to elements where the discontinuity lies very close to a node (Fig. 2.26b).

As explained in the introduction and in Section 2.4.2, the proposed strategy in these cases is to move the closest nodes onto the discontinuity itself, obtaining in this way the special type of element configuration described in Section 2.4.2. The efficiency of this technique is demonstrated again in this case, since its application leads to the new results also shown in Fig. 2.27, in which oscillations have disappeared.

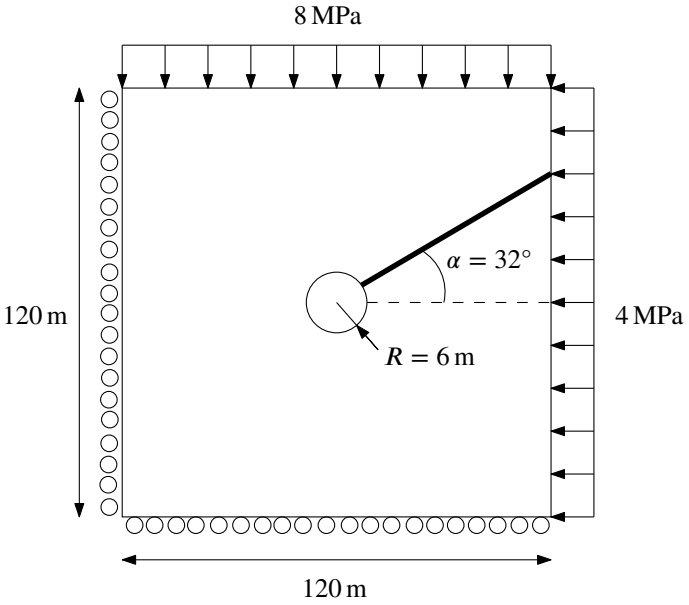

Figure 2.25: Geometry for the tunnel test problem of example 3.

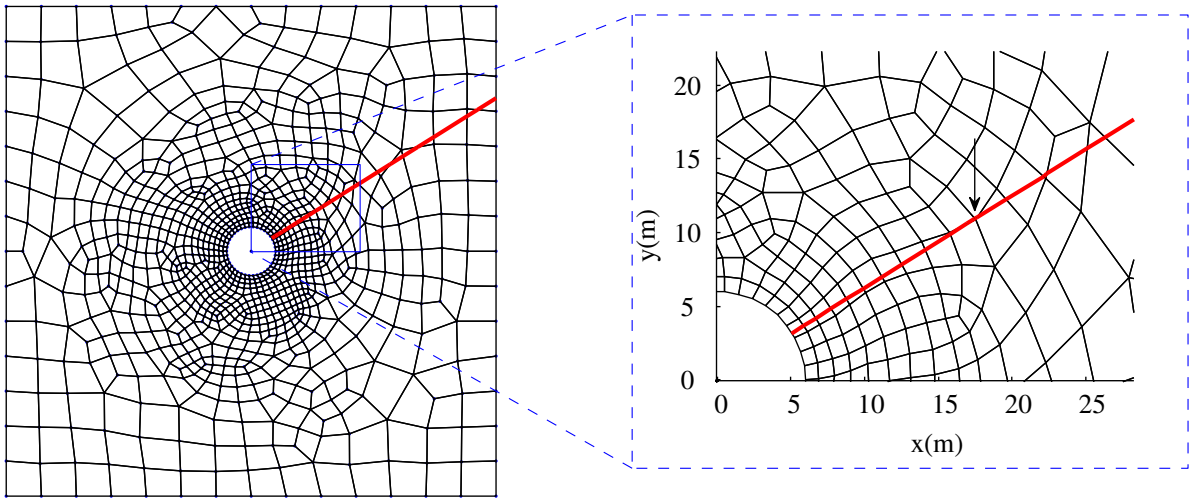

Figure 2.26: (a) Unstructured quadrangular mesh with 920 elements 25 of which are crossed by the discontinuity with configurations "2-2 " and "1-3 ". (b) Mesh detail to show the nodes closest to discontinuity line.

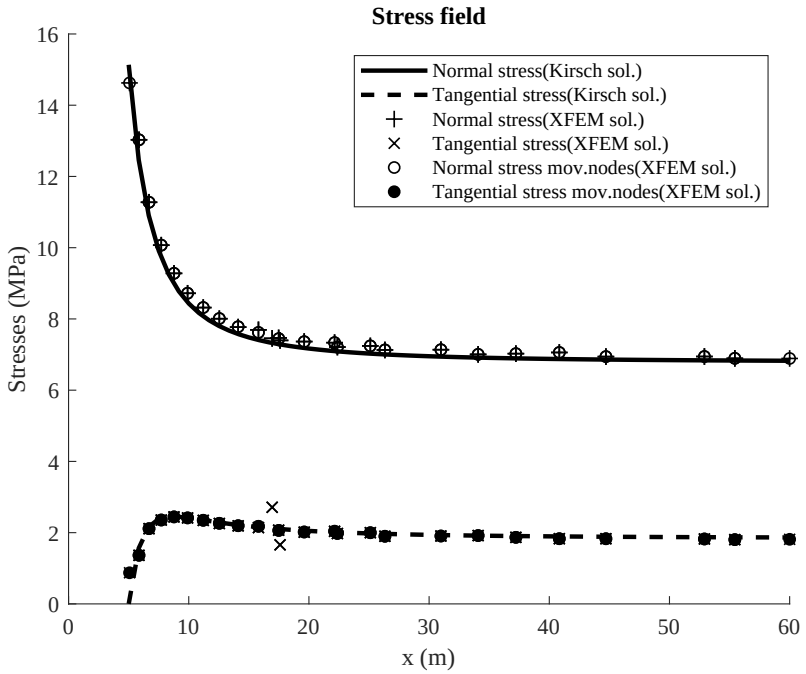

Figure 2.27: Numerical results for mesh of Fig. 2.26 moving closest nodes onto the discontinuity itself (Note +/× symbols for original results).

Compression test with non-linear constitutive law on the discontinuity

The proposed formulation can be also used to solve non linear problems. This schematic example consists of a rectangular specimen of two elements, one of them crossed by an inclined discontinuity (Figure 2.28), which incorporates a fracture mechanics-based elastoplastic constitutive model described in Carol et al. (1997). This model is based on a hyperbolic loading function depending on three parameters χ (tensile strength), c (apparent cohesion) and $\tan\phi$ (asymptotic friction angle), the evolution of which depends on the work spent during the fracture process W^{cr} (softening). The softening laws are such that tensile strength vanishes when W^{cr} reaches the fracture energy in mode I G_f^I, and apparent cohesion vanishes later, when W^{cr} reaches a second fracture energy for shear compression, G_f^{IIa}, generally larger than G_f^I (G_f^I and G_f^{IIa} are two of the model parameters).

The values assumed for material properties are Young modulus of $5 \cdot 10^6$MPa and Poisson's ratio $\nu = 0.1$ for the continuum. For the discontinuity, parameters are: normal and tangential stiffness coefficients $K_N = K_T = 10^{10}$MPa/m, apparent or asymptotic cohesion ($c = 40$MPa), tensile strength ($\chi = 10$MPa), asymptotic friction angle ($\tan\phi = 10°$) and fracture energies $G_f^I = 10^{-2}$MN/m and $G_f^{IIa} = 10^{-1}$MN/m. The specimen is subject to uniaxial compression loading along

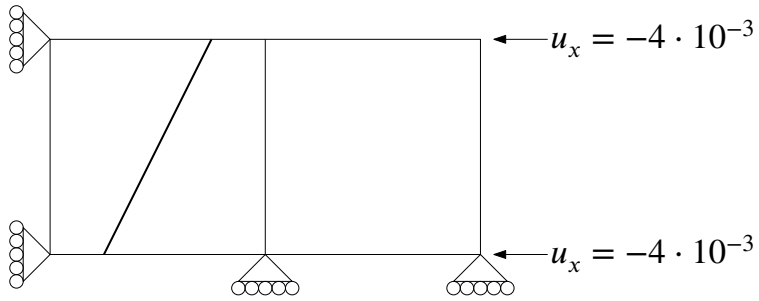

Figure 2.28: Geometry for compression specimen example.

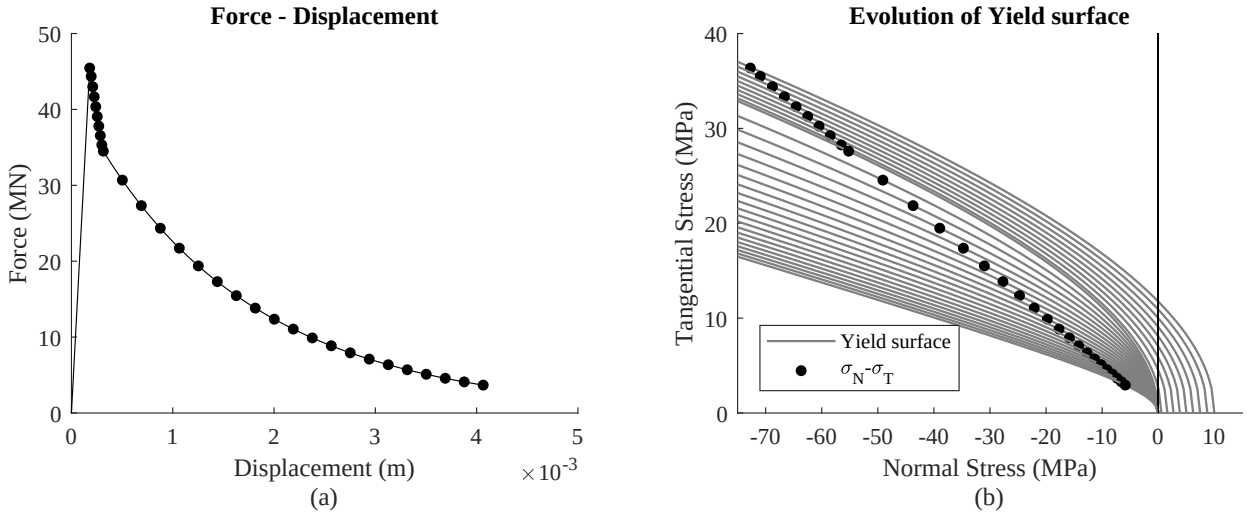

Figure 2.29: Results of example 3: (a) Resulting force-displacement diagram for whole specimen. (b) Evolution of normal and tangential stress on the discontinuity plane, and by yield surface evolution.

the horizontal direction with boundary conditions as also shown in Fig.2.28: increasing compressive displacements are prescribed to the right side of the specimen while the left side is allowed to move vertically.

The results obtained are represented in Figures 2.29 and 2.30. In Fig.2.29a the resulting force-displacement curve for the whole specimen exhibits an elastic part, followed by a peak value and softening branch, corresponding to the sliding with friction and softening along the discontinuity. In Fig.2.29b, the evolution of normal and shear stress on the discontinuity plane are represented together with the plastic surface at each stage of loading. It can be observed that the relation between normal and shear stress is (in this example) fixed by static condition along a straight line, while the hyperbolic surface is progressively degraded as the fracture process evolves.

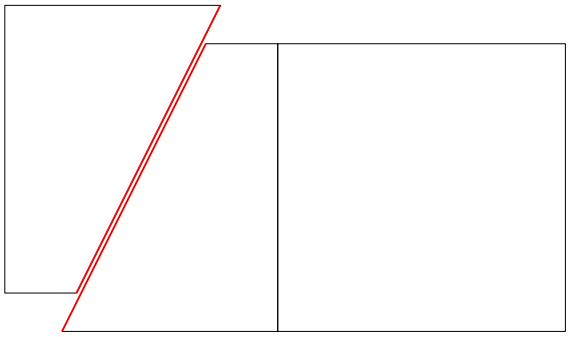

Figure 2.30: Magnified final deformation of specimen.

Finally, Fig.2.30 represents the deformed shape of specimen at the end of the test, showing that the left part of specimen has moved upwards as the right part moved to the left, as required by discontinuity kinematics.

2.4.5 Concluding remarks

A particular version of XFEM is proposed in this chapter, which is based on a double interpolation (or sub-interpolation) within each subdomain, and on the use of the "overhang" nodal displacements across the discontinuity (rather than the more usual jump variables themselves). The formulation turns out advantageous from various viewpoints. From the theoretical viewpoint, a direct relation may be established with the traditional formulation of the FEM with zero-thickness interface elements inserted along the same discontinuity line. In this chapter, full equivalence is proven in the case of quadrangular elements crossed by a discontinuity in a "2-2" configuration. In other configurations (such as "1-3" quadrangular elements, or in the case of triangles), the equivalence is to a restricted version of the FEM+z formulation, in which the original kinematic variables would not be all independent. It is also noted that the element stiffness matrix and force vector has been developed on the basis of the Principle of Virtual Work, which, although a standard procedure in the FEM, that seems not reported in existing XFEM literature.

From the numerical viewpoint, the double-interpolation approach also seems to lead to favorable results w.r.t. formulations based on natural interpolation in the case of quadrangular elements when the discontinuity runs skew to the mesh. The reason for this and numerical example showing the improvement obtained have been included in Appendix D. Example 2.4.4 corroborates numerically that, in the case of triangles, sub-interpolation would be equivalent to the usual XFEM formulation using natural interpolation functions, something already argued from the theoretical viewpoint. This example also shows that, in general, quadrangular elements seem to perform much better than

triangles for similar mesh densities, and also seem to be much less sensitive to high discontinuity (penalty) stiffness values, which in the case of triangles may easily lead to oscillations. The second example (tunnel cross-section) illustrates the numerical oscillations that may be observed when nodes lie too close to the discontinuity lines, and the effectivity of the strategy of moving those nodes onto the discontinuity line itself, provided of course that the resulting element configurations are properly identified and treated as special cases. This improvement is consistent with the fact that by doing this, the formulation becomes locally equivalent to FEM+z, maximizing the number of degrees of freedom to represent the discontinuity (not a restricted version). Finally, the third example illustrates the applicability of the formulation presented in combination with non-linear constitutive laws for the discontinuity.

Chapter 3

Cracking along non-preestablished paths

3.1 Introduction

The prediction of the mechanical behavior of quasi-brittle materials such as rocks or concrete is an essential topic in various engineering fields such as Structural Engineering, Geotechnical Engineering, mechanical Engineering, and lately also in petroleum Engineering. During the last few decades, much progress has been made in the modeling of cracking and fracture using the Finite Element Method (FEM).

Chapter 1 and Chapter 2 contain a discussion of the main families of models for representing numerically in the context of the FEM, the behavior of materials undergoing cracking and fracture such as concrete or rock. There, a first distinction is made between models belonging to the "smeared crack approach" and "discrete crack approach". Within the second family, in this chapter the attention is focused on approaches consisting on pre-inserting zero-thickness interface elements along the expected crack path, or if that path not known, along a sufficient number of possible alternative crack paths, so that the crack will emerge during the calculations depending on local stress and other conditions. However, this approach has one main shortcoming, that the orientation of the pre-inserted interface elements should be sufficiently close to the actual (physical) crack path. If that crack path is not known in advance, and a FE mesh is generated randomly, for instance using triangles approximately equilateral with lines at any point of the mesh lying about 60° apart from each other, the crack represented with that mesh will most probably exhibit a zig-zagging path deviating up to 30° to one side or another from the average physical crack path. And of course

this kind of "numerical roughness" may cause a significant deviation of the prediction, in terms of failure loads, deformations, crack trajectory, etc. This motivates the approach developed in this chapter, in which a procedure is established so that the pre-inserted interface elements, may get reoriented to approach the actual physical direction of the crack.

Any crack propagation model has to determine when a crack will propagate and in which direction. In general, these criteria may by based on energy or strength. For instance, Yang and Deeks (2007) assumes that a crack will grow when the mode-I stress intensity factor K_I vanishes in the direction determined by Linear Elastic Fracture Mechanics (LEFM) criteria. A more popular method in the context of LEFM was the remeshing procedure with a rosette in the crack tip, usually assumed to propagate at perpendicular direction with respect to the maximum tensile principal stress of the crack tip node (Yang and Chen, 2004). However, the most fundamental criterion must be an energetic one, and not local but based on global energy release, that is the crack should propagate in the direction which causes the fastest decrease of the global energy of the structure or domain. And this is precisely predicted by Configurational Mechanics, which focuses on how the change of the domain configuration (geometry, size, shape, also including cracks), will affect the overall domain elastic energy.

This chapter describes a methodology of fracture realignment strategy based on Configurational Mechanics theory. Basic knowledge of the large strain theory is necessary for its development, which motivates to include a brief introduction of large strain general concepts in Section 3.2. In addition, the finite element code has been complemented adding the possibility of solving problems of large deformations so validation examples are included.

The basic concepts of Configurational Mechanics theory are then described in Sec. 3.3. The interface reorientation criterion will be based on the directions indicated by configurational forces, which will come from the minimization of elastic energy with respect to the reference coordinates (original location of nodes), and turn out expressed as integrals of Eshelby's energy-momentum tensor. Original derivations of those forces are based on theoretical arguments and abstract reasoning. This motivates an alternative engineering-type derivation of the resulting FE expressions, which is obtained directly as the derivatives of the total energy of a finite element (Section 3.4). This is done in both large strain and small strain context.

The constitutive behavior of the zero-thickness interface elements involved in the Configurational Mechanics analysis is described by the elastoplastic law based on fracture mechanics concepts described in the previous chapter (Section 2.3.2). Due to the non-linearity of the constitutive model, the overall problem becomes non-linear and it is necessary to use an iterative method to solve the

underlying deformational problem. In the simplest scenario this method can be Newton-Raphson, but if "snap-back" instability occurs (prescribed displacement also decreasing transiently during the post-peak part of the load-displacement diagram), the use of indirect control methods such as Arc-Length methods may become necessary. The classical "cylindrical" Arc-Length method with the constraint in terms of the norm of nodal displacements, has been traditionally employed with success to pass limit points including "snap-back" response (Rots et al., 1985; Crisfield, 1991). However, the norm of displacement is a quadratic magnitude that in general leads to two possible solutions (or none if the discriminant becomes zero) for the variation of loading factor. This requires a choice which complicates the algorithm and may potentially create numerical problems such as spurious unphysical unloading. In order to control the fracture propagation process, it may be more suitable to impose as the indirect constraint a specific value of the fracture dissipation increment instead of the norm of displacements. Along this line, a new method for indirect control has been developed based on a prescribed increment of fracture dissipation (Section 3.5). Using dissipation as the constraint has the advantage that it leads to a linear solution instead of quadratic as it happened with the classical Arc-Length.

Configurational forces, also called material forces, represent the gradient of the total elastic energy of the mesh with respect to the nodal positions, so this information will be used to change nodal location. Therefore, based on these concepts a r-adaptivity method with length correction is established by which nodal coordinates are rearranged leading to optimal energy-position meshes. Furthermore, a simple r-adaptivity method and a tangent matrix approximation are also presented (Section 3.6).

In addition, it was observed that if all internal mesh nodes can change their position, the iterative process could get unstable because of the large variety of possibilities. Moreover, depending on mesh quality, the total energy value can be affected by "noise" such as the discretization errors due to bad shape or excessive size of elements. This additional drawback makes the application of the new method difficult since it is desired that the energy surface only reflects energy changes due to physical effects of crack length and position (Section 3.7). Therefore, it is important to reduce the discretization error. A possible solution is the application of configurational parameterization of certain elements (Section 3.7.1), it allows to solve the problem with refined meshes but without adding extra configurational free nodes. In this technique the mesh can be refined but new nodes are parametrized in such a way that they will simply follow a reduced number of main nodes, which remain the only unknowns of the configurational iterative problem. In this way the process becomes more stable. Another solution is the use of quadratic elements (Section 3.7.1), because the

FEM high order approximation leads to decrease the discretization error for the solution keeping element size and conditions.

The implementation of this model in a finite element code with zero-thickness interface elements is presented in Section 3.8. Based on the described methodology, verification examples are also solved (Section 3.9). This section includes an initial subsection with literature examples (Section 3.9.1) where mesh rearrangement is done in the continuum by discretization effects. After them, structural problems with well-known path cracks are solved, e.g. beam bending test, L-shaped panel, two notched beam, etc. Finally, concluding remarks about configurational mechanics theory and FEM with node rearrangement strategy are detailed in Section 3.10.

3.2 Large strain theory

3.2.1 Introduction

Large strain theory (also finite strain, or large deformation, of finite deformation theory), describes the behavior of solids undergoing deformations which are out of the scope of the small strain regime, i.e. $> 3\% - 5\%$. In this situation, the problem becomes geometrically non-linear, i.e. relations between displacements and strains cease to be linear (as they were in small strain), and also the magnitude measuring strain (and stress) ceases to be defined uniquely and a variety of possible tensors appear as possible alternative strain (or stress) measures. When deformations are not small, it is necessary to distinguish between initial or reference configuration (geometry of the body or domain at the beginning of the history analyzed) and the current or deformed configuration, which can be significantly different (Figure 3.1). As already mentioned, the kinematic relations between displacements and strain become non-linear, and finally, the constitutive models also become non-linear relations between stress and strain measures, even in the simplest case of elasticity (e.g. in the form of hyperelasticity).

In this section, a brief summary of the main aspects of the theory of solid mechanics are described from an engineering viewpoint (Sec. 3.2.2 and 3.2.3), followed by FE formulation and numerical implementation aspects (Sec. 3.2.4 and 3.2.5) including some simple examples of verification.

Equations and the content of this section are based on the following references: Zienkiewicz and Taylor (2000); Mase and Mase (1999); Lubarda (2001). Along this section we adopt the notation that upper-case letters are used in the reference configuration while lower-case letters in the current configuration, except body configurations (B_0 and B_t) to distinguish it from Finger tensor $\mathbf{b}$. Furthermore, equations expressed by index notation are based on the Cartesian coordinates.

Also, in the sections dealing with Finite Element formulation, Taylor's convention (Zienkiewicz and Taylor, 2000) is adopted of using superindices between parentheses (such as "$^{(a)}$", "$^{(b)}$", etc.) to denote nodal components, and implicit summation is also adopted with those nodal indices.

3.2.2 Governing equations

Kinematics of deformation and motion

The geometrical location occupied by a solid body at different times t are called configurations, and they are denoted by symbol B_t. The body configuration is a set containing the positions of all particles of the body, and in FEM context is fully defined by the current locations of the nodes (original location, plus nodal displacements). The physical description is based on the concept of material points, the location of which is represented by the reference (original) position vector $\mathbf{X}$. In Cartesian coordinates the reference position vector can be described in terms of the unity orthogonal base vectors ($\boldsymbol{e}_i$) as:

$$\mathbf{X} = X_i \boldsymbol{e}_i \tag{3.1}$$

After the application of loads and boundary conditions, the body passes from the initial configuration (B_0) to the current configuration (B_t), as shown in Figure 3.1. Then, the position that occupies the point which originally was at location $\mathbf{X}$, in the current configuration will become vector $\mathbf{x}$, also described in terms of the same unity orthogonal base vectors $\boldsymbol{e}_i$ as:

$$\mathbf{x} = x_i \boldsymbol{e}_i \tag{3.2}$$

The spatial position vector $\mathbf{x}$ of the material point $\mathbf{X}$ in the time t depends on body motion function $\varphi(\mathbf{X}, t)$ (Eq. 3.3). Which is injective, except in the boundary $\partial\Omega_0$, and satisfies the condition $\det \nabla\varphi(\mathbf{X}, t) > 0$.

$$\mathbf{x} = \varphi(\mathbf{X}, t) \tag{3.3}$$

The displacement vector ($\mathbf{u}$) can be defined as the difference between current and original position of a material point:

$$\mathbf{u} = \varphi(\mathbf{X}) - \mathbf{X} = \mathbf{x} - \mathbf{X} \tag{3.4}$$

Assuming the mapping function $\mathbf{x}$ to be continuous,

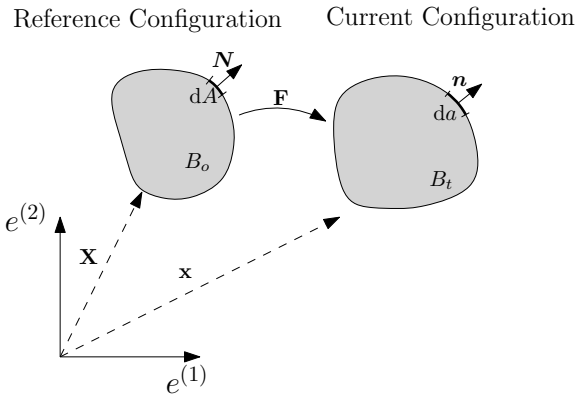

Figure 3.1: Schematic of the deformation gradient and configurations.

$$\mathrm{d}\mathbf{x} = \frac{\partial \mathbf{x}}{\partial \mathbf{X}}\mathrm{d}\mathbf{X}, \text{ or in Cartesian components } \mathrm{d}x_i = \frac{\partial x_i}{\partial X_j}\mathrm{d}X_j \tag{3.5}$$

where $\frac{\partial x_i}{\partial X_j}$ is the derivative of each component of the deformed $\mathbf{x}$ vector with respect to each component of the reference $\mathbf{X}$ vector. It is defined as the deformation gradient and usually represented by tensor $\mathbf{F}$ (Eq.(3.6)),

$$\mathbf{F} = \frac{\partial \mathbf{x}}{\partial \mathbf{X}} = \mathbf{I} + \frac{\partial \mathbf{u}}{\partial \mathbf{X}} \quad \text{or} \quad F_{ij} = \frac{\partial x_i}{\partial X_j} = \delta_{ij} + \frac{\partial u_i}{\partial X_j}, \tag{3.6}$$

deformation gradient matrix form in three-dimensional space,

$$\mathbf{F} = \begin{bmatrix} \frac{\partial x_1}{\partial X_1} & \frac{\partial x_1}{\partial X_2} & \frac{\partial x_1}{\partial X_3} \\ \frac{\partial x_2}{\partial X_1} & \frac{\partial x_2}{\partial X_2} & \frac{\partial x_2}{\partial X_3} \\ \frac{\partial x_3}{\partial X_1} & \frac{\partial x_3}{\partial X_2} & \frac{\partial x_3}{\partial X_3} \end{bmatrix} = \begin{bmatrix} 1 + \frac{\partial u_1}{\partial X_1} & \frac{\partial u_1}{\partial X_2} & \frac{\partial u_1}{\partial X_3} \\ \frac{\partial u_2}{\partial X_1} & 1 + \frac{\partial u_2}{\partial X_2} & \frac{\partial u_2}{\partial X_3} \\ \frac{\partial u_3}{\partial X_1} & \frac{\partial u_3}{\partial X_2} & 1 + \frac{\partial u_3}{\partial X_3} \end{bmatrix} \tag{3.7}$$

Some particularities of the deformation gradient and comparison with small strain theory:

- If there is no deformation the deformation gradient is the identity ($\mathbf{F} = \mathbf{I}$), whereas in small strain theory for no deformation all strain tensor components are all zero.
- $\mathbf{F}$ is not always symmetrical, while in small strain theory strain tensor is.
- Solid body motion, rotation and material deformation are mixed together into the deformation gradient, while in small strain theory, the strain tensor only includes the material deformation.
- The determinant of the deformation gradient is the Jacobian J, which describes the material

volume change. For the particular case of isochoric deformation (no volume change) $J = 1$ (whereas in small strain, this change is given by the trace of the strain tensor).

$$J = \det \mathbf{F} > 0 \tag{3.8}$$

By direct product, $\mathbf{F}$ defines the correspondence between any segment $d\mathbf{X}$ engraved on the body in the original configuration, and the same segment after deformation $d\mathbf{x}$ (Eq. (3.5)). Another important kinematic relation is Nanson's Formula, which, on the basis of geometric considerations (Lubarda, 2001), relates the areas in reference configuration $d\mathbf{A}$, and deformed configuration $d\mathbf{a}$:

$$\mathbf{da} = J \cdot \mathbf{F}^{-T} \cdot \mathbf{dA} \tag{3.9}$$

The deformation gradient is a two-point tensor because it is referred to the initial and the current configurations. Alternatively, strain tensors may be considered that are defined totally in the same configuration (either original or deformed). For instance, the Right Cauchy-Green (Eq. 3.10) and Green Lagrange (Eq. 3.11) tensors are defined in the reference configuration. While the Left Cauchy-Green or Almansi tensors (Eq. 3.12 and 3.13) are defined in the deformed configuration.

$$\mathbf{C} = \mathbf{F}^T \cdot \mathbf{F} \tag{3.10}$$

$$\mathbf{E} = \frac{1}{2}(\mathbf{C} - \mathbf{I}) \tag{3.11}$$

$$\mathbf{b} = \mathbf{F} \cdot \mathbf{F}^T \tag{3.12}$$

$$\mathbf{e} = \frac{1}{2}\left(\mathbf{I} - \mathbf{b}^{-1}\right) \tag{3.13}$$

The deformation gradient is, in general, a non-symmetric tensor. The polar decomposition theorem states that every real nonsingular matrix can be uniquely factored as the product of an orthogonal matrix and a symmetric positive definite matrix, which leads to the well known expressions

$$\mathbf{F} = \mathbf{R} \cdot \mathbf{U} = \mathbf{V} \cdot \mathbf{R} \tag{3.14}$$

where $\mathbf{R}$ is the orthogonal rotation matrix and $\mathbf{U}, \mathbf{V}$ are symmetric positive definite matrices. In

particular, $\mathbf{U}$ is the stretch tensor so only represents the deformation part (excluding rotations). Matrices $\mathbf{U}$ and $\mathbf{V}$ can be related by rotation tensor, and they can be used also to express the Right Cauchy-Green and Left Cauchy-Green deformation tensors (Eq. 3.10 and 3.12):

$$\mathbf{V} = \mathbf{R} \cdot \mathbf{U} \cdot \mathbf{R}^{-1} = \mathbf{R} \cdot \mathbf{U} \cdot \mathbf{R}^{-T} \tag{3.15}$$

$$\mathbf{C} = \mathbf{F}^T \cdot \mathbf{F} = \mathbf{U}^T \cdot \mathbf{R}^T \cdot \mathbf{R} \cdot \mathbf{U} = \mathbf{U}^T \cdot \mathbf{U} = \mathbf{U}^2 \tag{3.16}$$

$$\mathbf{b} = \mathbf{F} \cdot \mathbf{F}^T = \mathbf{V} \cdot \mathbf{R} \cdot \mathbf{R}^T \cdot \mathbf{V}^T = \mathbf{V}^T \cdot \mathbf{V} = \mathbf{V}^2 \tag{3.17}$$

Once the deformation tensors have been established, the next step is to introduce the rates of those variables. Rates of the deformation tensors defined in the reference configuration may be introduced trivially, e.g. $\dot{\mathbf{C}}$ is the rate of $\mathbf{C}$. However, for magnitudes defined in the deformed configuration, the rates also involve the derivatives of the base vectors. In particular, it is most relevant the definition of the rate-of-deformation tensor $\mathbf{d}$. For that purpose, first consider the velocity gradient $\mathbf{l}$ introduced as,

$$\mathbf{l} = \frac{\mathrm{d}\mathbf{v}}{\mathrm{d}\mathbf{x}} = \dot{\mathbf{F}} \cdot \mathbf{F}^{-1} \tag{3.18}$$

which may be decomposed in symmetric and antisymmetric parts:

$$\mathbf{l} = \mathbf{d} + \mathbf{w} \tag{3.19}$$

$$\begin{cases} \mathbf{d} = \frac{1}{2}\left(\mathbf{l} + \mathbf{l}^T\right) \\ \mathbf{w} = \frac{1}{2}\left(\mathbf{l} - \mathbf{l}^T\right) \end{cases} \tag{3.20}$$

The symmetric part, $\mathbf{d}$, is the rate-of-deformation tensor, while the antisymmetric part, $\mathbf{w}$, is the spin tensor. In general, the rate-of-deformation tensor $\mathbf{d}$ is not an exact tensor rate, in the sense that no total deformation tensor exists of which $\mathbf{d}$ would be the rate. But it is a very essential deformation rate variable because it has the same structure (and to some extent physical meaning) as the strain tensor in small strain theory, and also because it turns out to be the tensor rate conjugated to Cauchy stress tensor, which is also the most physical and intuitive stress measure.

Each tensor defined in the reference configuration has a counterpart in the deformed configuration. "Push-forward" transformations convert each tensor defined in the reference configuration

in its deformed counterpart, for instance in the case of rates of deformation magnitudes the rate of deformation tensor turns out to be the "Push-forward" of $1/2\dot{\mathbf{C}}$ and, conversely, $1/2\dot{\mathbf{C}}$ is the "Pull-back" of $\mathbf{d}$.

The precise correspondence and expressions of push-forward and pull-back operations for all types of tensors and in all circumstances, would require to formulate the theory in terms of curvilinear coordinates (see e.g. Steinmann, 1996). In that context, each tensor is expressed naturally in terms or some covariant or contravariant base vectors, and push forward and pull back operations consist of simply converting the base vectors without changing the tensor components. That is, however, out of the scope of the present thesis, which is developed in the framework of Cartesian coordinates. Nevertheless, some specific push-forward and pull back expressions are considered, such as the case of $1/2\dot{\mathbf{C}}$ and $\mathbf{d}$ the expressions are:

$$\mathbf{d} = \mathbf{F}^{-T} \cdot \left(\frac{1}{2}\dot{\mathbf{C}}\right) \cdot \mathbf{F}^{-1}, \quad \text{and} \quad \frac{1}{2}\dot{\mathbf{C}} = \mathbf{F}^{T} \cdot \mathbf{d} \cdot \mathbf{F} \tag{3.21}$$

Pre-multiplication by $\mathbf{F}^{-T}$ and post-multiplication by $\mathbf{F}^{-1}$ is the push-forward operation for all covariant tensors such as $\mathbf{C}$, and similarly for pull-back operation consisting of pre-multiplication by $\mathbf{F}^{T}$ and post-multiplication by $\mathbf{F}$.

Stress tensors

Perhaps, the most natural stress measure is the Cauchy Stress tensor σ that may be defined in a physical intuitive way through its components in Cartesian axes, which correspond to the components of the force per unit area that are acting on the faces of an elementary cube of dimensions $\mathrm{d}x_1, \mathrm{d}x_2, \mathrm{d}x_3$ which is "cut" from the body in the current deformed configuration (Figure 3.2). This concept is totally analogous to the classical definition as in small strain theory, an for the same reason of momentum balance is subjected to symmetry requirement.

The second stress measure considered is the First Piola-Kirchhoff ($\mathbf{P}$) that may be introduced as such tensor that projected on the area vector in the reference configuration will give the same net force as the Cauchy stress tensor projected on the corresponding deformed area, i.e.

$$\mathbf{t} = \boldsymbol{\sigma} \cdot \mathrm{d}\mathbf{a} = \mathbf{P} \cdot \mathrm{d}\mathbf{A} \tag{3.22}$$

Substituting $\mathrm{d}\mathbf{a}$ with the Nanson's Formula Eq.(3.9) leads to

$$\boldsymbol{\sigma} \cdot J\mathbf{F}^{-T} \cdot \mathbf{dA} = \mathbf{P} \cdot \mathrm{d}\mathbf{A} \tag{3.23}$$

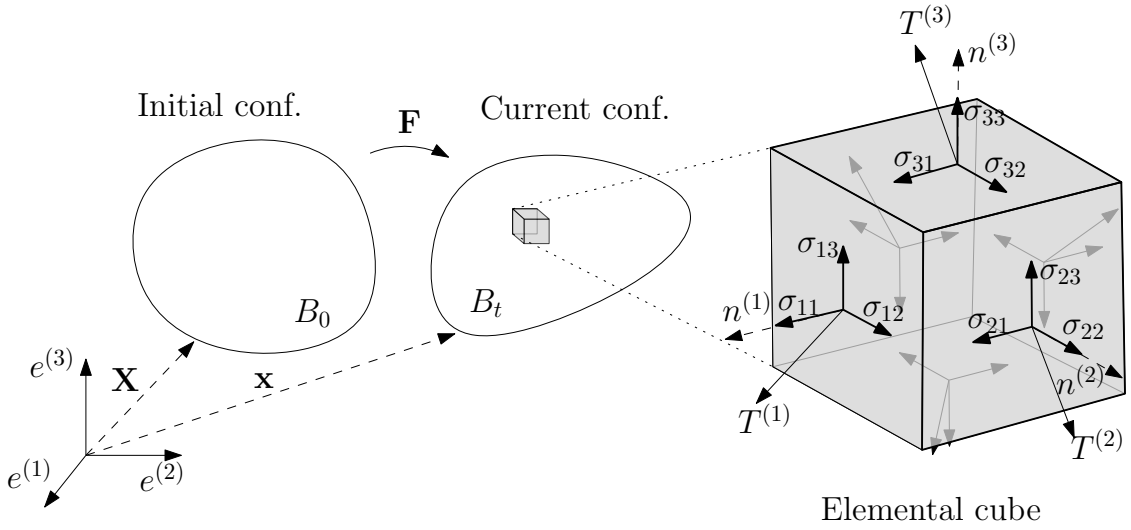

Figure 3.2: Cauchy stress tensor representation

Eliminating d$\mathbf{A}$ and isolating $\boldsymbol{\sigma}$ or $\mathbf{P}$, one obtains:

$$\boldsymbol{\sigma} = J^{-1}\mathbf{P}\cdot\mathbf{F}^{T} \quad \text{or} \quad \mathbf{P} = J\boldsymbol{\sigma}\cdot\mathbf{F}^{-T} \tag{3.24}$$

First Piola-Kirchhoff stress tensor $\mathbf{P}$ turns out to be two-point tensors; to obtain a stress tensor defined fully in the reference configuration, the remaining deformed base vector of $\mathbf{P}$ has to be also transformed, which leads to the Second Piola-Kirchhoff stress tensor $\mathbf{S}$:

$$\mathbf{S} = J\mathbf{F}^{-1}\cdot\boldsymbol{\sigma}\cdot\mathbf{F}^{-T} \tag{3.25}$$

Replacing finally the second of Eqs.(3.24) into (3.25), one obtains the relation between $\mathbf{P}$ and $\mathbf{S}$:

$$\mathbf{S} = \mathbf{F}^{-1}\cdot\mathbf{P} \quad \text{or} \quad \mathbf{P} = \mathbf{F}\cdot\mathbf{S} \tag{3.26}$$

An other relevant stress tensor in deformed configuration is the Kirchhoff stress, which is related to Cauchy stress tensor by a simple scalar factor J as:

$$\boldsymbol{\tau} = J\boldsymbol{\sigma} \tag{3.27}$$

Kirchhoff stress tensor turns out to be the Push-forward of $\mathbf{S}$, and conversely, $\mathbf{S}$ is the pull-back of $\boldsymbol{\tau}$:

Stress tensor	Strain rates
$\mathbf{P}$	$\dot{\mathbf{F}}$
$\mathbf{S}$	$\dot{\mathbf{E}}$, $\frac{1}{2}\dot{\mathbf{C}}$
$\boldsymbol{\sigma}, \boldsymbol{\tau}$	$\mathbf{d}$

Table 3.1: Conjugate pairs of stresses and strain rates

$$\boldsymbol{\tau} = \mathbf{F} \cdot \mathbf{S} \cdot \mathbf{F}^T, \quad \mathbf{S} = \mathbf{F}^{-1} \cdot \boldsymbol{\tau} \cdot \mathbf{F}^{-T} \tag{3.28}$$

Note that, in contrast to strain tensors, stress tensors are defined naturally as contravariant tensors and therefore the push-forward and pull back operations are not the same in this case.

Another essential concept is that of work conjugate. Each stress tensor is conjugate to a particular strain rate tensor in the sense that their full product contraction gives the work rate (stress power) per unit volume of of the appropriate configuration. Intuitively, based on physical meaning of Cauchy stress tensor and rate-of-deformation tensor, one can find that they are a conjugate pair, i.e. that

$$\dot{w} = \boldsymbol{\sigma} : \mathbf{d} \tag{3.29}$$

where $\dot{w}$ is the stress power per unit volume in deformed configuration.

The stress power per unit volume in reference configuration may now be expressed as the product by the Jacobian, the expression of rate of deformation Eq.(3.21) introduced, and the stress conjugate to the rate of Right Cauchy-Green strain tensor may be identified which turns out to be the Second Piola-Kirchhoff, i.e

$$\dot{W} = J\dot{w} = J\boldsymbol{\sigma} : \mathbf{d} = \boldsymbol{\sigma} : \left[\mathbf{F}^{-T} \cdot \left(\frac{1}{2}\dot{\mathbf{C}}\right) \cdot \mathbf{F}^{-1}\right] = \frac{1}{2}\left[\mathbf{F}^{-1} \cdot \boldsymbol{\sigma} \cdot \mathbf{F}^{-T}\right] : \dot{\mathbf{C}} = \frac{1}{2}\mathbf{S} : \dot{\mathbf{C}} \tag{3.30}$$

These and other basic conjugate pairs are summarized in Table 3.1.

Note that the above conjugate relations also imply that, in the original configuration and in the case that an elastic energy potential exists (see next Section), each stress tensor is equal to the derivative of the elastic energy with respect to the corresponding conjugate strain, e.g.

$$\mathbf{P} = \frac{\partial W}{\partial \mathbf{F}}, \quad \mathbf{S} = \frac{\partial W}{\partial \mathbf{E}}, \quad \text{etc.} \tag{3.31}$$

3.2.3 Constitutive models

Elastic behavior in small strain is usually assumed to be linear, most commonly in the form of linear isotropic elasticity characterized with two parameters E, ν (or, alternatively Λ, G, or K, G). In the large strain context, elastic models used are generally no-linear and most commonly isotropic hyperelastic, i.e. they exhibit a well-defined elastic energy density which may be defined as a function of the deformation tensor invariants. Two of such models have been considered in this section: the compressible Neo-Hooke and the Money-Rivlin models.

Neo-Hookean compressible model

The Neo-Hooke compressible model is one of the simplest hyperelastic models described in the literature. It represents a stress-strain relation which is initially linear (small strain) which eventually changes to non-linear curves as the strain is incresased. The compressible Neo-Hooke strain energy density is expressed by the following equation:

$$W = \frac{1}{2}\mu\left(\mathrm{tr}\mathbf{C} - 3\right) - \mu \ln J + \frac{1}{2}\Lambda\left(\ln J\right)^2 \tag{3.32}$$

As defined in Table 3.1, Second Piola Kirchhoff is the stress conjugate of right Cauchy-Green deformation tensor. Therefore, Second Piola Kirchhoff in a Neo-Hookean compressible material can be defined as the partial derivative of the strain energy density with respect to the right Cauchy Green deformation tensor,

$$\mathbf{S} = 2\frac{\partial W}{\partial \mathbf{C}} = \mu\left(\mathbf{I} - \mathbf{C}^{-1}\right) + \Lambda \ln J \mathbf{C}^{-1} \tag{3.33}$$

The second derivative of the Energy potential leads to the tangent matrix relating the differential increments of Second Piola Kirchhoff and Cauchy-Green strain,

$$^{\mathbf{C}}\mathcal{L}_2 = 2\left(\mu - \Lambda \ln J\right)\mathbf{C}^{-1}\underline{\bar{\otimes}}\mathbf{C}^{-1} + \Lambda \mathbf{C}^{-1} \otimes \mathbf{C}^{-1} \tag{3.34}$$

where the tensor products above correspond to the standard dyadic product of two second-order tensors, in indices $(\mathbf{A} \otimes \mathbf{B})_{ijkl} = A_{ij}B_{kl}$, and the cross-dyadic product $(\mathbf{A}\underline{\bar{\otimes}}\mathbf{B})_{ijkl} = \left(A_{ik}B_{jl} + A_{il}B_{jk}\right)/2$. In this case, coefficients μ and Λ are the same as in small strain theory, Lamé parameters: $\mu = E/(2\left(1+\nu\right))$ and $\Lambda = \nu E/((1+\nu)\left(1-2\nu\right))$, where E is the young modulus and ν the Poisson's ratio.

Mooney-Rivlin model

Mooney-Rivlin model is also a hyperelastic isotropic material model, similar to Neo-Hookean compressible model but with additional terms combination of two invariants of the right Cauchy-Green tensor, which makes the model a little more complex and able to predict a more realistic material behavior under compression conditions.
The expression of strain energy density contains additional terms, and parameter μ is replaced by two parameters A, B.

$$W = \frac{A}{2}\left(\mathrm{tr}\mathbf{C} - 3\right) + \frac{B}{2}\left(\mathrm{tr}\mathbf{C}^{-1} - 3\right) - (A+B)\ln J + \frac{1}{2}\Lambda\left(\ln J\right)^2 \tag{3.35}$$

Therefore, the Second Piola Kirchhoff stresses may be expressed as follows

$$\mathbf{S} = A\left(\mathbf{I} - \mathbf{C}^{-1}\right) + B\left(\mathbf{C}^{-2} - \mathbf{C}^{-1}\right) + \Lambda \ln J \mathbf{C}^{-1} \tag{3.36}$$

and the tangent matrix is

$$^{\mathbf{C}}\mathcal{L}_2 = 2\left(A + B - \Lambda \ln J\right)\mathbf{C}^{-1}\bar{\otimes}\mathbf{C}^{-1} - 2B\left[\mathbf{C}^{-1}\bar{\otimes}\mathbf{C}^{-2} + \mathbf{C}^{-2}\bar{\otimes}\mathbf{C}^{-1}\right] + \Lambda\mathbf{C}^{-1}\otimes\mathbf{C}^{-1} \tag{3.37}$$

By looking at the limit of small deformations, one can make the model equivalent to small strain elasticity, and find a correspondence between coefficients A, B and Λ, and the small strain shear modulus, E and ν:

$$\mu = A - B = \frac{E}{2\left(1+\nu\right)} \quad \text{and} \quad \Lambda = \frac{\nu E}{\left(1+\nu\right)\left(1-2\nu\right)} \tag{3.38}$$

3.2.4 Finite Element formulation and Principle of Virtual Work (PVW)

The most characteristic assumptions of the Finite Element Method are the subdivision of the domain into elements connected by nodes, and the definition of nodal values and interpolation functions. These functions are used to interpolate the main variable from the nodal values over the interior of the elements, for both geometry an unknown variables (isoparametric formulation). In this context, the reference configuration coordinates of any point within a given element may be defined as:

$$X_i = N^{(a)}(\boldsymbol{\xi})\, X_i^{(a)} \tag{3.39}$$

where $\boldsymbol{\xi}$ represents the element local coordinates, $N^{(a)}\left(\boldsymbol{\xi}\right)$ are the standard shape functions for

node a and $X_i^{(a)}$ represents the nodal reference configuration coordinates for a specific node a, and implicit summation is assumed for repeated indices, including those between parentheses. In the same way, the displacement field is interpolated by standard shape functions and nodal $u_i^{(a)}$.

$$u_i = N^{(a)}(\boldsymbol{\xi})\, u_i^{(a)} \tag{3.40}$$

The global expression of weak equilibrium for the finite element may be obtained in various ways (principle of virtual work, Galerkin method of weighted residuals, etc.) In this case, the PVW has been used in the reference configuration.

Assuming body forces negligible for the sake of simplicity, considering a field of stresses P_{ij} over the element domain and set of nodal forces in equilibrium with these stresses, $f_i^{(a)}$, as well as a field of virtual deformations δF_{ij} compatible with nodal displacements $\delta u_i^{(a)}$, the work done by nodal forces is:

$$W_{ext} = \delta u_i^{(a)} f_i^{(a)} \tag{3.41}$$

The internal work done by body stresses is:

$$W_{int} = \int_{\mathrm{V}} \delta F_{ij} P_{ij} \mathrm{dV} \tag{3.42}$$

Enforcing now that virtual work should be the same, one gets

$$W_{ext} = W_{int} \tag{3.43}$$

$$\delta u_i^{(a)} f_i^{(a)} = \int_{\mathrm{V}} \delta F_{ij} P_{ij} \mathrm{dV} \tag{3.44}$$

Virtual deformation increment δF_{ij} can now be related to $\delta u_i^{(a)}$. For that purpose (Eq.3.40) is introduced in (Eq.3.6) leading to:

$$\delta F_{ij} = \frac{\partial \delta u_i}{\partial X_j} = \frac{\partial N^{(a)}}{\partial X_j} \delta u_i^{(a)} \tag{3.45}$$

Replacing expression Eq.(3.45) into Eq.(3.44), grouping around $\delta u_i^{(a)}$ and enforcing the product to be zero for any virtual nodal displacement values, one obtains

$$f_i^{(a)} = \int_{\mathrm{V}} \left(\frac{\partial N^{(a)}}{\partial X_j} \right) P_{ij} \mathrm{dV} \tag{3.46}$$

This is the weak expression of equilibrium at large strain in terms of the First Piola-Kirchhoff stress $\mathbf{P}$. Note that the term between parentheses, conveniently arranged in matrix form, will constitute the finite element transposed B-matrix. In this case, the B-matrix components consist of Cartesian derivatives of the shape functions in the original configuration, and therefore it is a constant matrix. However, because it multiplies a non-symmetric tensor, it does not coincide fully in number of columns with the classical small strain format of matrix $\mathbf{B}$. for this reason, this matrix will be denoted as matrix $\hat{\mathbf{B}}$.

$$f_i^{(a)} = \int_{\mathrm{V}} \hat{B}_{jki}^{(a)} P_{kj} \mathrm{dV}, \quad \hat{B}_{jki}^{(a)} = \frac{\partial N^{(a)}}{\partial X_j} \delta_{ik} \tag{3.47}$$

If P_{ij} is replaced with the Second Piola-Kirchhoff stress tensor, Eq.(3.26), previous expression changes to Eq.(3.48) which, taking advantage of $\mathbf{S}$ being symmetric, may be rewritten as Eq.(3.49). In this case, the B-matrix, denoted as $\bar{\mathbf{B}}$, will also collect the Cartesian derivatives of shape functions in the reference configuration but this time multiplied by the deformation gradient, and therefore it will not be a constant matrix anymore. Additionally, since $\mathbf{S}$ is symmetric, $\bar{\mathbf{B}}$ will also reflect this feature:

$$f_i^{(a)} = \int_{\mathrm{V}} \left(\frac{\partial N^{(a)}}{\partial X_j} \right) F_{ik} S_{jk} \mathrm{dV} \tag{3.48}$$

$$f_i^{(a)} = \int_{\mathrm{V}} \bar{B}_{jki}^{(a)} S_{jk} \mathrm{dV}, \quad \bar{B}_{jki}^{(a)} = \frac{1}{2} \left(\frac{\partial N^{(a)}}{\partial X_j} F_{ik} + \frac{\partial N^{(a)}}{\partial X_k} F_{ij} \right) \tag{3.49}$$

Because many constitutive models are formulated in terms of the Second Piola-Kirchoff stresses S, a classical implementation of FE at large strain is based on this matrix (see e.g. Zienkiewicz and Taylor, 2000).

Taking now the rate of Eq.(3.49), one obtains the incremental form:

$$\dot{f}_i^{(a)} = \int_{\mathrm{V}} \left(\frac{\partial N^{(a)}}{\partial X_j} \right) F_{ik} \dot{S}_{jk} \mathrm{dV} + \int_{\mathrm{V}} \left(\frac{\partial N^{(a)}}{\partial X_j} \right) \dot{F}_{ik} S_{jk} \mathrm{dV} \tag{3.50}$$

Replacing $\dot{F}_{ik}$ according to equation (3.45) leads to:

$$\dot{f}_i^{(a)} = \int_{\mathrm{V}} \bar{B}_{jki}^{(a)} \dot{S}_{jk} \mathrm{dV} + \int_{\mathrm{V}} \frac{\partial N^{(a)}}{\partial X_j} \frac{\partial N^{(b)}}{\partial X_k} \dot{u}_i^{(b)} S_{jk} \mathrm{dV} \tag{3.51}$$

Knowing that the second Piola-Kirchhoff rate is $\dot{S}_{jk} = \mathcal{L}_{2\,jklm}\dot{E}_{lm} = \mathcal{L}_{2\,jklm}\bar{B}^{(b)}_{lmr}\dot{u}_r^{(b)}$ and replacing $\dot{u}_i^{(b)} = \delta_{ir}\dot{u}_r^{(b)}$, leads to

$$\dot{f}_i^{(a)} = \int_{\mathrm{V}} \bar{B}^{(a)}_{jki}\mathcal{L}_{2\,jklm}\bar{B}^{(b)}_{lmr}\mathrm{dV}\dot{u}_r^{(b)} + \int_{\mathrm{V}} \frac{\partial N^{(a)}}{\partial X_j}\frac{\partial N^{(b)}}{\partial X_k}S_{jk}\delta_{ir}\mathrm{dV}\dot{u}_r^{(b)} \tag{3.52}$$

Grouping terms, the final expression of the element tangential stiffness matrix $\mathbf{K}_T$ in the reference configuration is obtained as

$$\dot{f}_i^{(a)} = \left(K^{(a)(b)}_{M\,ir} + K^{(a)(b)}_{G\,ir}\right)\dot{u}_r^{(b)} = K^{(a)(b)}_{T\,ir}\dot{u}_r^{(b)} \tag{3.53}$$

where $\mathbf{K}_M$ is the material part of the stiffness matrix of the system and $\mathbf{K}_G$ the geometric contribution with expressions:

$$K^{(a)(b)}_{M\,ir} = \int_{\mathrm{V}} \bar{B}^{(a)}_{ikj}\mathcal{L}_{2\,jklm}\bar{B}^{(b)}_{rml}\mathrm{dV} \tag{3.54}$$

$$K^{(a)(b)}_{G\,ir} = \int_{\mathrm{V}} \frac{\partial N^{(a)}}{\partial X_j}S_{jk}\frac{\partial N^{(b)}}{\partial X_k}\mathrm{dV}\delta_{ir} = G^{(a)(b)}\delta_{ir} \tag{3.55}$$

where

$$G^{(a)(b)} = \int_{\mathrm{V}} \frac{\partial N^{(a)}}{\partial X_j}S_{jk}\frac{\partial N^{(b)}}{\partial X_k}\mathrm{dV} \tag{3.56}$$

3.2.5 FE numerical implementation and verification examples

The numerical implementation follows the scheme in reference configuration proposed in Zienkiewicz and Taylor (2000). Taking advantage of matrix $\bar{\mathbf{B}}$ defined in previous section, the Green Lagrange strain tensor at a point within the element may be expressed in terms of the nodal displacements as

$$\mathbf{E} = \bar{\mathbf{B}}^{(a)}\bar{\mathbf{u}}^{(a)} \tag{3.57}$$

Matrix $\bar{\mathbf{B}}^{(a)}$ may be in turn decomposed into a linear part $\mathbf{B}^{(a)}$ (which is the same as in small strain theory), and a non-linear part $\mathbf{B}^{\mathbf{NL}(a)}$:

$$\bar{\mathbf{B}}^{(a)} = \mathbf{B}^{(a)} + \mathbf{B}^{\mathbf{NL}(a)} \tag{3.58}$$

For a 3D continuum, these matrices exhibit the following components:

$$\left(\mathbf{B}^{(a)}\right)^T = \begin{bmatrix} \frac{\partial N^{(a)}}{\partial X_1} & 0 & 0 \\ 0 & \frac{\partial N^{(a)}}{\partial X_2} & 0 \\ 0 & 0 & \frac{\partial N^{(a)}}{\partial X_3} \\ \frac{\partial N^{(a)}}{\partial X_2} & \frac{\partial N^{(a)}}{\partial X_1} & 0 \\ 0 & \frac{\partial N^{(a)}}{\partial X_3} & \frac{\partial N^{(a)}}{\partial X_2} \\ \frac{\partial N^{(a)}}{\partial X_3} & 0 & \frac{\partial N^{(a)}}{\partial X_1} \end{bmatrix} \tag{3.59}$$

$$\left(\mathbf{B}^{\mathbf{NL}(a)}\right)^T = \begin{bmatrix} \frac{\partial N^{(a)}}{\partial X_1}\frac{\partial u_1}{\partial X_1} & \frac{\partial N^{(a)}}{\partial X_2}\frac{\partial u_2}{\partial X_1} & \frac{\partial N^{(a)}}{\partial X_1}\frac{\partial u_3}{\partial X_1} \\ \frac{\partial N^{(a)}}{\partial X_2}\frac{\partial u_1}{\partial X_2} & \frac{\partial N^{(a)}}{\partial X_2}\frac{\partial u_2}{\partial X_2} & \frac{\partial N^{(a)}}{\partial X_2}\frac{\partial u_3}{\partial X_2} \\ \frac{\partial N^{(a)}}{\partial X_3}\frac{\partial u_1}{\partial X_3} & \frac{\partial N^{(a)}}{\partial X_3}\frac{\partial u_2}{\partial X_3} & \frac{\partial N^{(a)}}{\partial X_3}\frac{\partial u_3}{\partial X_3} \\ \frac{\partial N^{(a)}}{\partial X_2}\frac{\partial u_1}{\partial X_1} + \frac{\partial N^{(a)}}{\partial X_1}\frac{\partial u_1}{\partial X_2} & \frac{\partial N^{(a)}}{\partial X_2}\frac{\partial u_2}{\partial X_1} + \frac{\partial N^{(a)}}{\partial X_1}\frac{\partial u_2}{\partial X_2} & \frac{\partial N^{(a)}}{\partial X_2}\frac{\partial u_3}{\partial X_1} + \frac{\partial N^{(a)}}{\partial X_1}\frac{\partial u_3}{\partial X_2} \\ \frac{\partial N^{(a)}}{\partial X_3}\frac{\partial u_1}{\partial X_2} + \frac{\partial N^{(a)}}{\partial X_2}\frac{\partial u_1}{\partial X_3} & \frac{\partial N^{(a)}}{\partial X_3}\frac{\partial u_2}{\partial X_2} + \frac{\partial N^{(a)}}{\partial X_2}\frac{\partial u_2}{\partial X_3} & \frac{\partial N^{(a)}}{\partial X_3}\frac{\partial u_3}{\partial X_2} + \frac{\partial N^{(a)}}{\partial X_2}\frac{\partial u_3}{\partial X_3} \\ \frac{\partial N^{(a)}}{\partial X_1}\frac{\partial u_1}{\partial X_3} + \frac{\partial N^{(a)}}{\partial X_3}\frac{\partial u_1}{\partial X_1} & \frac{\partial N^{(a)}}{\partial X_1}\frac{\partial u_2}{\partial X_3} + \frac{\partial N^{(a)}}{\partial X_3}\frac{\partial u_2}{\partial X_1} & \frac{\partial N^{(a)}}{\partial X_1}\frac{\partial u_3}{\partial X_3} + \frac{\partial N^{(a)}}{\partial X_3}\frac{\partial u_3}{\partial X_1} \end{bmatrix} \tag{3.60}$$

In 2D space, the expressions are:

$$\left(\mathbf{B}^{(a)}\right)^T = \begin{bmatrix} \frac{\partial N^{(a)}}{\partial X_1} & 0 \\ 0 & \frac{\partial N^{(a)}}{\partial X_2} \\ \frac{\partial N^{(a)}}{\partial X_2} & \frac{\partial N^{(a)}}{\partial X_1} \end{bmatrix} \tag{3.61}$$

$$\left(\mathbf{B}^{\mathbf{NL}(a)}\right)^T = \begin{bmatrix} \frac{\partial u_1}{\partial X_1}\frac{\partial N^{(a)}}{\partial X_1} & \frac{\partial u_2}{\partial X_1}\frac{\partial N^{(a)}}{\partial X_1} \\ \frac{\partial u_1}{\partial X_2}\frac{\partial N^{(a)}}{\partial X_2} & \frac{\partial u_2}{\partial X_2}\frac{\partial N^{(a)}}{\partial X_2} \\ \frac{\partial u_1}{\partial X_1}\frac{\partial N^{(a)}}{\partial X_2} + \frac{\partial u_1}{\partial X_2}\frac{\partial N^{(a)}}{\partial X_1} & \frac{\partial u_2}{\partial X_1}\frac{\partial N^{(a)}}{\partial X_2} + \frac{\partial u_2}{\partial X_2}\frac{\partial N^{(a)}}{\partial X_1} \end{bmatrix} \tag{3.62}$$

Note that before any deformation takes place (or if the deformation gradient $\mathbf{F}$ is very small), matrix $\left(\mathbf{B}^{\mathbf{NL}(a)}\right)^T$ is all zeros (or has negligible values) and $\bar{\mathbf{B}}^{(a)} = \mathbf{B}^{(a)}$, i.e. the B-matrix coincides with that of small strain theory.

Finally, the element tangential stiffness matrix is evaluated according to Eq.(3.52), including the material part (Eq.3.54) and the geometrical parts (Eq.3.55 and 3.56). Figure 3.3 represents a scheme of the contributing matrices for a two-dimensional linear quadrilateral element.

A few verification examples of the implementation developed are also included in this Section.

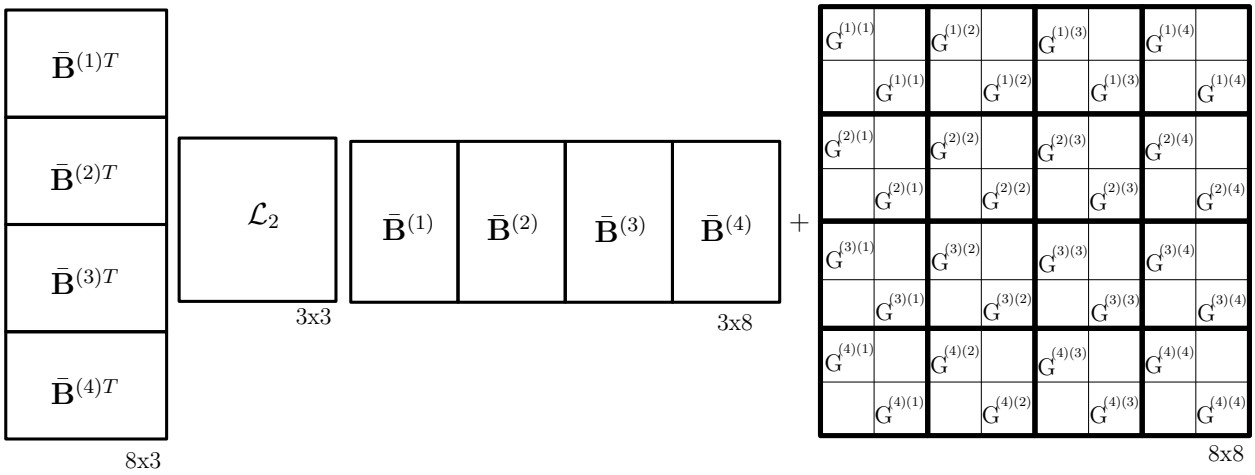

Figure 3.3: General scheme of the total stiffness matrix in a two-dimensional problem discretized by linear quadrangles.

a) Single element subject to 360° rotation

The first example is a simple linear quadrangular finite element subject to a complete 360° rotation imposed in four consecutive steps of approximately 90° (Figure 3.4a). In the first step, the x displacement of the top left node is increased a magnitude equal to the square side; in the second, the y displacement of the same node is decreased by the same magnitude; in the third and fourth steps the displacement prescribed will be again x and y with same magnitude but opposite signs as in steps 1 and 2. In this way, the final state must be the same as the initial state, that is, an undistorted unstressed element. Plane strain is assumed and Neo-Hooke with material properties corresponding to $E = 1000$ MPa and $\nu = 0.3$.

Using a standard small strain implementation, already in the first loading step the results deviate significantly from the desired outcome as shown in Fig. 3.4b, where the imposed displacement changes the element position and also causes a gradual increase of its area. For this reason, this calculation has not been taken beyond the first step of 90° rotation. However, solving the same problem in the context of large strain theory, the calculation succeeds in maintaining the element geometry and simply changing its orientation (Figure 3.4c), without accumulating neither spurious stresses nor deformations.

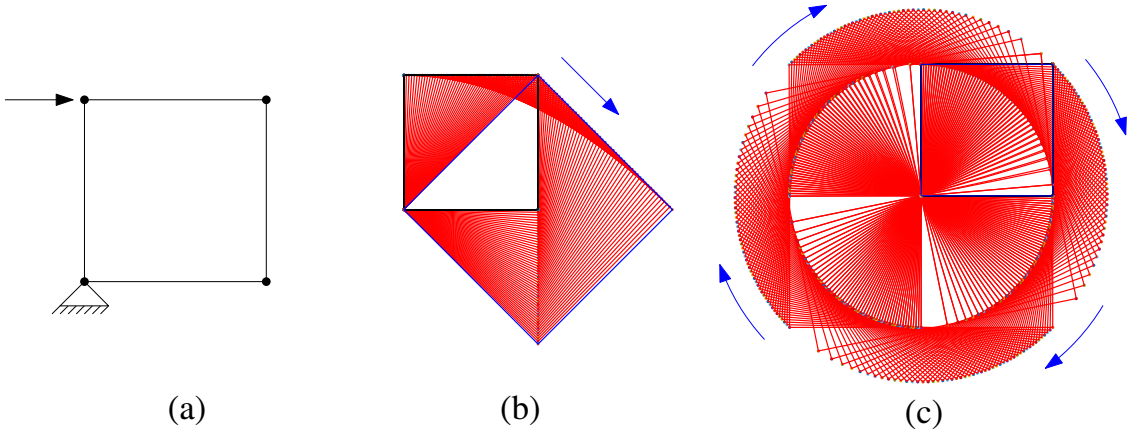

Figure 3.4: (a) Boundary conditions describing rotation of a single quadrangular element, (b) small strain theory response and (c) large strain theory solution. The intermediate incremental configurations are depicted in red while the final configuration is represented in blue, arrows indicate the rotation direction.

b) Cantilever beam bending

The case consists of a cantilever beam of 100m long and 2m wide with a very large displacement imposed at the free end (Figure 3.5a). The applied displacement $\boldsymbol{\delta}$ is always perpendicular to the end of the beam and corresponds to a rotation of 2 degrees by each deformational increment. To solve the FEM problem, the beam is discretized into 20 quadrangular linear elements (see Figure 3.5b).

Solving this problem by both small strain theory and large strain theory, the envelope-curves of the beam trajectory are similar since the imposed displacement are also the same. However, as shown in Figures 3.5c-d, the beam length is only preserved in the large strain calculation, while the small strain calculation shows unphysical features such as element folding, negative areas, and vanishing beam length (Fig. 3.5c-d represents in red the incremental deformed configurations and in blue the final deformation, which in diagram c is reduced to a point).

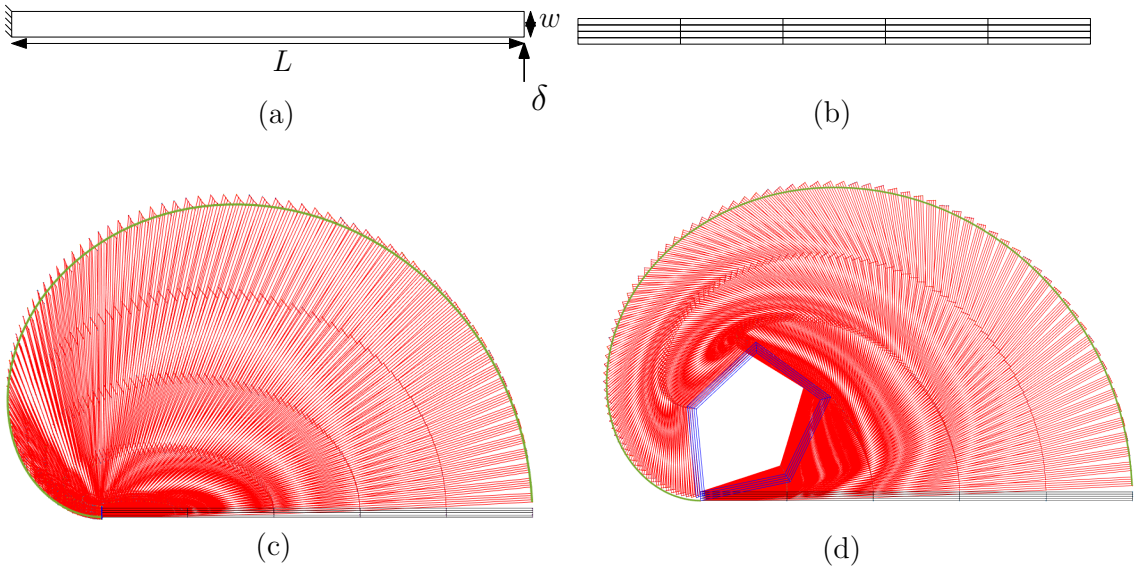

Figure 3.5: (a) Boundary conditions to describe a cantilever beam bending, (b) mesh discretization, (c) small strain theory response and (d) large strain theory solution. The intermediate incremental configurations are depicted in red while the final configuration is represented in blue. In addition, the envelope-curve of the beam path is represented in green color.

c) Column under uniaxial load

The purpose of this example is verifying the case of high compression with loading values reaching the same magnitude as the Young's modulus value. It consists of a vertical column of dimensions 100×10m, with elastic parameters $E = 10$MPa and $\nu = 0$. The column is subject to vertical load, and zero lateral displacements are prescribed (edometric conditions) (Figure 3.6a).

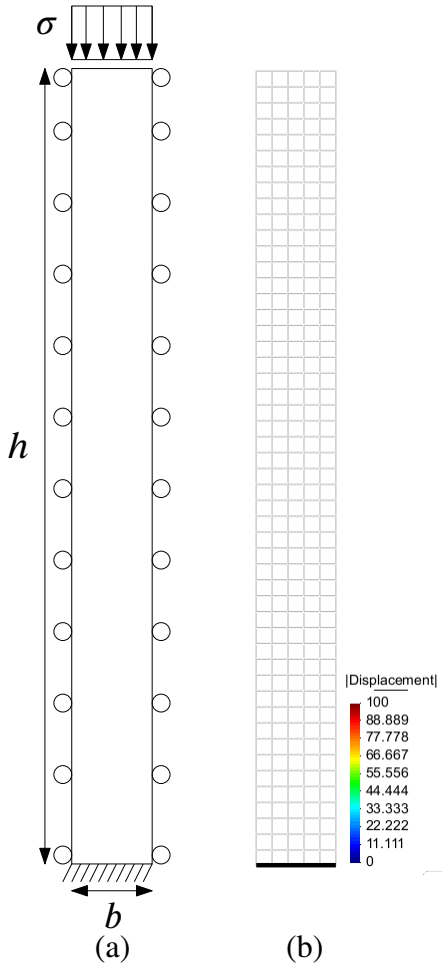

Figure 3.6: (a) Column under edometric compression (b) Displacement field calculated by FEM based on small strain theory. The reference configuration is shown in gray while the final configuration is represented in black (volume reduced to zero, mesh folded at the bottom).

Using the small strain formulation, the stress intensity equal to the elasticity modulus causes strain to be 100% and the elements collapse vertically, all mesh being reduced to a line (Figure 3.6b). In contrast, the large strain implementation leads to more physical results, with progressive stiffening as volume is reduced, final column shortening near 60% (Figure 3.7a). Figures 3.7c

depict vertical component of Cauchy stress consistent with external load, and vertical stretch that is consistent with displacements, since it can be calculated as follows:

$$\lambda = \frac{l_f}{l_0} = \frac{100 - 58.579}{100} = 0.41421 \tag{3.63}$$

and Cauchy stress tensor remains constant and equal to the imposed load.

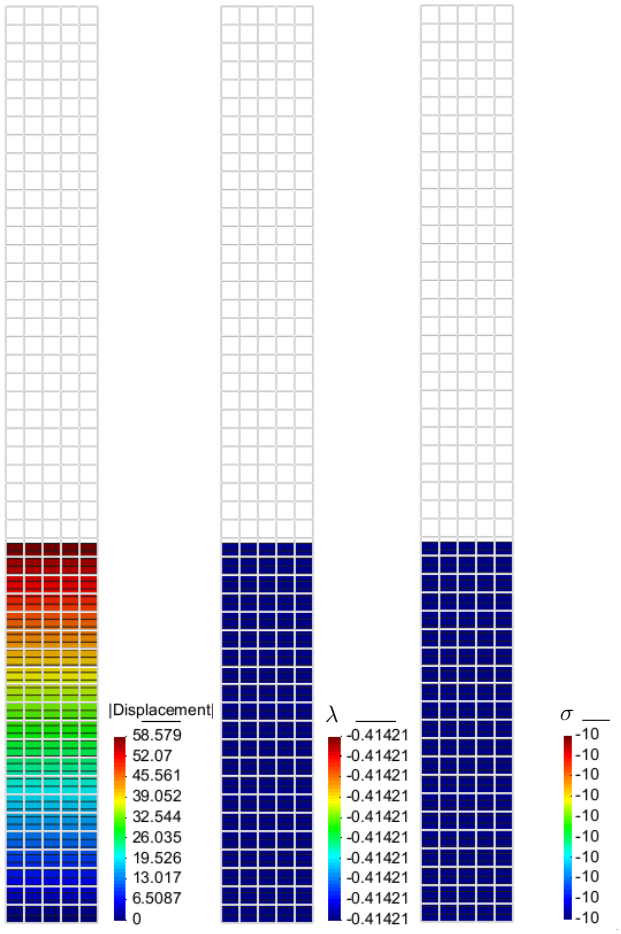

Figure 3.7: Column under uniaxial load solved by large strain theory implementation: (a) Displacement field (b) vertical stretch (c) Vertical component of Cauchy stress tensor. The reference configuration is shown in gray while the final configuration is represented by the color map values.

d) Geological dome

The last verification example of the large strain theory implementation is a 100×25m rectangular domain with two symmetrically distributed loads of $\sigma = 20$MPa applied on the top face of the domain, leaving the center free of load (Fig. 3.8a).

Plane strain is assumed and material properties are Young modulus of $E = 1$MPa and a high value of Poisson's ratio $\nu = 0.499$ which makes the material to behave as almost incompressible. Small strain theory does not solve this problem correctly since stresses get to values higher than Young's modulus and therefore the final result of the deformed configuration contains overlapped elements, FE with negative areas or too large volume changes (Fig. 3.8c). On the other hand, solving the same problem by the large strain theory leads to a dome-type shape observed in the geological context, e.g. in the case of salt domes (Fig. 3.8b)

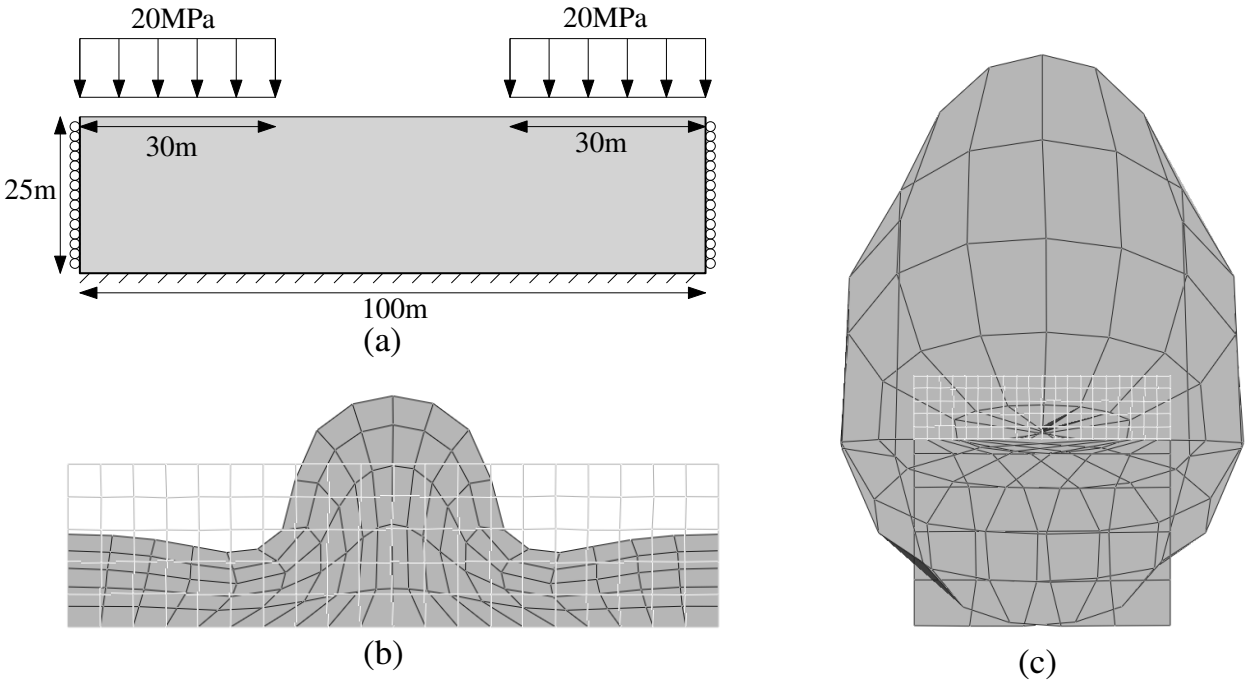

Figure 3.8: (a) Boundary conditions, (b) Large strain results, final configuration (c) Small strain theory final configuration. The reference configuration grid is represented (light gray lines) to compare with the deformed configuration (dark gray filled figures).

3.3 Configurational Mechanics theory

Configurational mechanics has developed into a successful topic in continuum and computational mechanics. It is based on considering energy variations associated to changes of the reference configuration, that is in the original geometry of the domain. In addition, it allows us to solve a large variety of problems such as mechanics of dielectrics (Pak, 1990), thermodynamic problems (Mueller and Maugin, 2002), or mechanical problems with presence of dislocations and fractures (Steinmann et al., 2009). The calculation of configurational forces was introduced by Eshelby in the fifties by calculating the "force" on defects and inhomogeneities of a solid on the basis on the energy-momentum tensor or Eshelby stress tensor (Eshelby, 1951, 1975, 1999). The close similarities with the concept of J-Integral used in fracture mechanics motivated many researchers to study material forces application to crack propagation (Stumpf and Le, 1990; Maugin and Trimarco, 1992; Steinmann, 2000; Steinmann et al., 2009; Kienzler and Herrmann, 2012).

The forces associated with the Eshelby stresses are known as configurational forces, quasi-Newton forces or material forces, whereby we will adopt the first terminology in the sequel ("configurational forces"). In particular, in the context of finite element methods the material force method has been developed, it consists on the use of configurational forces to change the original nodal location (before deformation) in the search of a lower energy configuration motivated by either fracture/defect propagation (as mentioned earlier), or simply for mesh optimization in combination with remeshing or r-adaptivity methods (Steinmann, 2000; Mueller and Maugin, 2002; Mueller et al., 2002, 2004; Steinmann et al., 2009).

The objective of the present chapter is to establish a theoretical and computational framework for fracture mechanics based on material force method using zero-thickness interface elements which have been pre-inserted in the FE mesh. This will be done in the context of an iterative process, and at each iteration configurational forces will indicate the direction in which the interface elements opening into cracks should be moved in order to approach an energy minimum.

Most Configurational Mechanics papers start with the traditional standard equilibrium equation of the continuum. Same as in small strain theory, equilibrium equation in the deformed configuration may be expressed as follows:

$$\mathrm{div}\boldsymbol{\sigma} = -\mathbf{b}_{\mathrm{t}} \tag{3.64}$$

where $\mathrm{div}\boldsymbol{\sigma}$ is the spatial divergence of Cauchy stress tensor (derivatives w.r.t. the components of te deformed position of the material points, x_i) and $\mathbf{b}_t$ represents the physical body forces per unit

volume of the current configuration. Applying now the Piola transform to the previous equation, previous equation becomes:

$$\text{Div}\mathbf{P} = -\mathbf{b}_0 \tag{3.65}$$

where Div$\mathbf{P}$ is the material divergence of First Piola-Kirchhoff stress tensor (derivatives w.r.t. components of the original position of the material points, X_i) and $\mathbf{b}_0$ represents the body forces per unit volume of the reference configuration. Finally, applying additionally a Pull-back operation to the remaining spatial base vector of $\mathbf{P}$, a new expression is obtained:

$$\text{Div}\boldsymbol{\Sigma} = -\mathbf{B}_0 \tag{3.66}$$

where Div$\boldsymbol{\Sigma}$ is the material divergence of the Eshelby stress tensor and $\mathbf{B}_0$ represents some "configurational body forces" per unit volume of the reference configuration. Configurational body forces are null in the absence of physical body forces, and therefore for the sake of simplicity they will be assumed zero for most developments in the remaining of this section. The Eshelby stress tensor or energy-momentum tensor, is deduced algebraically in the literature (e.g. Eshelby, 1951, 1975, 1999; Mueller and Maugin, 2002), and may be expressed as:

$$\boldsymbol{\Sigma} = W\mathbf{I} - \mathbf{F}^T \cdot \mathbf{P} \quad \text{or} \quad \Sigma_{pj} = W\delta_{pj} - F_{ip}P_{ij} \tag{3.67}$$

In this expression W is the elastic energy per unit volume of reference configuration and the resulting tensor is in general non-symmetric. Physically, this tensor has been interpreted as providing information about the elastic energy changes (per unit volume of reference configuration) for variations of the reference configuration and fixed deformed configuration (Kienzler and Herrmann, 1997). Note that except for different meaning of the magnitudes involved, Eq.(3.66) is formally analogous to Eq.(3.65), which motivates an analogy between "configurational mechanics" and the most traditional "deformational mechanics" and leads to similar/dual concepts such as configurational forces, and similar/dual expressions in the finite element context such as weak equilibrium, etc.

3.4 Finite element formulation of configurational forces

On the basis of the analogy mentioned in the last section, Mueller and Maugin (2002) use weighed residuals to obtain a weak expression analogous to (3.47), but written for configurational forces

and Eshelby stress:

$$\hat{f} = \int_{\mathrm{V}} \hat{\mathbf{B}} \boldsymbol{\Sigma} \mathrm{dV} \tag{3.68}$$

where matrix $\hat{\mathbf{B}}$ is the same as in the weak equilibrium equation based on $\mathbf{P}$ (3.65).

In this section, a direct procedure to obtain the above expression of configurational forces, is obtained as a direct derivative of the element elastic energy, and a similar equation is derived for the small strain case.

3.4.1 Direct derivation of FE configurational forces at large strain

The elastic energy of a finite element subject to large strain may be expressed in reference configuration as:

$$W_{el} = \int_{\mathrm{V}} W \mathrm{dV} \tag{3.69}$$

where W is the specific elastic energy of the body per unit volume of original configuration.
Configurational forces for the element are defined as the derivatives of the total elastic energy of the element with respect to the initial nodal coordinates. In this section, index notation is used to develop such derivatives. Tensor indices will be indicated as subscripts, not to be confused with superscripts between parentheses that are used to designate nodal components (Taylor's notation already introduced in Section 3.2.4).

$$\hat{f}_i^{(a)} = \left. \frac{\partial W_{el}}{\partial X_i^{(a)}} \right|_{x=const.} \tag{3.70}$$

In order to perform the derivatives above, two aspects have to be considered. First, the constitutive energy function will be assumed to depend on the deformation gradient $W = W(\mathbf{F})$. Second, the element geometry is typically interpolated isoparametrically on the basis of a local curvilinear coordinate system ξ_i using the standard shape functions $N^{(a)}$. This mapping may be interpreted as a large strain transformation with deformation gradient $\mathbf{F}_\xi$ and Jacobian J_ξ i.e.

$$J_\xi = \det \mathbf{F}_\xi, \qquad \text{where} \qquad \mathbf{F}_\xi = \frac{\partial \mathbf{X}}{\partial \boldsymbol{\xi}} \tag{3.71}$$

This transformation is represented schematically, together with the physical deformation transformation $\mathbf{F}$, in Figure 3.9.

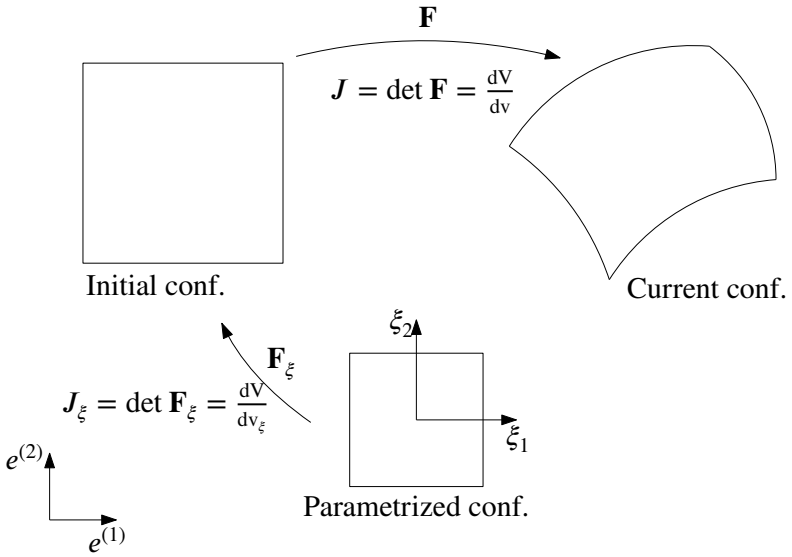

Figure 3.9: Scheme of reference, parametrized and current configurations

This changes (3.69) into the typical FE expression of the integral over the element domain in local coordinates, v_ξ.

$$W_{el} = \int_{v_\xi} W(\mathbf{F}) J_\xi \mathrm{dv}_\xi \tag{3.72}$$

The derivative (3.70) is now performed applying the product rule because both strain energy function and the Jacobian depend on initial nodal location:

$$f_i^{(a)} = \int_{\mathrm{v}_\xi} \frac{\partial W}{\partial X_i^{(a)}} J_\xi \mathrm{dv}_\xi + \int_{\mathrm{v}_\xi} W \frac{\partial J_\xi}{\partial X_i^{(a)}} \mathrm{dv}_\xi \tag{3.73}$$

The first term derivative is developed applying the chain rule formula with intermediate variables F_{ij} the components of deformation gradient, and the First Piola-Kirchhoff may be identified (Eq.3.31). In addition, the deformation gradient is replaced by the expression in Eq.(3.6) and for convenience in this first term $J_\xi \mathrm{dv}_\xi$ is replaced back to dV:

$$\int_{\mathrm{V}} \frac{\partial W}{\partial F_{jk}} \frac{\partial F_{jk}}{\partial X_i^{(a)}} \mathrm{dV} = \int_{\mathrm{V}} P_{jk} \frac{\partial \left(\delta_{jk} + \frac{\partial u_j}{\partial X_k} \right)}{\partial X_i^{(a)}} \mathrm{dV} \tag{3.74}$$

The displacement field is then replaced by the interpolation of nodal displacements Eq.(3.40) and because Kronecker delta is a constant, this leads to:

$$\int_{\mathrm{V}} P_{jk} \frac{\partial}{\partial X_i^{(a)}} \left(\frac{\partial N^{(b)} u_j^{(b)}}{\partial X_k} \right) \mathrm{dV} = \int_{\mathrm{V}} P_{jk} \frac{\partial}{\partial X_i^{(a)}} \left(\frac{\partial N^{(b)}}{\partial X_k} \right) u_j^{(b)} \mathrm{dV} + \int_{\mathrm{V}} P_{jk} \frac{\partial N^{(b)}}{\partial X_k} \left(\frac{\partial u_j^{(b)}}{\partial X_i^{(a)}} \right) \mathrm{dV} \tag{3.75}$$

The derivative with respect to nodal coordinates of the shape function Cartesian derivatives, is derived in Appendix E. By replacing the final equation (Eq.E.13) and expressing the displacement as current minus initial position $u_j^{(b)} = x_j^{(b)} - X_j^{(b)}$, one obtains

$$\int_{\mathrm{V}} \frac{\partial W}{\partial F_{jk}} \frac{\partial F_{jk}}{\partial X_i^{(a)}} \mathrm{dV} = - \int_{\mathrm{V}} P_{jk} \frac{\partial N^{(b)}}{\partial X_i} \frac{\partial N^{(a)}}{\partial X_j} u_j^{(b)} \mathrm{dV} + \int_{\mathrm{V}} P_{jk} \frac{\partial N^{(a)}}{\partial X_k} \left(\frac{\partial x_j^{(b)}}{\partial X_i^{(a)}} - \frac{\partial X_j^{(b)}}{\partial X_i^{(a)}} \right) \mathrm{dV} \tag{3.76}$$

Noting that $N^{(b)} u_j^{(b)} = u_j$, that $\partial x_j^{(b)} / \partial X_i^{(a)} = 0$ because final position x_i and initial position X_j are independent variables, and that $\partial X_j^{(b)} / \partial X_i^{(a)} = \delta^{(b)(a)} \delta_{ji}$, the expression becomes

$$\int_{\mathrm{V}} \frac{\partial W}{\partial F_{jk}} \frac{\partial F_{jk}}{\partial X_i^{(a)}} \mathrm{dV} = - \int_{\mathrm{V}} P_{jk} \frac{\partial u_j}{\partial X_i} \frac{\partial N^{(a)}}{\partial X_k} \mathrm{dV} + \int_{\mathrm{V}} P_{jk} \frac{\partial N^{(b)}}{\partial X_k} \left(-\delta^{(b)(a)} \delta_{ji} \right) \mathrm{dV} \tag{3.77}$$

Grouping terms, the final expression of the first term of equation Eq.(3.73) is obtained as:

$$\int_{\mathrm{V}} \frac{\partial W}{\partial F_{jk}} \frac{\partial F_{jk}}{\partial X_i^{(a)}} \mathrm{dV} = - \int_{\mathrm{V}} P_{jk} \frac{\partial N^{(a)}}{\partial X_k} \left(\frac{\partial u_j}{\partial X_i} + \delta_{ji} \right) \mathrm{dV} \tag{3.78}$$

The second part of configurational force equation (Eq.3.73) is the partial derivative of parametrized Jacobian with respect to nodal coordinates. The parametrized Jacobian is a measure of the volume change which relates the initial or reference (physical) element volume with the parametrized one (volume of the element in local coordinates),

$$J_\xi = \frac{\mathrm{dV}}{\mathrm{dv}_\xi} = \det \left(\frac{\partial \mathbf{X}}{\partial \boldsymbol{\xi}} \right) \tag{3.79}$$

where ξ represents the local coordinates of the finite element. Jacobian derivative is detailed in Appendix F and concludes with the parametrized Jacobian derivative:

$$\int_{\mathrm{v}_\xi} W \frac{\partial J_\xi}{\partial X_i^{(a)}} \mathrm{dv}_\xi = \int_{\mathrm{v}_\xi} W \left(\frac{\partial N^{(a)}}{\partial X_k} \right) \delta_{ki} \mathrm{dV} \tag{3.80}$$

Finally, summing Eq.(3.78) and Eq.(3.80) configurational forces may be expressed as:

$$\hat{f}_i^{(a)} = \int_{\mathrm{V}} \frac{\partial N^{(a)}}{\partial X_k} \left[W\delta_{ik} - \left(\frac{\partial u_j}{\partial X_i} + \delta_{ji} \right) P_{jk} \right] \mathrm{dV} \tag{3.81}$$

i.e., identifying the various matrices involved,

$$\hat{f} = \int_{\mathrm{V}} \hat{\mathbf{B}}^T \cdot \boldsymbol{\Sigma} \mathrm{dV} \tag{3.82}$$

It is reassuring that the above final expression, obtained by direct derivation of finite element elastic energy at large strain, coincides with Mueller and Maugin (2002)'s equation (Eq. 3.68) obtained by application of weighted residuals to Eq.(3.66). Note that, as indicated by Mueller and Maugin (2002), the differential Eq.(3.66), and the corresponding weak form Eq.(3.82) do not imply the definition of a new boundary value problem, since kinematic variables conjugate to configurational stress and forces have not been defined. Application of equation 3.82 is always a mere post-processing calculation on the basis of the results of the corresponding deformational problem solved in the traditional way.

3.4.2 Direct derivation of FE configurational forces in small strain

In a similar way as in the previous Section, configurational forces for a finite element in the context of small strain theory, may be obtained as the partial derivative of the total elastic energy of the element W_{el}, with respect to the initial nodal coordinates $X_i^{(a)}$ (Eq. 3.72). In this case, this derivation may be more relevant than in the large strain case. This is because most literature of configurational mechanics has been developed in the large strain context, and therefore most expressions such as Mueller and Maugin (2002)'s (Eq. 3.68), or the definition of the Eshelby stress tensor itself (3.67) are given in this context. Large strain theory provides the formalism to distinguish reference configuration from deformed configuration, and therefore it naturally allows us to make the proper derivatives required in configurational mechanics. In contrast, in small strain theory, although nodal displacements are obviously considered and evaluated, geometry changes are assumed to be very small, and for many purposes (including equilibrium) the domain geometry is assumed to remain constant. For this reason, using the formalism of small strain it is not so immediate to define some of the concepts of configurational mechanics. In the literature, artifacts have been proposed to reach a definition of Eshelby stress in small strain, for instance see Kienzler and Herrmann (1997); however, that definition lacks one term w.r.t what would be expected from particularizing the classical large strain expression (3.67), and therefore an alternative derivation such as the one provided in this section may contribute to clarify the matter.

The main advantage of deriving the configurational forces in small strain at the level of a finite element, is that the isoparametric FE formalism (regardless of whether the displacements and deformations are small or large) always includes the set of local coordinates for the elements, which may be used as a "material" reference system required to properly perform the material derivatives involved in configurational derivations.

In small strain, the total elastic energy of a finite element is also equal to the integral over the element domain energy density, Eq. (3.69). However, energy density depends now on the classical small-strain symmetric deformation tensor, $\boldsymbol{\varepsilon}$:

$$W_{el} = \int_{\mathrm{V}} W\left(\boldsymbol{\varepsilon}\right) \mathrm{dV} = \int_{\mathrm{v}_\xi} W\left(\boldsymbol{\varepsilon}\right) J_\xi \mathrm{dv}_\xi \tag{3.83}$$

The derivative (3.72) is also performed applying the product rule and obtaining Eq. (3.73), in which the second term development is identical as the one obtained in the large strain derivation (Eq.3.80). Therefore, only the derivation of the first term on the right-hand side of Eq. (3.80), that is, the partial derivative of deformation tensor with respect to nodal coordinates, is needed and is developed below.

The first term derivative is developed applying the chain rule formula with intermediate variables the components of small-strain deformation tensor, ε_{ij}, after which the small-strain (Cauchy) stress tensor may be immediately identified as the derivative of the specific energy potential with respect to strain. In addition, the small-strain deformation tensor may be replaced in terms of the classical small-strain B-matrix, the submatrices of which coincide with $\mathbf{B}^{(b)}$ defined in (3.59) for 3D or (3.61) in 2D, that is

$$\varepsilon_{jk} = B^{(b)}_{jkl} u^{(b)}_l, \quad B^{(b)}_{jkl} = \frac{1}{2}\left(\frac{\partial N^{(b)}}{\partial X_j}\delta_{kl} + \frac{\partial N^{(b)}}{\partial X_k}\delta_{jl}\right) \tag{3.84}$$

By doing all this, and for convenience in this first term, replacing $J_\xi \mathrm{dv}_\xi$ back with dV, the first term of the right-hand side of Eq. (3.80) becomes:

$$\int_{\mathrm{V}} \frac{\partial W}{\partial \varepsilon_{jk}} \frac{\partial \varepsilon_{jk}}{\partial X^{(a)}_i} \mathrm{dV} = \int_{\mathrm{V}} \sigma_{jk} \frac{\partial \left(B^{(b)}_{jkl} u^{(b)}_l\right)}{\partial X^{(a)}_i} \mathrm{dV} \tag{3.85}$$

The derivative is performed applying the product rule because both $B^{(b)}_{jkl}$ matrix and displacement field vector depend on nodal coordinates $X^{(a)}_i$:

$$\int_{\mathrm{V}} \frac{\partial W}{\partial \varepsilon_{jk}} \frac{\partial \varepsilon_{jk}}{\partial X_i^{(a)}} \mathrm{dV} = \int_{\mathrm{V}} \sigma_{jk} \frac{\partial B_{jkl}^{(b)}}{\partial X_i^{(a)}} u_l^{(b)} \mathrm{dV} + \int_{\mathrm{V}} \sigma_{jk} B_{jkl}^{(b)} \frac{\partial u_l^{(b)}}{\partial X_i^{(a)}} \mathrm{dV} \tag{3.86}$$

Expanding $B_{jkl}^{(b)}$ by the corresponding shape functions derivatives (3.84), and replacing the nodal displacements by displaced positions of the nodes minus initial positions, one has

$$\int_{\mathrm{V}} \frac{\partial W}{\partial \varepsilon_{jk}} \frac{\partial \varepsilon_{jk}}{\partial X_i^{(a)}} \mathrm{dV} = \int_{\mathrm{V}} \sigma_{jk} \frac{\partial \left(\frac{\partial N^{(b)}}{\partial X_k} \delta_{jl} + \frac{\partial N^{(b)}}{\partial X_j} \delta_{kl} \right)}{2 \partial X_i^{(a)}} u_l^{(b)} \mathrm{dV} + \int_{\mathrm{V}} \sigma_{jk} B_{jkl}^{(b)} \left(\frac{\partial x_l^{(b)}}{\partial X_i^{(a)}} - \frac{\partial X_l^{(b)}}{\partial X_i^{(a)}} \right) \mathrm{dV} \tag{3.87}$$

Using from previous section that $\partial X_l^{(b)} / \partial X_i^{(a)} = \delta^{(b)(a)} \delta_{li}$ and $\partial x_l^{(b)} / \partial X_i^{(a)} = 0$ (because configurational derivatives are made for constant displaced position of the body, either for large or small strain), one obtains:

$$\int_{\mathrm{V}} \frac{\partial W}{\partial \varepsilon_{jk}} \frac{\partial \varepsilon_{jk}}{\partial X_i^{(a)}} \mathrm{dV} = \int_{\mathrm{V}} \left[\sigma_{jk} \frac{1}{2} \frac{\partial}{\partial X_i^{(a)}} \frac{\partial N^{(b)}}{\partial X_k} \delta_{jl} u_l^{(b)} + \sigma_{jk} \frac{1}{2} \frac{\partial}{\partial X_i^{(a)}} \frac{\partial N^{(b)}}{\partial X_j} \delta_{kl} u_l^{(b)} - \sigma_{jk} B_{jkl}^{(b)} \left(\delta^{(b)(a)} \delta_{li} \right) \right] \mathrm{dV} \tag{3.88}$$

The partial derivative of shape functions with respect to nodal coordinates is derived in Appendix E. Using that and replacing back $\partial N^{(b)} u_l^{(b)} = \partial u_l$, previous equation becomes

$$\int_{\mathrm{V}} \frac{\partial W}{\partial \varepsilon_{jk}} \frac{\partial \varepsilon_{jk}}{\partial X_i^{(a)}} \mathrm{dV} = - \int_{\mathrm{V}} \sigma_{jk} \left[\frac{\partial u_j}{2 \partial X_i} \frac{\partial N^{(a)}}{\partial X_k} + \frac{\partial u_k}{2 \partial X_i} \frac{\partial N^{(a)}}{\partial X_j} + \frac{\partial N^{(a)}}{2 \partial X_k} \delta_{ji} + \frac{\partial N^{(a)}}{2 \partial X_j} \delta_{ki} \right] \mathrm{dV} \tag{3.89}$$

The Cauchy stress tensor symmetry allows to compact Eq.(3.89) into the following equation:

$$\begin{aligned} \int_{\mathrm{V}} \frac{\partial W}{\partial \varepsilon_{jk}} \frac{\partial \varepsilon_{jk}}{\partial X_i^{(a)}} \mathrm{dV} &= - \int_{\mathrm{V}} \sigma_{jk} \left[\frac{\partial u_j}{\partial X_i} \frac{\partial N^{(a)}}{\partial X_i} + \left(\frac{\partial N^{(a)}}{\partial X_k} \delta_{ji} \right) \right] \mathrm{dV} \\ &= - \int_{\mathrm{V}} \sigma_{jk} \frac{\partial N^{(a)}}{\partial X_k} \left(\frac{\partial u_j}{\partial X_i} + \delta_{ji} \right) \mathrm{dV} \end{aligned} \tag{3.90}$$

Finally, summing Eq.(3.90) and Eq.(3.80) configurational forces may be expressed as:

$$\hat{f}_i^{(a)} = \int_{\mathrm{V}} \frac{\partial N^{(a)}}{\partial X_k} \left[W \delta_{ik} - \left(\frac{\partial u_j}{\partial X_i} + \delta_{ji} \right) \sigma_{jk} \right] \mathrm{dV} \tag{3.91}$$

Identifying the partial derivative of shape functions as $\hat{\mathbf{B}}$ (see Eq.(3.47)), one may rewrite previous equation as:

$$\hat{f} = \int_{\mathrm{V}} \hat{\mathbf{B}}^T \cdot \hat{\boldsymbol{\sigma}} \mathrm{dV} \tag{3.92}$$

where

$$\hat{\sigma}_{ik} = W\delta_{ik} - \left(\frac{\partial u_j}{\partial X_i} + \delta_{ji}\right)\sigma_{jk} \tag{3.93}$$

Tensor $\hat{\boldsymbol{\sigma}}$ turns out to be the small-strain counterpart of the Eshelby configurational stress tensor. Note however that, uncommonly in the small strain theory, $\hat{\boldsymbol{\sigma}}$ is non-symmetric. Therefore, it is not surprising that the corresponding B-matrix in the integral expression (3.92) be the non-symmetric version same as it corresponds to the first Piola-Kirchhoff stresses P in the large strain theory (3.47).

The final expression obtained Eq.(3.93) may be now compared to the one obtained in the literature (Kienzler and Herrmann, 1997; Maugin, 2011), and the difference observed is in the last term $-\delta_{ip}\sigma_{ij} = -\sigma_{pj}$.

In those references it is argued that in the absence of body forces ($\mathbf{b_t} = 0$) this term is superfluous because it should vanish when replaced in the equilibrium equation (3.64). This reflects the fact that stresses should be in equilibrium and therefore the resulting net force on the body due to these stresses should be zero. In a finite element context, this is reflected by the fact that assembling the element forces equivalent to an equilibrated stress distribution gives a global force vector which is zero except at boundary nodes with prescribed loads or displacements. However, this does not mean that the forces for each element should be zero. Indeed, the nodal forces of an individual element corresponding to an equilibrated stress distribution, although when summed they have a zero total resultant, they are in general different from zero. And because expression 3.70 refers to the nodal forces of a given element, it is consistent that this term shows up in the resulting expression of the configuration stresses at small strain. Additionally, keeping this term means less restrictions regarding future extension to the case with non-zero body forces.

3.4.3 Configurational and deformational boundary conditions

The final outcome of a finite element approximation in linear problems is an equation system in which the boundary conditions have to be specified to describe the physical situation of loads and/or prescribed displacements. Boundary conditions must be specified for each point $\tilde{\mathbf{X}}$ the solid

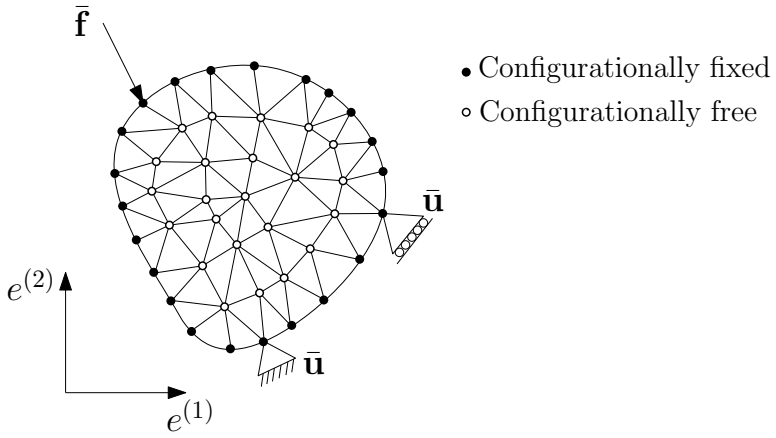

Figure 3.10: Configurational and deformational boundary conditions

surface. In general, two types of boundary conditions are considered:

- Dirichlet or essential boundary conditions are conditions imposed on the main variables. In the solid mechanics problem, this means to specify the displacement values to prescribed values $\bar{\mathbf{u}}$:

$$\mathbf{u}\left(\tilde{\mathbf{X}}\right) = \bar{\mathbf{u}}\left(\tilde{\mathbf{X}}\right) \tag{3.94}$$

- Neumann or natural boundary conditions are those specifying the surface fluxes, which in the solid mechanics problem means to specify the surface loads to prescribed values $\bar{\mathbf{f}}$:

$$\boldsymbol{\sigma}\left(\tilde{\mathbf{X}}\right) \cdot \mathbf{n} = \bar{\mathbf{f}}\left(\tilde{\mathbf{X}}\right) \tag{3.95}$$

Additional to the deformational BCs, the procedure developed will imply configurational changes (change of nodal coordinates in the direction indicated by configurational forces) that also require the definition of configurational boundary conditions. In this regard, each nodal coordinate can be:

- Configurationally free: nodal coordinate that can change reference (initial) value.
- Configurationally fixed: nodal coordinate which are not allowed to modify their reference value.

$$\tilde{\mathbf{X}} = \bar{\mathbf{X}} \tag{3.96}$$

The concept of configurationally free or prescribed nodal coordinate is graphically represented in a way similar to standard (deformational) boundary conditions, in Fig. 3.10.

3.5 Indirect displacement control based on fracture dissipation strategy

Basic iterative methods such as Newton-Raphson have been used extensively in the analysis of non-linear solid mechanics and Geo-mechanics problems, in which loads or nodal displacement values are prescribed directly with given values. However, these methods may not converge properly in the presence of high nonlinearity, such as post-peak regime with brittle behavior (sharp decrease of stresses at little variation of strain), and they surely fail in the presence of "snap-back" (extremely brittle response with receding displacement as well as force after the peak of load-displacement diagram). For these situations, more sophisticated iterative techniques such as Arc-Length (AL) or Indirect Displacement Control (IDC) methods have been proposed. Both strategies are based on the recalculation of the external load at each iteration with the objective to satisfy a prescribed indirect "constraint", generally established in terms of displacement increments of nodes other than the ones with applied loads, e.g. as a prescribed increment of the norm of the overall nodal displacement vector (AL), or as the increment of a difference between two specific nodes (IDC) (for instance to prescribe crack opening values). In this way, the applied load (or prescribed displacement) at the nodes with external loads can actually decrease through the iterations or even become negative during the load history (case of "snap-back").

AL or IDC methods work generally well but are not free of shortcomings either. In AL, which is the most popular of these methods, the quadratic nature of the constraint leads to a second-degree polynomial of the loading factor variation for the subsequent iteration, which complicates solution with possibility of negative discriminant, that in general requires choosing between the two roots, and may lead sometimes to unphysical unloading responses. The standard IDC method based on displacement differences leads to a linear constraint but its applicability is restricted to cases with a well-defined pre-established single crack trajectory. In both cases, the fact that the constraint is formulated in terms of displacements, may make it inconvenient for certain applications such as fracture opening or slip in Geomechanics, in which the more relevant always-growing magnitude is energy dissipation.

The above considerations motivate the development of a new indirect control iterative method in which the constraint is the total fracture dissipation. Similar to arc-length or IDC methods,

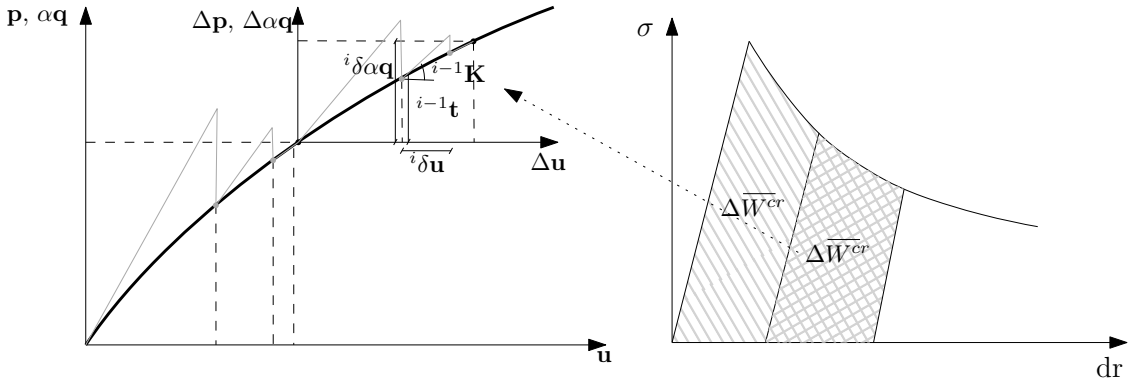

Figure 3.11: Iterative process.

"increments" refer to the pseudo-time in which the deformation, failure or fracture process is developing. In each of those increments, the external load (or prescribed displacement) factor is not known in advance, but is obtained as a by-product of the iterative calculation. The total displacement increment vector (accumulation of the iterative calculation process until current iteration i) is denoted as ${}^{i}\Delta\mathbf{u}$, and that of the previous iteration ${}^{i-1}\Delta\mathbf{u}$. If the correction obtained in the current iteration is ${}^{i}\delta\mathbf{u}$, we have:

$$ {}^{i}\Delta\mathbf{u} = {}^{i-1}\Delta\mathbf{u} + {}^{i}\delta\mathbf{u} \tag{3.97} $$

The correction of the current iteration is obtained as the solution of a linear problem with the residual force vector from previous iteration, ${}^{i-1}\mathbf{t}$, plus the variation of external forces ${}^{i}\delta\alpha\mathbf{q}$ (where $\mathbf{q}$ is the nominal load vector):

$$ {}^{i}\delta\mathbf{u} = {}^{i-1}\mathbf{K}^{-1}\left({}^{i}\delta\alpha\mathbf{q} + {}^{i-1}\mathbf{t}\right) \tag{3.98} $$

In previous equation, ${}^{i-1}\mathbf{K}$ is the stiffness tangent matrix of the previous iteration, and the residual of the previous iteration may be obtained as ${}^{i-1}\mathbf{t} = {}^{i-1}\Delta\alpha\mathbf{q} + {}^{i-1}\Delta\mathbf{p}$, with ${}^{i-1}\Delta\mathbf{p}$ =total increment of internal forces vector accumulated until previous iteration, and ${}^{i-1}\Delta\alpha$ = total increment of load factor also accumulated until previous iteration (Fig. 3.11).

Equation (3.98) may be rewritten as:

$$ {}^{i}\delta\mathbf{u} = {}^{i}\delta\alpha \;\; {}^{i}\delta\mathbf{u}^{I} + {}^{i}\delta\mathbf{u}^{II} \tag{3.99} $$

where ${}^{i}\delta\mathbf{u}^{I} = {}^{i-1}\mathbf{K}^{-1}\cdot\mathbf{q}$ and ${}^{i}\delta\mathbf{u}^{II} = {}^{i-1}\mathbf{K}^{-1}.{}^{i-1}\mathbf{t}$. Until here all is similar to classical "cylindrical"

arc-length method (e.g. see Rots, 1988; Crisfield, 1991).

However, now a path-following constraint based on fracture dissipation is introduced. For this purpose, the first step is to evaluate fracture dissipation at the interface constitutive level. The increment of work spent during the fracture process per unit area of the interface, δw^{cr}, may be expressed as:

$$\delta w^{cr} = \frac{\partial w^{cr}}{\partial \boldsymbol{\varepsilon}^J} \delta \boldsymbol{\varepsilon}^J \tag{3.100}$$

where $\boldsymbol{\varepsilon}^J$ is the relative displacement vector at a point of the interface. The partial derivative in previous equation may be developed via chain rule with intermediate variables the crack opening part of the relative displacements $\left(\boldsymbol{\varepsilon}^{crJ}\right)$, and the total relative displacements at the interface point may be related to the nodal displacements via matrix $\mathbf{B}$:

$$\delta w^{cr} = \frac{\partial w^{cr}}{\partial \boldsymbol{\varepsilon}^{crJ}} \frac{\partial \boldsymbol{\varepsilon}^{crJ}}{\partial \boldsymbol{\varepsilon}^J} \delta \boldsymbol{\varepsilon}^J = \frac{\partial w^{cr}}{\partial \boldsymbol{\varepsilon}^{crJ}} \frac{\partial \boldsymbol{\varepsilon}^{crJ}}{\partial \boldsymbol{\varepsilon}^J} \mathbf{B} \cdot \delta \mathbf{u}_{el} \tag{3.101}$$

Therefore, partial derivative $\partial w^{cr}/\partial \mathbf{u}$ may be written as:

$$\frac{\partial w^{cr}}{\partial \mathbf{u}_{el}} = \frac{\partial w^{cr}}{\partial \boldsymbol{\varepsilon}^{crJ}} \frac{\partial \boldsymbol{\varepsilon}^{crJ}}{\partial \boldsymbol{\varepsilon}^J} \mathbf{B} \tag{3.102}$$

For the fracture-based interface constitutive model described in previous section, the first derivatives in the previous chain rule may be obtained from Eq. (2.15):

$$\frac{\partial w^{cr}}{\partial \boldsymbol{\varepsilon}^{cr\,J}} = \begin{cases} \begin{bmatrix} \sigma_N & \sigma_T \end{bmatrix}^T & \sigma_N \geq 0 \,(\text{tension}) \\ \begin{bmatrix} 0 & \sigma_T - |\sigma_N \tan\phi| \end{bmatrix}^T & \sigma_N < 0 \,(\text{compression}) \end{cases} \tag{3.103}$$

while the second partial derivative is a standard expression in elasto-plasticity:

$$\frac{\partial \boldsymbol{\varepsilon}^{crJ}}{\partial \boldsymbol{\varepsilon}^J} = \frac{\mathbf{m} \otimes \mathbf{n} \cdot \mathbf{K}_0}{H + \mathbf{n} \cdot \mathbf{K}_0 \cdot \mathbf{m}} \tag{3.104}$$

where $\mathbf{m}$ is the flow rule, $\mathbf{n}$ the normal to the yield or cracking surface ($F = 0$), $\mathbf{K}_0$ the elastic tangent matrix and H the hardening parameter (Eqns. 3.105 and 3.106).

$$\mathbf{m} = \frac{\partial Q}{\partial \boldsymbol{\sigma}}, \; \mathbf{n} = \frac{\partial F}{\partial \boldsymbol{\sigma}}, \; \mathbf{K}_0 = \begin{bmatrix} K_N & 0 \\ 0 & K_T \end{bmatrix} \tag{3.105}$$

$$H = -\frac{\partial F}{\partial \lambda} = -\frac{\partial F}{\partial w^{cr}} \frac{\partial w^{cr}}{\partial \lambda} \tag{3.106}$$

Note that in this particular model, H is always negative (softening).

Once the fracture energy dissipation increment is defined at constitutive level δw^{cr} (3.100), a similar expression needs to be established for the total fracture dissipation at the interface element level, δW_{el}^{cr}:

$$\delta W_{el}^{cr} = \frac{\partial W_{el}^{cr}}{\partial \mathbf{u}_{el}} \delta \mathbf{u}_{el} \tag{3.107}$$

$$\frac{\partial W_{el}^{cr}}{\partial \mathbf{u}_{el}} = \int_S \frac{\partial w^{cr}}{\partial \mathbf{u}_{el}} dS = \int_S \frac{\partial w^{cr}}{\partial \boldsymbol{\varepsilon}^{crJ}} \frac{\partial \boldsymbol{\varepsilon}^{crJ}}{\partial \boldsymbol{\varepsilon}^{J}} \mathbf{B} dS \tag{3.108}$$

where the vector of derivative of total element dissipation with respect to nodal displacements is the integral along the discontinuity surface (S) of the similar derivative at constitutive level Eq. (3.108).

Previous equations may be finally assembled for all elements in the mesh, to obtain total mesh fracture dissipation δW^{cr}:

$$\delta W^{cr} = \sum_{n.el} \delta W_{el}^{cr} = \frac{\partial W^{cr}}{\partial \mathbf{u}} \delta \mathbf{u} \tag{3.109}$$

$$\frac{\partial W^{cr}}{\partial \mathbf{u}} = \sum_{n.el} \frac{\partial W_{el}^{cr}}{\partial \mathbf{u}_{el}} \tag{3.110}$$

Now, first order expansion of the total fracture dissipation is written for a given iteration i:

$${}^{i}\Delta W^{cr} = {}^{i-1}\Delta W^{cr} + \frac{\partial W^{cr}}{\partial \mathbf{u}} {}^{i}\delta \mathbf{u} \tag{3.111}$$

where ${}^{i-1}\Delta W_{el}^{cr}$ is the total fracture dissipation accumulated during the current iterative process since the last converged state, and ${}^{i}\delta \mathbf{u}$ may be expressed in terms of displacement increments $\left({}^{i}\delta \mathbf{u}^{I}, {}^{i}\delta \mathbf{u}^{II}\right)$ Eq. (3.99):

$${}^{i}\Delta W^{cr} = {}^{i-1}\Delta W^{cr} + \frac{\partial W^{cr}}{\partial \mathbf{u}} \left({}^{i}\delta\alpha {}^{i}\delta \mathbf{u}^{I} + {}^{i}\delta \mathbf{u}^{II}\right) \tag{3.112}$$

Therefore, enforcing ${}^{i}\Delta W^{cr} = \Delta \bar{W}^{cr}$the imposed value of work dissipated on fracture opening, ${}^{i}\delta\alpha$ can be isolated:

$${}^{i}\delta\alpha = \frac{\Delta \bar{W}^{cr} - {}^{i-1}\Delta W^{cr} - \left(\frac{\partial W^{cr}}{\partial \mathbf{u}}\right) {}^{i}\delta \mathbf{u}^{II}}{\left(\frac{\partial W^{cr}}{\partial \mathbf{u}}\right) {}^{i}\delta \mathbf{u}^{I}} \tag{3.113}$$

One important advantage of this procedure is that load factor $\delta\alpha_i$ has a linear expression, in contrast to classical arc-length where the constraint was quadratic leading two possible solutions (or none if discriminant is negative) and all the subsequent difficulties.

3.6 Criterion for selective node relocation (r-adaptivity)

As discussed in the previous section, configurational mechanics can be used as a method for nodal relocation. This should be useful for crack propagation because with the change of node location, interface elements could be re-oriented along the most favorable directions for crack opening/extension. In the current implementation, cracks are represented via zero-thickness interface elements which are equipped with a fracture-based elasto-plastic constitutive law (Sec. 2.3.2).

As already mentioned, the final objective is to develop a method for "crack realignment", that is a method by which nodal coordinates of zero-thickness interface elements (and possibly of elements in their vicinity) may be modified progressively so that mesh lines may be realigned to facilitate fracture development along non-preestablished paths. In a first stage of development, for this purpose it was proposed to apply configurational forces on all nodes of the mesh. However, practical implementation of that strategy has shown that allowing a general reallocation of all nodes simultaneously may lead to unstable iterative processes. Therefore, a selective re-location of the mesh nodes is proposed.

Additionally, in order to discriminate the energy changes due to physical configurational changes, from those due to the "background noise" associated to discretization errors, the configurational change is permitted exclusively to those interface elements that reach elasto-plastic behavior. The criterion used for this purpose is to release configurationally the degrees of freedom of a linear interface element when one (of the two) integration points remains elastic and the other starts to crack. For quadratic interface element a similar criterion is used, one (of the three) integration points remains elastic and the other two start to crack.

In order to achieve a progressive configurational change, it is necessary to control the opening of interface elements, in the sense of not allowing the opening of more than one consecutive interface elements at the same time. If that were detected to happen, the current load increment would be discarded, load factor would be reduced and this process would be repeated until no more than one consecutive interface element would open (although more than one interfaces are allowed to open in the same load increment, if they are not consecutive).

Note that, in general, progressive realignment of interface elements approaching the correct direction of physical cracks, may lead to crack initiation/propagation loads which might be lower

for subsequent iterations until they become lowest when the orientation becomes optimal. This is the main reason that the process may in general require of an indirect displacement control method such as the one proposed (Section 3.5), in which the external load factor is not fixed but is allowed to change during the iterative process.

Once the nodes to be moved have been selected, a strategy needs to be established regarding how to move these nodes. Different techniques have been explored and three of them are described in the following: (1) modifying the nodal coordinates in the direction indicated by configurational forces and a sufficiently small magnitude; (2) using a tangent matrix approximation based on Taylor series expansion of the structure/domain energy, and (3) combining the first method with a length correction of the reoriented interfaces.

During configurational changes the mesh may become distorted, or even entangled. This is why mesh improvement techniques may also be required. In this thesis, a simple "mesh relaxation" method capable of reallocating the nodes around the interfaces just realigned has been implemented. Also, after changing nodal coordinates, it is necessary to map the displacement values at the new location of each node, both for nodes moved by configurational forces and for those moved during the mesh-relaxation steps. These and other strategies to reduce the discretization errors are described in the following section 3.7.

3.6.1 Moving nodes in the direction of configurational forces

By definition, configurational forces $\hat{\mathbf{f}}$ indicate the direction in which nodes should be moved so that the whole structure or domain experiences the fastest decrease in elastic energy. Therefore, a first, simple "tangential approach" to modify nodal coordinates consists of moving the nodes of interest in the direction indicated by $\hat{\mathbf{f}}$, i.e.:

$$\mathbf{X}_{new} = \mathbf{X}_{old} - c\,\hat{\mathbf{f}} \tag{3.114}$$

where c is a small enough constant used to obtain the new nodal coordinates ($\mathbf{X}_{new}$) on the basis of the previous nodal coordinates ($\mathbf{X}_{old}$) and the configurational forces ($\hat{\mathbf{f}}$).

Some authors in the literature have used this technique in the context of mesh optimization, on the basis of the idea that the optimal mesh geometry is the one that provides the lowest elastic energy (Mueller and Maugin, 2002; Mueller et al., 2002). Some of the examples of application provided in those papers have been used to verify the procedure implemented and the results are presented in Section 3.9.1.

The method has the advantage of its simplicity; however, its unrestricted direct application

has some disadvantages such as that the mesh may get significantly distorted, and in particular the application to reorientation of opening dissipative cracks has some additional implications, such as potential crack length changes and subsequent additional dissipation not predicted by the configurational forces (which only account for variations of elastic energy in continuum elements). These shortcomings motivate the third method described in Section 3.6.3.

3.6.2 Tangent matrix approximation

Any smooth and derivable function can be approximated by using Taylor series. In this case, a second order expansion of the energy function is considered; whereby the first derivative represents the slope of the energy surface or energy gradient ($\hat{\mathbf{f}}$), and the second derivative represents the curvature or tangent matrix ($\hat{\mathbf{K}}$):

$$W = W_0 + \frac{\partial W}{\partial \mathbf{X}}\delta\mathbf{X} + \frac{1}{2}\delta\mathbf{X}\frac{\partial^2 W}{\partial \mathbf{X}^2}\delta\mathbf{X} \tag{3.115}$$

$$W = W_0 + \hat{\mathbf{f}}\delta\mathbf{X} + \frac{1}{2}\delta\mathbf{X}\hat{\mathbf{K}}\delta\mathbf{X} \tag{3.116}$$

To find the minimum energy, the derivative with respect to the nodal position should be zero, which means:

$$\hat{\mathbf{f}} + \hat{\mathbf{K}}\delta\mathbf{X} = \mathbf{0} \tag{3.117}$$

which leads to a similar algebraic system as for classical deformational displacements and forces.

$$\delta\mathbf{X} = -\hat{\mathbf{K}}^{-1}\hat{\mathbf{f}} \tag{3.118}$$

Using a tangent matrix approximation, the iterative solution should in principle converge faster than the previous approach (of using the direction of configurational forces directly). The tangent matrix $\hat{\mathbf{K}}$ may be calculated analytically, by developing the second derivative of energy density with respect to nodal position, or numerically, by repeated evaluation of the configurational forces after varying selectively and by a small amount each one of the nodal coordinates of the element. In the current study, the numerical tangent matrix has been implemented.

Obviously, these selective small variations are only applied to the position of degrees of freedom considered "free" from the configurational viewpoint (that is of degrees of freedom for which we allow the nodes to change initial position) and the rest are assumed to be zero.

To reduce oscillations, if a configurational force component is sufficiently small with respect to the other components, the corresponding degree of freedom is changed to "fixed" configurational status (similar to prescribed displacement in the standard deformational analysis).

3.6.3 Moving nodes in the direction of configurational forces, with interface length correction

The shortcomings described in Sec. 3.6.1, mesh distortion and significant changes in the crack length, motivate the third method described in this section. As the simplest way to avoid those effects, the nodes of the moving interface element are configurationally moved according to the three-step procedure described below, and shown in Figure 3.12:

1. The configurational force on the node to be moved, $\hat{\mathbf{f}}$, according to (3.117) would move the node to point 1,
2. $\hat{\mathbf{f}}$ is projected on the direction normal to the initial interface element to obtain the new $\hat{\mathbf{f}}_N$ which, instead moves the node to point 2 according to:

$$\mathbf{X}_{new} = \mathbf{X}_{old} - c_{min}\ \hat{\mathbf{f}}_N \tag{3.119}$$

3. The new interface direction is fixed to point 2, and the length of final interface element is modified to reduce element distortion, to the point over new interface element direction from which a normal (to the new direction) leads to the original node location (point 3).

3.7 Strategies to reduce discretization error

Configurational forces show the direction in which nodes should be moved to reduce the global structural/domain energy. However, these energy changes that take place when the nodes change position may be due to two reasons: (1) physical changes in structural/domain geometry including crack propagation, and (2) discretization errors. Discretization errors are in fact intrinsic to the FEM, surely affect not only stresses and displacements but also energy values calculated, and they cannot be avoided, only reduced by mesh refinement or alternative procedures. In fact, some of the applications of configurational mechanics found in the literature (and also the first examples included in Section 3.9.1 for comparison) aim precisely at this type of error, by relocating nodes within a continuum of fixed geometry only to find the discretization that corresponds to an energy

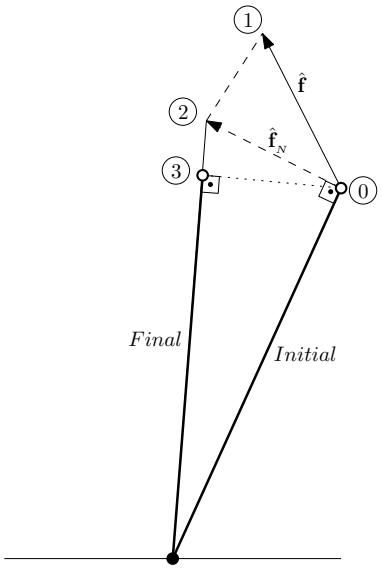

Figure 3.12: Scheme of the procedure for nodal relocation of an interface element. Bold lines represent initial and final interface positions.

minimum (concept on the other side not totally clear; mesh with lowest elastic energy and mesh with the minimum discretization error are not identical concepts...).

The main focus of this chapter is oriented to the first type of energy changes (material geometry), that in general should be dominant. However, if discretization is not adequate, discretization errors might cause a background noise in the energy values that might interfere with the configurational process, the configurational forces evaluated might indicate directions different than the ones related to the physical dimensions or crack geometry changes. In order to reduce the discretization error, two strategies have been developed: (1) Parametrization or h-adaptive mesh refinement and (2) quadratic elements and mesh relaxation applied over nodes close to the moved one. These strategies are described in the following sub-sections, together with some examples of application.

3.7.1 Parametrization or h-adaptive mesh refinement

This procedure for reducing the discretization error basically consists of mesh refinement; however, if mesh is refined without any additional precautions, the number of nodes to move in the configurational iterations would also increase, something that may complicate the numerical treatment of the crack realignment iterations. In order to refine meshes without increasing the number of configurationally moving nodes, the procedure described in this section has been introduced. It consists of parameterizing the coordinates of newly introduced nodes in (linear) terms of the old

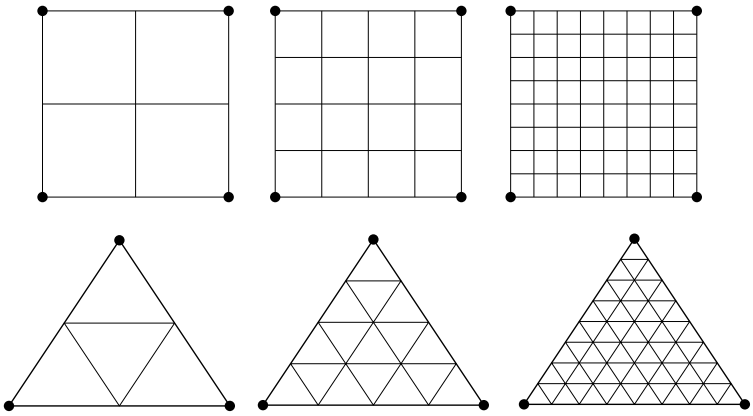

Figure 3.13: Parametrized subdivisions in triangular and quadrangular elements.

nodes. In this way, the number of nodes to move configurationally will not change and the newly introduced nodes will just follow the original ones in their configurational changes.

In the code, parametrization is only implemented for linear quadrangular and triangular elements using the configurations shown in Figure 3.13. These structures are based on the principle of recursive spatial decomposition of cells into smaller equal size cells, it is also known as quadtree meshes (see for instance Tabarraei and Sukumar, 2007).

Configurational parametrization

Let $\mathbf{X}$ be the vector of nodal coordinates of all nodes in the refined mesh, and $\mathbf{X}^{red}$ be the reduced vector of nodal coordinates of the original mesh including only the nodes that would be used to describe the configurational changes. Then, the rectangular transformation matrix $\mathbf{T}_c$ is introduced that relates both vectors:

$$\Delta\mathbf{X} = \mathbf{T}_c \cdot \Delta\mathbf{X}^{red} \tag{3.120}$$

Matrix $\mathbf{T}_c$ contains many zeros and a few fixed non-zero coefficients, that reflect the position of one new node of the refined mesh w.r.t. the original (unrefined mesh) nodes, such as for instance if a new node is at mid-distance between two older nodes, the corresponding rows of this matrix will contain all zeros except the 0.5 factor in the columns corresponding to the two older nodes.

By standard application of the Principle of Virtual Work, a reciprocal expression for the corresponding nodal forces $\hat{\mathbf{f}}^{red}$ and $\hat{\mathbf{f}}$, which involves the transpose of the same transformation matrix is obtained:

$$\hat{\mathbf{f}}^{red} = \mathbf{T}_c^T \cdot \hat{\mathbf{f}} \tag{3.121}$$

Now, the configurational forces $\hat{\mathbf{f}}$ are related to the change of coordinates ($\Delta\mathbf{X}$) by means of configurational mechanics, equation (3.117) for method 2, and making the equivalence $\hat{\mathbf{K}} = c^{-1}\mathbf{I}$ in method 1:

$$\hat{\mathbf{f}} = -\hat{\mathbf{K}} \cdot \Delta\mathbf{X} \tag{3.122}$$

If equation (3.120) is replaced into (3.122), and the result into (3.121), the final result is:

$$\hat{\mathbf{f}}^{red} = -\hat{\mathbf{K}}^{red} \cdot \Delta\hat{\mathbf{X}}^{red} \tag{3.123}$$

where

$$\hat{\mathbf{K}}^{red} = \mathbf{T}_c^T \cdot \hat{\mathbf{K}} \cdot \mathbf{T}_c \tag{3.124}$$

Matrix $\hat{\mathbf{K}}^{red}$ constitutes the "configurational stiffness" matrix for the reduced system of nodes which needs to be inverted to obtain the increment of nodal coordinates:

$$\Delta\mathbf{X}^{red} = -\left(\hat{\mathbf{K}}^{red}\right)^{-1} \hat{\mathbf{f}}^{red} \tag{3.125}$$

Finally, from this result, the increment of nodal coordinates of the total mesh (including parametrized nodes) may be obtained via equation (3.120) as a post-processing step.

Short example

A basic example is presented to clarify the concept of configurational parametrization matrix $\mathbf{T}_c$. It consists of the mesh shown in Figure 3.14.

The "reduced" vector of nodal coordinates, $\mathbf{X}^{red}$, complete vector of nodal coordinates, $\mathbf{X}$, and parametrization matrix, $\mathbf{T}_c$ for this mesh are the following (where $\mathbf{I}$ is the 2×2 identity matrix):

$$\mathbf{X}^{red} = \begin{bmatrix} \mathbf{X}^{(1)} & \mathbf{X}^{(2)} & \mathbf{X}^{(3)} & \mathbf{X}^{(4)} & \mathbf{X}^{(5)} & \mathbf{X}^{(6)} \end{bmatrix}^T \tag{3.126}$$

$$\mathbf{X} = \begin{bmatrix} \mathbf{X}^{(1)} & \mathbf{X}^{(2)} & \mathbf{X}^{(3)} & \mathbf{X}^{(4)} & \mathbf{X}^{(5)} & \mathbf{X}^{(6)} & \mathbf{X}^{(7)} & \mathbf{X}^{(8)} & \mathbf{X}^{(9)} & \mathbf{X}^{(10)} & \mathbf{X}^{(11)} & \mathbf{X}^{(12)} & \mathbf{X}^{(13)} & \mathbf{X}^{(14)} & \mathbf{X}^{(15)} \end{bmatrix}^T \tag{3.127}$$

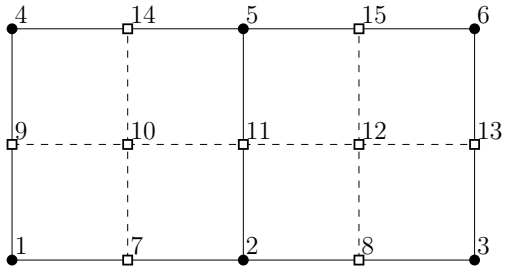

Figure 3.14: Example of configurational parametrization. Solid lines and solid dots represent the (original) coarse mesh, and dashed lines with empty squares correspond to the additional nodes and lines in the refined mesh subdivision

$$\mathbf{T}_c^T = \begin{bmatrix} \mathbf{I} & \mathbf{0} & \mathbf{0} & \mathbf{0} & \mathbf{0} & \mathbf{0} & 0.5\mathbf{I} & \mathbf{0} & 0.5\mathbf{I} & 0.25\mathbf{I} & \mathbf{0} & \mathbf{0} & \mathbf{0} & \mathbf{0} & \mathbf{0} \\ \mathbf{0} & \mathbf{I} & \mathbf{0} & \mathbf{0} & \mathbf{0} & \mathbf{0} & 0.5\mathbf{I} & 0.5\mathbf{I} & \mathbf{0} & 0.25\mathbf{I} & 0.5\mathbf{I} & 0.25\mathbf{I} & \mathbf{0} & \mathbf{0} & \mathbf{0} \\ \mathbf{0} & \mathbf{0} & \mathbf{I} & \mathbf{0} & \mathbf{0} & \mathbf{0} & \mathbf{0} & 0.5\mathbf{I} & \mathbf{0} & \mathbf{0} & \mathbf{0} & 0.25\mathbf{I} & 0.5\mathbf{I} & \mathbf{0} & \mathbf{0} \\ \mathbf{0} & \mathbf{0} & \mathbf{0} & \mathbf{I} & \mathbf{0} & \mathbf{0} & \mathbf{0} & \mathbf{0} & 0.5\mathbf{I} & 0.25\mathbf{I} & \mathbf{0} & \mathbf{0} & \mathbf{0} & 0.5\mathbf{I} & \mathbf{0} \\ \mathbf{0} & \mathbf{0} & \mathbf{0} & \mathbf{0} & \mathbf{I} & \mathbf{0} & \mathbf{0} & \mathbf{0} & \mathbf{0} & 0.25\mathbf{I} & 0.5\mathbf{I} & 0.25\mathbf{I} & \mathbf{0} & 0.5\mathbf{I} & 0.5\mathbf{I} \\ \mathbf{0} & \mathbf{0} & \mathbf{0} & \mathbf{0} & \mathbf{0} & \mathbf{I} & \mathbf{0} & \mathbf{0} & \mathbf{0} & \mathbf{0} & \mathbf{0} & 0.25\mathbf{I} & 0.5\mathbf{I} & \mathbf{0} & 0.5\mathbf{I} \end{bmatrix} \tag{3.128}$$

Deformational parametrization

Deformational parametrization is the same concept applied to the deformational problem. Also known as Local Grid Refinement (or LGR), it is a useful technique to refine coarse meshes only in specific areas (Fig. 3.15), without causing the refinements necessary at one zone to extend throughout the domain in x, y and z directions. However, the tree-based structure decomposition shown in the figure, generates, at the limit between refined and non-refined zones, nodes from the finer mesh to be located along sides of elements of the larger mesh, what we will call "hanging nodes". This type of meshes would not be acceptable in a general FEM context because conformity would not be guaranteed between the elements on both sides of the limit line between refined and non-refined meshes. However, deformational parametrization makes possible to use this kind of mesh.

Deformational parametrization exhibits the same type of rectangular transformation matrix $\mathbf{T}_d$ which relates the vector of displacements in all nodes ($\mathbf{u}$) and the reduced vector of displacements ($\mathbf{u}^{red}$) which this time contains all non-hanging nodes:

$$\mathbf{u} = \mathbf{T}_d \cdot \mathbf{u}^{red} \tag{3.129}$$

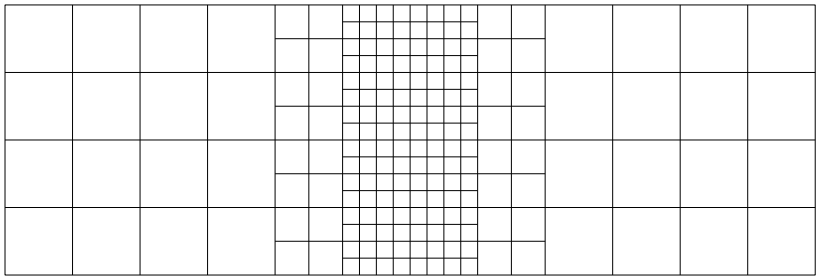

Figure 3.15: Local Grid Refinement by quad-tree meshes.

Similarly, by application of the PVW the complete vector of reduced external forces $\mathbf{f}^{red}$ may be expressed as the product of the transposed of transformation matrix $\mathbf{T}_d$ and the full vector of displacements $\mathbf{f}$.

$$\mathbf{f}^{red} = (\mathbf{T}_d)^T \mathbf{f} \tag{3.130}$$

Formulating the finite element problem for the full mesh, one obtains the (full) stiffness matrix $\mathbf{K}$:

$$\mathbf{f} = \mathbf{K} \cdot \mathbf{u} \tag{3.131}$$

If now (3.129) is replaced into the previous equation, and the result is substituted in (3.130), the matrix equation for the reduced displacement and force vectors is obtained, which may be solved by matrix inversion to yield

$$\mathbf{u}^{red} = \left(\mathbf{K}^{red}\right)^{-1} \cdot \mathbf{f}^{red} \tag{3.132}$$

where the reduced stiffness matrix is:

$$\mathbf{K}^{red} = \mathbf{T}_d^T \cdot \mathbf{K} \cdot \mathbf{T}_d \tag{3.133}$$

After solving Eq.(3.132) and obtaining the reduced displacement vector, Eq. (3.129) may be used to obtain the full displacement vector as a post-processing step.

Short example

A basic example is presented to clarify the concept of deformational parametrization matrix $\mathbf{T}_d$. It consists of the mesh shown in Figure 3.16. The "reduced" vector of nodal displacements, $\mathbf{u}^{red}$, complete vector of nodal displacements, $\mathbf{u}$, and parametrization matrix, $\mathbf{T}_d$, for this mesh

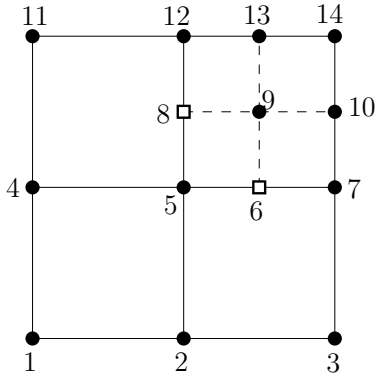

Figure 3.16: Example of deformational parametrization. Solid lines represent a coarse mesh, dashed lines the subdivision done involving hanging nodes represented by empty squared points and solid points which are the main nodes of the resulting refined mesh.

would be (where $\mathbf{I}$ is the 2×2 identity matrix):

$$\mathbf{u}^{red} = \left[\mathbf{u}^{(1)}\ \mathbf{u}^{(2)}\ \mathbf{u}^{(3)}\ \mathbf{u}^{(4)}\ \mathbf{u}^{(5)}\ \mathbf{u}^{(7)}\ \mathbf{u}^{(9)}\ \mathbf{u}^{(10)}\ \mathbf{u}^{(11)}\ \mathbf{u}^{(12)}\ \mathbf{u}^{(13)}\ \mathbf{u}^{(14)}\right]^T \tag{3.134}$$

$$\mathbf{u} = \left[\mathbf{u}^{(1)}\ \mathbf{u}^{(2)}\ \mathbf{u}^{(3)}\ \mathbf{u}^{(4)}\ \mathbf{u}^{(5)}\ \mathbf{u}^{(6)}\ \mathbf{u}^{(7)}\ \mathbf{u}^{(8)}\ \mathbf{u}^{(9)}\ \mathbf{u}^{(10)}\ \mathbf{u}^{(11)}\ \mathbf{u}^{(12)}\ \mathbf{u}^{(13)}\ \mathbf{u}^{(14)}\right]^T \tag{3.135}$$

$$\mathbf{T}_d^T = \begin{bmatrix}
\mathbf{I} & \mathbf{0} & \mathbf{0} & \mathbf{0} & \mathbf{0} & \mathbf{0} & \mathbf{0} & \mathbf{0} & \mathbf{0} & \mathbf{0} & \mathbf{0} & \mathbf{0} & \mathbf{0} & \mathbf{0} \\
\mathbf{0} & \mathbf{I} & \mathbf{0} & \mathbf{0} & \mathbf{0} & \mathbf{0} & \mathbf{0} & \mathbf{0} & \mathbf{0} & \mathbf{0} & \mathbf{0} & \mathbf{0} & \mathbf{0} & \mathbf{0} \\
\mathbf{0} & \mathbf{0} & \mathbf{I} & \mathbf{0} & \mathbf{0} & \mathbf{0} & \mathbf{0} & \mathbf{0} & \mathbf{0} & \mathbf{0} & \mathbf{0} & \mathbf{0} & \mathbf{0} & \mathbf{0} \\
\mathbf{0} & \mathbf{0} & \mathbf{0} & \mathbf{I} & \mathbf{0} & \mathbf{0} & \mathbf{0} & \mathbf{0} & \mathbf{0} & \mathbf{0} & \mathbf{0} & \mathbf{0} & \mathbf{0} & \mathbf{0} \\
\mathbf{0} & \mathbf{0} & \mathbf{0} & \mathbf{0} & \mathbf{I} & 0.5\mathbf{I} & \mathbf{0} & 0.5\mathbf{I} & \mathbf{0} & \mathbf{0} & \mathbf{0} & \mathbf{0} & \mathbf{0} & \mathbf{0} \\
\mathbf{0} & \mathbf{0} & \mathbf{0} & \mathbf{0} & \mathbf{0} & 0.5\mathbf{I} & \mathbf{I} & \mathbf{0} & \mathbf{0} & \mathbf{0} & \mathbf{0} & \mathbf{0} & \mathbf{0} & \mathbf{0} \\
\mathbf{0} & \mathbf{0} & \mathbf{0} & \mathbf{0} & \mathbf{0} & \mathbf{0} & \mathbf{0} & \mathbf{0} & \mathbf{I} & \mathbf{0} & \mathbf{0} & \mathbf{0} & \mathbf{0} & \mathbf{0} \\
\mathbf{0} & \mathbf{0} & \mathbf{0} & \mathbf{0} & \mathbf{0} & \mathbf{0} & \mathbf{0} & \mathbf{0} & \mathbf{0} & \mathbf{I} & \mathbf{0} & \mathbf{0} & \mathbf{0} & \mathbf{0} \\
\mathbf{0} & \mathbf{0} & \mathbf{0} & \mathbf{0} & \mathbf{0} & \mathbf{0} & \mathbf{0} & \mathbf{0} & \mathbf{0} & \mathbf{0} & \mathbf{I} & \mathbf{0} & \mathbf{0} & \mathbf{0} \\
\mathbf{0} & \mathbf{0} & \mathbf{0} & \mathbf{0} & \mathbf{0} & \mathbf{0} & \mathbf{0} & 0.5\mathbf{I} & \mathbf{0} & \mathbf{0} & \mathbf{0} & \mathbf{I} & \mathbf{0} & \mathbf{0} \\
\mathbf{0} & \mathbf{0} & \mathbf{0} & \mathbf{0} & \mathbf{0} & \mathbf{0} & \mathbf{0} & \mathbf{0} & \mathbf{0} & \mathbf{0} & \mathbf{0} & \mathbf{0} & \mathbf{I} & \mathbf{0} \\
\mathbf{0} & \mathbf{0} & \mathbf{0} & \mathbf{0} & \mathbf{0} & \mathbf{0} & \mathbf{0} & \mathbf{0} & \mathbf{0} & \mathbf{0} & \mathbf{0} & \mathbf{0} & \mathbf{0} & \mathbf{I}
\end{bmatrix} \tag{3.136}$$

Example of the influence of mesh refinement and parametrization on the results of configurational analysis

A three-point beam bending test is presented to analyze the influence of mesh refinement on the outcome of the configurational strategy. As Figure 3.17 depicts, vertical displacement is constrained at the bottom end corner nodes and, on the center of top face, horizontal displacement is not allowed and vertical displacement is prescribed downwards with increasing value. The continuum material is assumed elastic and interface elements follow the constitutive model presented in Section 2.3.2. The beam is originally discretized with linear triangular continuum elements and also a line of interface elements representing a possible propagation trajectory starting at the bottom center of the beam and zigzagging to the prescribed displacement point at top center (Figure 3.18).

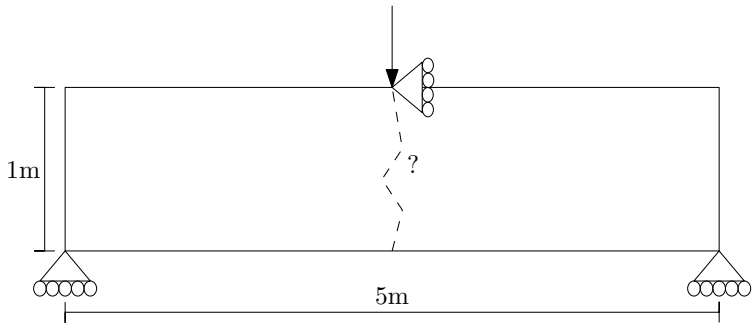

Figure 3.17: Three-point beam bending boundary conditions.

Due to symmetry, it is known that the crack should develop vertically from the bottom at the center span of the beam just under the prescribed displacement point. Therefore, the expected result would be that the interface elements would align vertically during the configurational process. The first node to be moved during the configurational process is the one indicated in Figure 3.18 with the label "Relevant node". Changing the position of that node to a grid of positions over a small area around it, and calculating the global energy of the mesh for each of those positions, an energy surface can be plotted. This has been done in Fig. 3.20a , and as seen in the figure the energy surface exhibits a minimum at $x = 2.58$m, which does not coincide exactly with the (expected) midpoint at $x = 2.50$m.

In order to check whether the deviation may be caused discretization errors, an h-adaptive deformational and configurational parametrized mesh refinement is performed . The refinement consists of subdividing each of the elements at the beam center first in 4 smaller elements, then in 16 elements and finally in 64 elements. The discretization topology is depicted in Figure 3.13 (triangular elements) and parametrized meshes are represented in Figure 3.19.

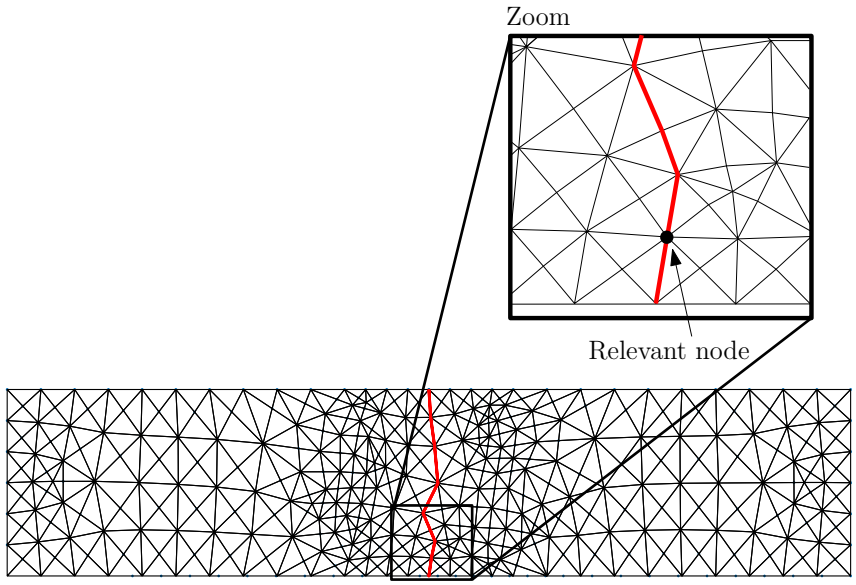

Figure 3.18: Original mesh discretization. Interface elements are represented in red.

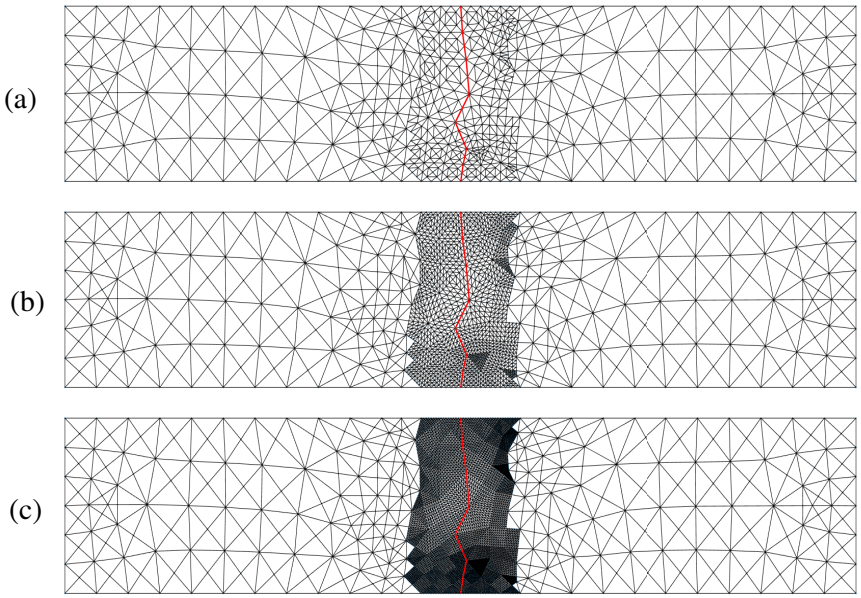

Figure 3.19: In a finite area close to the discontinuity the elements are discretized in (a) 4 elements, (b) 16 elements and (c) 64 elements.

Figures 3.20b-d show the energy surface that corresponds to the refined meshes. Due to configurational parametrization, it was possible to make the same change of position of the relevant node in the four meshes because the extra nodes (all nodes that exist in the refined meshes but

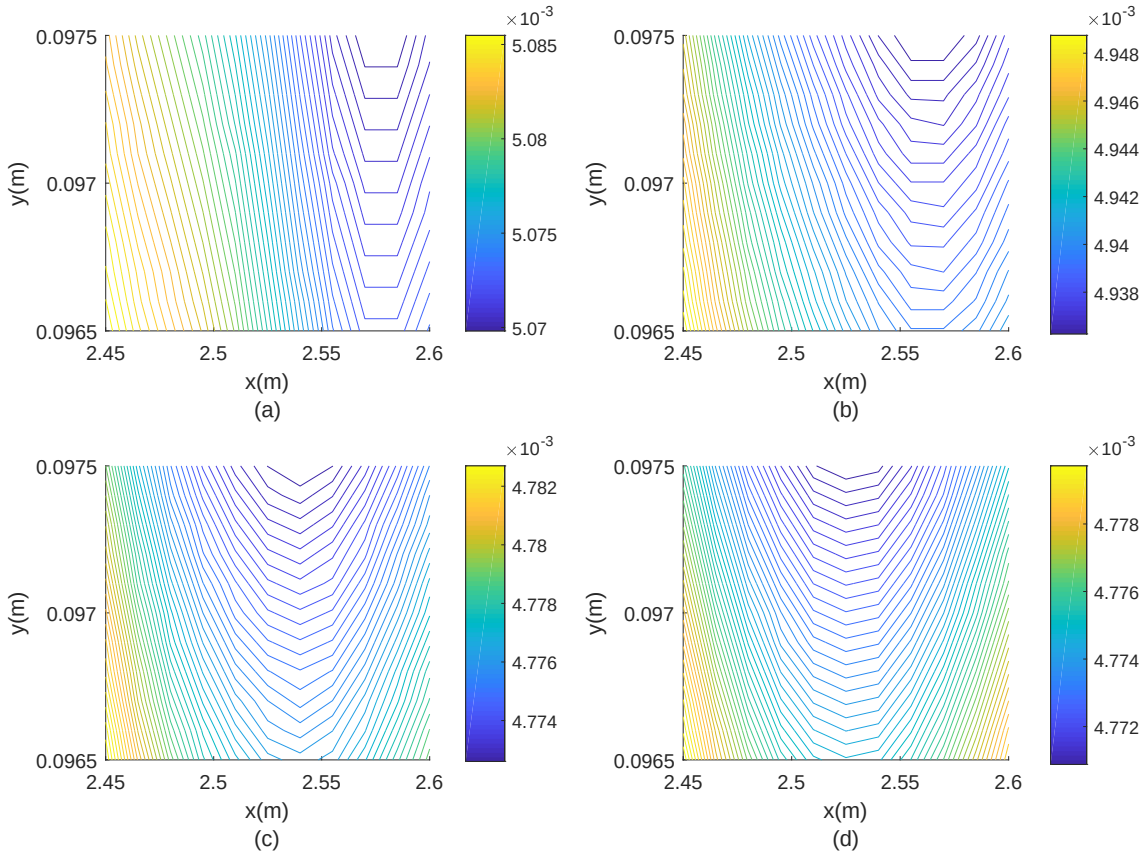

Figure 3.20: Energy surface by different relevant node location. The process is repeated by the four presented meshes: (a) Original mesh, (b) mesh parametrized into 4 elements, (b) mesh parametrized into 16 elements and (b) mesh parametrized into 64 elements.

were not present in the original mesh) change their location automatically when the relevant node is moved. As the graphs show, the minimum of global beam energy becomes progressively closer to $x = 2.5$m with the refinement of the mesh.

This example shows that discretization error may have a significant influence on the location of minimum energy points for crack propagation, and therefore deformational and configurational parametrization may be useful tools to reduce the discretization error and improve realignment method.

3.7.2 Quadratic elements and mesh relaxation

As seen in the previous example, linear triangular elements require a relatively fine mesh to reduce the error to negligible values. This can be improved by using quadratic elements, which have more degrees of freedom and the interpolation is done by richer shape functions, so convergence relative to mesh size is generally faster. This has motivated the additional implementation of the quadratic triangles and the corresponding interface elements, as shown in Fig.3.21.

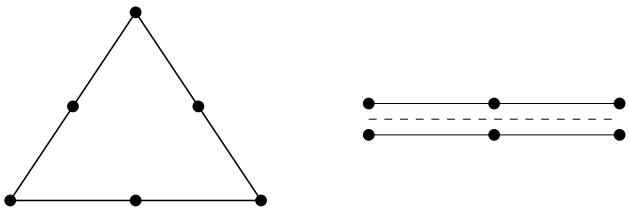

Figure 3.21: : Quadratic elements introduced in the code: (left) quadratic triangular continuum element, and (right) quadratic zero-thickness interface element.

Aside from mesh size, another factor that may affect discretization error is mesh quality, in the sense of the distorted shape of the element with regard to their regular shape (i.e. equilateral triangles, or square elements). In this regard, the quality of the mesh may be degrading as the configurational process advances and the nodes progressively change location. This is why a mesh relaxation strategy has been also implemented, which is performed after each step of the configurational process. This technique for mesh improvement (Frey and Field, 1991; Schweingruber and Rank, 1992) consists of an iterative process that makes mesh geometry more regular around each of the nodes which have moved during the configurational step. First, the list of the nodes moved ("configurational nodes") is created. Then the desired number of element and node "layers" around each of those nodes are identified, and then all of them are moved in order to make all elements in the area more regular. The process is repeated sequentially for each of the configurational nodes in the list, two or three times until no changes are obtained in node locations. The strategy is applied over nodes that are not configurationally fixed by previous configurational steps or the ones on the boundary. The results of the mesh relaxation strategy just described, applied to a typical mesh example are depicted in (Figure 3.22).

3.8 Code structure

The Matlab code developed for nodal relocation to describe crack propagation consists of applying both configurational and deformational changes simultaneously in the context of finite elements.

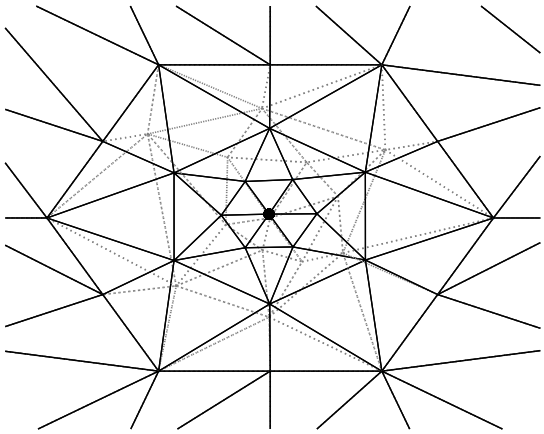

Figure 3.22: Mesh relaxation applied to nodes around two layers with respect to a node that has moved in a previous configurational step (black point). Discontinuous lines represent initial mesh and in solid lines the final mesh after mesh relaxation

Both processes are iterative, and therefore the code requires a structure formed by clearly defined loops where configurational and deformational iterations are performed and appropriate convergence criteria are taken into account. Basically, an outer configurational loop has been added to an existing standard deformational code.

The main tasks performed by the code, are represented in the flow chart of Fig. 3.23, and are summarized in the following:

1. First, the general input is read by the code. It contains the coordinates, nodal connectivity, material properties, problem characteristics (small/large strain, plane stress/plane strain, etc.) as well as deformational and configurational boundary conditions.

2. Initialization of the variables: nodal and element variables are initialized or read from a restart file.

3. In the first configurational iteration, the reference mesh is defined by the input coordinates. In the following ones the updated coordinates will be read separately. A new configurational step begins with kinematic, static and constitutive variables from the last step configurationally converged.

4. The deformational increment is applied over the configuration described in step 3.

5. The calculation of a deformational increment starts with the evaluation of stiffness matrix and external forces.

6. Deformational iterative process based on energy dissipation starts, with a given value of the fracture energy constraint.

7. Solve the mechanical FEM system ($\mathbf{K} \cdot \mathbf{u} = \mathbf{f}$)

8. Update the stiffness matrix, residual force vector and external load factor according to the indirect displacement control procedure based on fracture dissipation, and back to step 6 until the deformational convergence is reached.

9. Once deformational convergence is reached, evaluate configurationally free nodes and elasto-plastic state of the interfaces. Possible cases:

   (a) If more than one consecutive interface element have reached crack opening condition during the increment, the deformational increment is repeated with a smaller fracture energy constraint. A simple factor division does the reduction automatically, in general, $factor = 2$.

   $$\Delta \bar{W}^{cr}_{new} = \Delta \bar{W}^{cr}_{old} / factor \tag{3.137}$$

   (b) If no element has reached the crack opening condition during the increment, loop back to next deformational increment (step 4).

   (c) If one or more non-consecutive interface elements have reached the crack opening condition during the increment (Section 3.6), select tip nodes of those interface elements as configurationally free nodes and go to step 10.

10. Change nodal location of the configurationally free nodes by r-adaptivity method with length correction (Section 3.6.3), and perform mesh relaxation.

11. Interpolate nodal displacements from last configuration at the new nodal coordinate locations.

12. Back to step 3 until the configurational convergence is reached.

13. If configurational convergence has been reached, fix configurationally selected nodes.

14. Finally, once the configurational and deformational convergence are achieved, the results are stored in an output file.

The general structure of the code is presented in the flow diagram of Figure 3.23.

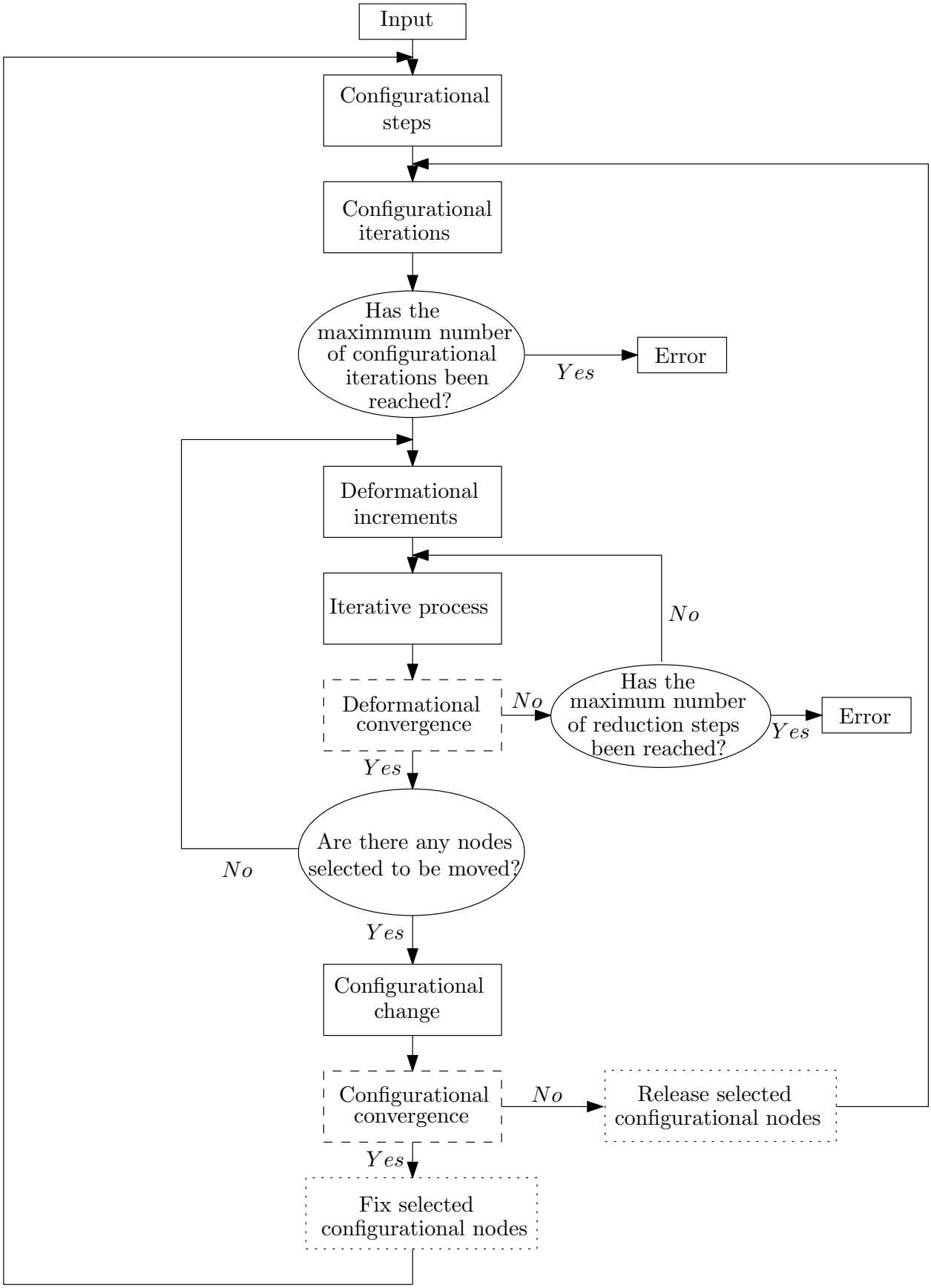

Figure 3.23: Flow chart representing the code structure.

3.9 Examples

3.9.1 Literature examples (Continuum)

The three examples included in this section consist of literature examples involving simple square blocks with fixed geometry and no cracks. In these examples, nodes are moved on the basis of configurational forces with the only purpose to reaching an energy minimum, which corresponds to an "optimal" discretization. These examples are solved applying the r-adaptivity method 1 (Sec. 3.6.1), where c_{min} is obtained by trial error and, in the following, $\left|\hat{\mathbf{f}}\right|/c_{min}$ are in the range of 10^{-4} to 10^{-3}. The purpose of these examples is the comparison and verification of the strategy implemented.

Example 1

This example consists on a block loaded by displacement u_y on the top side and fixed on the bottom and plane strain is assumed. The prescribed displacement value is $u_y = 0.01$m, and the calculation is run assuming large strain with Neo-Hooke model with parameter values $\lambda = 1000$MPa, $\mu = 400$MPa (Lamé Constants).

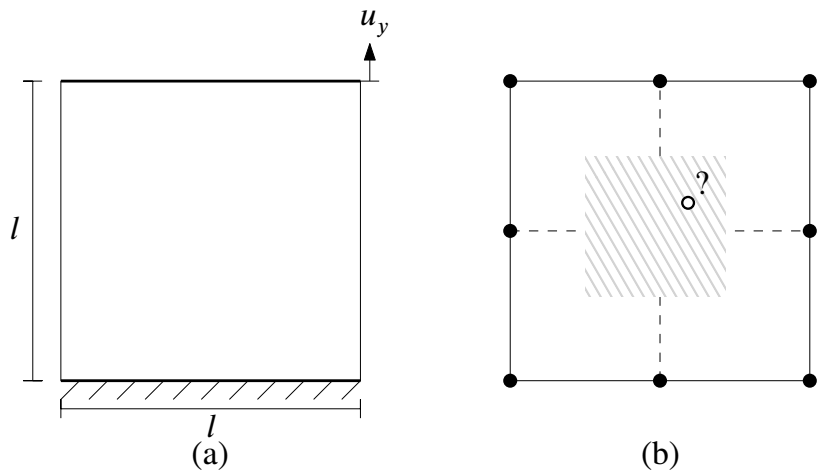

Figure 3.24: (a) Boundary conditions of example 1 (b) Finite element discretization.

The block is discretized using four quadrilateral elements, and the central node location is studied in order to get the minimum total energy in the domain. As it is shown in Figure 3.25a, for $l = 1$m the energy density function is a parabola with a minimum on $\mathbf{X} = (0.5, 0.5)$.Therefore, also the norm of configurational force (gradient of the energy surface) vanishes at that point, Figure 3.25b.

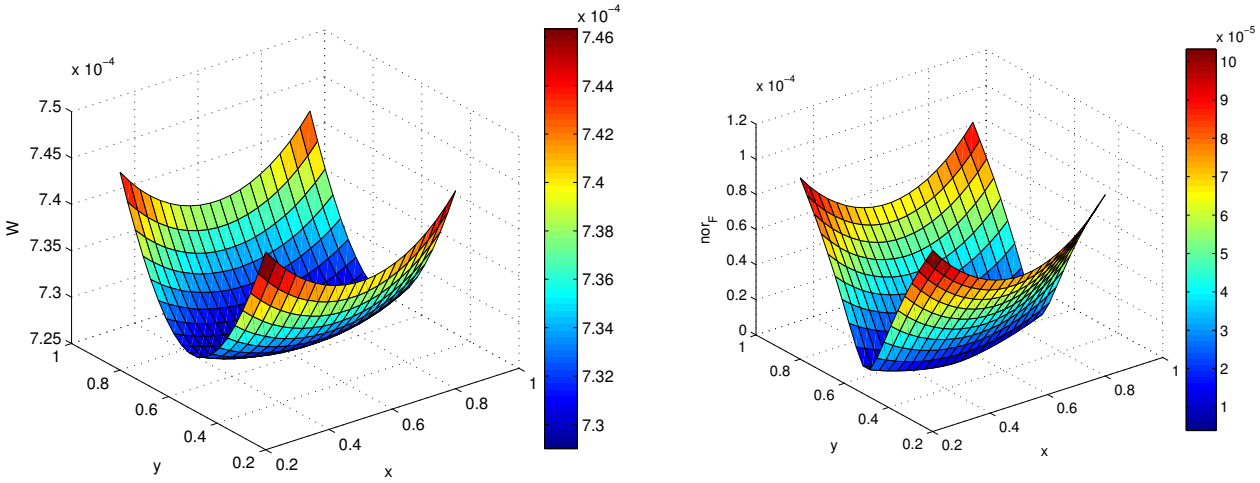

(a) **(b)**

Figure 3.25: (a) Energy density distribution depending on the central node position. (b) Norm of configurational forces depending on the central node position.

As Figure 3.26 depicts, starting from different initial configurations, configurational forces lead the central node to the minimum energy point. The various meshes obtained through the iterations are shown in gray, and the converged optimal position $\mathbf{X}_{opt} = (0.5, 0.5)$ in black. In Figure 3.26a with $X_0 = (0.5, 0.55)$ configurational forces act on the vertical direction. In the Figure 3.26b with $\mathbf{X}_0 = (0.55, 0.5)$ horizontal configurational forces move the central node to X_{opt}. Figures 3.26c and 3.26d are correspond to $\mathbf{X}_0 = (0.55, 0.55)$ and $\mathbf{X}_0 = (0.35, 0.2)$ so vertical and horizontal configurational forces act over the central node. Vertical energy changes are larger (as shown in Figures 3.25a and 3.25b) because the stresses are higher in the (loading) y-direction.

To be noted is that applying r-adaptivity method, various nodal initial position different paths but all bring the node to the same position, $\mathbf{X} = (0.5, 0.5)$, to which is consistent with the fact that configurational forces (gradient of energy surface) always drive central node to minimum energy position at the center.

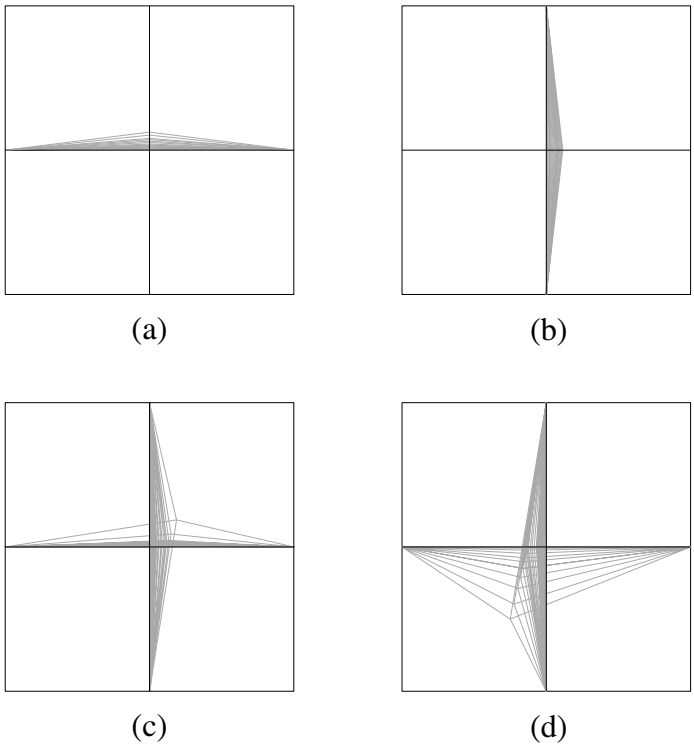

Figure 3.26: Gray lines represent different mesh geometries driven by configurational forces before reaching the optimal one, represented in black ($\mathbf{X}_{opt} = (0.5, 0.5)$), for four different initial positions of the central node: (a) $\mathbf{X}_0 = (0.5, 0.55)$, (b) $\mathbf{X}_0 = (0.55, 0.5)$, (c) $\mathbf{X}_0 = (0.55, 0.55)$, (d) $\mathbf{X}_0 = (0.35, 0.2)$.

Example 2

This second example is a case that has been already analyzed in the configurational mechanics literature (Mueller and Maugin, 2002). It consist of a 1×1m homogeneous square block loaded in tension by a vertical displacement prescribed on the top side and discretized with a regular mesh of 4×4 square element , as shown in Figure 3.27. The material is assumed to behave as Neo-Hooke hyperleasticity, with parameters that correspond to $\lambda = 1000$MPa, $\mu = 400$MPa.

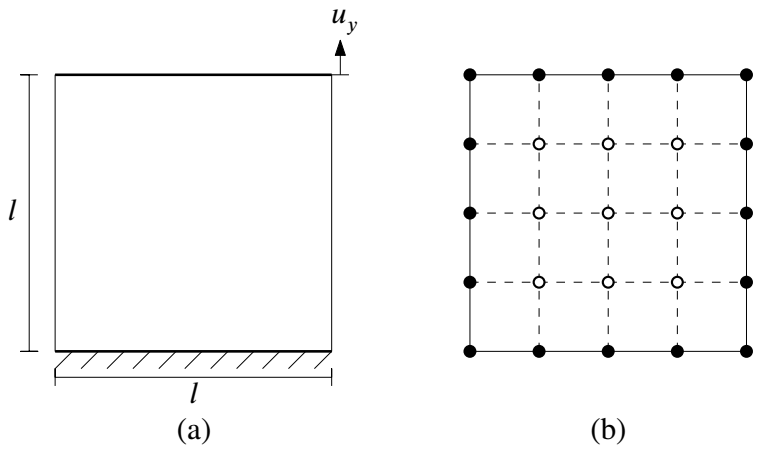

Figure 3.27: Boundary conditions of example 2 (b) Finite element discretization, and nodes considered configurationally fixed (solid nodes) and free (hollow nodes).

In this extension problem, the most significant configurational forces turn out to be concentrated along the top and bottom sides of the boundary, precisely where the displacement is prescribed (Figure 3.28a).However, since geometry and boundary conditions are fixed, the boundary nodes are all configurationally fixed (Figure 3.27b), only internal nodes are allowed to change coordinates. Since the strategy to move nodes used in this example is r-adaptivity method 1 (Sec. 3.6.1), the only configurational forces that are relevant are those on internal nodes (Figure 3.28b).

The results obtained after the iterative configurational procedure, is the mesh shown in Figure 3.29a , in which the nodes have been relocated in the directions indicated by the forces of Fig. 3.28b. These results agree well with those shown in the above mentioned reference Mueller and Maugin (2002). Finally, Fig. 3.29b,c show the evolution of the energy and configurational force intensity on the node which experiences largest force and coordinate change, which is labeled “Relevant node” in Fig. 3.29a. As seen, energy comes to a minimum and configurational force vanishes as this node approaches its final “optimal” location shown in Fig.3.29a.

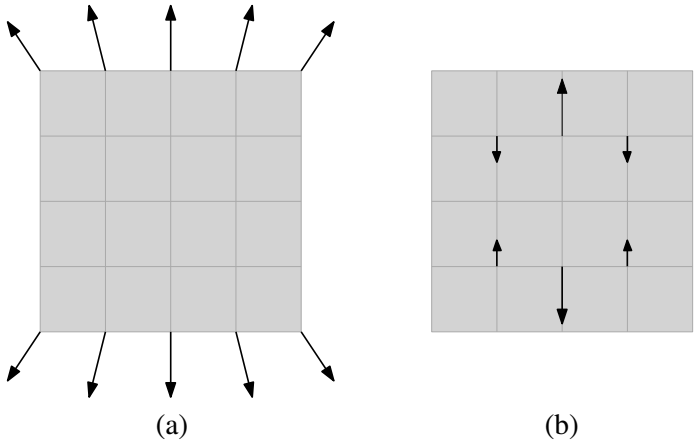

Figure 3.28: (a) Configurational forces at the scale needed for representing the larger values, in which only forces on the outer nodes (all configurationally fixed) show up, and (b) configurational forces on internal nodes at a much larger scale, these are the only forces that will move nodes.

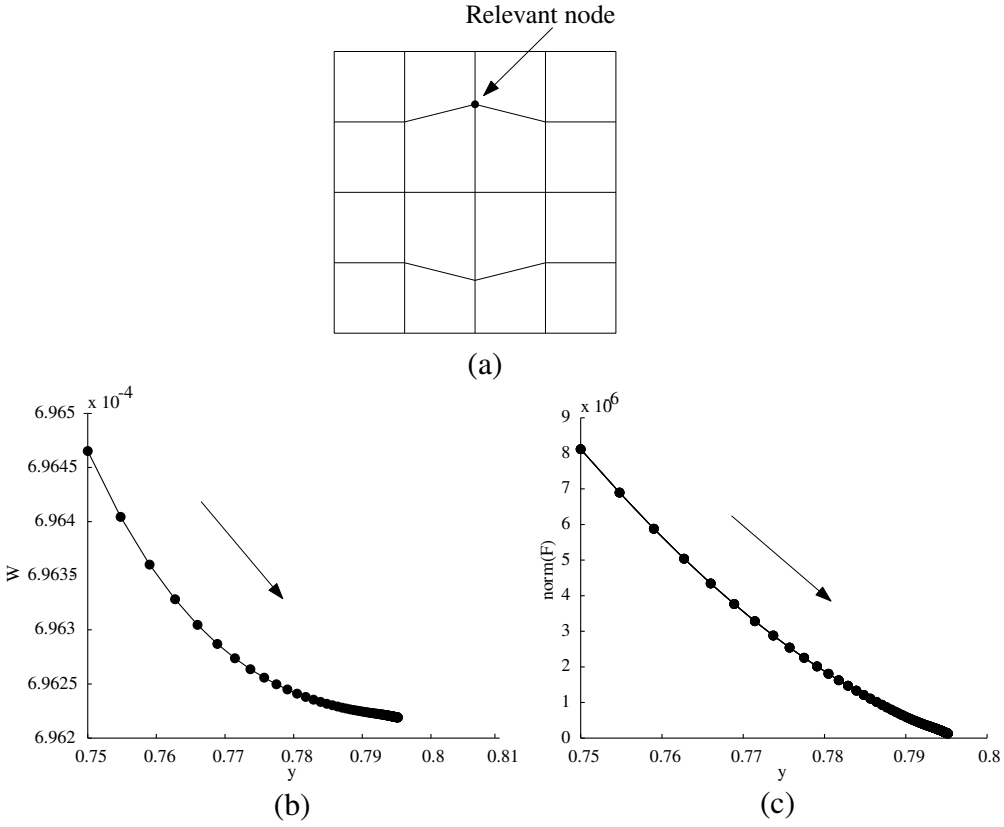

Figure 3.29: (a) Optimal mesh distribution obtained at the end of analysis, (b) total block energy evolution with respect to vertical coordinate of the "relevant node", and (c) norm of configurational forces with respect to the same vertical coordinate of the "relevant node".

Example 3

The third example is from the paper Mueller et al. (2002), it consists again of a 1m x 1m homogeneous square block which is subject to a uniform vertical distributed load applied on the central half of the top surface, from $\mathbf{X} = (0.25, 1)$ to $\mathbf{X} = (0.75, 1)$ and the material is assumed to behave as Neo-Hooke hyperleasticity, with parameters that correspond to material properties $\lambda = \mu = 400$MPa (Lamé Constants). In this example, along the block base only vertical displacements are restricted, except for the left corner node which is fixed in both vertical and horizontal directions.

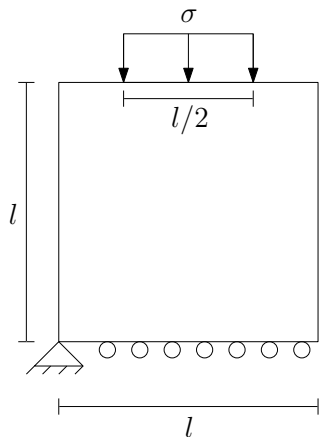

Figure 3.30: Geometry and boundary conditions of example 3.

Similarly to previous examples, to maintain the geometry and boundary conditions all boundary nodes are configurationally prescribed, while the internal nodes are allowed to change their location (configurationally free). Regarding the boundary nodes, however, two different types of configurational boundary conditions are considered: one in which all boundary nodes are totally fixed (Figure 3.31),and the second one in which the nodes located along vertical side faces and bottom face (but no corner nodes), are set free to move along their corresponding face (Figure 3.31b).

The relevant components of the resulting configurational forces obtained in the initial configuration are depicted in Fig.3.32, for the two cases of configurational b.c.s mentioned above, and in Fig. 3.33 the final mesh distributions are shown, which are in agreement with the results in the literature Mueller et al. (2002).

In order to plot the evolution of the energy, however, this example requires an additional consideration. Because a distributed load is applied (instead of a prescribed displacement), with

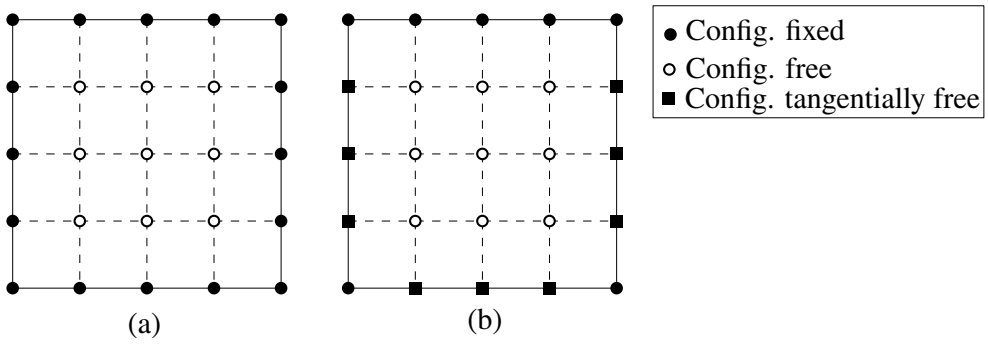

Figure 3.31: Finite element discretization and configurational force restrictions: (a) all boundary nodes totally fixed, and (b) corner nodes fixed and nodes along sides and bottom face tangentially free.

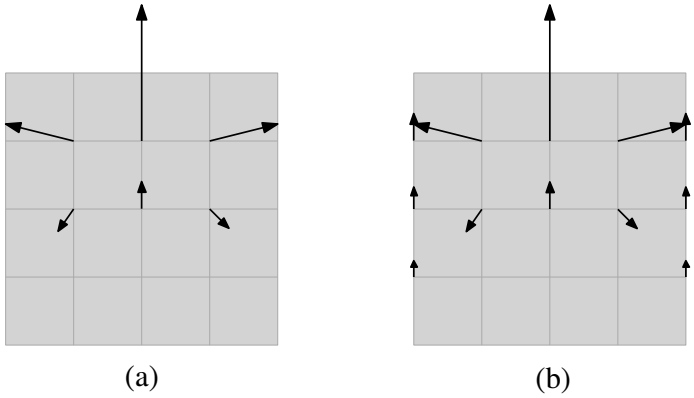

Figure 3.32: (a) Configurational forces on internal nodes , and (b) configurational forces on internal nodes plus tangential components of forces on the boundary nodes. The direction represented correspond to negative energy gradient.

a load that is assumed to remain constant in magnitude and intensity regardless of the nodal displacements, the expression of the elastic potential (W) must include one additional term due to the work of those loads (or potential difference), as the product of the external force vector ($\mathbf{f}^{ext}$) and displacement vector $\mathbf{U}$:

$$W = \frac{1}{2}\mathbf{U}^T\mathbf{K}\mathbf{U} - \mathbf{U}^T\mathbf{f}^{ext} \tag{3.138}$$

Since the elastic energy accumulated in the elements only accounts for the first term of previous expression, one needs to additionally subtract the second term of Eq. (3.138) in order to obtain the total energy W. Taking this into account, the evolution of W with respect to the y-coordinate of the relevant node indicated in Figure 3.33, is represented in Figures 3.34a, 3.34b for the case with totally fixed configurational boundary, and Figures 3.34c, 3.34d for the case with tangentially

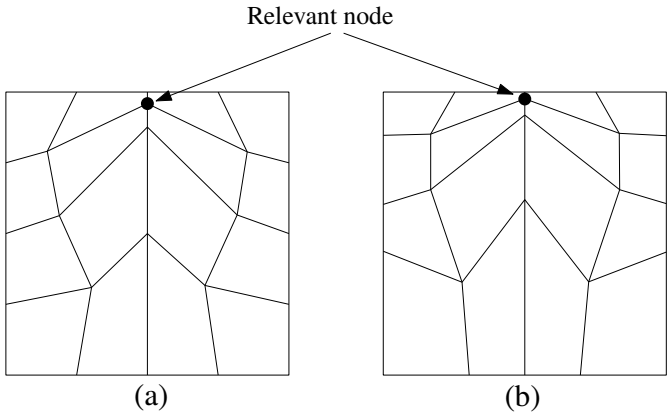

Figure 3.33: (a) Optimal mesh distribution of the mesh with fixed and free nodes (b) Optimal mesh distribution of the mesh tangentially free nodes along vertical sides and bottom face.

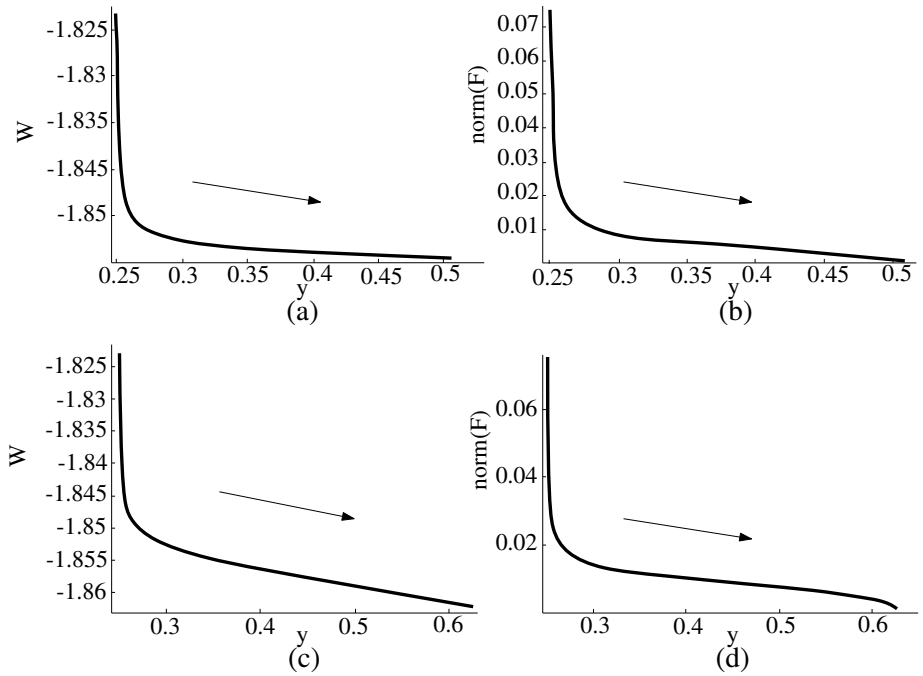

Figure 3.34: Influence of the position of the vertical position of the "relevant node" on: (a) total energy of the mesh with totally fixed configurational boundary, (b) norm of configurational forces for the same case, (c) total energy of the mesh with tangentially free configurational boundary along vertical sides and bottom case, and (d) the norm of configurational forces in the same case.

free nodes at configurational boundaries along vertical faces and bottom side. Curves in Figure 3.34 show that in both cases global energy tends to a minimum value and norm of configurational forces to zero during the configurational iterative process.

3.9.2 Three-point beam bending test with one possible path

The first example of application to crack propagation is the 5×1m three-point bending beam test is represented in Fig. 3.35. The three-point bending test is a good example to verify simulations of cracking along non-pre-established path because, due to symmetry, it is known that the crack path should be vertical, along the plane of symmetry and starting from the bottom face of the beam. If the process works correctly, the initial zig-zagging mesh lines should get realigned to this vertical crack path.

Deformational boundary conditions consist of nodes at the lower vertices vertically constrained, and a node at the middle of the upper face with horizontal displacements restricted. The loading consists of vertical displacements at this point prescribed with an increasing value (Figure 3.35).

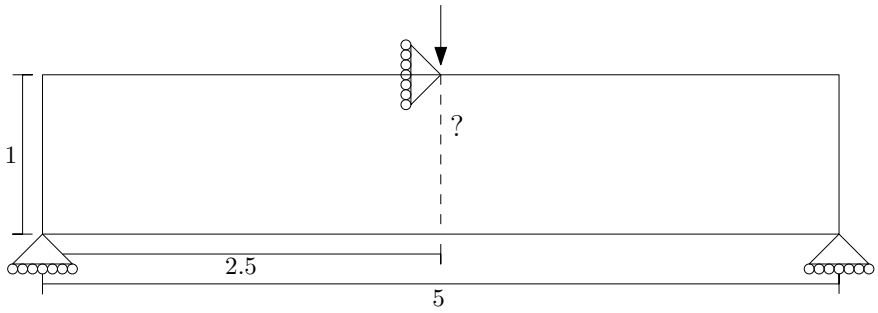

Figure 3.35: Boundary conditions of three-point bending test example.

The beam is discretized into triangular elements of quadratic order in order to reduce the discretization error (Fig. 3.36). The method used to change coordinates during configurational iterations is "r-adaptivity method with length corrections" (method 3, described in Sec. 3.6.3 where c_{min} is adjusted so that the change of interface orientation does not exceed 1°), and the iterative strategy for the deformational iterative procedure is the indirect displacement control based on fracture dissipation (Sec. 3.5), with an automatic adjustment of the value of dissipation constraint during the deformational increments, as described in Section 3.8. Due to the expected crack trajectory, and to deal with increasing complexity, interface elements are pre-inserted along a single line zig-zagging around the symmetry line of the beam (red line in Fig. 3.36).

The continuum material is assumed linear elastic (small strain), with Young's modulus of $E =$ 15000MPa and Poisson's ratio $\nu = 0.0$.The constitutive model for the interface is the fracture-based constitutive model described in Sec. 2.3.2, with the following parameter values: normal and tangential elastic stiffness $K_N = K_T = 10^7$MPa/m, friction angle $\tan\phi = 0.7°$, tensile strength $\chi =$ 3MPa, cohesion $c = 6$MPa, energy mode I $G_f^I = 10^{-2}$MPa·m, energy mode IIa $G_f^{IIa} = 10^{-1}$MPa·m

and sigma dilatation $\sigma_{dil} = 30\text{MPa}$.

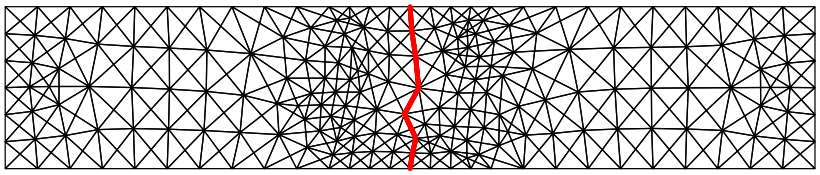

Figure 3.36: Initial configuration of beam bending realignment.

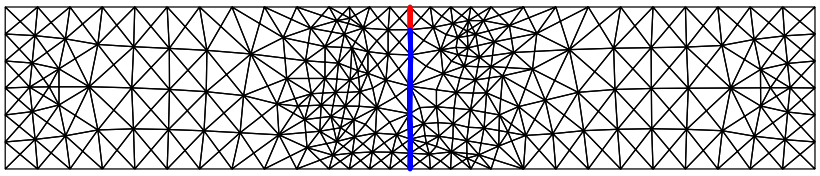

Figure 3.37: Final configuration of beam bending realignment.

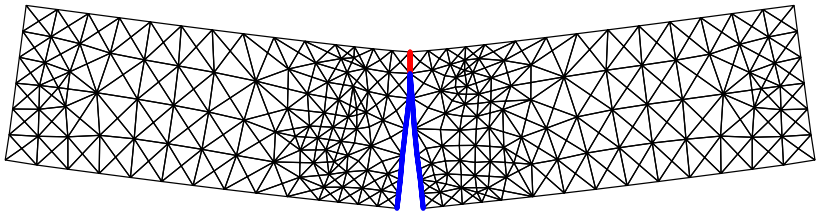

Figure 3.38: Three-point bending test deformation after solving the deformational and configurational problem (displacement magnification x100).

As Figure 3.38 depicts the failure is initialized at the center of the lower face of the beam. As expected, due to the symmetric setup the crack path propagates upwards. In Figures 3.37 and 3.38 the final state of the beam is depicted. They show that the iterative configurational process succeeds in orienting the crack along the correct vertical direction (Figure 3.37).

In the figures, red lines correspond to the zero-thickness interface elements which have not started cracking yet, and therefore, in the scheme implemented they have not triggered the process of moving nodes (although some of them may have changed orientation if they share nodes with an interface which has started cracking, such is the case of the top interface in Fig. 3.37 and 3.38). Blue lines correspond to the interface elements that have started cracking, and therefore configurational forces may have moved them to an optimal position.

The Figure 3.39 displays two load-displacement curves, the one obtained for the initial configuration fixed (mesh with the distorted crack trajectory), and the other one obtained after crack

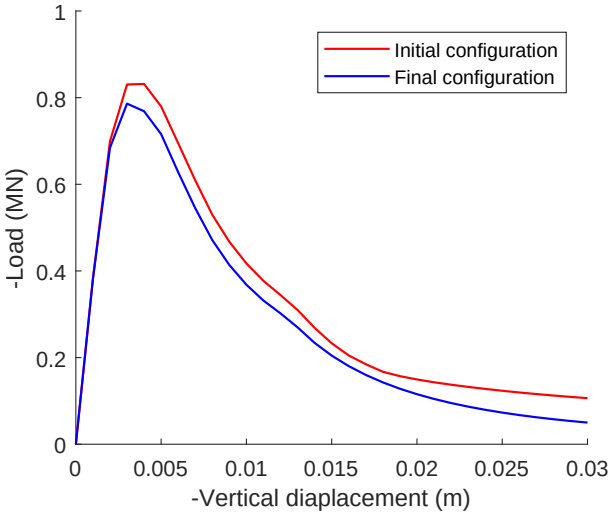

Figure 3.39: Three-point bending test load-displacement curves.

realignment (solving the FEM problem with the final configuration, mesh with the vertical crack path). As it could be expected, the load-displacement curve obtained from the final configuration exhibits a lower, more realistic peak and post-peak response. This is because in the final configuration interface elements are better oriented and therefore the crack initiates and propagates with lower applied load values.

3.9.3 Three-point beam bending test with two possible path

To explore the possibility of analysis of meshes containing more interface elements inserted than those corresponding to a single crack line, the previous example has been analyzed with the same conditions, properties and strategies but adding a second line of interfaces (constituting in practice an alternative crack path) as represented in Figure 3.40.

Figure 3.41 shows the final finite element mesh obtained at the end of the configurational iterations, after most of the interfaces along the main crack path have been realigned (in blue). Note the blue segment also at the bottom of the second crack path which finally does propagate, which reflects the fact that this second crack starts opening at the beginning in competition with the main crack, but then in the following increments it gets arrested while the main central crack continues propagation. This capability of representing competing cracks is a very positive and promising feature of the procedure developed.

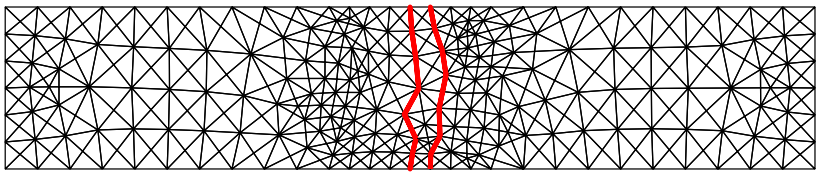

Figure 3.40: Initial configuration of beam bending realignment with two possible cracking paths.

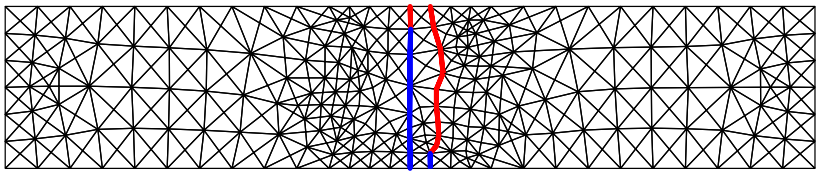

Figure 3.41: Final configuration of beam bending realignment with two possible cracking paths.

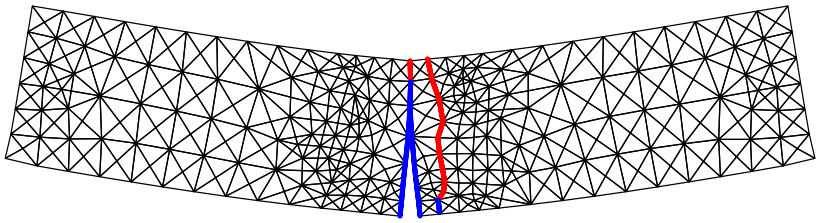

Figure 3.42: Three-point bending test deformation after solving the deformational and configurational problem (displacement magnification x50).

The resulting load-displacement curve obtained in the present calculation with two possible crack paths, turns out practically identical to the one obtained in previous section with only one crack path (Figure 3.39).

3.9.4 Eccentric three-point beam bending test with one possible path

This numerical example consists of an eccentric three-point bending beam, where the initial notch is not aligned vertically with the loading point of prescribed displacement at the middle of the top side of the beam García (1997); Xie and Gerstle (1995). The desired path must follow some inclined line connecting the notch tip with loading point, as depicted in Figure 3.43.

The beam is discretized into triangular quadratic elements and the initial path trajectory is defined by twelve interface elements that zig-zag from the tip of the notch until the loading point at middle top of the beam (Figure 3.44). Material properties of the continuum (assuming small strain and linear elasticity) are: Young's modulus of $E = 10000$MPa and Poisson's ratio $\nu = 0.2$,

normal and tangential stiffness $K_N = K_T = 10^5$MPa/m, friction angle $\tan\phi = 0.7°$, tensile strength $\chi = 3$MPa, cohesion $c = 9$MPa, sigma dilatation $\sigma_{dil} = 50$MPa and high values of energy mode I and IIa to simulate perfect plasticity ($G_f^I = 10^2$MPa·m, $G_f^{IIa} = 10^3$MPa·m) in order to facilitate convergence in this first attempt to model a possibly curved crack. The remaining options are similar to previous examples.

At the end of the calculation process, interface elements are reoriented replacing the unlikely zig-zag path to a smooth and slightly curved line trajectory (see Figures 3.45 and 3.46), where red lines represent the interface elements still not cracked and blue lines are the ones that have already cracked and therefore may have been moved to the optimal position by configurational forces.

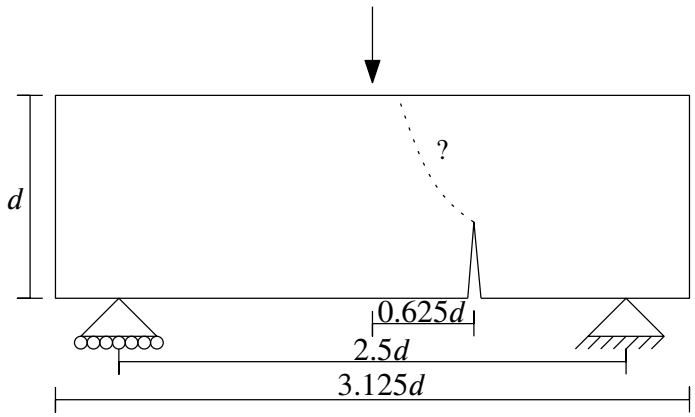

Figure 3.43: Boundary conditions of eccentric three-point bending test example assuming $d = 1$m.

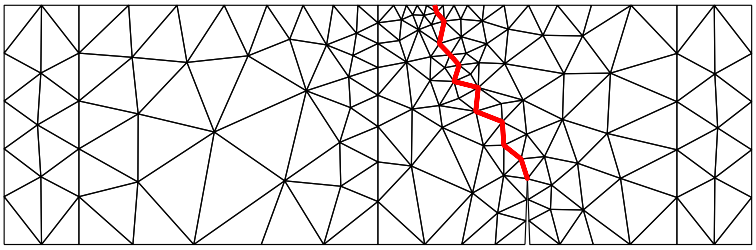

Figure 3.44: Initial configuration of eccentric three-point bending test example.

Load-displacement curves of Figure 3.47 show that solving the problem with the fixed geometry provided by the initial configuration leads to sensibly higher loads than using the mesh with the interfaces realigned. Loads turn out pretty high and always hardening due to the assumption of very high fracture energy used.

Additional calculations have been run with all parameters identical but the fracture energies, that have been given values of $G_f^I = 0.01$MPa·m and $G_f^I = 0.001$MPa·m, and in both cases

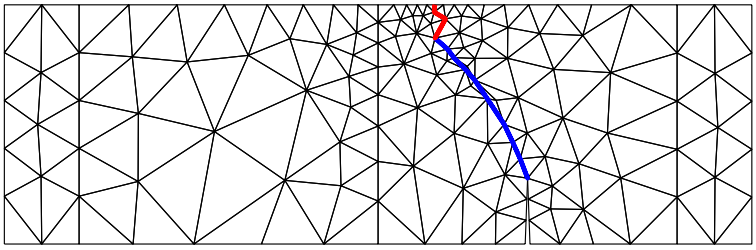

Figure 3.45: Final configuration of eccentric three-point bending test example.

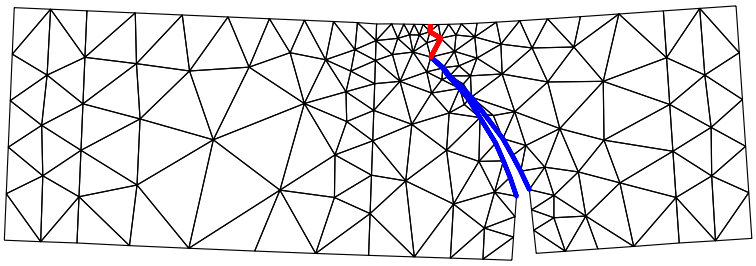

Figure 3.46: Eccentric three-point bending test deformation after solving the deformational and configurational problem (displacement magnification x10).

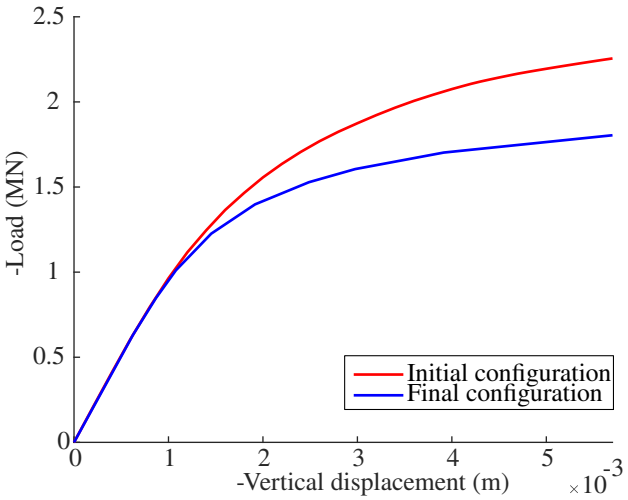

Figure 3.47: Eccentric three-point bending test load-displacement curves.

$G_f^{IIa} = 10G_f^I$. The results are depicted in Figures 3.48-3.51. In Figure 3.48 the final crack geometry and deformed shape of specimen are represented for the case with $G_f = 0.01$MPa·m , and in Figure 3.49 for $G_f = 0.001$MPa·m. These results look similar to the case of perfect plasticity (Fig. 3.46). However, the crack paths are not totally identical, as it can be seen in Figure 3.50, which shows that with perfect plasticity the crack trajectory near the tip follows a lower path, which turns out

progressively higher for lower values of G_f. Therefore, an interesting observation is that by means of the present approach one can evaluate the non-trivial influence of material parameters on crack trajectory.

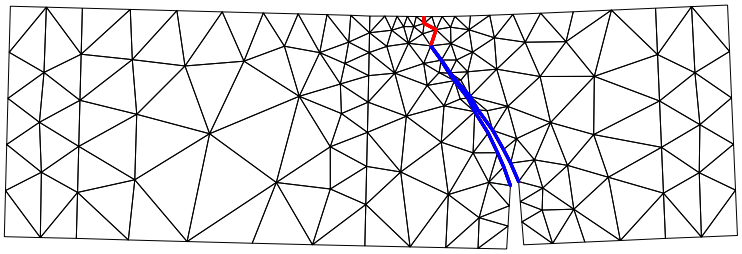

Figure 3.48: Eccentric three-point bending test deformation after solving the deformational and configurational problem with $G_f^I = 0.01$MPa·m and $G_f^{IIa} = 10G_f^I$ (displacement magnification x10).

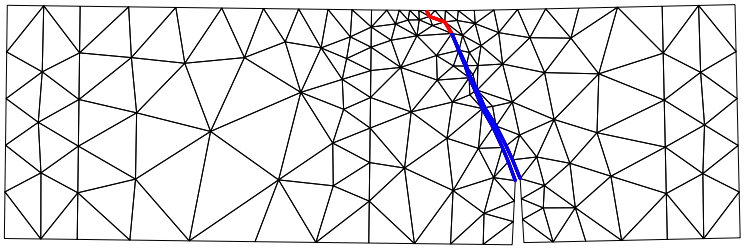

Figure 3.49: Eccentric three-point bending test deformation after solving the deformational and configurational problem with $G_f^I = 0.001$MPa·m and $G_f^{IIa} = 10G_f^I$ (displacement magnification x10).

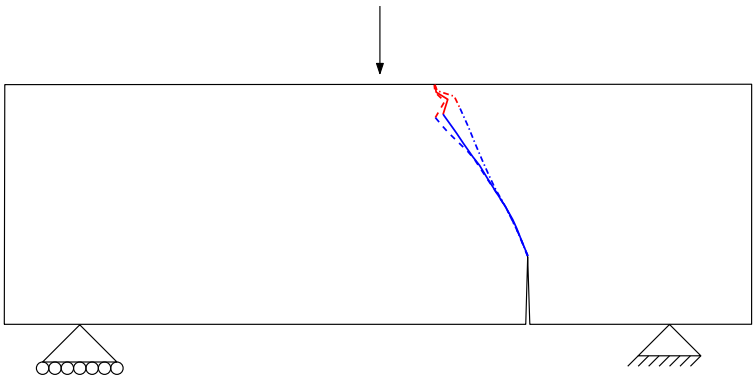

Figure 3.50: Comparison of final crack orientation depending on G_f values. Dashed line represents perfect plasticity crack path while solid line is obtained by $G_f^I = 0.01$MPa·m and $G_f^{IIa} = 10G_f^I$.

Finally, Figure 3.51 shows the load-displacement curves corresponding to each value of G_f and the final crack geometry (in blue), together with the curves that would have been obtained for each value of G_f by using the original crack geometry (no reorientation) (in red). As seen in the Figure, crack reorientation with the same G_f leads to lower peak load and lower peak deformations, which shows the benefit of the reorientation strategy implemented. On the other hand, the effects of changing G_f are also clear, with lower peaks and softening curves (more brittle) for lower G_f values, in contrast to the always increasing (hardening) curve obtained for perfect plasticity.

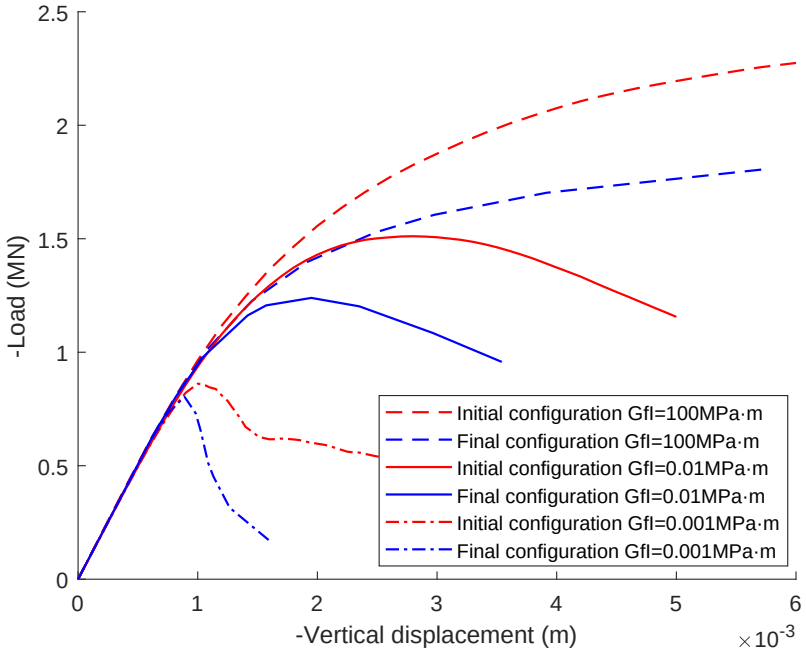

Figure 3.51: Eccentric three-point bending test load-displacement curves.

3.9.5 L-Shaped panel with one possible path

The fifth example consists of an inverted "L-shaped" panel represented in Fig. 3.52. The panel is fixed on the bottom side of the inverted "L" and is subject to a vertically ascending load at the cantilever end that creates an overall bending moment. As the result, the inner side of the "L" is subject to tensile stresses. As described by Winkler (2001), this type of panels usually fails due to a dominant crack that starts at the inner vertex and progresses towards the opposite lateral face with a relatively low angle. Other authors have developed similar experimental and numerical studies, e.g. Feist et al. (2004); Meschke and Dumstorff (2007).

Based on the proposed strategy, this L-Shaped panel is modeled by using the geometry and boundary conditions of Winkler (2001) (Figure 3.52). The panel has been discretized with quadratic triangles for the continuum (as depicted in Fig. 3.53a), and a line of interface elements has been inserted along a path zig-zagging along the expected crack trajectory, from the internal vertex of the structure to a point slightly higher on the right edge. Continuum material has been assumed linear elastic (small strain) with Young's modulus $E = 25850$MPa and Poisson's ratio $\nu = 0.18$. For interface elements, the constitutive parameter values are: normal and tangential stiffness $K_N = K_T = 10^8$MPa/m, friction angle $\tan\phi = 0.7°$, tensile strength $\chi = 2.7$MPa, cohesion $c = 15$MPa, sigma dilatation $\sigma_{dil} = 27$MPa, energy mode I $G_f^I = 9 \cdot 10^{-5}$MPa·m and energy mode IIa $G_f^{IIa} = 9 \cdot 10^{-4}$MPa·m.

Figure 3.53b displays the FE-mesh at the end of the calculation, after the reorientation of interface elements and relocation of nodes. In both diagrams of Fig. 3.53, the gray shaded area shows the scatter of the experimental results from Winkler (2001). In Fig 3.53b, red lines represent the interface elements which did not reach cracking and therefore were not moved directly in the direction of configurational forces (although they might have been reoriented if they were connected to a cracked element), and blue lines are the ones which have been reoriented to the optimal position. As seen in the figure, the final crack alignment exhibits a relatively smooth path (if compared with the original interface path), which falls within scatter of experimental results.

Figure 3.54 shows the same final configuration together with a magnification of displacements showing clearly the deformed shape of specimen and the opening of the crack.

Finally, Figure 3.55 shows the load-displacement curves resulting from the calculation, both with the original (in blue) as well as the re-oriented mesh (in red), together with the gray shaded area representing the scatter of experimental results (Winkler, 2001). It can be seen that, except for some minor drift in elastic initial stiffness, the results obtained after realignment fall well within scatter, while the ones obtained with the original mesh led to a clearly higher peak load and post-peak response.

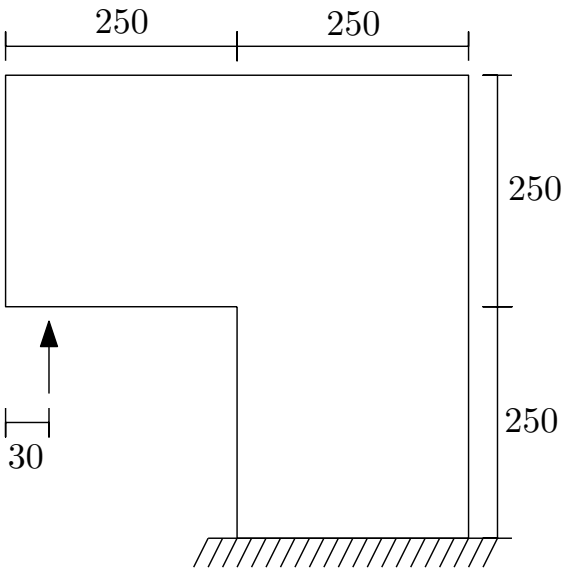

Figure 3.52: Geometry and boundary conditions of the L-Shaped panel

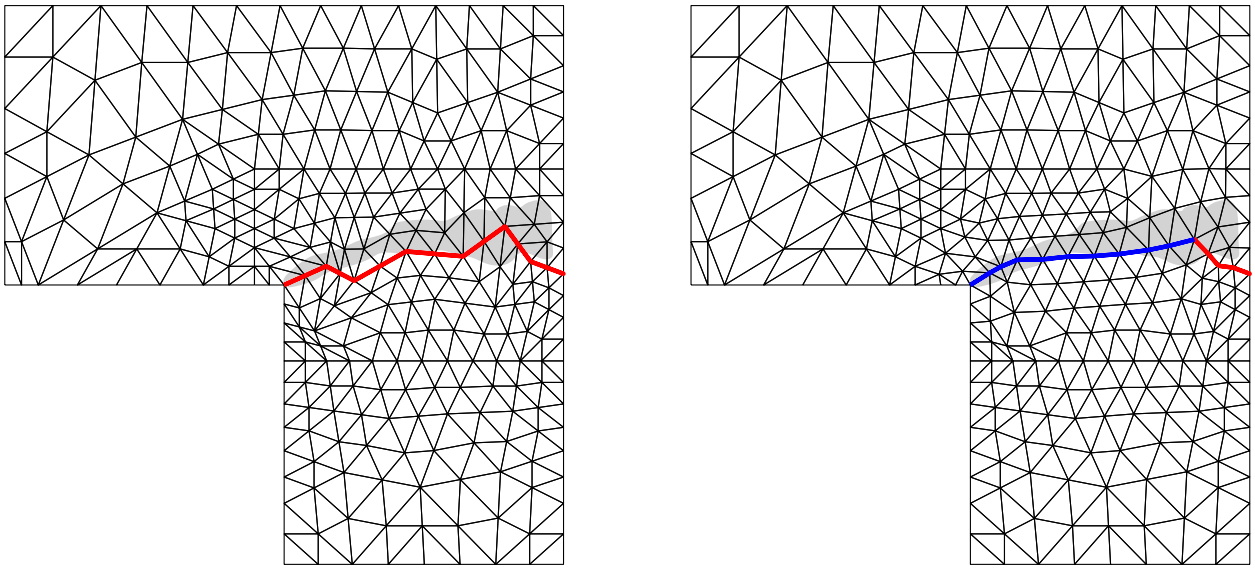

(a) **(b)**

Figure 3.53: (a) Initial mesh configuration of L-Shaped panel problem. (b) Final mesh configuration of L-Shaped panel problem.

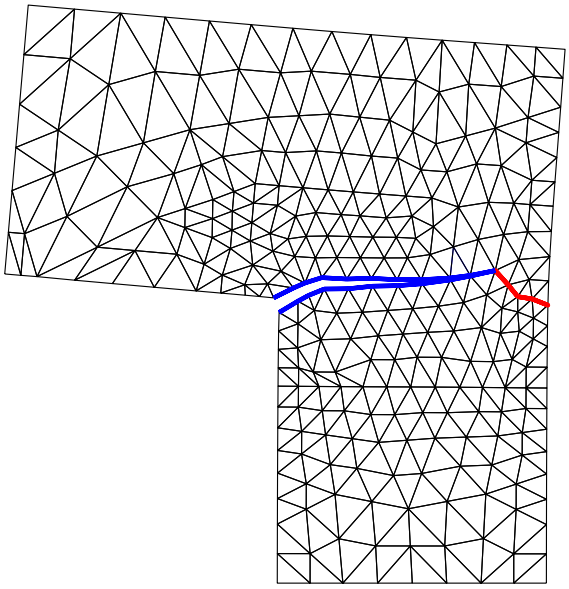

Figure 3.54: L-Shaped panel deformation after solving the deformational and configurational problem (displacement magnification x100).

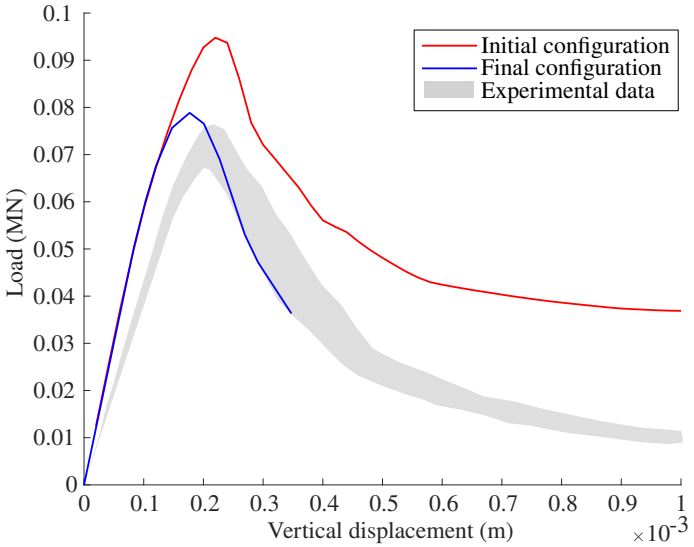

Figure 3.55: Load-displacement curves of L-Shaped panel problem.

3.9.6 Two notched beam with two possible paths

This example corresponds to the two-notch mixed-mode fracture beam test originally developed by Nooru-Mohamed and van Mier at TU-Delft (Nooru-Mohamed, 1992), and later extended in the work of Feist et al. (2004) and Zhu and Tang (2002). The specific geometry and parameters used in the present analysis have been extracted from Zhu and Tang (2002). Geometry and boundary conditions are depicted in Figure 3.56. This example has been chosen in order to verify the performance of the approach proposed in a case with simultaneous development of more than one non-consecutive cracks.

The beam is discretized with quadratic triangular continuum elements, and the mesh is a little finer in the zone of interest (central part of the beam between and around notches), see Fig. 3.57. From the experimental results of Zhu and Tang (2002) it is known that for these conditions two cracks are formed that start at the tip of the notch and grow towards the load/displacement application points. Consequently, two zig-zagging lines of interface elements have been pre-inserted along mesh lines connecting the top and bottom notches on each side of the beam ligament irregular paths have been selected to simulate the crack propagation (red lines in Figure 3.57).

The material model for the continuum is linear elasticity (small strain) with Young's modulus $E = 30000\text{MPa}$ and Poisson's ratio $\nu = 0.18$. The interface parameter values are: normal and tangential stiffness $K_N = K_T = 10^8\text{MPa/m}$, friction angle $\tan\phi = 0.7°$, tensile strength $\chi = 2.7\text{MPa}$, cohesion $c = 15\text{MPa}$, sigma dilatation $\sigma_{dil} = 27\text{MPa}$ and energy mode I and IIa $G_f^I = 1.1 \cdot 10^{-4}\text{MPa}\cdot\text{m}$ and $G_f^{IIa} = 1.1 \cdot 10^{-3}\text{MPa}\cdot\text{m}$.

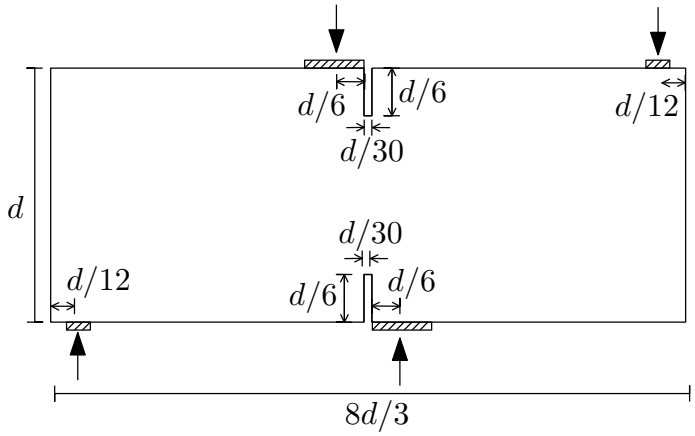

Figure 3.56: Boundary conditions of the two notched beam with $d = 150\text{mm}$.

During the iterations of the deformational/configurational analysis, the interface orientations

and locations are modified, and the resulting final mesh is shown in Figure 3.58. Same as in previous examples, the interface elements which have not reached cracking remain in red color, while blue lines correspond to those interface elements which have cracked and for which configurational forces have acted to getting them realigned. As seen, the interfaces have realigned nicely to configure a pair of smooth curved wing cracks which embrace a central bridge of solid material crossing the ligament from top left to bottom right, consistently with the kinematics of the prescribed displacements (Fig.3.59).

Figure 3.60 depicts the mesh evolution for each individual configurational step, so that progressive mesh reorientation may be appreciated. For each step of the process, only the zone of interest is represented. In this case, the realignment takes place along 13 configurational steps. At each step, the process involves the progressive relocation of the nodes that on one side belong to an opening interface element, and that at the same time are marked as configurationally free. During the iterations of a given configurational step more than one (non-consecutive) interface elements can reach the cracking condition and be selected to change their orientation. However, it is also possible that after the iterative process one or more of those interface elements initially selected would finally remain uncracked. In Figure 3.60, these interface elements are represented in orange. On the other hand, blue lines represent the interface elements that have reached their new fixed location driven by configurational forces. Finally, note that the surrounding continuum mesh (black lines) and some interface elements that have not reached cracking (in red or orange) may also modify their position, because they may be connected to a moving interface, or due to the mesh relaxation technique described in Section 3.7.2, which moves nodes around moving interfaces in order to make all elements in the area more regular.

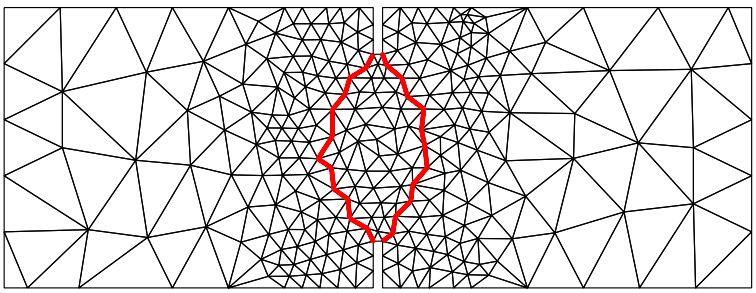

Figure 3.57: Initial configuration of the two notch beam example.

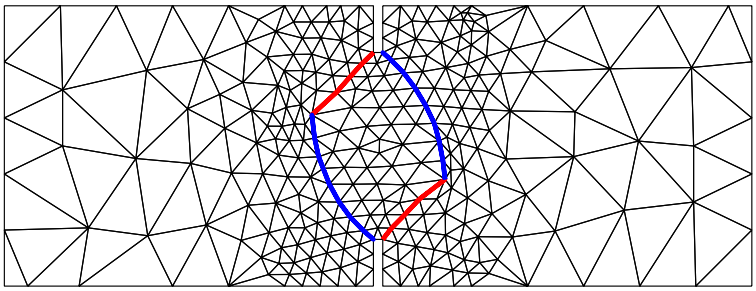

Figure 3.58: Final configuration of the two notch beam example.

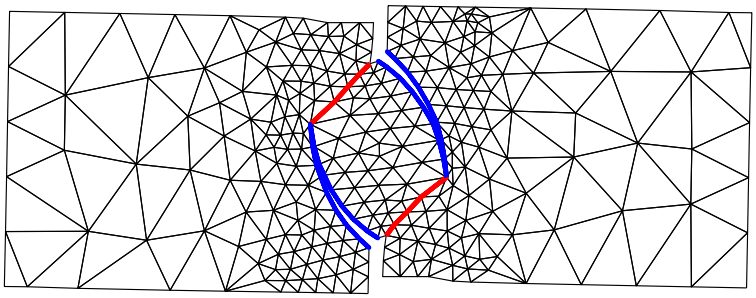

Figure 3.59: Two-notch beam deformation after solving the deformational and configurational problem (displacement magnification x100).

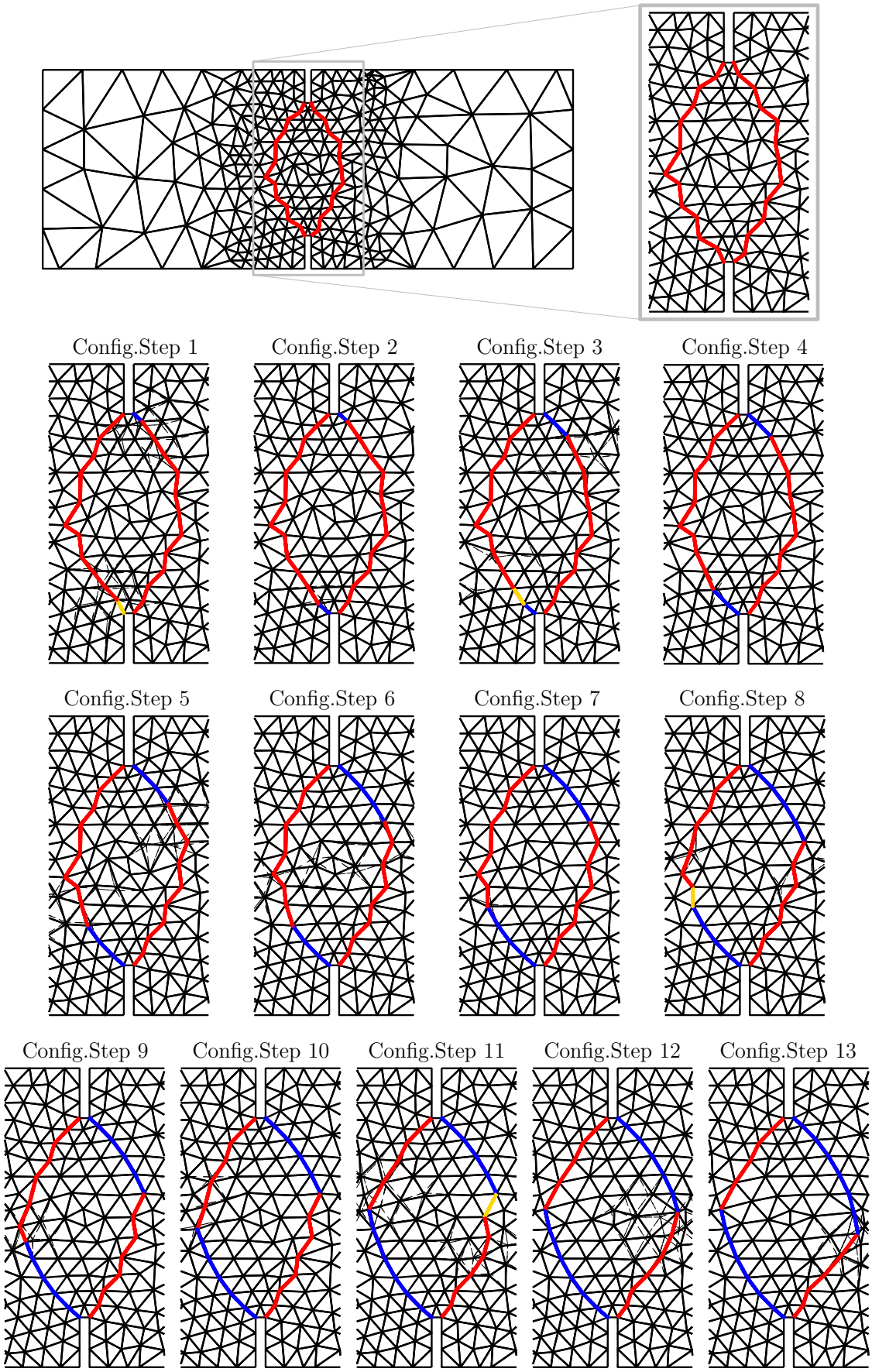

Figure 3.60: Geometric evolution of the two-notch beam during configurational iterations.

3.9.7 Three-point beam bending test with a wide zone of possible paths

All examples in previous sections contain only one or two lines of interface elements. With the iterative configurational process, these elements become aligned and to certain extent also move, but there is no possibility of cracks starting at any point of the mesh, or crack branching, coalescing, etc. In order to represent those phenomena, a zone of the mesh in which interface elements would be inserted along all (or a sufficient number) of mesh lines, would be needed. And this is precisely the purpose of this example, to explore the effect of the approach developed on a wider area of possible fractures in which the cracks would have the maximum freedom to start, develop, compete, get arrested, etc. To this end, the case of the three-point beam bending test Section 3.9.2 (see Figure 3.35) is considered again, with the same geometry, material parameters and boundary conditions already defined in that section.

The beam is discretized again into quadratic triangular continuum elements, and the novelty is that interface elements are pre-inserted along all mesh lines in a central section of the beam of length dimension similar to the beam width. The resulting finite element mesh is depicted in Figure 3.61, where red lines represent the pre-inserted zero-thickness interface elements.

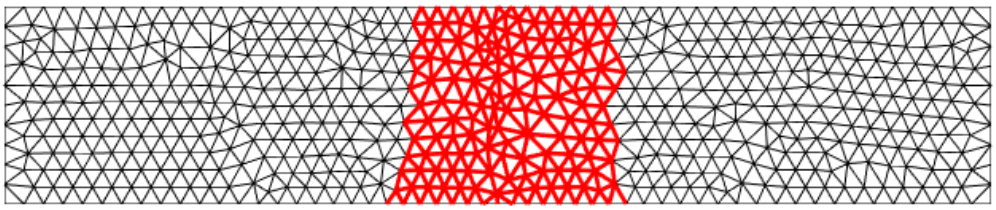

Figure 3.61: Initial mesh configuration of the three-point beam bending test example.

The configurational strategy used to change nodal location is again the "r-adaptivity method with length corrections" (strategy 3 described in Sec. 3.6.3) and the deformational iterative method is the indirect displacement control based on fracture dissipation described in Sec 3.5.

Figure 3.62 shows the results of the calculation after prescribing a top displacement of 2.5mm, with blue lines indicating the interface elements that have been realigned during the calculation. Fig. 3.63 shows the same results on a deformed mesh, with a detailed view of the central part of the beam where all cracks develop.

In this example, it could be expected that central interface elements would develop a single fracture similar to the one obtained in the same beam example with only one or two crack lines, Sections 3.9.2 and 3.9.3. However, Figures 3.62 and 3.63 show various competing cracks developing near the beam center. The main one certainly is the one at the beam center as expected, but also two

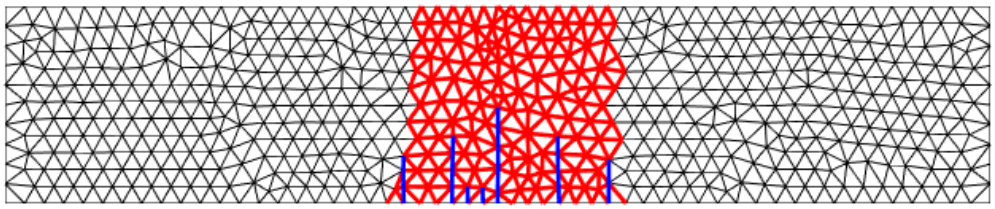

Figure 3.62: Final mesh configuration of the three-point beam bending test example.

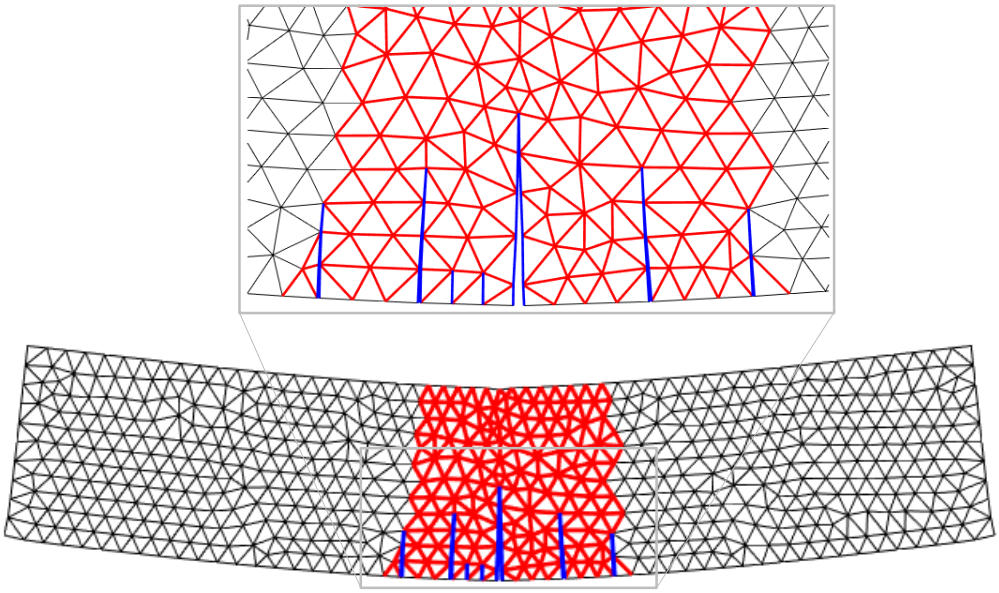

Figure 3.63: Three-point bending test deformation after solving the deformational and configurational problem (displacement magnification x100).

more have developed on each side which are progressively shorter but nevertheless comparable in length. The obvious discussion is whether these cracks are realistic, or could be spurious secondary cracking due to the numerical strategy.

Spurious secondary cracking could appear when the main developing crack finds a mesh line not well aligned with the crack direction which "blocks" its progression. Then, external load has to be increased beyond physical values to get a crack on that inclined line started, before the realignment process is triggered and the load decreases again to realistic values. If no secondary cracking starts during the interval of artificially higher load (either because there is a single zig-zagging crack trajectory as in previous sections, or because the other interfaces pre-inserted do not reach their opening stresses), the fact that loads have gone spuriously higher during the calculation, will leave no trace in the results. This is because each time the configurational process is activated

and nodes are moved, the iterative scheme (described in Sec.3.8 and depicted in Fig.3.23) brings the calculation back to the last configurationally converged state, so basically the calculation is restarted from that previous point with the better crack orientation.

However, if secondary cracking is triggered while the loads are artificially higher, the current scheme (with return to the last configurationally converged state) would "fix" those unrealistic cracks, because basically the restart of the calculation should have been made to an earlier point before the secondary spurious cracks would have started.

Whether the secondary cracks observed in Figs. 3.61 and 3.62 are physical cracks or a spurious numerical effect, may be clarified by a simple direct calculation of the mesh of Fig. 3.61, that is with all the cracks (main one and secondary ones) well aligned. This has been done to the same level of prescribed displacement at the loading point, of 2.5mm with the results shown in Fig. 3.64, which depicts practically the same cracking scheme as in the configurational calculation. This example therefore confirms that at least in this case the scheme proposed is capable of representing simultaneous competing cracks within a context of systematic pre-insertion of interfaces along all mesh lines.

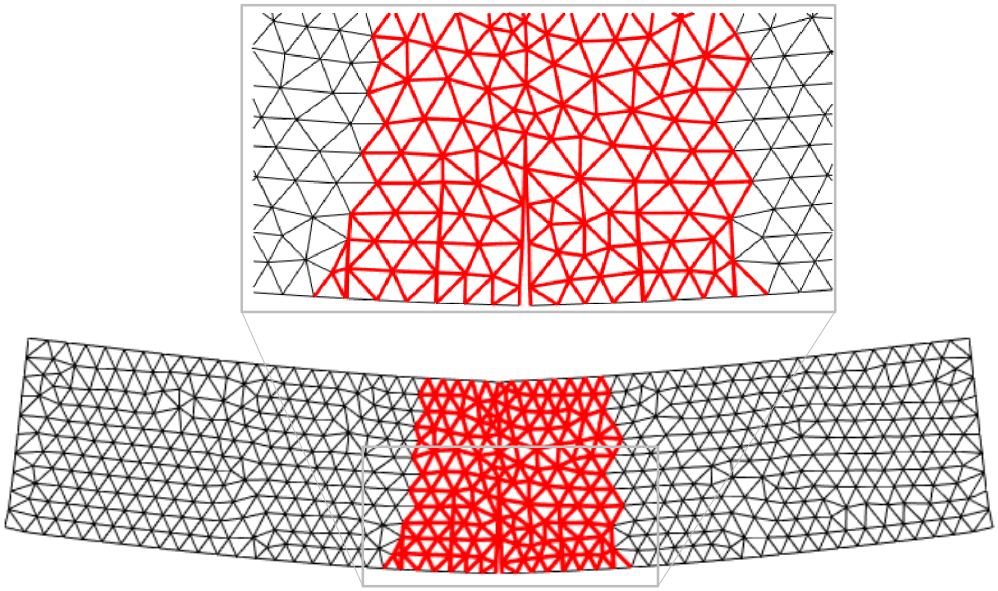

Figure 3.64: Deformed mesh and cracking obtained in direct calculation using final configuration (displacement magnification x100).

3.10 Concluding remarks

In this chapter a method has been presented to evaluate the crack propagation with non-preestablished paths by combining traditional zero-thickness interface elements (FEM+z approach) with the contribution of configurational mechanics. FEM+z has been extensively used in the past to describe the behavior of fractures with a fixed position, while configurational mechanics provides information on how to move nodes to reorient interface elements when they start cracking, in order to approach a global energy minimum.

In the FEM context, the gradient of the global structural/domain energy w.r.t. nodal location is known as configurational force vector or material force vector. This vector indicates the direction in which the nodes have to move to get the steepest variation of the global energy.

The procedure to move nodes according to configurational forces may become very complicated and potentially unmanageable when too many nodes are moved at the same time. Also, it may get polluted by "configurational noise" coming from the oscillation of total energy with nodal positions, which is inevitably associated to the intrinsic FE discretization error. For that reason, a selective methodology of node configurational release has been developed. It consists of selecting the crack tip nodes when the corresponding interface starts to open, and convert them to configurationally free nodes. In this way, the configurational forces will have greater physical contribution and less effect coming from the mesh discretization error. In addition, to reduce the discretization error, two solutions have been proposed: (a) Configurational parameterization and (b) use of FE-meshes with quadratic order elements. In this chapter, both strategies have been demonstrated with examples of verification.

Several techniques to achieve the FEM solution on the equilibrium path were presented in literature such as Newton-Raphson or Arc-Length. These techniques are based on displacement control, so a new Indirect Displacement Control (IDC) strategy based on energy dissipation has been presented. This strategy has been very helpful because by controlling energy dissipation instead of displacement, the progressive opening of the interface elements can be controlled better and it is easier to limit interface opening to one consecutive element at a time.

Finally, the approach developed has been applied to classical examples for which the final fracture position is known. By means of this approach, the propagation trajectories have been well reproduced. Three-point bending examples show that, although starting with different configurations (one path/two paths/full zone of interface elements), the dominant fracture ends up being totally vertical and aligned with the imposed load or displacement. The examples of eccentric three-point bending test, L-Shaped panel and mixed mode fracture tests present more complex

trajectories that have been compared with experimental tests of different authors and approach also seems to lead to realistic crack paths.

In conclusion, the approach of FEM+z combined with the theory of configurational mechanics seems a promising method for the description of cracking along non-preestablished paths, at least in the type of problems analyzed. The main advantages of the proposed method are: first, it incorporates the very fundamental assumption that fractures are formed in the minimum energy release direction; and second, it reduces mesh dependence in the sense of excessive crack roughness due to mesh line orientation because nodes from initial configuration are rearranged and mesh lines reoriented to allow most dissipative cracking. As for any new technique in its initial stage of development, there are many aspects pending for future research, such as for instance verifying its effectiveness in more complex cases with multiple fractures or possible trajectories of the branching or bridging type, involving not only tensile-dominated cracking but also shear-compression cracking, or extension to 3D.

Chapter 4

Summary, conclusions and future research

4.1 Summary and Conclusions

This thesis main objective was the numerical description of discrete cracks without pre-established path. To that end, attention has been payed first to methods for representing discrete cracks with pre-established (or potential) paths along mesh lines (chapter 2), and later on how to extend those methods to cracking along non-preestablished paths (chapter 3).

Regarding pre-fixed crack path (chapter 2), one traditional approach is the use of zero-thickness interface elements (also known as cohesive elements) which are inserted along mesh lines in the context of the standard Finite Element Method (FEM+z). Although a wide variety of problems may be accurately solved in this manner, the FEM+z approach exhibits some disadvantages, a significant one being that interface elements can only be inserted along mesh lines, and therefore their potential crack trajectories and therefore their capability to represent realistic crack paths is very dependent on the original mesh layout.

A second more recent approach to represent individual cracks or discontinuities is the eXtended Finite Element Method (XFEM), which includes the independent definition of the continuum mesh on one side, and the discontinuities on the other (usually introduced via Level Set function). The basic concept of XFEM is to enrich the displacement field of the continuum elements, by defining extra nodal variables for those elements crossed by the discontinuity. The extra variables are shared by adjacent elements, in this way guarantying "continuity of the discontinuity", something not satisfied by a number other methods in the literature. In most XFEM implementations, the

extra degrees of freedom correspond to the displacement "jump", and the interpolation functions is the natural interpolation.

In this Thesis, the two approaches mentioned above (FEM+z and XFEM) have been described and implemented first for cracks or discontinuities of pre-established location. FEM+z is a standard approach and therefore it is only briefly described in the corresponding chapter. XFEM, however, has been developed in more detail, with a formulation that includes some non-standard features and novelties. First, as extra nodal variables, the fictitious "overhang" displacements across the discontinuity have been preferred over the displacement jumps themselves, because of a clearer physical meaning and easier boundary conditions. In addition, after implementing the classical formulation based on natural interpolation functions, severe oscillations were observed in the results. As shown in Appendix D, it was found that using natural interpolation on continuum elements may be responsible, at least in part, of not representing smoothly the solution when the discontinuity is not parallel to the element faces. As a remedy, a double interpolation scheme has been developed and implemented. This scheme has been shown to the lead to a theoretical equivalence with the FEM+z approach, and also to yield much smoother numerical results for discontinuities skew to the mesh.

Finally regarding XFEM, the problem has been tackled of oscillations due to discontinuities crossing the mesh too close to a node. To remedy this effect, the strategy has been proposed which consists of slightly moving the node affected onto the discontinuity itself. This creates especial collapsed elements that need to be identified and treated separately, but eliminates the oscillation problem.

The resulting XFEM formulation has been implemented in Matlab code and used to solve several verification examples: an elastic beam bending problem is solved using five different meshes to analyze the influence of element type (triangular/quadrangular), mesh structure (structured/unstructured) and stiffness values, and to compare to other literature results. Conclusions are that all results for quadrangular elements seem much less sensitive to the increase of stiffness coefficient, and similar accuracies are obtained with much lower density of elements as compared to linear triangles, provided the strategy of moving close nodes the discontinuity itself is applied. The second example consist on evaluating the stress field on a plane on a tunnel cross-section which distribution is well described by Kirsch's solution. It can be seen that the XFEM results are in general very close to the analytical solution and punctual oscillations disappears applying the rearrangement strategy where the discontinuity lies very close to a node. A third example shows applicability of the formulation in combination with a non-linear material model for the

discontinuity (in this case a fracture-based elasto-plastic constitutive law), leading to the expected results.

The second part of the thesis (chapter 3) deals with the development of cracks or discontinuities with no pre-established path. In general terms, such model has to determine not only when a crack propagates but also in which direction. The first point (when) will be addressed via fracture-based constitutive model for the crack/discontinuity. The model employed is well established, has been well tested, and has the structure of elasto-plastic model driven by energy consumption, therefore it naturally includes the concept of fracture energies in tension (mode I) and shear-compression (mode IIa). The second point (in what direction), requires some new developments based on Configurational Mechanics. The original intention of this thesis was to apply such new developments to "move" discontinuities in the two approaches analyzed in chapter 2: FEM+z and XFEM. Strict time constraints linked to new academic regulations, however, have prevented that, and application of configurational mechanics to XFEM has been left out of the scope of the thesis, for future research. Therefore, the FEM+z approach has been combined with configurational mechanics to provide the possibility of crack reorientation. The core concept is that of configurational forces or material forces. These forces, defined as derivatives of the elastic energy of the structure or domain with respect to the original nodal coordinates, are calculated at the end of a standard FE analysis as a post-processing step. These forces indicate the direction in which mesh nodes would have to be moved in order to cause the steepest descent in overall elastic energy. This leads a node relocation process which is combined iteratively with the standard deformational analysis.

The theory of configurational mechanics and configurational forces has been developed in the literature in the context of large strain formulation. This is why the chapter includes a summary of this theory before describing the configurational mechanics concepts and equations, and the application to finite elements in large and small strain. Direct derivatives of the finite element expression of the elastic energy, lead to the existing known expressions of the configurational forces. To the knowledge of the author, these direct derivations were not available in the literature, and provide an engineering insight to a subject so far restricted to a small elite of advanced academic mechanics experts.

The proposed method is the result of combining deformational and configurational techniques. For each configurational step (determined nodal coordinates) a deformational increment is solved, when deformational convergence is reached nodal configuration is evaluated and if it is correct next deformational increment is applied, if not, the configuration must be modified and the deformational increment repeated. Several aspects of the implementation require specific numerical

procedures. In the crack propagation examples presented, the change of node location on the basis of configurational forces, is done by means of the "modified r-adaptivity method", a strategy of node rearrangement through small steps (in general $< 1°$) into a more favorable propagation position.

The evolution process is done through a selective and gradual release of the nodes that form the crack tip, in this case constituted by newly cracking interface elements. Another key concept to this development is the "noise" in the values of elastic energy, which is caused by discretization errors implicit to FE method itself. If an internal node of a FE mesh changes coordinate, discretization errors change, stresses, displacements etc. also change, and so does elastic energy. If the mesh is fine enough, these changes should be negligible in comparison to energy changes due to a change in physical dimensions, crack extension, etc. But FE configurational forces include a mix of both, and because of this, two solutions are considered to reduce the discretization error: first a configurational parameterization, and second, the use of quadratic elements and mesh relaxation strategy. Both solutions have been independently applied to different examples and both improve the overall solution by reducing the discretization error.

A new iterative strategy has been proposed and implemented to solve the deformational increments; it is an Indirect Displacement Control Method (IDC) with a control based on fracture energy consumption. This method has some advantages in this case w.r.t existing methods such as Newton-Raphson or Arc-Length techniques, since it is based on energy dissipation and therefore it makes it easier to ensure a progressive opening of the fracture with only one consecutive interface element opening at a time.

The overall scheme developed is complemented with some auxiliary procedures from the literature, a mesh relaxation technique (to recover good shape triangles after interface reorientation) and transport of the displacement values to any node which changes coordinates.

Finally, several verification examples have been solved in which the trajectory of the propagation is known a priori. In particular, three-point bending test, eccentric three-point bending test, L-shaped panel and mixed mode fracture tests have been compared with experimental tests of different authors and have been successfully solved giving rise to the expected results.

4.2 Future Research

The development of the present thesis has opened many new possibilities of future research; only the main ones are mentioned in the following:

Application of configurational mechanics to XFEM

To combine the proposed XFEM with Configuratonal Mechanics in order to really represent cracks and discontinuities of non-preestablished path. It has been mentioned that this was an original objective, that later had to be postponed due time constraints In the literature there are articles on the efficiency of XFEM to describe the evolution of fractures although few article has been found that precisely combines concepts of configurational mechanics and XFEM (Larsson and Fagerström, 2005; Glaser and Steinmann, 2007).

Parametrization technique with quadratic elements, and other code improvements

In Section 3.7 two strategies to reduce the discretization error have been presented, both strategies are actually independently implemented. Therefore, a short-term future line is to combine quadratic elements, mesh relaxation and parametrization in such a way that discretization error decreases and physical effects become more relevant.

Another aspect of the algorithm that could be improved, is to what step the calculation is returned when one or more interface elements have been configurationally reoriented. In Sec. 3.8 (code structure) and 3.9.2 (last example with competing cracks) it is explained that once elements have been reoriented, the calculation is sent back to the previous configurationally converged state, technique that requires only to store and update that previously converged state. It was also explained that in the case of that example this strategy was shown to give the right result, but it was not guaranteed to be always correct. A more general algorithm would imply to store all previously converged configurational steps, and check the load factor for each of them to identify the correct step to go back to, and then start calculation from that one (rather than always from the last one as currently implemented).

Proposed FEM+z with configurational mechanics applied in multi-crack examples

It can be interesting to reproduce real examples of multiple fractures to check the effectiveness of the r-adaptivity method with length control. In the examples run so far, this has been a simple and effective method of changing the nodal position while maintaining a regular geometry. However, some particular cases remain unresolved, e.g. the simulation of two symmetrical cracks that start from the same point. As it is currently implemented, these interface elements would be considered as

consecutive joints and would enter to an endless loop to divide the dissipation constrain. Therefore, it is still pending to develop a strategy of nodal rearrangement to describe crack bifurcation and other special cases.

Extension of FEM+z with configurational mechanics to coupled formulation

Extension of the current (mechanical only) FEM+z formulation with configurational Mechanics-based interface reorientation, to the HM coupled context, and application of the code to relevant problems such as geometry of hydraulic fractures.

Extension to 3D

The strategies presented in this thesis have been implemented in 2D. Extension to 3D seems possible since the concepts used are general. However, many details of strategies should be adapted and extended to the more general 3D context.

References

Alfaiate, J., Simone, A., and Sluys, L. J. (2003). Non-homogeneous displacement jumps in strong embedded discontinuities. *International Journal of Solids and Structures*, 40(21):5799–5817.

Areias, P. M. and Belytschko, T. (2005). Analysis of three-dimensional crack initiation and propagation using the extended finite element method. *International journal for numerical methods in engineering*, 63(5):760–788.

Babuška, I., Caloz, G., and Osborn, J. E. (1994). Special finite element methods for a class of second order elliptic problems with rough coeficients. *SIAM J Numerical Analysis*, 31(4):745–981.

Babuška, I. and Melenk, J. (1997). The partition of unity method. *International journal for numerical methods in engineering*, 40(4):727–758.

Baines, M. J. (1994). *Moving finite elements*. Oxford University Press, Inc.

Barenblatt, G. I. (1962). The mathematical theory of equilibrium cracks in brittle fracture. *Advances in applied mechanics*, 7:55–129.

Bažant, Z. P., Gettu, R., and Kazemi, M. T. (1991). Identification of nonlinear fracture properties from size effect tests and structural analysis based on geometry-dependent R-curves. *International Journal of Rock Mechanics and Mining Sciences & Geomechanics Abstracts*, 28:43–51.

Bažant, Z. P. and Oh, B. H. (1983). Crack band theory for fracture of concrete. *Matériaux et construction*, 16:155–177.

Belytschko, T. and Black, T. (1999). Elastic crack growth in finite elements with minimal remeshing. *International journal for numerical methods in engineering*, 45(5):601–620.

Belytschko, T. and Gracie, R. (2007). On XFEM applications to dislocations and interfaces. *International Journal of Plasticity*, 23(10):1721–1738.

Belytschko, T., Gracie, R., and Ventura, G. (2009). A review of extended/generalized finite element methods for material modeling. *Modelling and Simulation in Materials Science and Engineering*, 17(4).

Belytschko, T., Krongauz, Y., Organ, D., Fleming, M., and Krysl, P. (1996). Meshless methods: an overview and recent developments. *Computer methods in applied mechanics and engineering*, 139(1-4):3–47.

Belytschko, T., Parimi, C., Moës, N., Sukumar, N., and Usui, S. (2003). Structured extended finite element methods for solids defined by implicit surfaces. *International journal for numerical methods in engineering*, 56(4):609–635.

Borja, R. I. (2008). Assumed enhanced strain and the extended finite element methods: A unification of concepts. *Computer Methods in Applied Mechanics and Engineering*, 197(33-40):2789–2803.

Bouchard, P. O., Bay, F., Chastel, Y., and Tovena, I. (2000). Crack propagation modelling using an advanced remeshing technique. *Computer methods in applied mechanics and engineering*, 189(3):723–742.

Caballero, A. (2005). *3D meso-mechanical numerical analysis of concrete fracture using interface elements*. PhD thesis, Universitat Politècnica de Catalunya (UPC), Barcelona.

Caballero, A., López, C. M., and Carol, I. (2006). 3D meso-structural analysis of concrete specimens under uniaxial tension. *Computer Methods in Applied Mechanics and Engineering*, 195(52):7182–7195.

Caballero, A., Willam, K., and Carol, I. (2008a). Consistent tangent formulation for 3D interface modelling of cracking/fracture in quasi-brittle materials. *Computer Methods in Applied Mechanics and Engineering*, 197:2804—2822.

Caballero, A., William, K. J., and Carol, I. (2008b). Consistent tangent formulation for 3D interface modeling of cracking/fracture in quasi-brittle materials. *Computer methods in applied mechanics and engineering*, 197(33):2804–2822.

Camacho, G. T. and Ortiz, M. (1996). Computational modelling of impact damage in brittle materials. *International Journal of solids and structures*, 33(20-22):2899–2938.

Carlson, N. N. and Miller, K. (1998). Design and application of a gradient-weighted moving finite element code I: in one dimension. *SIAM Journal on Scientific Computing*, 19(3):728–765.

Carol, I. and López, C. M. (1998). Fracture-based interface model: theory, implementation and aplications. *Computational Mechanics*. S. Idelsohn, E. Oñate and E. Dvorkin (Eds). CIMNE, Barcelona.

Carol, I., Prat, P., and López, C. M. (1997). Normal/shear cracking model: application to discrete crack analysis. *Journal of engineering mechanics*, 123(8):765–773.

Chen, L., Rabczuk, T., Bordas, S. P., Liu, G. R., Zeng, K. Y., and Kerfriden, P. (2012). Extended finite element method with edge-based strain smoothing (ESM-XFEM) for linear elastic crack growth. *Computer Methods in Applied Mechanics and Engineering*, pages 250–265.

Cherepanov, G. P. (1979). *Mechanics of Brittle Fracture*. McGraw-Hill, New York, NY (USA).

Choi, Y. J., Hulsen, M. A., and Meijer, H. E. (2012). Simulation of the flow of a viscoelastic fluid around a stationary cylinder using an extended finite element method. *Computers and Fluids*, 57:183–194.

Ciancio, D., Carol, I., and Cuomo, M. (2006). On inter-element forces in the FEM-displacement formulation, and implications for stress recovery. *International journal for numerical methods in engineering*, 66(3):502–528.

Ciancio, D., Carol, I., and Cuomo, M. (2013). A method for the calculation of inter-element stresses in 3D. *Computer Methods in Applied Mechanics and Engineering*, 254:222–237.

Crisfield, M. (1991). *Non-linear finite element analysis of solids and structures*, volume 1, chapter 6. John Wiley and Sons.

Crusat, L., Carol, I., and Garolera, D. (2018). XFEM formulation with sub-interpolation, and equivalence to zero-thickness interface elements. *International Journal for Numerical and Analytical Methods in Geomechanics*. DOI: 10.1002/nag.2853.

Das, K. C., Ausas, R., Carol, I., Rodrigues, E., Sandha, S. S., Vargas, P. E., González, N. A., Segura, J. M., Lakshmikantha, M. R., and Mello, U. T. (2015a). Discrete Modeling of Multiple. Discontinuities in Rock Mass using XFEM. In *Proc. 49th US Rock Mechanics/Geomechanics Symposium, American Rock Mechanics Association (ARMA)*, San Francisco, CA (USA).

Das, K. C., Ausas, R. F., Segura, J. M., Narang, A., Rodrigues, E. R., Carol, I., Lakshmikantha, M. R., and Mello, U. T. (2015b). Efem vs. XFEM: A Comparative Study for Modeling Strong Discontinuity in Geomechanics. In *13th ISRM International Congress of Rock Mechanics. International Society for Rock Mechanics and Rock Engineering.*

Das, K. C., Sandha, S. S., Carol, I., Vargas, P. E., González, N. A., Rodrigues, E., Segura, J. M., Lakshmikantha, M. R., and Mello, U. (2016a). Multiple intersecting cohesive discontinuities in 3D eservoir Geomechanics. In *Proc. 50th US Rock Mechanics/Geomechanics Symposium, American Rock Mechanics Association (ARMA)*, Houston, TX (USA).

Das, K. C., Sandha, S. S., Rodrigues, E., Mello, U., Carol, I., Vargas, P. E., González, N. A., Segura, J. M., and Lakshmikantha, M. R. (2016b). *Modeling of discrete intersecting discontinuities in rock mass using XFEM/level set approach.* Energy Geotechnics, London.

de Borst, R. (2002). Fracture in quasi-brittle materials: a review of continuum damaged-based approaches. *Engineering Fracture Mechanics*, 69:95–112.

de Borst, R., Pamin, J., Peerlings, R., and Sluys, L. (1995). On gradient-enhanced damage and plasti-city models for failure in quasi-brittle and frictional materials. *Computational Mechanics*, 17:130–141.

de Borst, R., Remmers, J., Needleman, A., and Abellan, M. (2004). Discrete vs smeared crack models for concrete fracture: bridging the gap. *International Journal for Numerical and Analytical Methods in Geomechanics*, 28:583–607.

Denzer, R., Barth, F. J., and Steinmann, P. (2003). Studies in elastic fracture mechanics based on the material force method. *International journal for numerical methods in engineering*, 58(12):1817–1835.

Desai, C. S., Zaman, M. M., Lightner, J. G., and Siriwardane, H. J. (1984). Thin-layer element for interfaces and joints. *International Journal for Numerical and Analytical Methods in Geomechanics*, 8(1):19–43.

Duarte, C. A., Babuška, I., and Oden, J. T. (2000). Generalized finite element methods for three-dimensional structural mechanics problems. *Computers and Structures*, 77(2):215–232.

Duarte, C. A. and Oden, J. T. (1996). An hp adaptive method using clouds. *Computer methods in applied mechanics and engineering*, 139:237–262.

Dugdale, D. S. (1960). Yielding of steel sheets containing slits. *Journal of the Mechanics and Physics of Solids*, 8(2):100–104.

Dumstorff, P. and Meschke, G. (2007). Crack propagation criteria in the framework of X-FEM-based structural analyses. *International Journal for Numerical and Analytical Methods in Geomechanics*, 31(2):239–259.

Dvorkin, E. N., Cuitiño, A. M., and Gioia, G. (1990). Finite elements with displacement interpolated embedded localization lines insensitive to mesh size and distortions. *International Journal for Numerical Methods in Engineering*, 30(3):541–564.

Erdogan, F. and Sih, G. C. (1963). On the crack extension in plates under plane loading and transverse shear. *Journal of basic engineering*, 85(4):519–525.

Eshelby, J. D. (1951). The force on an elastic singularity. *Philosophical Transactions of the Royal Society of London A: Mathematical, Physical and Engineering Sciences*, 244(877):87–112.

Eshelby, J. D. (1975). The elastic energy-momentum tensor. *Journal of Elasticity*, 5(3-4):321–335.

Eshelby, J. D. (1999). Energy relations and the energy-momentum tensor in continuum mechanics. *In fundamental contributions to the continuum theory of evolving phase interfaces in solids*, pages 82–119.

Feist, C., Kerber, W., Lehar, H., and Hofstetter, G. (2004). A comparative study of numerical models for concrete cracking. *European Congress on Computational Methods in Applied Sciences and Engineering (ECCOMAS)*.

Frey, W. H. and Field, D. A. (1991). Mesh relaxation: a new technique for improving triangulations. *International Journal for Numerical Methods in Engineering*, 31(6):1121–1133.

Fries, T. P. and Belytschko, T. (2006). The intrinsic XFEM: a method for arbitrary discontinuities without additional unknowns. *International journal for numerical methods in engineering*, 68(13):1358–1385.

Fries, T. P. and Belytschko, T. (2010). The extended/generalized finite element method: an overview of the method and its applications. *International Journal for Numerical Methods in Engineering*, 84(3):253–304.

García, V. O. (1997). *Estudio de la fractura en modo mixto de los materiales cuasifrágiles: aplicación al hormigón convencional y al hormigón de alta resistencia.* PhD thesis, Universitat Politècnica de Catalunya (UPC), Barcelona.

Garolera, D. (2017). *Zero-thickness interface elements in petroleum geomechanics: sand production and hydraulic fracture.* PhD thesis, Universitat Politècnica de Catalunya (UPC), Barcelona.

Garolera, D., López, C. M., Carol, I., and Papanastasiou, P. (2005). Micromechanical analysis of the rock sanding problem. *Journal of the Mechanical Behavior of Materials*, 16(1-2):45–54.

Gelinas, R. J., Doss, S. K., and Miller, K. (1981). The moving finite element method: applications to general partial differential equations with multiple large gradients. *Journal of Computational Physics*, pages 202–249.

Gens, A., Carol, I., and Alonso., E. E. (1989). An interface element formulation for the analysis of soil-reinforcement interaction. *Computers and Geotechnics*, 7(1-2):133–151.

Gens, A., Carol, I., and Alonso, E. E. (1995). Rock joints: FEM implementation and applications. *Studies in Applied Mechanics*, 42:395–320.

Ghaboussi, J., Wilson, E. L., and Isenberg, J. (1973). Finite element for rock joints and interfaces. *Journal of Soil Mechanics and Foundations Division.*

Glaser, J. and Steinmann, P. (2007). Material force method within the framework of the X-FEM distribution of nodal material forces. *PAMM: Proceedings in Applied Mathematics and Mechanics*, 7(1).

Goodman, R. E., Taylor, R. L., and Brekke, T. L. (1968). A model for the mechanics of jointed rock. *Journal of the Soil Mechanics and Foundation Division*, 94(SM3):637–659.

Griffith, A. A. (1921). The phenomena of rupture and flow in solids. *Philosophical transactions of the Royal Society of London*, 221:163–198.

Hillerborg, K., Modéer, M., and Petersson, P. (1976). Analysis of crack formation and crack growth in concrete by means of fracture mechanics and finite elements. *Cement and Concrete Research*, 6:773–781.

Idiart, A. E. (2009). *Coupled analysis of degradation processes in concrete specimens at the meso-level.* PhD thesis, Universitat Politècnica de Catalunya (UPC), Barcelona.

Idiart, A. E., López, C. M., and Carol, I. (2011). Chemo-mechanical analysis of concrete cracking and degradation due to external sulfate attack: a meso-scale model. *Cement and Concrete Composites*, 33(3):411–423.

Inglis, C. (1913). Stresses in plate due to the presence of cracks and sharp corners. *Transactions of the Royal Institution of Naval Architects*, 55:219—241.

Ingraffea, A. R., Linsbauer, H. N., and Rossmanith, H. P. (1987). *Computer simulation of cracking in a large arch dam: downstream side cracking.* Fracture of Concrete and Rock, Verlag, NY (USA). 334-342.

Irwin, G. (1958). Fracture. *Encyclopedia of Physics*, VI:551–590.

Jirásek, M. (2000). Comparative study on finite elements with embedded discontinuities. *Computer methods in applied mechanics and engineering*, 188(1):307–330.

Jirásek, M. and Belytschko, T. (2002). Computational resolution of strong discontinuities. In H.A. Mang, F. R. and Eberhardsteiner, J., editors, *Fifth World Congress on Computational Mechanics*, pages Abstract in page 788 volume I. Full paper CD–room (p.1–20), Vienna. WCCM V Fifth World Congress on Computational Mechanics, Vienna University of Technology.

Kaczmarczyk, Ł., Nezhad, M. M., and Pearce, C. (2014). Three-dimensional brittle fracture: configurational-force-driven crack propagation. *International Journal for Numerical Methods in Engineering*, 97(7):531–550.

Kaliakin, V. N. and Li, J. (1995). Insight into deficiencies associated with commonly used zero-thickness interface elements. *Computers and Geotechnics*, 17(2):225–252.

Kienzler, R. and Herrmann, G. (1997). On the properties of the Eshelly tensor. *Acta mechanica*, 125(1-4):73–91.

Kienzler, R. and Herrmann, G. (2012). *Mechanics in material space: with applications to defect and fracture mechanics.* Springer Science and Business Media.

Kirsch, E. G. (1898). Die theorie der elastizität und die bedürfnisse der festigkeitslehre. *Zeitschrift des Vereines deutscher Ingenieure*, 42:797–807.

Kumar, S., Singh, I. V., and Mishra, B. K. (2013). Numerical investigation of stable crack growth in ductile materials using XFEM. *Procedia Engineering, International Conference on Design and Manufacturing (IConDM2013)*, 64:652–660.

Laborde, P., Pommier, J., Renard, Y., and Salaün, M. (2005). High order extended finite element method for cracked domains. *International Journal for Numerical Methods in Engineering*, 64(3):354–381.

Larsson, R. and Fagerström, M. (2005). A framework for fracture modelling based on the material forces concept with XFEM kinematics. *International Journal for Numerical Methods in Engineering*, 62(13):1763–1788.

Lasry, D. and Belytschko, T. (1988). Localization limiters in transient problems. *International Journal of Solids and Structures*, 24:581–597.

Linder, C. and Armero, F. (2007). Finite elements with embedded strong discontinuities for the modeling of failure in solids. *International Journal for Numerical Methods in Engineering*, 72(12):1391–1433.

López, C. M. (1999). *Análisis microestructural de la fractura del hormigón utilizando elementos finitos tipo junta. Aplicación a diferentes hormigones.* PhD thesis, Universitat Politècnica de Catalunya (UPC), Barcelona, Barcelona.

Lubarda, V. A. (2001). *Elastoplasticity theory.* CRC press, Boca Raton, FL (USA).

Manzoli, O. L. and Shing, P. B. (2005). Finite elements with embedded multiple cracks and non-uniform discontinuity modes. *Latin American Journal of Solids and Structures.*

Mase, G. T. and Mase, G. E. (1999). *Continuum mechanics for engineers.* CRC press, Boca Raton, FL (USA). Chapters 4-6.

Maugin, G. A. (2011). *Configurational forces: thermomechanics, physics, mathematics, and numerics.* Chapman and Hall/CRC.

Maugin, G. A. and Trimarco, C. (1992). Psuedomentum and material forces in nonlinear elasticity: variational formulations and application to brittle fracture. *Acta Mechanica*, 94:1–28.

Melenk, J. M. (1995). *On generalized finite element methods.* PhD thesis, University of Maryland, Maryland (USA).

Melenk, J. M. and Babuška, I. (1996). The partition of unity finite element method: Basic theory and applications. *Computer Methods in Applied Mechanics and Engineering*, 139:289–314.

Menouillard, T. and Belytschko, T. (2010). Smoothed nodal forces for improved dynamic crack propagation modeling in XFEM. *International Journal for Numerical Methods in Engineering*, 84(1):47–72.

Meschke, G. and Dumstorff, P. (2007). Energy-based modeling of cohesive and cohesionless cracks via X-FEM. *Computer methods in applied mechanics and engineering*.

Miehe, C., Gürses, E., and Birkle, M. (2007). A computational framework of configurational-force-driven brittle fracture based on incremental energy minimization. *International Journal of Fracture*, 145(4):245–249.

Miehe, C., Hofacker, M., and Welschinger, F. (2010). A phase field model for rate-independent crack propagation: Robust algorithmic implementation based on operator splits. *Computer Methods in Applied Mechanics and Engineering*, 199:2765–2778.

Moës, N., Béchet, E., and Tourbier, M. (2006). Imposing Dirichlet boundary conditions in the extended finite element method. *International Journal for Numerical Methods in Engineering*, 67(12):1641–1669.

Moës, N., Dolbow, J., and Belytschko, T. (1999). A finite element method for crack growth without remeshing. *International journal for numerical methods in engineering*, pages 131–150.

Mohammadi, S. (2008). *Extended finite element method: for fracture analysis of structures*. Blackwell Publishing Ltd. Hoboken, NJ (USA).

Mosler, J. and Meschke, G. (2004). Embedded crack vs. smeared crack models: a comparison of elementwise discontinuous crack path approaches with emphasis on mesh bias. *Computer Methods in Applied Mechanics and Engineering*, 193(30-32):3351–3375.

Mueller, R., Gross, D., and G.A.Maugin (2004). Use of material forces in adaptive finite element methods. *Computational Mechanics*, 33(6):421–434.

Mueller, R., Kolling, S., and Gross, D. (2002). On configurational forces in the context of the finite element method. *International Journal for Numerical Methods in Engineering*.

Mueller, R. and Maugin, G. A. (2002). On material forces and finite element discretizations. *Computational mechanics*, 29(1):52–60.

Needleman, A. (1987). A continuum model for void nucleation by inclusion debonding. *Journal of applied mechanics*, 54(3):525–531.

Ngo, D. and Scordelis, A. C. (1967). Finite element analysis of reinforced concrete beams. *Journal Proceedings*, 64(3):152–163.

Nguyen, T. D., Govindjee, S., Klein, P. A., and Gao, H. (2005). A material force method for inelastic fracture mechanics. *Journal of the Mechanics and Physics of Solids*, 53(1):91–121.

Nguyen, V. P., Rabczuk, T., Bordas, S., and Duflot, M. (2008). Meshless methods: a review and computer implementation aspects. *Mathematics and computers in simulation*, 79(3):763–813.

Nooru-Mohamed, M. B. (1992). *Mixed-mode fracture of concrete: An experimental approach*. PhD thesis, Delft University of Technology, Delft (The Netherlands).

Nuismer, R. J. (1975). An energy release rate criterion for mixed mode fracture. *International journal of fracture*, 11(2):245–250.

Oden, J. T., Duarte, C. A., and Zienkiewicz, O. C. (1998). A new cloud-based hp finite element method. *Computer methods in applied mechanics and engineering*, 153(1-2):117–126.

Oliver, J. (1989). A consistent characteristic length for smeared cracking models. *International Journal for Numerical Methods in Engineering*, 28(2):461–474.

Ortiz, M., Leroy, Y., and Needleman, A. (1987). A finite element method for localized failure analysis. *Computer methods in applied mechanics and engineering*, 61(2):189–214.

Ortiz, M. and Pandolfi, A. (1999). Finite-deformation irreversible cohesive elements for three-dimensional crack-propagation analysis. *International journal for numerical methods in engineering*, 44(9):1267–1282.

Pak, Y. E. (1990). Force on a piezoelectric screw dislocation. *Journal of Applied Mechanics*, 57(4):863–869.

Pandolfi, A., Krysl, P., and Ortiz, M. (1999). Finite element simulation of ring expansion and fragmentation: the capturing of length and time scales through cohesive models of fracture. *International Journal of Fracture*, 95:279–297.

Pathak, H., Singh, A., and Singh, I. V. (2013). Fatigue crack growth simulations of 3-D problems using XFEM. *International Journal of Mechanical Sciences*, 76:112–131.

Peerlings, R. H. (1999). *Enhanced damage modelling for fracture and fatigue*. PhD thesis, Technische Universiteit Eindhoven, Eindhoven (The Netherlands).

Petersen, K. B. and Pedersen, M. S. (2012). *The matrix cookbook*, volume 7 of *510*. Technical University of Denmark.

Pijaudier-Cabot, G. and Bažant, Z. P. (1987). Nonlocal damage theory. *ASCE Journal of Engineering Mechanics*, 113:1512–1533.

Prat, P., Gens, A., Carol, I., Ledesma, A., and Gili, J. A. (1993). DRAC:A computer software for the analysis of rock mechanics problems. In Liu, H., editor, *Application of Computer Methods in Rock Mechanics*, pages 1361–1368. Shaanxi Science and Technology Press.

Rashid, Y. R. (1968). Ultimate strength analysis of prestressed concrete pressure vessels. *Nuclear engineering and design*, 7(4):334–344.

Rice, J. R. (1968). A path independent integral and the approximate analysis of strain concentration by notches and cracks. *Journal of applied mechanics*, 35(2):379–386.

Rots, J. G. (1988). Computational modeling of concrete fracture. *Doctoral thesis, Technische Universiteit Delft*.

Rots, J. G., Nauta, P., Kuster, G. M. A., and Blaauwendraad, J. (1985). Smeared crack approach and fracture localization in concrete. *HERON*, 30.

Sanders, J. D., Dolbow, J. E., and Laursen, T. A. (2009). On methods for stabilizing constraints over enriched interface in elasticity. *International Journal for Numerical Methods in Engineering*, 78(9):1009–1036.

Schweingruber, M. and Rank, E. (1992). Adaptive mesh generation for triangular or quadrilateral elements. *In Proceedings of the First European Conference on Numerical Methods, Brussels, Belgium*.

Segura, J. M. (2007). *Coupled HM analysis using zero-thickness interface elements with double nodes*. PhD thesis, Universitat Politècnica de Catalunya (UPC), Barcelona.

Segura, J. M. and Carol, I. (2004). On zero-thickness interface elements for diffusion problems. *International journal for numerical and analytical methods in geomechanics*, 28(9):947–962.

Shedbale, A. S., Singh, I. V., and Mishra, B. K. (2013). Nonlinear simulation of an embedded crack in the presence of holes and inclusions by XFEM. *Procedia Engineering*, 64:642–651. International Conference on Design and Manufacturing (IConDM2013).

Shibanuma, K. and Utsunomiya, T. (2011). Evaluation on reproduction of priori knowledge in XFEM. *Finite Elements in Analysis and Design*, 47(4):424–433.

Stankowski, T. (1990). *Numerical simulation of progressive failure in particle composites*. PhD thesis, University of Colorado, Boulder (USA).

Stankowski, T., Runesson, K., and Sture, S. (1993). Fracture and slip of interfaces in cementitious composites. I: Characteristics. *Journal of engineering mechanics*, 2(119):292–314.

Steinmann, P. (1996). An introduction to geometrically non-linear elasticity and plasticity. *Course Notes*.

Steinmann, P. (2000). Application of material forces to hyperelastostatic fracture mechanics. I. Continuum mechanical setting. *International Journal of Solids and Structures*, 37(48-50):7371–7391.

Steinmann, P. and Maugin, G. A., editors (2005). *Mechanics of material forces*. Springer-Verlag.

Steinmann, P., Scherer, M., and Denzer, R. (2009). Secret and joy of configurational mechanics: From foundations in continuum mechanics to applications in computational mechanics. *ZAMM-Journal of Applied Mathematics and Mechanics*, 89(8):614–630.

Strouboulis, T., Babuška, I., and Copps, K. (2000). The design and analysis of the generalized finite element method. *Computer Methods in Applied Mechanics and Engineering*, 81(1-3):43–69.

Stumpf, H. and Le, K. C. (1990). Variational principles of nonlinear fracture mechanics. *Acta Mechanica*, 83:25–37.

Sukumar, N., Chopp, D. L., Moës, N., and Belytschko, T. (2001). Modeling holes and inclusions by level sets in the extended finite-element method. *Computer Methods in Applied Mechanics and Engineering*, 190(46-47):6183–6200.

Tabarraei, A. and Sukumar, N. (2007). Adaptive computations using material forces and residual-based error estimators on quadtree meshes. *Computer methods in applied mechanics and engineering*, 196(25):2657–2680.

Unger, J. F., Eckardt, S., and Könke, C. (2007). Modelling of cohesive crack growth in concrete structures with the extended finite element method. *Computer Methods in Applied Mechanics and Engineering*, 196(41-44):4087–4100.

Vonk, R. A. (1992). *Softening of concrete loaded in compression.* PhD thesis, Eindhoven University of Technology, Eindhoven (The Netherlands).

Wacher, A. and Givoli, D. (2006). Remeshing and refining with moving finite elements: application to nonlinear wave problems. *Computer modeling in engineering and sciences*, 15(3):147–164.

Weihe, S., Kröplin, B., and Borst, R. (1998). Classification of smeared crack models based on material and structural properties. *International Journal of Solids and Structures*, 35(12):1289–1308.

Wells, G. N. and Sluys, L. J. (2001). Three-dimensional embedded discontinuity model for brittle fracture. *International Journal of Solids and Structures*, 38(5):897–913.

Winkler, B. (2001). *Traglastuntersuchungen von unbewehrten und bewehrten Betonstrukturen auf der Grundlage eines objektiven Werkstoffgesetzes für Beton.* PhD thesis, University of Innsbruck, Innsbruck (Austria).

Wu, T., Carpiuc-Prisacari, A., Poncelet, M., and de Lorenzis, L. (2017). Phase-field simulation of interactive mixed-mode fracture tests on cement mortar with full-field displacement boundary conditions. *Engineering Fracture Mechanics.*

Wu, T. and de Lorenzis, L. (2016). A phase-field approach to fracture coupled with diffusion. *Computer Methods in Applied Mechanics and Engineering*, 312:196–223.

Wu, T. and Wriggers, P. (2015). Multiscale diffusion–thermal–mechanical cohesive zone model for concrete. *Computational Mechanics*, 66:999–1016.

Xie, M. and Gerstle, W. H. (1995). Energy-based cohesive crack propagation modeling. *Journal of engineering mechanics*, 121(12):1349–1358.

Xu, X. P. and Needleman, A. (1994). Numerical simulations of fast crack growth in brittle solids. *Journal of the Mechanics and Physics of Solids*, 42(9):1397–1434.

Yang, Z. and Chen, J. (2004). Fully automatic modelling of cohesive discrete crack propagation in concrete beams using local arc-length methods. *International Journal of Solids and Structures*, 41(3-4):801–826.

Yang, Z. J. and Deeks, A. J. (2007). Fully-automatic modelling of cohesive crack growth using a finite element–scaled boundary finite element coupled method. *Engineering fracture mechanics*, 74(16):2547–2573.

Zhu, W. C. and Tang, C. A. (2002). Numerical simulation on shear fracture process of concrete using mesoscopic mechanical model. *Construction and Building Materials*, 16(8):453–463.

Zi, G. and Belytschko, T. (2003). New crack-tip elements for XFEM and applications to cohesive cracks. *International Journal for Numerical Methods in Engineering*, 57(15):2221–2240.

Zienkiewicz, O. C., Best, B., Dullage, C., and Stagg, K. G. (1970). Analysis of nonlinear problems in rock mechanics with particular reference to jointed rock systems. *Proceedings of the Second International Congress on Rock Mechanics*.

Zienkiewicz, O. C. and Taylor, R. L. (2000). *The finite element method: solid mechanics*, volume 5.

Zienkiewicz, O. C. and Taylor, R. L. (2005). *The finite element method for solid and structural mechanics*, volume 1. Butterworth-heinemann. New York, NY (USA).

Appendices

Appendix A

XFEM interpolation matrix $\bar{\mathbf{N}}$ for the "2-2" and "1-3" configurations of quadrangular elements

In this appendix, the above shape function matrices will be specified for quadrangular elements. The same exercise for triangles is included in Apendix C.

In quadrangular elements, the vector of unknowns is:

$$\bar{\mathbf{u}}_e = \left(\begin{array}{cccc|cccc} \mathbf{u}_{(1)}^T & \mathbf{u}_{(2)}^T & \mathbf{u}_{(3)}^T & \mathbf{u}_{(4)}^T & \boldsymbol{\delta}_{(1)}^T & \boldsymbol{\delta}_{(2)}^T & \boldsymbol{\delta}_{(3)}^T & \boldsymbol{\delta}_{(4)}^T \end{array} \right)^T \tag{A.1}$$

For these elements it is possible to distinguish two basic configuration depending on the discontinuity position, which are denoted "2-2" or "1-3" (Fig. 2.16).

A.1 "2-2" configuration

The geometry of a quadrangular element with a "2-2" intersection is shown in Fig.2.16a. Intersection points will be called α and β; α is located between nodes 1 and 2, and β between 4 and 3. The element domain is divided into three parts: The negative domain Ω^-, the positive domain Ω^+ and discontinuity itself (line α to β).

1. Negative subdomain:

   On the negative side, vector $\mathbf{u}_e{}^-$, and matrices $\hat{\mathbf{N}}^-$ and $\mathbf{T}^-$ have the following components:

$$\mathbf{u}_e{}^{-} = \begin{pmatrix} \mathbf{u}_{(1)}^T & \mathbf{u}_{(\alpha^-)}{}^T & \mathbf{u}_{(\beta^-)}{}^T & \mathbf{u}_{(4)}^T \end{pmatrix}^T \tag{A.2}$$

$$\begin{aligned} \hat{\mathbf{N}}^{-} &= \left[\begin{array}{cc|cc|cc|cc} \hat{N}^-_{(1)} & 0 & \hat{N}^-_{(\alpha)} & 0 & \hat{N}^-_{(\beta)} & 0 & \hat{N}^-_{(4)} & 0 \\ 0 & \hat{N}^-_{(1)} & 0 & \hat{N}^-_{(\alpha)} & 0 & \hat{N}^-_{(\beta)} & 0 & \hat{N}^-_{(4)} \end{array}\right] = \\ &= \left[\begin{array}{c|c|c|c} \hat{N}^-_{(1)}\mathbf{I} & \hat{N}^-_{(\alpha)}\mathbf{I} & \hat{N}^-_{(\beta)}\mathbf{I} & \hat{N}^-_{(4)}\mathbf{I} \end{array}\right] \end{aligned} \tag{A.3}$$

$$\mathbf{T}^{-} = \left[\begin{array}{cccc|cccc} \mathbf{I} & \mathbf{0} & \mathbf{0} & \mathbf{0} & \mathbf{0} & \mathbf{0} & \mathbf{0} & \mathbf{0} \\ N_{(1)}(\alpha)\mathbf{I} & \mathbf{0} & \mathbf{0} & \mathbf{0} & \mathbf{0} & N_{(2)}(\alpha)\mathbf{I} & \mathbf{0} & \mathbf{0} \\ \mathbf{0} & \mathbf{0} & \mathbf{0} & N_{(4)}(\beta)\mathbf{I} & \mathbf{0} & \mathbf{0} & N_{(3)}(\beta)\mathbf{I} & \mathbf{0} \\ \mathbf{0} & \mathbf{0} & \mathbf{0} & \mathbf{I} & \mathbf{0} & \mathbf{0} & \mathbf{0} & \mathbf{0} \end{array}\right] \tag{A.4}$$

Therefore, the format of the resulting overall interpolation matrix $\bar{\mathbf{N}}^{-}$ is:

$$\bar{\mathbf{N}}^{-} = \hat{\mathbf{N}}^{-}\mathbf{T}^{-} = \left[\begin{array}{c|c} \bar{\mathbf{N}}^-_u & \bar{\mathbf{N}}^-_\delta \end{array}\right] \tag{A.5}$$

where

$$\bar{\mathbf{N}}^-_u = \left[\begin{array}{cccc} \left(\hat{N}^-_{(1)} + \hat{N}^-_{(\alpha)}N_{(1)}(\alpha)\right)\mathbf{I} & \mathbf{0} & \mathbf{0} & \left(\hat{N}^-_{(\beta)}N_{(4)}(\beta) + \hat{N}^-_{(4)}\right)\mathbf{I} \end{array}\right] \tag{A.6}$$

$$\bar{\mathbf{N}}^-_\delta = \left[\begin{array}{ccc} \mathbf{0} & \left(\hat{N}^-_{(\alpha)}N_{(2)}(\alpha)\right)\mathbf{I} & \left(\hat{N}^-_{(\beta)}N_{(3)}(\beta)\right)\mathbf{I} \quad \mathbf{0} \end{array}\right] \tag{A.7}$$

2. Positive subdomain:

On the positive side, vector $\mathbf{u}_e{}^{+}$, and matrices $\hat{\mathbf{N}}^{+}$ and $\mathbf{T}^{+}$ have the following components:

$$\mathbf{u}_e{}^{+} = \begin{pmatrix} \mathbf{u}^T_{(\alpha^+)} & \mathbf{u}^T_{(2)} & \mathbf{u}^T_{(3)} & \mathbf{u}^T_{(\beta^+)} \end{pmatrix}^T \tag{A.8}$$

$$\hat{\mathbf{N}}^{+} = \left[\begin{array}{cc|cc|cc|cc} \hat{N}^{+}_{(\alpha)} & 0 & \hat{N}^{+}_{(2)} & 0 & \hat{N}^{+}_{(3)} & 0 & \hat{N}^{+}_{(\beta)} & 0 \\ 0 & \hat{N}^{+}_{(\alpha)} & 0 & \hat{N}^{+}_{(2)} & 0 & \hat{N}^{+}_{(3)} & 0 & \hat{N}^{+}_{(\beta)} \end{array}\right] =$$
$$= \left[\begin{array}{c|c|c|c} \hat{N}^{+}_{(\alpha)}\mathbf{I} & \hat{N}^{+}_{(2)}\mathbf{I} & \hat{N}^{+}_{(3)}\mathbf{I} & \hat{N}^{+}_{(\beta)}\mathbf{I} \end{array}\right] \tag{A.9}$$

$$\mathbf{T}^{+} = \left[\begin{array}{cccc|cccc} \mathbf{0} & N_{(2)}(\alpha)\,\mathbf{I} & \mathbf{0} & \mathbf{0} & N_{(1)}(\alpha)\,\mathbf{I} & \mathbf{0} & \mathbf{0} & \mathbf{0} \\ \mathbf{0} & \mathbf{I} & \mathbf{0} & \mathbf{0} & \mathbf{0} & \mathbf{0} & \mathbf{0} & \mathbf{0} \\ \mathbf{0} & \mathbf{0} & \mathbf{I} & \mathbf{0} & \mathbf{0} & \mathbf{0} & \mathbf{0} & \mathbf{0} \\ \mathbf{0} & \mathbf{0} & N_{(3)}(\beta)\,\mathbf{I} & \mathbf{0} & \mathbf{0} & \mathbf{0} & \mathbf{0} & N_{(4)}(\beta)\,\mathbf{I} \end{array}\right] \tag{A.10}$$

Therefore, the format of the resulting overall interpolation matrix $\bar{\mathbf{N}}^{+}$ is:

$$\bar{\mathbf{N}}^{+} = \hat{\mathbf{N}}^{+}\mathbf{T}^{+} = \left[\begin{array}{c|c} \bar{\mathbf{N}}^{+}_{u} & \bar{\mathbf{N}}^{+}_{\delta} \end{array}\right] \tag{A.11}$$

where

$$\bar{\mathbf{N}}^{+}_{u} = \left[\begin{array}{cccc} \mathbf{0} & \left(\hat{N}^{+}_{(\alpha)}N_{(2)}(\alpha) + \hat{N}^{+}_{(2)}\right)\mathbf{I} & \left(\hat{N}^{+}_{(3)} + \hat{N}^{+}_{(\beta)}N_{(3)}(\beta)\right)\mathbf{I} & \mathbf{0} \end{array}\right] \tag{A.12}$$

$$\bar{\mathbf{N}}^{+}_{\delta} = \left[\begin{array}{cccc} \left(\hat{N}^{+}_{(\alpha)}N_{(1)}(\alpha)\right)\mathbf{I} & \mathbf{0} & \mathbf{0} & \left(\hat{N}^{+}_{(\beta)}N_{(4)}(\beta)\right)\mathbf{I} \end{array}\right] \tag{A.13}$$

3. *D*iscontinuity:

Along the discontinuity itself, the key kinematic variable is the displacement jump, which is equal to the difference between the displacement on each side of the discontinuity.

$$\mathbf{a}(\mathbf{x}) = \mathbf{u}\left(\mathbf{x}^{J^{+}}\right) - \boldsymbol{u}\left(\mathbf{x}^{J^{-}}\right) =$$
$$= \left[\begin{array}{c|c} \bar{\mathbf{N}}^{+}_{u} - \bar{\mathbf{N}}^{-}_{u} & \bar{\mathbf{N}}^{+}_{\delta} - \bar{\mathbf{N}}^{-}_{\delta} \end{array}\right] \left(\begin{array}{c} \mathbf{u}_e \\ \boldsymbol{\delta}_e \end{array}\right) =$$
$$= \bar{\mathbf{N}}^{J}\bar{\mathbf{u}}_e \tag{A.14}$$

Note that, along the discontinuity $\mathbf{x}^J \in \overline{\alpha\beta}$, $\hat{N}^{+}_{(\lambda)}\left(\mathbf{x}^J\right) = \hat{N}^{-}_{(\lambda)}\left(\mathbf{x}^J\right) = \hat{N}_{(\lambda)}\left(\mathbf{x}^J\right)$ for $\lambda = \alpha, \beta$.

And $\hat{N}^{-}_{(1)}\left(\mathbf{x}^{J}\right) = \hat{N}^{-}_{(4)}\left(\mathbf{x}^{J}\right) = \hat{N}^{+}_{(2)}\left(\mathbf{x}^{J}\right) = \hat{N}^{+}_{(3)}\left(\mathbf{x}^{J}\right) = 0$, which leads to:

$$\begin{aligned}\bar{\mathbf{N}}_{u}^{J} &= \bar{\mathbf{N}}_{u}^{+} - \bar{\mathbf{N}}_{u}^{-} = \\ &= \left[\begin{array}{c|c|c|c} -\hat{N}_{(\alpha)}N_{(1)}(\alpha)\,\mathbf{I} & \hat{N}_{(\alpha)}N_{(2)}(\alpha)\,\mathbf{I} & \hat{N}_{(\beta)}N_{(3)}(\beta)\,\mathbf{I} & -\hat{N}_{(\beta)}N_{(4)}(\beta)\,\mathbf{I} \end{array}\right]\end{aligned} \tag{A.15}$$

$$\begin{aligned}\bar{\mathbf{N}}_{\delta}^{J} &= \bar{\mathbf{N}}_{\delta}^{+} - \bar{\mathbf{N}}_{\delta}^{-} = \\ &= \left[\begin{array}{c|c|c|c} \hat{N}_{(\alpha)}N_{(1)}(\alpha)\,\mathbf{I} & -\hat{N}_{(\alpha)}N_{(2)}(\alpha)\,\mathbf{I} & -\hat{N}_{(\beta)}N_{(3)}(\beta)\,\mathbf{I} & \hat{N}_{(\beta)}N_{(4)}(\beta)\,\mathbf{I} \end{array}\right]\end{aligned} \tag{A.16}$$

The above expressions may be also rewritten in the following way

$$\bar{\mathbf{N}}^{J} = \hat{\mathbf{N}}^{J}\mathbf{T}^{J} \tag{A.17}$$

where

$$\hat{\mathbf{N}}^{J} = \left[\begin{array}{c|c|c|c} -\hat{N}_{(\beta)}\mathbf{I} & -\hat{N}_{(\alpha)}\mathbf{I} & \hat{N}_{(\beta)}\mathbf{I} & \hat{N}_{(\alpha)}\mathbf{I} \end{array}\right] \tag{A.18}$$

$$\mathbf{T}^{J} = \left[\begin{array}{ccccc|ccccc} \mathbf{0} & & \mathbf{0} & & \mathbf{0} & N_{(4)}(\beta)\,\mathbf{I} & \mathbf{0} & & \mathbf{0} & & \mathbf{0} \\ N_{(1)}(\alpha)\,\mathbf{I} & & \mathbf{0} & & \mathbf{0} & \mathbf{0} & \mathbf{0} & & \mathbf{0} & & \mathbf{0} \\ \mathbf{0} & & \mathbf{0} & & N_{(3)}(\beta)\,\mathbf{I} & \mathbf{0} & \mathbf{0} & & \mathbf{0} & & \mathbf{0} \\ \mathbf{0} & & N_{(2)}(\alpha)\,\mathbf{I} & & \mathbf{0} & \mathbf{0} & N_{(1)}(\alpha)\,\mathbf{I} & & \mathbf{0} & & \mathbf{0} \end{array}\right] \tag{A.19}$$

A.2 "1-3" configurations

In this configuration, the discontinuity divides the quadrangular element into a triangular ("negative") part with only one node, and a pentagonal ("positive") part containing three nodes. Since, eventually, an integral has to be performed over each element subdomain, the pentagonal part is further subdivided into three triangular subdomains Ω^{+1},Ω^{+2} and Ω^{+3}, while the negative part is maintained as a single triangular subdomain Ω^{-} (Fig.2.16b).

1. *N*egative subdomain:

   In the negative (triangular) subdomain (Fig. 2.16b), vector $\mathbf{u}_e{}^{-}$, and matrices $\hat{\mathbf{N}}^{-}$ and $\mathbf{T}^{-}$ have the following structure:

$$\mathbf{u}_e{}^{-} = \left(\begin{array}{ccc} \mathbf{u}_{(\alpha^-)}{}^T & \mathbf{u}_{(\beta^-)}{}^T & \mathbf{u}_{(4)}^T \end{array} \right)^T \tag{A.20}$$

$$\begin{aligned} \hat{\mathbf{N}}^{-} &= \left[\begin{array}{cc|cc|cc} \hat{N}_{(\alpha)} & 0 & \hat{N}_{(\beta)} & 0 & \hat{N}_{(4)} & 0 \\ 0 & \hat{N}_{(\alpha)} & 0 & \hat{N}_{(\beta)} & 0 & \hat{N}_{(4)} \end{array} \right] = \\ &= \left[\begin{array}{c|c|c} \hat{N}_{(\alpha)}\mathbf{I} & \hat{N}_{(\beta)}\mathbf{I} & \hat{N}_{(4)}\mathbf{I} \end{array} \right] \end{aligned} \tag{A.21}$$

$$\mathbf{T}^{-} = \left[\begin{array}{cccc|ccc} \mathbf{0} & \mathbf{0} & \mathbf{0} & N_{(4)}(\alpha)\,\mathbf{I} & N_{(1)}(\alpha)\,\mathbf{I} & \mathbf{0} & \mathbf{0} & \mathbf{0} \\ \mathbf{0} & \mathbf{0} & \mathbf{0} & N_{(4)}(\beta)\,\mathbf{I} & \mathbf{0} & \mathbf{0} & N_{(3)}(\beta)\,\mathbf{I} & \mathbf{0} \\ \mathbf{0} & \mathbf{0} & \mathbf{0} & \mathbf{I} & \mathbf{0} & \mathbf{0} & \mathbf{0} & \mathbf{0} \end{array} \right] \tag{A.22}$$

   Therefore, the resulting overall interpolation matrix $\bar{\mathbf{N}}^{-}$ is:

$$\bar{\mathbf{N}}^{-} = \left[\begin{array}{c|c} \bar{\mathbf{N}}_u^{-} & \bar{\mathbf{N}}_\delta^{-} \end{array} \right] \tag{A.23}$$

   where

$$\bar{\mathbf{N}}_u^{-} = \left[\begin{array}{ccc} \mathbf{0}| & \mathbf{0}| & \mathbf{0}| \end{array} \left(\hat{N}_{(\alpha)} N_{(4)}(\alpha) + \hat{N}_{(\beta)} N_{(4)}(\beta) + \hat{N}_{(4)} \right) \mathbf{I} \right] \tag{A.24}$$

$$\bar{\mathbf{N}}_\delta^{-} = \left[\begin{array}{c|ccc} \hat{N}_{(\alpha)} N_{(1)}(\alpha)\,\mathbf{I} & \mathbf{0}| & \hat{N}_{(\beta)} N_{(3)}(\beta)\,\mathbf{I} & \mathbf{0} \end{array} \right] \tag{A.25}$$

2. *P*ositive subdomain:

   As already mentioned, the pentagonal positive part of the element is in turn subdivided into three triangle subdomains denoted as Ω^{+1}, Ω^{+2} and Ω^{+3}, see Fig.2.16b.

   Subdomain Ω^{+1} is formed by nodes 1, 2 and α. Consequently, vector $\mathbf{u}_e{}^{+1}$, and matrices $\hat{\mathbf{N}}^{+1}$ and $\mathbf{T}^{+1}$ have the following components:

$$\mathbf{u}_e{}^{+1} = \left(\begin{array}{ccc} \mathbf{u}_{(1)}^T & \mathbf{u}_{(2)}^T & \mathbf{u}_{(\alpha^+)}{}^T \end{array} \right)^T \tag{A.26}$$

$$\hat{\mathbf{N}}^{+1} = \left[\begin{array}{cc|cc|cc} \hat{N}_{(1)} & 0 & \hat{N}_{(2)} & 0 & \hat{N}_{(\alpha)} & 0 \\ 0 & \hat{N}_{(1)} & 0 & \hat{N}_{(2)} & 0 & \hat{N}_{(\alpha)} \end{array}\right] = \\ = \left[\begin{array}{c|c|c} \hat{N}_{(1)}\mathbf{I} & \hat{N}_{(2)}\mathbf{I} & \hat{N}_{(\alpha)}\mathbf{I} \end{array}\right] \tag{A.27}$$

$$\mathbf{T}^{+1} = \left[\begin{array}{cccc|cccc} \mathbf{I} & \mathbf{0} & \mathbf{0} & \mathbf{0} & \mathbf{0} & \mathbf{0} & \mathbf{0} & \mathbf{0} \\ \mathbf{0} & \mathbf{I} & \mathbf{0} & \mathbf{0} & \mathbf{0} & \mathbf{0} & \mathbf{0} & \mathbf{0} \\ N_{(1)}(\alpha)\,\mathbf{I} & \mathbf{0} & \mathbf{0} & \mathbf{0} & \mathbf{0} & \mathbf{0} & \mathbf{0} & N_{(4)}(\alpha)\,\mathbf{I} \end{array}\right] \tag{A.28}$$

Therefore, the resulting overall interpolation matrix $\bar{\mathbf{N}}^{+1}$ is:

$$\bar{\mathbf{N}}^{+1} = \left[\begin{array}{c|c} \bar{\mathbf{N}}_u^{+1} & \bar{\mathbf{N}}_\delta^{+1} \end{array}\right] \tag{A.29}$$

where

$$\bar{\mathbf{N}}_u^{+1} = \left[\begin{array}{c|c|c|c} \left(\hat{N}_{(1)} + \hat{N}_{(\alpha)} N_{(1)}(\alpha)\right)\mathbf{I} & \hat{N}_{(2)}\mathbf{I} & \mathbf{0} & \mathbf{0} \end{array}\right] \tag{A.30}$$

$$\bar{\mathbf{N}}_\delta^{+1} = \left[\begin{array}{c|c|c|c} \mathbf{0} & \mathbf{0} & \mathbf{0} & \hat{N}_{(\alpha)} N_{(4)}(\alpha)\,\mathbf{I} \end{array}\right] \tag{A.31}$$

Subdomain Ω^{+2} is formed by nodes α^+, 2 and β^+. Vector $\mathbf{u}_e{}^{+2}$, matrix $\hat{\mathbf{N}}^{+2}$ and $\mathbf{T}^{+2}$ have the following components:

$$\mathbf{u}_e{}^{+2} = \left(\begin{array}{ccc} \mathbf{u}_{(\alpha^+)}{}^T & \mathbf{u}_{(2)}^T & \mathbf{u}_{(\beta^+)}{}^T \end{array}\right)^T \tag{A.32}$$

$$\hat{\mathbf{N}}^{+2} = \left[\begin{array}{cc|cc|cc} \hat{N}_{(\alpha)} & 0 & \hat{N}_{(2)} & 0 & \hat{N}_{(\beta)} & 0 \\ 0 & \hat{N}_{(\alpha)} & 0 & \hat{N}_{(2)} & 0 & \hat{N}_{(\beta)} \end{array}\right] = \\ = \left[\begin{array}{c|c|c} \hat{N}_{(\alpha)}\mathbf{I} & \hat{N}_{(2)}\mathbf{I} & \hat{N}_{(\beta)}\mathbf{I} \end{array}\right] \tag{A.33}$$

$$\mathbf{T}^{+2} = \left[\begin{array}{cccc|cccc} N_{(1)}(\alpha)\,\mathbf{I} & 0 & \mathbf{0} & \mathbf{0} & \mathbf{0} & \mathbf{0} & \mathbf{0} & N_{(4)}(\alpha)\,\mathbf{I} \\ \mathbf{0} & \mathbf{I} & \mathbf{0} & \mathbf{0} & \mathbf{0} & \mathbf{0} & \mathbf{0} & 0 \\ \mathbf{0} & \mathbf{0} & N_{(3)}(\beta)\,\mathbf{I} & \mathbf{0} & \mathbf{0} & \mathbf{0} & \mathbf{0} & N_{(4)}(\beta)\,\mathbf{I} \end{array}\right] \tag{A.34}$$

Therefore, the resulting overall interpolation matrix $\bar{\mathbf{N}}^{+2}$ is:

$$\bar{\mathbf{N}}^{+2} = \left[\begin{array}{c|c} \bar{\mathbf{N}}_u^{+2} & \bar{\mathbf{N}}_\delta^{+2} \end{array}\right] \tag{A.35}$$

where

$$\bar{\mathbf{N}}_u^{+2} = \left[\begin{array}{c|c|c} \hat{N}_{(\alpha)} N_{(1)}(\alpha)\,\mathbf{I} & \hat{N}_{(2)}\mathbf{I} & \hat{N}_{(\beta)} N_{(3)}(\beta)\,\mathbf{I} \end{array}\right] \quad \mathbf{0} \Big] \tag{A.36}$$

$$\bar{\mathbf{N}}_\delta^{+2} = \left[\begin{array}{ccc} \mathbf{0} | & \mathbf{0} | & \mathbf{0} | \end{array}\right] \quad \Big(\hat{N}_{(\alpha)} N_{(4)}(\alpha) + \hat{N}_{(\beta)} N_{(4)}(\beta)\Big)\,\mathbf{I} \Big] \tag{A.37}$$

Subdomain $\Omega^{(+3)}$ is formed by nodes 2, 3 and β. So integration is done with shape functions of this subdomain, vector ${\mathbf{u}_e}^{+3}$, and matrices $\hat{\mathbf{N}}^{+3}$ and $\mathbf{T}^{+3}$ have the following components:

$${\mathbf{u}_e}^{+3} = \Big(\begin{array}{ccc} \mathbf{u}_{(2)}^T & \mathbf{u}_{(3)}^T & {\mathbf{u}_{(\beta^+)}}^T \end{array} \Big)^T \tag{A.38}$$

$$\begin{aligned} \hat{\mathbf{N}}^{+3} &= \left[\begin{array}{cc|cc|cc} \hat{N}_{(2)} & 0 & \hat{N}_{(3)} & 0 & \hat{N}_{(\beta)} & 0 \\ 0 & \hat{N}_{(2)} & 0 & \hat{N}_{(3)} & 0 & \hat{N}_{(\beta)} \end{array}\right] = \\ &= \left[\begin{array}{c|c|c} \hat{N}_{(2)}\mathbf{I} & \hat{N}_{(3)}\mathbf{I} & \hat{N}_{(\beta)}\mathbf{I} \end{array}\right] \end{aligned} \tag{A.39}$$

$$\mathbf{T}^{+3} = \left[\begin{array}{cccc|cccc} \mathbf{0} & \mathbf{I} & \mathbf{0} & \mathbf{0} & \mathbf{0} & \mathbf{0} & \mathbf{0} & \mathbf{0} \\ \mathbf{0} & \mathbf{0} & \mathbf{I} & \mathbf{0} & \mathbf{0} & \mathbf{0} & \mathbf{0} & \mathbf{0} \\ \mathbf{0} & \mathbf{0} & N_{(3)}(\beta)\,\mathbf{I} & \mathbf{0} & \mathbf{0} & \mathbf{0} & \mathbf{0} & N_{(4)}(\beta)\,\mathbf{I} \end{array}\right] \tag{A.40}$$

Therefore, the resulting overall interpolation matrix $\bar{\mathbf{N}}^{+3}$ is:

$$\bar{\mathbf{N}}^{+3} = \left[\begin{array}{c|c} \bar{\mathbf{N}}_u^{+3} & \bar{\mathbf{N}}_\delta^{+3} \end{array}\right] \tag{A.41}$$

where

$$\bar{\mathbf{N}}_u^{+3} = \left[\begin{array}{c|c|c} \mathbf{0} & \hat{N}_{(2)}\mathbf{I} & \left(\hat{N}_{(3)} + \hat{N}_{(\beta)}N_{(3)}(\beta)\right)\mathbf{I} \end{array} \right] \quad \mathbf{0} \quad \Big] \tag{A.42}$$

$$\bar{\mathbf{N}}_\delta^{+3} = \left[\begin{array}{c|c|c|c} \mathbf{0} & \mathbf{0} & \mathbf{0} & \hat{N}_{(\beta)}N_{(4)}(\beta)\,\mathbf{I} \end{array} \right] \tag{A.43}$$

3. *D*iscontinuity:

Along the discontinuity itself, the key kinematic variable is the displacement jump, which is equal to the difference between the displacement on each side of the discontinuity.

$$\begin{aligned} \mathbf{a}(\mathbf{x}) &= \mathbf{u}\left(\mathbf{x}^{J^{+2}}\right) - \mathbf{u}\left(\mathbf{x}^{J^{-}}\right) = \\ &= \left[\begin{array}{c|c} \bar{\mathbf{N}}_u^{+2} - \bar{\mathbf{N}}_u^{-} & \bar{\mathbf{N}}_\delta^{+2} - \bar{\mathbf{N}}_\delta^{-} \end{array} \right] \left(\begin{array}{c} \mathbf{u}_e \\ \boldsymbol{\delta}_e \end{array} \right) = \bar{\mathbf{N}}^J \bar{\mathbf{u}}_e \end{aligned} \tag{A.44}$$

Note that, along the discontinuity $\mathbf{x}^J \in \overline{\alpha\beta}$, $\hat{N}_{(\lambda)}^{+2}\left(\mathbf{x}^J\right) = \hat{N}_{(\lambda)}^{-}\left(\mathbf{x}^J\right) = \hat{\mathbf{N}}_{(\lambda)}\left(\mathbf{x}^J\right)$ for $\lambda = \alpha, \beta$, and $\hat{N}_{(4)}^{-}\left(\mathbf{x}^J\right) = \hat{N}_{(1)}^{+2}\left(\mathbf{x}^J\right) = \hat{N}_{(2)}^{+2}\left(\mathbf{x}^J\right) = \hat{N}_{(3)}^{+2}\left(\mathbf{x}^J\right) = 0$, which leads to:

$$\begin{aligned} \bar{\mathbf{N}}_u^J &= \bar{\mathbf{N}}_u^{+2} - \bar{\mathbf{N}}_u^{-} = \\ &= \left[\begin{array}{c|c|c|c} \hat{N}_{(\alpha)}N_{(1)}(\alpha)\,\mathbf{I} & \mathbf{0} & \hat{N}_{(\beta)}N_{(3)}(\beta)\,\mathbf{I} & -\left(\hat{N}_{(\alpha)}N_{(4)}(\alpha) + \hat{N}_{(\beta)}N_{(4)}(\beta)\right)\mathbf{I} \end{array} \right] \end{aligned} \tag{A.45}$$

$$\begin{aligned} \bar{\mathbf{N}}_\delta^J &= \bar{\mathbf{N}}_\delta^{+2} - \bar{\mathbf{N}}_\delta^{-} = \\ &= \left[\begin{array}{c|c|c|c} -\hat{N}_{(\alpha)}N_{(1)}(\alpha)\,\mathbf{I} & \mathbf{0} & -\hat{N}_{(\beta)}N_{(3)}(\beta)\,\mathbf{I} & \left(\hat{N}_{(\alpha)}N_{(4)}(\alpha) + \hat{N}_{(\beta)}N_{(4)}(\beta)\right)\mathbf{I} \end{array} \right] \end{aligned} \tag{A.46}$$

The above expressions may be also rewritten in the following way

$$\bar{\mathbf{N}}^J = \hat{\mathbf{N}}^J \mathbf{T}^J \tag{A.47}$$

where

$$\hat{\mathbf{N}}^J = \left[\begin{array}{c|c|c|c} -\hat{N}_{(\beta)}\mathbf{I} & -\hat{N}_{(\alpha)}\mathbf{I} & \hat{N}_{(\beta)}\mathbf{I} & \hat{N}_{(\alpha)}\mathbf{I} \end{array} \right] \tag{A.48}$$

$$\mathbf{T}^{J}=\left[\begin{array}{cccc|cccc} \mathbf{0} & \mathbf{0} & \mathbf{0} & N_{(4)}(\beta)\,\mathbf{I} & \mathbf{0} & \mathbf{0} & N_{(3)}(\beta)\,\mathbf{I} & \mathbf{0} \\ \mathbf{0} & \mathbf{0} & \mathbf{0} & N_{(4)}(\alpha)\,\mathbf{I} & N_{(1)}(\alpha)\,\mathbf{I} & \mathbf{0} & \mathbf{0} & \mathbf{0} \\ \mathbf{0} & \mathbf{0} & N_{(3)}(\beta)\,\mathbf{I} & \mathbf{0} & \mathbf{0} & \mathbf{0} & \mathbf{0} & N_{(4)}(\beta)\,\mathbf{I} \\ N_{(1)}(\alpha)\,\mathbf{I} & \mathbf{0} & \mathbf{0} & \mathbf{0} & \mathbf{0} & \mathbf{0} & \mathbf{0} & N_{(4)}(\alpha)\,\mathbf{I} \end{array}\right] \tag{A.49}$$

Appendix B

XFEM interpolation matrix $\bar{\mathbf{N}}$ for special configurations of quadrangular elements

The special configurations of a discontinuity crossing a quadrangular element are represented in Fig. B.1.

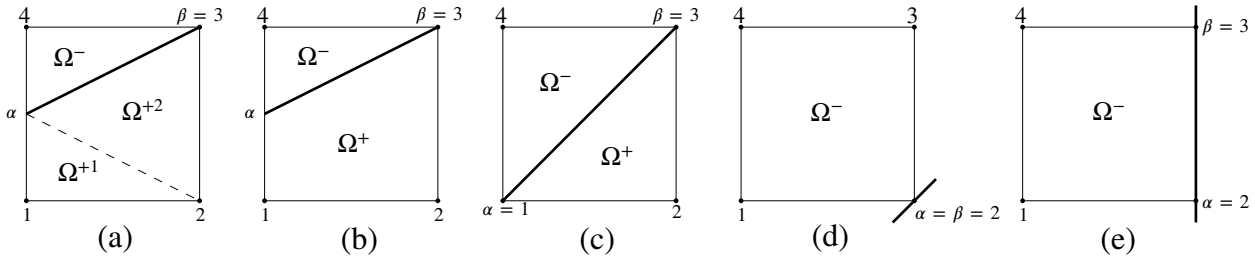

Figure B.1: Special configurations for quadrangular elements (a) discontinuity coinciding with a node and crossing an edge (positive subdomain is discretized in two triangles). (b) discontinuity coinciding with a node and crossing an edge (positive subdomain is discretized in one quadrangle). (c) discontinuity coinciding with two node crossing diagonally the element. (d) discontinuity coinciding with only one node. (e) discontinuity coinciding with an edge.

B.1 Quadrangular element with special configuration for a discontinuity coinciding with a node and crossing an edge, and positive part subdivided into two triangular subdomains (Fig.B.1a)

Matrices $\hat{\mathbf{N}}^{-}$ and $\mathbf{T}^{-}$ for the triangular negative subdomain $\left(\Omega^{-}\right)$:

$$\hat{\mathbf{N}}^{-} = \left[\begin{array}{c|c|c} \hat{N}^{-}_{(\alpha)}\mathbf{I} & \hat{N}^{-}_{(3)}\mathbf{I} & \hat{N}^{-}_{(4)}\mathbf{I} \end{array} \right] \tag{B.1}$$

$$\mathbf{T}^{-} = \left[\begin{array}{ccc|c|ccc} \mathbf{0} & \mathbf{0} & \mathbf{0} & N_{(4)}(\alpha)\,\mathbf{I} & N_{(1)}(\alpha)\,\mathbf{I} & \mathbf{0} & \mathbf{0} & \mathbf{0} \\ \mathbf{0} & \mathbf{0} & \mathbf{0} & \mathbf{0} & \mathbf{0} & \mathbf{0} & \mathbf{I} & \mathbf{0} \\ \mathbf{0} & \mathbf{0} & \mathbf{0} & \mathbf{I} & \mathbf{0} & \mathbf{0} & \mathbf{0} & \mathbf{0} \end{array} \right] \tag{B.2}$$

Matrices $\hat{\mathbf{N}}^{+1}, \mathbf{T}^{+1}$ and $\hat{\mathbf{N}}^{+2}, \mathbf{T}^{+2}$ for the positive side divided into triangular subdomains $\left(\Omega^{+1}\right)$ and $\left(\Omega^{+2}\right)$:

$$\hat{\mathbf{N}}^{+1} = \left[\begin{array}{c|c|c} \hat{N}^{+1}_{(1)}\mathbf{I} & \hat{N}^{+1}_{(2)}\mathbf{I} & \hat{N}^{+1}_{(\alpha)}\mathbf{I} \end{array} \right] \tag{B.3}$$

$$\mathbf{T}^{+1} = \left[\begin{array}{ccc|c|ccc} \mathbf{I} & \mathbf{0} & \mathbf{0} & \mathbf{0} & \mathbf{0} & \mathbf{0} & \mathbf{0} & \mathbf{0} \\ \mathbf{0} & \mathbf{I} & \mathbf{0} & \mathbf{0} & \mathbf{0} & \mathbf{0} & \mathbf{0} & \mathbf{0} \\ N_{(1)}(\alpha)\,\mathbf{I} & \mathbf{0} & \mathbf{0} & \mathbf{0} & \mathbf{0} & \mathbf{0} & \mathbf{0} & N_{(4)}(\alpha)\,\mathbf{I} \end{array} \right] \tag{B.4}$$

$$\hat{\mathbf{N}}^{+2} = \left[\begin{array}{c|c|c} \hat{N}^{+2}_{(\alpha)}\mathbf{I} & \hat{N}^{+2}_{(2)}\mathbf{I} & \hat{N}^{+2}_{(3)}\mathbf{I} \end{array} \right] \tag{B.5}$$

$$\mathbf{T}^{+2} = \left[\begin{array}{ccc|c|ccc} N_{(1)}(\alpha)\,\mathbf{I} & \mathbf{0} & \mathbf{0} & \mathbf{0} & \mathbf{0} & \mathbf{0} & \mathbf{0} & N_{(4)}(\alpha)\,\mathbf{I} \\ \mathbf{0} & \mathbf{I} & \mathbf{0} & \mathbf{0} & \mathbf{0} & \mathbf{0} & \mathbf{0} & \mathbf{0} \\ \mathbf{0} & \mathbf{0} & \mathbf{I} & \mathbf{0} & \mathbf{0} & \mathbf{0} & \mathbf{0} & \mathbf{0} \end{array} \right] \tag{B.6}$$

Matrices $\hat{\mathbf{N}}^{J}$ and $\mathbf{T}^{J}$ on the discontinuity:

$$\hat{\mathbf{N}}^{J} = \left[\begin{array}{c|c|c|c} -\hat{N}_{(3)}\mathbf{I} & -\hat{N}_{(\alpha)}\mathbf{I} & \hat{N}_{(3)}\mathbf{I} & \hat{N}_{(\alpha)}\mathbf{I} \end{array} \right] \tag{B.7}$$

$$\mathbf{T}^{J} = \left[\begin{array}{cccc|cccc} \mathbf{0} & \mathbf{0} & \mathbf{0} & \mathbf{0} & \mathbf{0} & \mathbf{0} & \mathbf{I} & \mathbf{0} \\ \mathbf{0} & \mathbf{0} & \mathbf{0} & N_{(4)}(\alpha)\,\mathbf{I} & \mathbf{N_{(1)}}(\alpha)\,\mathbf{I} & \mathbf{0} & \mathbf{0} & \mathbf{0} \\ \mathbf{0} & \mathbf{0} & \mathbf{I} & \mathbf{0} & \mathbf{0} & \mathbf{0} & \mathbf{0} & \mathbf{0} \\ N_{(1)}(\alpha)\,\mathbf{I} & \mathbf{0} & \mathbf{0} & \mathbf{0} & \mathbf{0} & \mathbf{0} & \mathbf{0} & N_{(4)}(\alpha)\,\mathbf{I} \end{array}\right] \tag{B.8}$$

B.2 Quadrangular element with special configuration for a discontinuity coinciding with a node and crossing an edge, and positive part taken as a single quadrangular subdomain (Fig.B.1b)

Matrices $\hat{\mathbf{N}}^{-}$ and $\mathbf{T}^{-}$ for the triangular negative subdomain are the same as (B.1), (B.2).

Matrices $\hat{\mathbf{N}}^{+}$ and $\mathbf{T}^{+}$ for the quadrangular positive subdomain:

$$\hat{\mathbf{N}}^{+} = \left[\begin{array}{c|c|c|c} \hat{N}^{+}_{(1)}\mathbf{I} & \hat{N}^{+}_{(2)}\mathbf{I} & \hat{N}^{+}_{(3)}\mathbf{I} & \hat{N}^{+}_{(\alpha)}\mathbf{I} \end{array}\right] \tag{B.9}$$

$$\mathbf{T}^{+} = \left[\begin{array}{cccc|cccc} \mathbf{I} & \mathbf{0} & \mathbf{0} & \mathbf{0} & \mathbf{0} & \mathbf{0} & \mathbf{0} & \mathbf{0} \\ \mathbf{0} & \mathbf{I} & \mathbf{0} & \mathbf{0} & \mathbf{0} & \mathbf{0} & \mathbf{0} & \mathbf{0} \\ \mathbf{0} & \mathbf{0} & \mathbf{I} & \mathbf{0} & \mathbf{0} & \mathbf{0} & \mathbf{0} & \mathbf{0} \\ N_{(1)}(\alpha)\,\mathbf{I} & \mathbf{0} & \mathbf{0} & \mathbf{0} & \mathbf{0} & \mathbf{0} & \mathbf{0} & N_{(4)}(\alpha)\,\mathbf{I} \end{array}\right] \tag{B.10}$$

Matrices $\hat{\mathbf{N}}^{J}$ and $\mathbf{T}^{J}$ on the discontinuity are the same as (B.7), (B.8).

B.3 Quadrangular element with special configuration for a discontinuity coinciding with two nodes crossing diagonally the element (Fig.B.1c)

Matrices $\hat{\mathbf{N}}^{-}$ and $\mathbf{T}^{-}$ for the triangular negative subdomain:

$$\hat{\mathbf{N}}^{-} = \left[\begin{array}{c|c|c} \hat{N}^{-}_{(1)}\mathbf{I} & \hat{N}^{-}_{(3)}\mathbf{I} & \hat{N}^{-}_{(4)}\mathbf{I} \end{array}\right] \tag{B.11}$$

$$\mathbf{T}^{-} = \left[\begin{array}{cccc|cccc} \mathbf{0} & \mathbf{0} & \mathbf{0} & \mathbf{0} & \mathbf{I} & \mathbf{0} & \mathbf{0} & \mathbf{0} \\ \mathbf{0} & \mathbf{0} & \mathbf{0} & \mathbf{0} & \mathbf{0} & \mathbf{0} & \mathbf{I} & \mathbf{0} \\ \mathbf{0} & \mathbf{0} & \mathbf{0} & \mathbf{I} & \mathbf{0} & \mathbf{0} & \mathbf{0} & \mathbf{0} \end{array}\right] \tag{B.12}$$

Matrices $\hat{\mathbf{N}}^{+}$ and $\mathbf{T}^{+}$ for the triangular positive subdomain:

$$\hat{\mathbf{N}}^{+} = \left[\begin{array}{c|c|c} \hat{N}^{+}_{(1)}\mathbf{I} & \hat{N}^{+}_{(2)}\mathbf{I} & \hat{N}^{+}_{(3)}\mathbf{I} \end{array}\right] \tag{B.13}$$

$$\mathbf{T}^{+} = \left[\begin{array}{cccc|cccc} \mathbf{I} & \mathbf{0} & \mathbf{0} & \mathbf{0} & \mathbf{0} & \mathbf{0} & \mathbf{0} & \mathbf{0} \\ \mathbf{0} & \mathbf{I} & \mathbf{0} & \mathbf{0} & \mathbf{0} & \mathbf{0} & \mathbf{0} & \mathbf{0} \\ \mathbf{0} & \mathbf{0} & \mathbf{I} & \mathbf{0} & \mathbf{0} & \mathbf{0} & \mathbf{0} & \mathbf{0} \end{array}\right] \tag{B.14}$$

Matrices $\hat{\mathbf{N}}^{J}$ and $\mathbf{T}^{J}$ on the discontinuity:

$$\hat{\mathbf{N}}^{J} = \left[\begin{array}{c|c|c|c} -\hat{N}_{(3)}\mathbf{I} & -\hat{N}_{(1)}\mathbf{I} & \hat{N}_{(3)}\mathbf{I} & \hat{N}_{(1)}\mathbf{I} \end{array}\right] \tag{B.15}$$

$$\mathbf{T}^{J} = \left[\begin{array}{cccc|cccc} \mathbf{0} & \mathbf{0} & \mathbf{0} & \mathbf{0} & \mathbf{0} & \mathbf{0} & \mathbf{I} & \mathbf{0} \\ \mathbf{0} & \mathbf{0} & \mathbf{0} & \mathbf{0} & \mathbf{I} & \mathbf{0} & \mathbf{0} & \mathbf{0} \\ \mathbf{0} & \mathbf{0} & \mathbf{I} & \mathbf{0} & \mathbf{0} & \mathbf{0} & \mathbf{0} & \mathbf{0} \\ \mathbf{I} & \mathbf{0} & \mathbf{0} & \mathbf{0} & \mathbf{0} & \mathbf{0} & \mathbf{0} & \mathbf{0} \end{array}\right] \tag{B.16}$$

B.4 Quadrangular element with special configuration for a discontinuity coinciding with only one node (Fig.B.1d)

Matrices $\hat{\mathbf{N}}^{-}$ and $\mathbf{T}^{-}$ for the quadrangular negative subdomain:

$$\hat{\mathbf{N}}^{-} = \left[\begin{array}{c|c|c|c} \hat{N}^{-}_{(1)}\mathbf{I} & \hat{N}^{-}_{(2)}\mathbf{I} & \hat{N}^{-}_{(3)}\mathbf{I} & \hat{N}^{-}_{(4)}\mathbf{I} \end{array}\right] \tag{B.17}$$

$$\mathbf{T}^{-} = \left[\begin{array}{cccc|cccc} \mathbf{I} & \mathbf{0} & \mathbf{0} & \mathbf{0} & \mathbf{0} & \mathbf{0} & \mathbf{0} & \mathbf{0} \\ \mathbf{0} & \mathbf{0} & \mathbf{0} & \mathbf{0} & \mathbf{0} & \mathbf{I} & \mathbf{0} & \mathbf{0} \\ \mathbf{0} & \mathbf{0} & \mathbf{I} & \mathbf{0} & \mathbf{0} & \mathbf{0} & \mathbf{0} & \mathbf{0} \\ \mathbf{0} & \mathbf{0} & \mathbf{0} & \mathbf{I} & \mathbf{0} & \mathbf{0} & \mathbf{0} & \mathbf{0} \end{array}\right] \tag{B.18}$$

B.5 Quadrangular element with special configuration for a discontinuity coinciding with an edge (Fig.B.1e)

Matrices $\hat{\mathbf{N}}^{-}$ and $\mathbf{T}^{-}$ for the quadrangular negative subdomain:

$$\hat{\mathbf{N}}^{-} = \left[\begin{array}{c|c|c|c} \hat{N}^{-}_{(1)}\mathbf{I} & \hat{N}^{-}_{(2)}\mathbf{I} & \hat{N}^{-}_{(3)}\mathbf{I} & \hat{N}^{-}_{(4)}\mathbf{I} \end{array} \right] \tag{B.19}$$

$$\mathbf{T}^{-} = \left[\begin{array}{cccc|cccc} \mathbf{I} & \mathbf{0} & \mathbf{0} & \mathbf{0} & \mathbf{0} & \mathbf{0} & \mathbf{0} & \mathbf{0} \\ \mathbf{0} & \mathbf{0} & \mathbf{0} & \mathbf{0} & \mathbf{0} & \mathbf{I} & \mathbf{0} & \mathbf{0} \\ \mathbf{0} & \mathbf{0} & \mathbf{0} & \mathbf{0} & \mathbf{0} & \mathbf{0} & \mathbf{I} & \mathbf{0} \\ \mathbf{0} & \mathbf{0} & \mathbf{0} & \mathbf{I} & \mathbf{0} & \mathbf{0} & \mathbf{0} & \mathbf{0} \end{array} \right] \tag{B.20}$$

Matrices $\hat{\mathbf{N}}^{J}$ and $\mathbf{T}^{J}$ on the discontinuity:

$$\hat{\mathbf{N}}^{J} = \left[\begin{array}{c|c|c|c} -\hat{N}_{(3)}\mathbf{I} & -\hat{N}_{(2)}\mathbf{I} & \hat{N}_{(3)}\mathbf{I} & \hat{N}_{(2)}\mathbf{I} \end{array} \right] \tag{B.21}$$

$$\mathbf{T}^{J} = \left[\begin{array}{cccc|cccc} \mathbf{0} & \mathbf{0} & \mathbf{0} & \mathbf{0} & \mathbf{0} & \mathbf{0} & \mathbf{I} & \mathbf{0} \\ \mathbf{0} & \mathbf{0} & \mathbf{0} & \mathbf{0} & \mathbf{0} & \mathbf{I} & \mathbf{0} & \mathbf{0} \\ \mathbf{0} & \mathbf{0} & \mathbf{I} & \mathbf{0} & \mathbf{0} & \mathbf{0} & \mathbf{0} & \mathbf{0} \\ \mathbf{0} & \mathbf{I} & \mathbf{0} & \mathbf{0} & \mathbf{0} & \mathbf{0} & \mathbf{0} & \mathbf{0} \end{array} \right] \tag{B.22}$$

Appendix C

XFEM interpolation matrix $\bar{\mathbf{N}}$ for triangular elements, and special configurations

The geometry of the general case and special configurations of a triangular element crossed by a discontinuity and represented in Fig.C.1

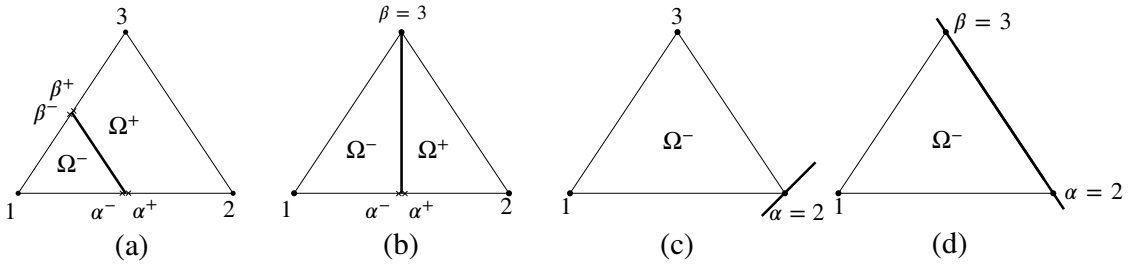

Figure C.1: (a) General case of a triangular element crossed by the discontinuity. (b) Triangular element with special configuration for a discontinuity coinciding with one node and crossing an edge. (c) Triangular element with special configuration for a discontinuity coinciding with only one node. (d) Triangular element with special configuration for a discontinuity coinciding with an edge.

C.1 General matrices for triangular elements (Fig.C.1a)

Matrices $\hat{\mathbf{N}}^-$ and $\mathbf{T}^-$ for the triangular negative subdomain:

$$\hat{\mathbf{N}}^{-} = \left[\begin{array}{c|c|c} \hat{N}^{-}_{(1)}\mathbf{I} & \hat{N}^{-}_{(\alpha)}\mathbf{I} & \hat{N}^{-}_{(\beta)}\mathbf{I} \end{array} \right] \tag{C.1}$$

$$\mathbf{T}^{-} = \left[\begin{array}{ccc|ccc} \mathbf{I} & \mathbf{0} & \mathbf{0} & \mathbf{0} & \mathbf{0} & \mathbf{0} \\ N_{(1)}(\alpha)\mathbf{I} & \mathbf{0} & \mathbf{0} & \mathbf{0} & N_{(2)}(\alpha)\mathbf{I} & \mathbf{0} \\ N_{(1)}(\beta)\mathbf{I} & \mathbf{0} & \mathbf{0} & \mathbf{0} & \mathbf{0} & N_{(3)}(\beta)\mathbf{I} \end{array} \right] \tag{C.2}$$

Matrices $\hat{\mathbf{N}}^{+}$ and $\mathbf{T}^{+}$ for the triangular positive subdomain:

$$\hat{\mathbf{N}}^{+} = \left[\begin{array}{c|c|c|c} \hat{N}^{+}_{(\alpha)}\mathbf{I} & \hat{N}^{+}_{(2)}\mathbf{I} & \hat{N}^{+}_{(3)}\mathbf{I} & \hat{N}^{+}_{(\beta)}\mathbf{I} \end{array} \right] \tag{C.3}$$

$$\mathbf{T}^{+} = \left[\begin{array}{ccc|ccc} \mathbf{0} & N_{(2)}(\alpha)\mathbf{I} & \mathbf{0} & N_{(1)}(\alpha)\mathbf{I} & \mathbf{0} & \mathbf{0} \\ \mathbf{0} & \mathbf{I} & \mathbf{0} & \mathbf{0} & \mathbf{0} & \mathbf{0} \\ \mathbf{0} & \mathbf{0} & \mathbf{I} & \mathbf{0} & \mathbf{0} & \mathbf{0} \\ \mathbf{0} & \mathbf{0} & N_{(3)}(\beta)\mathbf{I} & N_{(1)}(\beta)\mathbf{I} & \mathbf{0} & \mathbf{0} \end{array} \right] \tag{C.4}$$

Matrices $\hat{\mathbf{N}}^{J}$ and $\mathbf{T}^{J}$ on the discontinuity:

$$\hat{\mathbf{N}}^{J} = \left[\begin{array}{c|c|c|c} -\hat{N}_{(\beta)}\mathbf{I} & -\hat{N}_{(\alpha)}\mathbf{I} & \hat{N}_{(\beta)}\mathbf{I} & \hat{N}_{(\alpha)}\mathbf{I} \end{array} \right] \tag{C.5}$$

$$\mathbf{T}^{J} = \left[\begin{array}{ccc|ccc} N_{(1)}(\beta)\mathbf{I} & \mathbf{0} & \mathbf{0} & \mathbf{0} & \mathbf{0} & N_{(3)}(\beta)\mathbf{I} \\ N_{(1)}(\alpha)\mathbf{I} & \mathbf{0} & \mathbf{0} & \mathbf{0} & N_{(2)}(\alpha)\mathbf{I} & \mathbf{0} \\ \mathbf{0} & \mathbf{0} & N_{(3)}(\beta)\mathbf{I} & N_{(1)}(\beta)\mathbf{I} & \mathbf{0} & \mathbf{0} \\ \mathbf{0} & N_{(2)}(\alpha)\mathbf{I} & \mathbf{0} & N_{(1)}(\alpha)\mathbf{I} & \mathbf{0} & \mathbf{0} \end{array} \right] \tag{C.6}$$

C.2 Triangular element with special configuration for a discontinuity coinciding with one node and crossing an edge (Fig.C.1b)

Matrices $\hat{\mathbf{N}}^{-}$ and $\mathbf{T}^{-}$ for the triangular negative subdomain:

$$\hat{\mathbf{N}}^{-} = \left[\begin{array}{c|c|c} \hat{N}^{-}_{(1)}\mathbf{I} & \hat{N}^{-}_{(\alpha)}\mathbf{I} & \hat{N}^{-}_{(3)}\mathbf{I} \end{array} \right] \tag{C.7}$$

$$\mathbf{T}^{-} = \left[\begin{array}{ccc|ccc} \mathbf{I} & \mathbf{0} & \mathbf{0} & \mathbf{0} & \mathbf{0} & \mathbf{0} \\ N_{(1)}(\alpha)\,\mathbf{I} & \mathbf{0} & \mathbf{0} & \mathbf{0} & N_{(2)}(\alpha)\,\mathbf{I} & \mathbf{0} \\ \mathbf{0} & \mathbf{0} & \mathbf{0} & \mathbf{0} & \mathbf{0} & \mathbf{I} \end{array}\right] \tag{C.8}$$

Matrices $\hat{\mathbf{N}}^{+}$ and $\mathbf{T}^{+}$ for the triangular positive subdomain:

$$\hat{\mathbf{N}}^{+} = \left[\begin{array}{c|c|c} \hat{N}^{+}_{(\alpha)}\mathbf{I} & \hat{N}^{+}_{(2)}\mathbf{I} & \hat{N}^{+}_{(3)}\mathbf{I} \end{array}\right] \tag{C.9}$$

$$\mathbf{T}^{+} = \left[\begin{array}{ccc|ccc} \mathbf{0} & N_{(2)}(\alpha)\,\mathbf{I} & \mathbf{0} & N_{(1)}(\alpha)\,\mathbf{I} & \mathbf{0} & \mathbf{0} \\ \mathbf{0} & \mathbf{I} & \mathbf{0} & \mathbf{0} & \mathbf{0} & \mathbf{0} \\ \mathbf{0} & \mathbf{0} & \mathbf{I} & \mathbf{0} & \mathbf{0} & \mathbf{0} \end{array}\right] \tag{C.10}$$

Matrices $\hat{\mathbf{N}}^{J}$ and $\mathbf{T}^{J}$ on the discontinuity:

$$\hat{\mathbf{N}}^{J} = \left[\begin{array}{c|c|c|c} -\hat{N}_{(\beta)}\mathbf{I} & -\hat{N}_{(\alpha)}\mathbf{I} & \hat{N}_{(\beta)}\mathbf{I} & \hat{N}_{(\alpha)}\mathbf{I} \end{array}\right] \tag{C.11}$$

$$\mathbf{T}^{J} = \left[\begin{array}{ccc|ccc} \mathbf{0} & \mathbf{0} & \mathbf{0} & \mathbf{0} & \mathbf{0} & \mathbf{I} \\ N_{(1)}(\alpha)\,\mathbf{I} & \mathbf{0} & \mathbf{0} & \mathbf{0} & N_{(2)}(\alpha)\,\mathbf{I} & \mathbf{0} \\ \mathbf{0} & \mathbf{0} & \mathbf{I} & \mathbf{0} & \mathbf{0} & \mathbf{0} \\ \mathbf{0} & N_{(2)}(\alpha)\,\mathbf{I} & \mathbf{0} & N_{(1)}(\alpha)\,\mathbf{I} & \mathbf{0} & \mathbf{0} \end{array}\right] \tag{C.12}$$

C.3 Triangular element with special configuration for a discontinuity coinciding with only one node (Fig.C.1c)

Matrices $\hat{\mathbf{N}}^{-}$ and $\mathbf{T}^{-}$ for the triangular negative subdomain:

$$\hat{\mathbf{N}}^{-} = \left[\begin{array}{c|c|c} \hat{N}^{-}_{(1)}\mathbf{I} & \hat{N}^{-}_{(2)}\mathbf{I} & \hat{N}^{-}_{(3)}\mathbf{I} \end{array}\right] \tag{C.13}$$

$$\mathbf{T}^{-} = \left[\begin{array}{ccc|ccc} \mathbf{I} & \mathbf{0} & \mathbf{0} & \mathbf{0} & \mathbf{0} & \mathbf{0} \\ \mathbf{0} & \mathbf{0} & \mathbf{0} & \mathbf{0} & \mathbf{I} & \mathbf{0} \\ \mathbf{0} & \mathbf{0} & \mathbf{I} & \mathbf{0} & \mathbf{0} & \mathbf{0} \end{array}\right] \tag{C.14}$$

C.3.1 Triangular element with special configuration for a discontinuity coinciding with an edge (Fig.C.1d)

Matrices $\hat{\mathbf{N}}^{-}$ and $\mathbf{T}^{-}$ for the triangular negative subdomain:

$$\hat{\mathbf{N}}^{-} = \left[\begin{array}{c|c|c} \hat{N}^{-}_{(1)}\mathbf{I} & \hat{N}^{-}_{(2)}\mathbf{I} & \hat{N}^{-}_{(3)}\mathbf{I} \end{array} \right] \tag{C.15}$$

$$\mathbf{T}^{-} = \left[\begin{array}{ccc|ccc} \mathbf{I} & \mathbf{0} & \mathbf{0} & \mathbf{0} & \mathbf{0} & \mathbf{0} \\ \mathbf{0} & \mathbf{0} & \mathbf{0} & \mathbf{0} & \mathbf{I} & \mathbf{0} \\ \mathbf{0} & \mathbf{0} & \mathbf{0} & \mathbf{0} & \mathbf{0} & \mathbf{I} \end{array} \right] \tag{C.16}$$

Matrices $\hat{\mathbf{N}}^{J}$ and $\mathbf{T}^{J}$ on the discontinuity:

$$\hat{\mathbf{N}}^{J} = \left[\begin{array}{c|c|c|c} -\hat{N}_{(3)}\mathbf{I} & -\hat{N}_{(2)}\mathbf{I} & \hat{N}_{(3)}\mathbf{I} & \hat{N}_{(2)}\mathbf{I} \end{array} \right] \tag{C.17}$$

$$\mathbf{T}^{J} = \left[\begin{array}{cccc|cccc} \mathbf{0} & \mathbf{0} & \mathbf{0} & \mathbf{0} & \mathbf{0} & \mathbf{0} & \mathbf{I} & \mathbf{0} \\ \mathbf{0} & \mathbf{0} & \mathbf{0} & \mathbf{0} & \mathbf{0} & \mathbf{I} & \mathbf{0} & \mathbf{0} \\ \mathbf{0} & \mathbf{0} & \mathbf{I} & \mathbf{0} & \mathbf{0} & \mathbf{0} & \mathbf{0} & \mathbf{0} \\ \mathbf{0} & \mathbf{I} & \mathbf{0} & \mathbf{0} & \mathbf{0} & \mathbf{0} & \mathbf{0} & \mathbf{0} \end{array} \right] \tag{C.18}$$

Appendix D

XFEM formulation based on natural shape functions, spurious oscillations and interpretation

D.1 Natural interpolation matrix N

The "natural" interpolation scheme, generally assumed in existing XFEM formulations, represented in Figure D.1, is based on the following assumptions:

1. The discontinuity subdivides element in two subdomains, crossing element edges at intersection points α and β, with local coordinates $\boldsymbol{r}_\alpha$, $\boldsymbol{r}_\beta$ and classical Gauss points are defined within each subdomain (Fig. D.1a)

2. classical interpolation functions of the original element (Fig. D.1c) are used to interpolate the main variable in terms of the original nodal variables (regular $\mathbf{u}_k$ and additional $\boldsymbol{\delta}_k$). For points in the negative and positive subdomains this gives:

$$\mathbf{u}^{-}(\boldsymbol{r}) = N_{(1)}(\boldsymbol{r})\,\mathbf{u}(1) + N_{(2)}(\boldsymbol{r})\,\boldsymbol{\delta}_{(2)} + N_{(3)}(\boldsymbol{r})\,\boldsymbol{\delta}_{(3)} + N_{(4)}(\boldsymbol{r})\,\mathbf{u}(4) \tag{D.1}$$

$$\mathbf{u}^{+}(\boldsymbol{r}) = N_{(1)}(\boldsymbol{r})\,\boldsymbol{\delta}_{(1)} + N_{(2)}(\boldsymbol{r})\,\mathbf{u}(2) + N_{(3)}(\boldsymbol{r})\,\mathbf{u}(3) + N_{(4)}(\boldsymbol{r})\,\boldsymbol{\delta}_{(4)} \tag{D.2}$$

In order to better interpret the consequences of these assumptions and compare to the new approach proposed with sub-interpolation, it is convenient to replace the additional variables at

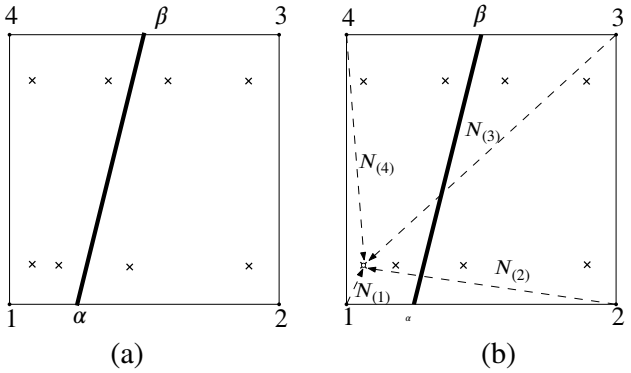

Figure D.1: Natural interpolation: (a) Intersection points α, β and subdomain Gauss points location. (b) Standard interpolation functions $N_{(i)}$ of the global element are used already to interpolate nodal variables to the subdomain Gauss points.

the nodes $\boldsymbol{\delta}_k\,(k=1,4)$ by the physical displacements at the negative and positive sides of the intersection points $\boldsymbol{u}^-_{(\alpha)}$,$\boldsymbol{u}^+_{(\alpha)}$,$\boldsymbol{u}^-_{(\beta)}$,$\boldsymbol{u}^+_{(\beta)}$. This is achieved by considering first the linear interpolation along element edge 1-2 (where $N_{(3)}=N_{(4)}=0$):

$$\mathbf{u}^-_{(\alpha)} = \boldsymbol{u}^-\big(\boldsymbol{r}_{(\alpha)}\big) = N_{(1)}\big(\boldsymbol{r}_{(\alpha)}\big)\,\mathbf{u}_{(1)} + N_{(2)}\big(\boldsymbol{r}_{(\alpha)}\big)\,\boldsymbol{\delta}_{(2)} \tag{D.3}$$

$$\mathbf{u}^+_{(\alpha)} = \boldsymbol{u}^+\big(\boldsymbol{r}_{(\alpha)}\big) = N_{(1)}\big(\boldsymbol{r}_{(\alpha)}\big)\,\boldsymbol{\delta}_{(1)} + N_{(2)}\big(\boldsymbol{r}_{(\alpha)}\big)\,\mathbf{u}_{(2)} \tag{D.4}$$

from which one obtains:

$$\boldsymbol{\delta}_{(2)} = \frac{1}{N_{(2)}\big(\boldsymbol{r}_{(\alpha)}\big)}\mathbf{u}^-_{(\alpha)} - \frac{N_{(1)}\big(\boldsymbol{r}_{(\alpha)}\big)}{N_{(2)}\big(\boldsymbol{r}_{(\alpha)}\big)}\mathbf{u}_{(1)} \tag{D.5}$$

$$\boldsymbol{\delta}_{(1)} = \frac{1}{N_{(1)}\big(\boldsymbol{r}_{(\alpha)}\big)}\mathbf{u}^+_{(\alpha)} - \frac{N_{(2)}\big(\boldsymbol{r}_{(\alpha)}\big)}{N_{(1)}\big(\boldsymbol{r}_{(\alpha)}\big)}\mathbf{u}_{(2)} \tag{D.6}$$

By doing similarly along edge 3-4 one obtains:

$$\boldsymbol{\delta}_{(4)} = \frac{1}{N_{(4)}\big(\boldsymbol{r}_{(\beta)}\big)}\boldsymbol{u}^+_{(\beta)} - \frac{N_{(3)}\big(\boldsymbol{r}_{(\beta)}\big)}{N_{(4)}\big(\boldsymbol{r}_{(\beta)}\big)}\boldsymbol{u}_{(3)} \tag{D.7}$$

$$\boldsymbol{\delta}_{(3)} = \frac{1}{N_{(3)}\big(\boldsymbol{r}_{(\beta)}\big)}\boldsymbol{u}^-_{(\beta)} - \frac{N_{(4)}\big(\boldsymbol{r}_{(\beta)}\big)}{N_{(3)}\big(\boldsymbol{r}_{(\beta)}\big)}\boldsymbol{u}_{(4)} \tag{D.8}$$

Replacing now (D.5-D.6) and (D.7-D.8) into equation (D.3) leads to the new interpolation expression for the negative subdomain

$$\mathbf{u}^{-}(\boldsymbol{r}) = \hat{N}^{-}_{(1)}(\boldsymbol{r})\,\mathbf{u}_{(1)} + \hat{N}^{-}_{(\alpha)}(\boldsymbol{r})\,\mathbf{u}^{-}_{(\alpha)} + \hat{N}^{-}_{(\beta)}(\boldsymbol{r})\,\mathbf{u}^{-}_{(\beta)} + \hat{N}^{-}_{(4)}(\boldsymbol{r})\,\mathbf{u}_{(4)} \tag{D.9}$$

where $\hat{N}^{-}_{(1)}$, $\hat{N}^{-}_{(\alpha)}$, $\hat{N}^{-}_{(\beta)}$ and $\hat{N}^{-}_{(4)}$ are the subdomain local interpolation functions in terms of the displacement values at the corners of that subdomain, with expressions:

$$\hat{N}^{-}_{(1)}(\boldsymbol{r}) = N_{(1)}(\boldsymbol{r}) - \frac{N_{(1)}\big(\boldsymbol{r}_{(\alpha)}\big)}{N_{(2)}\big(\boldsymbol{r}_{(\alpha)}\big)} N_{(2)}(\boldsymbol{r}) \tag{D.10}$$

$$\hat{N}^{-}_{(\alpha)}(\boldsymbol{r}) = \frac{1}{N_{(2)}\big(\boldsymbol{r}_{(\alpha)}\big)} N_{(2)}(\boldsymbol{r}) \tag{D.11}$$

$$\hat{N}^{-}_{(\beta)}(\boldsymbol{r}) = \frac{1}{N_{(3)}\big(\boldsymbol{r}_{(\beta)}\big)} N_{(3)}(\boldsymbol{r}) \tag{D.12}$$

$$\hat{N}^{-}_{(4)}(\boldsymbol{r}) = N_{(4)}(\boldsymbol{r}) - \frac{N_{(4)}\big(\boldsymbol{r}_{(\alpha)}\big)}{N_{(3)}\big(\boldsymbol{r}_{(\alpha)}\big)} N_{(3)}(\boldsymbol{r}) \tag{D.13}$$

$$\tag{D.14}$$

Consider now the edge $\alpha - \beta$ of this negative sub-element, which coincides with the discontinuity line. A basic finite element requirement for inter-element continuity (conformity) is that the interpolation on any element edge or face should depend only on the nodal variables on the same element edge or face (and not on the nodal variables of any other node of the element). In this case, this means that the displacement value along that edge should not depend on $\boldsymbol{u}_{(1)}$ or $\boldsymbol{u}_{(4)}$, and the only way for that to happen is if $\hat{N}^{-}_{(1)}$ and $\hat{N}^{-}_{(4)}$ both vanish along that edge, that is, if

$$\hat{N}^{-}_{(1)}(\boldsymbol{r}) = N_{(1)}(\boldsymbol{r}) - \frac{N_{(1)}\big(\boldsymbol{r}_{(\alpha)}\big)}{N_{(2)}\big(\boldsymbol{r}_{(\alpha)}\big)} N_{(2)}(\boldsymbol{r}) = 0 \tag{D.15}$$

$$\hat{N}^{-}_{(4)}(\boldsymbol{r}) = N_{(4)}(\boldsymbol{r}) - \frac{N_{(4)}\big(\boldsymbol{r}_{(\alpha)}\big)}{N_{(3)}\big(\boldsymbol{r}_{(\alpha)}\big)} N_{(3)}(\boldsymbol{r}) = 0 \tag{D.16}$$

$$\tag{D.17}$$

In the Q4 linear element considered, this only can happen along lines parallel to edges $1-4$ and $2-3$ (parallel in the sense of local coordinates), and therefore this means that the local

interpolation functions implied by natural interpolation cannot satisfy the conformity requirement along the discontinuity line in the general case that the discontinuity runs skew to the FE mesh. Similarly, for the positive subdomain the interpolation expression reads

$$\mathbf{u}^{+}(\boldsymbol{r}) = \hat{N}^{+}_{(\alpha)}(\boldsymbol{r})\,\mathbf{u}^{+}_{(\alpha)} + \hat{N}^{+}_{(2)}(\boldsymbol{r})\,\mathbf{u}_{(2)} + \hat{N}^{+}_{(3)}(\boldsymbol{r})\,\mathbf{u}_{(3)} + \hat{N}^{+}_{(\beta)}(\boldsymbol{r})\,\mathbf{u}^{+}_{(\beta)} \tag{D.18}$$

with the local subdomain interpolation functions

$$\hat{N}^{+}_{(\alpha)}(\boldsymbol{r}) = \frac{1}{N_{(1)}\big(\boldsymbol{r}_{(\alpha)}\big)} N_{(1)}(\boldsymbol{r}) \tag{D.19}$$

$$\hat{N}^{+}_{(2)}(\boldsymbol{r}) = N_{(2)}(\boldsymbol{r}) - \frac{N_{(2)}\big(\boldsymbol{r}_{(\alpha)}\big)}{N_{(1)}\big(\boldsymbol{r}_{(\alpha)}\big)} N_{(1)}(\boldsymbol{r}) \tag{D.20}$$

$$\hat{N}^{+}_{(3)}(\boldsymbol{r}) = N_{(3)}(\boldsymbol{r}) - \frac{N_{(3)}\big(\boldsymbol{r}_{(\alpha)}\big)}{N_{(4)}\big(\boldsymbol{r}_{(\alpha)}\big)} N_{(4)}(\boldsymbol{r}) \tag{D.21}$$

$$\hat{N}^{+}_{(\beta)}(\boldsymbol{r}) = \frac{1}{N_{(4)}\big(\boldsymbol{r}_{(\beta)}\big)} N_{(4)}(\boldsymbol{r}) \tag{D.22}$$

$$\tag{D.23}$$

The conformity condition would require in this case that $\hat{N}^{+}_{(2)}(\boldsymbol{r})$ and $\hat{N}^{+}_{(3)}(\boldsymbol{r})$ vanish along the discontinuity line, which can only happen if that line is parallel (in the sense of local coordinates) to the element edges, and therefore the conditions *cannot* be satisfied for skew discontinuities. Figure D.2 depicts the local subdomain shape functions in elements where the discontinuity is not parallel to the element faces. Shape functions of original nodes $\hat{N}^{-}_{(1)}$, $\hat{N}^{+}_{(2)}$, $\hat{N}^{+}_{(3)}$ and $\hat{N}^{-}_{(4)}$ do not vanish along the discontinuity line as one would expect. Shape functions of intersection points $\hat{N}^{-}_{(\alpha)}$, $\hat{N}^{-}_{(\beta)}$, $\hat{N}^{+}_{(\alpha)}$ and $\hat{N}^{+}_{(\beta)}$ are non-linear along the discontinuity line and, as shown in the last two diagrams, do not coincide one-to-one along that line even in the case that the two nodes of each pair would take the same values.

Therefore, it is not surprising that when the discontinuity is skew to the mesh lines this scheme leads to spurious oscillations (although these oscillations may be reduced by mesh refinement), as seen in Figures D.4 and D.5. Note that all these problems disappear in the new scheme proposed with sub-interpolation, since displacement fields along the discontinuity line become linear and conformity is guaranteed.

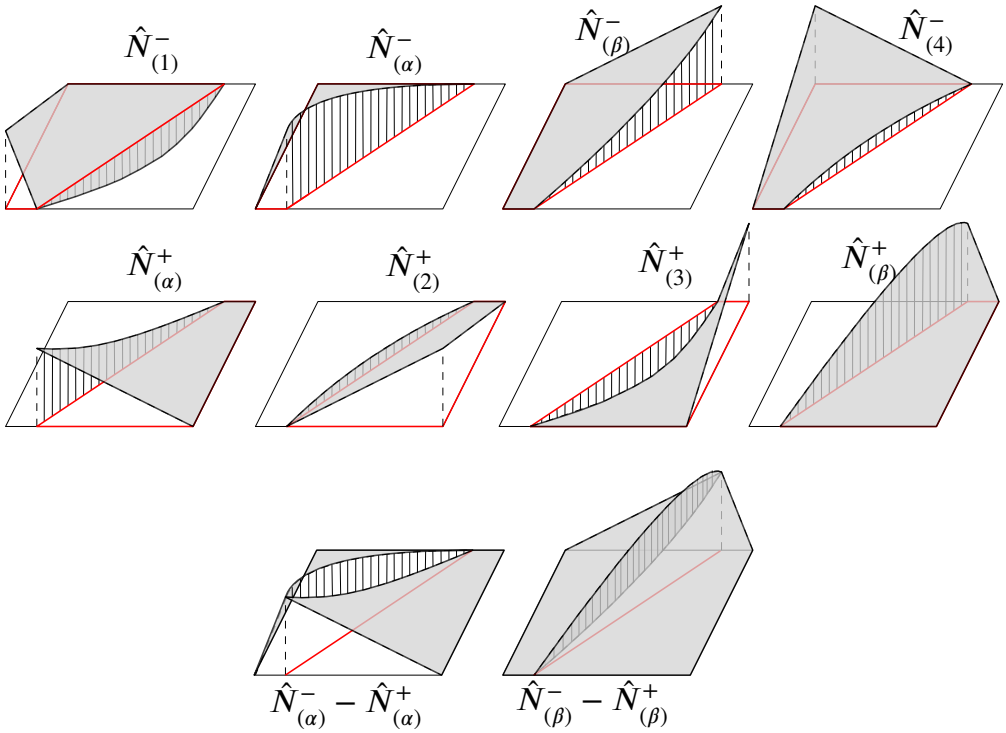

Figure D.2: Subdomain shape functions used in the natural interpolation.

D.2 Verification example

The above arguments are illustrated with the following example of application consisting of a short rectangular beam of 4×1m subject to axial tension, which is crossed by a skew XFEM elastic discontinuity (Fig. D.3). The load is applied via horizontal displacement of value $u_x = 0.001$m, on the right end of the beam, while horizontal movement on the left end is prescribed to zero. In this example, small deformations, plane strain and isotropic elastic material are assumed, with Young modulus $E = 1000$MPa, Poisson's ratio $\nu = 0$, and XFEM discontinuity stiffness has been assumed very high $K_N = K_T = 10^8$MPa/s.

Note that with the high values assumed for K_N, K_T, the case analyzed should correspond to uniform uniaxial tension, and stress on the discontinuity should be constant and equal to the normal and shear stress projections on the plane oriented with the discontinuity, of that uniaxial state.

The stress values obtained solving that problem with natural interpolation and sub-interpolation

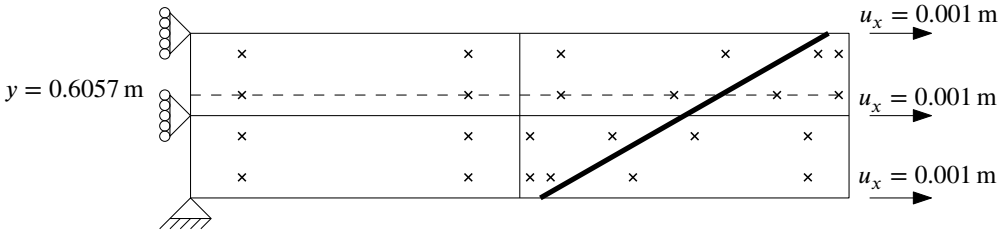

Figure D.3: Short rectangular beam of 4×1m discretized into four quadrangular elements and crossed by an inclined discontinuity (bold line). Crosses represent Gauss points of the resulting elements and subdomains.

are depicted in Fig. D.4 (continuum) and D.5 (discontinuity). In order to discriminate the possible effect of the integration rule along the discontinuity segments contained within each element, the calculations have been repeated using three different integration rules: trapezoidal rule, Gauss 2-points rule and Simpson's rule. Using natural interpolation, stresses in the continuum (Fig. D.4) turn out not constant, varying from $\sigma_x = 0.2203$MPa to $\sigma_x = 0.2618$MPa, while the correct result should be $\sigma_x = 0.2500$MPa, as it is obtained correctly using double interpolation (Fig. D.4a). Also σ_{yy} and τ_{xy} should be identically zero in this uniaxial case, and this is correct with double interpolation while natural interpolation leads to spurious non-zero values. Note that the stress values in the continuum are the same for the three integration rules along the discontinuity.

Stress tractions along the discontinuity, represented in Fig. D.5, reflect the same situation. Double interpolation leads to the correct constant values of normal and tangential stress tractions $\sigma_j = 0.0589$m and $\tau_j = 0.1061$MPa, while natural solution oscillates significantly for any of the three integration rules used.

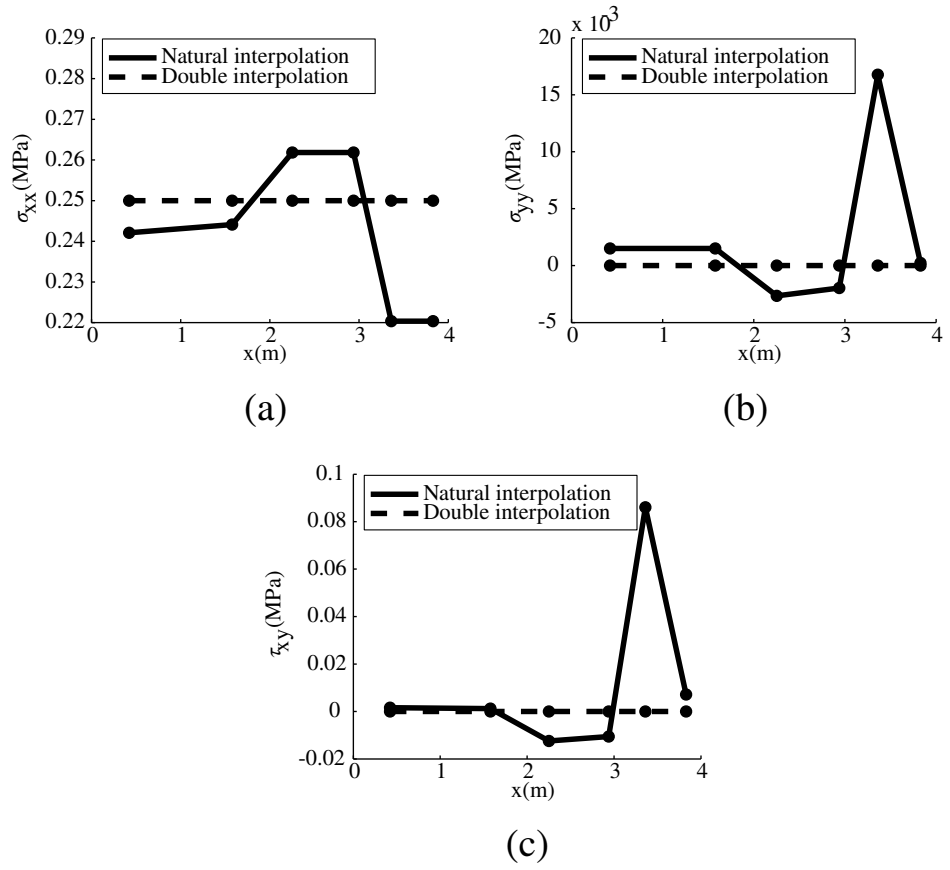

Figure D.4: Stress component values along a horizontal line containing the Gauss points at $y = 0.6057$m. The solid line corresponds to the traditional XFEM formulation with natural interpolation (same results for all integration rules along the discontinuity), and the dashed line for the formulation described with double interpolation. (a) σ_{xx}, (b) σ_{yy} and (c) σ_{xy}.

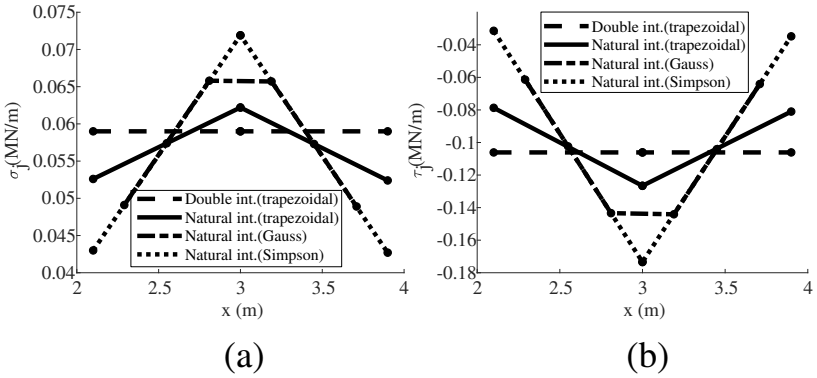

Figure D.5: Stress field along the discontinuity line obtained using three different integration rules along the discontinuity section corresponding to each element: (a) Normal component, σ_j. (b) Tangential component, τ_j.

Appendix E

Derivative with respect to nodal coordinates of the shape function Cartesian derivatives

Applying the chain rule, the derivative with respect to nodal coordinates of the shape function Cartesian derivatives, can be expressed as a function of local coordinates as follows:

$$\frac{\partial}{\partial X_i^{(a)}}\left(\frac{\partial N^{(b)}}{\partial X_k}\right) = \frac{\partial}{\partial X_i^{(a)}}\left(\frac{\partial N^{(b)}}{\partial \xi_j}\frac{\partial \xi_j}{\partial X_k}\right) \tag{E.1}$$

Noting that the derivative of nodal shape functions with respect to local coordinates does not depend on global coordinates,

$$\frac{\partial}{\partial X_i^{(a)}}\left(\frac{\partial N^{(b)}}{\partial X_k}\right) = \frac{\partial N^{(b)}}{\partial \xi_j}\frac{\partial}{\partial X_i^{(a)}}\left(\frac{\partial \xi_j}{\partial X_k}\right) \tag{E.2}$$

To develop the derivative with respect to nodal coordinates of the local coordinates Cartesian derivatives, it is convenient first to express the later in terms of its inverse by taking advantage of the following tensor relation:

$$\mathbf{A}\mathbf{A}^{-1} = \mathbf{I} \tag{E.3}$$

which, by differentation leads to:

$$\frac{\partial \mathbf{A}}{\partial \mathbf{X}}\mathbf{A}^{-1} + \mathbf{A}\frac{\partial \mathbf{A}^{-1}}{\partial \mathbf{X}} = 0 \tag{E.4}$$

and finally to:

$$\frac{\partial \mathbf{A}}{\partial \mathbf{X}} = -\mathbf{A}\frac{\partial \mathbf{A}^{-1}}{\partial \mathbf{X}}\mathbf{A} \tag{E.5}$$

Therefore, assuming $\mathbf{A} = \partial \xi_j / \partial X_k$ equation (E.2) may be expressed as:

$$\frac{\partial}{\partial X_i^{(a)}}\left(\frac{\partial N^{(b)}}{\partial X_k}\right) = \frac{\partial N^{(b)}}{\partial \xi_j}\left[-\frac{\partial \xi_j}{\partial X_l}\ \frac{\partial}{\partial X_i^{(a)}}\left(\frac{\partial X_l}{\partial \xi_q}\right)\frac{\partial \xi_q}{\partial X_k}\right] \tag{E.6}$$

Now, the derivative with respect to the nodal coordinates of the central term between brackets may be trivially developed using 3.39, leading to:

$$\frac{\partial}{\partial X_i^{(a)}}\left(\frac{\partial X_l}{\partial \xi_q}\right) = \frac{\partial}{\partial X_i^{(a)}}\left(\frac{\partial\left(N^{(b)}X_l^{(b)}\right)}{\partial \xi_q}\right) \tag{E.7}$$

$$= \frac{\partial N^{(b)}}{\partial \xi_q}\frac{\partial X_l^{(b)}}{\partial X_i^{(a)}} \tag{E.8}$$

$$= \frac{\partial N^{(b)}}{\partial \xi_q}\delta^{(a)(b)}\delta_{li} \tag{E.9}$$

$$= \frac{\partial N^{(a)}}{\partial \xi_q}\delta_{li} \tag{E.10}$$

Replacing this into E.6, the final expression is obtained:

$$\frac{\partial}{\partial X_i^{(a)}}\left(\frac{\partial N^{(b)}}{\partial X_k}\right) = -\frac{\partial N^{(b)}}{\partial \xi_j}\left[\frac{\partial \xi_j}{\partial X_l}\frac{\partial N^{(a)}}{\partial \xi_q}\delta_{li}\frac{\partial \xi_q}{\partial X_k}\right] \tag{E.11}$$

$$= -\frac{\partial N^{(b)}}{\partial \xi_j}\frac{\partial \xi_j}{\partial X_i}\frac{\partial N^{(a)}}{\partial \xi_q}\frac{\partial \xi_q}{\partial X_j} \tag{E.12}$$

$$= -\frac{\partial N^{(b)}}{\partial X_i}\frac{\partial N^{(a)}}{\partial X_k} \tag{E.13}$$

Appendix F

Jacobian derivative with respect to nodal coordinates

The Jacobian J_ξ can be expressed as the determinant of the derivative of global coordinates with respect to the local ones (Eq. 3.71):

$$\frac{\partial J_\xi}{\partial X_i^{(a)}} = \frac{\partial}{\partial X_i^{(a)}} \left(\det \frac{\partial \mathbf{X}}{\partial \boldsymbol{\xi}} \right) \tag{F.1}$$

Applying the chain rule it leads to,

$$\frac{\partial}{\partial X_i^{(a)}} \left(\det \frac{\partial \mathbf{X}}{\partial \boldsymbol{\xi}} \right) = \frac{\partial \left(\det \frac{\partial \mathbf{X}}{\partial \boldsymbol{\xi}} \right)}{\partial \left(\frac{\partial X_j}{\partial \xi_k} \right)} \frac{\partial \left(\frac{\partial X_j}{\partial \xi_k} \right)}{\partial X_i^{(a)}} \tag{F.2}$$

The first term can be solved by the well known algebraic expression of a derivative of a determinant (Petersen and Pedersen, 2012).

$$\frac{\partial \det \mathbf{A}}{\partial \mathbf{A}} = (\det \mathbf{A})\, \mathbf{A}^{-1} \tag{F.3}$$

Assuming $\mathbf{A} = (\partial \mathbf{X} / \partial \boldsymbol{\xi})$, leads to:

$$\frac{\partial \left(\det \frac{\partial \mathbf{X}}{\partial \boldsymbol{\xi}} \right)}{\partial \left(\frac{\partial X_j}{\partial \xi_k} \right)} = \left(\det \frac{\partial \mathbf{X}}{\partial \boldsymbol{\xi}} \right) \frac{\partial \xi_k}{\partial X_j} \tag{F.4}$$

Using now Eq. (E.10) for the last partial derivative in Eq.(F.2), one obtains the final expression:

$$\frac{\partial J_\xi}{\partial X_i^{(a)}} = J_\xi \frac{\partial \xi_k}{\partial X_j} \frac{\partial N^{(a)}}{\partial \xi_k} \delta_{ji} = J_\xi \frac{\partial N^{(a)}}{\partial X_i} \tag{F.5}$$